UNIVERSITY OF OKLAHOMA

GRADUATE COLLEGE

FREQUENCY-AGILE MICROWAVE FILTERS FOR RADARS WITH SIMULTANEOUS TRANSMISSION AND RECEPTION

A DISSERTATION

SUBMITTED TO THE GRADUATE FACULTY

in partial fulfillment of the requirements for the

Degree of

DOCTOR OF PHILOSOPHY

By

SHAHROKH SAEEDI
Norman, Oklahoma
2015

FREQUENCY-AGILE MICROWAVE FILTERS FOR RADARS WITH SIMULTANEOUS TRANSMISSION AND RECEPTION

A DISSERTATION APPROVED FOR THE
SCHOOL OF ELECTRICAL AND COMPUTER ENGINEERING

BY

Dr. Hjalti H. Sigmarsson, Chair

Dr. Yang Hong

Dr. Mark Yeary

Dr. Jessica Ruyle

Dr. Caleb J. Fulton

© Copyright by SHAHROKH SAEEDI 2015
All Rights Reserved.

This dissertation is dedicated to my dear wife.
None of this would have been possible without her
unconditional love and support.

Acknowledgments

The completion of this work would not have been possible without the help and encouragement of many people. First, I would like to sincerely thank my research advisor Professor Hjalti Sigmarsson for his continuous support, patient mentoring, supportive advising and encouragement. I am particularly grateful to him for the opportunity he provided for me to conduct independent research. Professor Sigmarsson has provided invaluable vision and a wealth of technical guidance throughout my graduate studies at the University of Oklahoma. I have deeply admired his commitment to academic excellence and dedication to the community and the society. I also sincerely thank my other committee members, Professor Mark Yeary, Professor Yang Hong, Professor Jessica Ruyle, and Professor Caleb Fulton for their interest and valuable expertise, time, and effort in advising my dissertation work. I also wish to thank Professor Juseop Lee for his support, discussions and guidance throughout my research.

I am grateful to the generous financial support for my research by Agency for Defense Development (ADD), Republic of Korea. The staff members at the Advanced Radar Research Center (ARRC) and School of Electrical and Computer Engineering (ECE) deserve my sincere thanks as well.

I would like to extend my thanks to all my colleagues at ARRC and ECE Lukasz Szolc, Hossein Lotfi, Blake James, Mirhamed Mirmozafari, Djordje

Mirkovic, Hossein Hosseini, Robin Irazoqui, Ramesh Nepal, Serkan Ozturk, Sudantha Perera, Hadi Saeidi Manesh, Dakota Benge, Blake McGuire, and Zachary Dunn. My special thanks to Sattar Atash-bahar, William Wilson, C. Justin Smith, David Noel, Jonathan Christian, Tyler Ashley, Zachary Potts, and Dr. Himanshu Joshi who have helped me in fabrication and implementation of my ideas. I wish them all the best of luck with their studies and future careers.

I would also like to thank all my friends, near and distant, whose names I know so well but are too many to be listed here. They have been a constant source of support and strength. My special thanks to my good friends, Dr. Hessam Yazdani and Dr. Shaya Karimkashi, for their invaluable friendship and support since I came to Oklahoma.

Finally, I would like to thank my parents, brothers, wife and my little son for their unfailing support, boundless love, encouragement, and sacrifice. None of this work would have been possible without them. My gratitude to them is more than that can be expressed in words. Thank you.

Table of Contents

List of Tables

List of Figures

Abstract

Multi-band/multi-mode wireless communication systems have been receiving increased attention recently due to their potential for spectrum management in a dynamic spectral environment. Similarly radar systems, which can operate in a variety of frequency bands, could provide significant flexibility in the operation for the future applications. However, multi-band/multi-mode operation adds to the complexity of the microwave systems. Reconfigurable RF/microwave components in general, and tunable filters in particular, have been shown to be promising in significantly reducing the system complexity.

On the other hand, current trend of development in wireless communication and radar systems, forces more stringent requirements for electromagnetic spectrum sharing. Therefore, in many microwave applications a very high level of isolation between the channels are required. This is including simultaneous transmit-receive systems or co-site interference scenarios where the leakage from high power transmitter into receiver degrades the system performance. In these applications, conventional tunable bandpass/bandstop filters cannot provide enough isolation between transmitter and receiver. A promising solution which provides a tunable null, independent of the tunable transmission passband, is a dynamic-tunable bandpass-bandstop filter cascade.

In this research, a frequency-agile bandpass-bandstop filter cascade for radar systems with simultaneous transmission and reception is designed to

create advanced filtering functionality to isolate the desired signals from interfering signals in a spectrally-crowded environment. For a radar with simultaneous transmit and receive, two filter cascade will be required. Each filter will be used on a separate frequency agile transceiver but they will be synchronized to provide simultaneously a deep isolation region at one frequency for receive and a high power tolerant passband at an adjacent frequency for transmit.

Chapter 1

Introduction

1.1 Overview

Future microwave systems operating in an ever-crowded spectrum will require agile front-ends. Agility enables cognitive frequency response control suitable for dynamic spectral environments. Therefore, such sophisticated systems are not bound to single front-end architectures in contrast to past and current systems [1], [2]. Reconfigurable microwave filters will play an important role in such high-performance systems enabling different system architectures for future software-based radios, satellite communication systems, and multi-band/multi-functional radars. Consequently, extensive research has been conducted over the past decade on the synthesis, design, and implementation of reconfigurable microwave filters [3]. An electronically fully-controllable filter with tunable center frequency, bandwidth, and phase performance along with reconfigurable frequency response, order, and location/number of poles is the ultimate goal of filter designers. Such an optimum filter can be field- programmed to adaptively process RF signals with arbitrary frequency content for any given application in any dynamic spectral environment.

From a system point of view, non-cognitive microwave systems with single

front-end architectures need to filter the input signals using a bandpass filter, as knowledge of the spectral environment is unavailable. This requirement is the base of *"fear-based front-end architecture"* in which all input frequencies except the range of interest are attenuated [1], [2]. These architectures with tunable bandpass filters have been shown to be promising for mitigating interference in an environment containing multiple interfering signals. However, the added insertion loss of such filters causes an increase in noise figure, resulting in degraded system sensitivity and thus reduced overall system performance [4].

In contrast, future cognitive microwave systems will be capable of operating in the following modes: (1) no filtering when no significant interfering signals are present; (2) bandpass filtering when there are multiple interfering signals; or (3) bandstop filtering when strong adjacent interference is encountered. Many systems would benefit greatly from the last mode, which can be referred to as a bandstop-based front-end architecture. This configuration exhibits a reduced system noise figure, as the insertion loss of bandstop filters can be kept low, and at the same time used to protect the system from receiver non-linearities resulting from suppression of the interfering signals [2]. Therefore, tunable bandstop filters are going to be utilized in conjunction with tunable bandpass filters in high performance reconfigurable filters to add such flexibility to future systems. This is a new application added to the previous tasks of bandstop filters in attenuating harmonic frequencies at the output of a nonlinear power amplifier or suppressing local oscillator re-radiation.

In a more advanced system, a tunable bandpass filter is combined with a dynamic bandstop filter to take advantage of the last two scenarios. In such a system, a bandpass-bandstop cascade can be used to create advanced

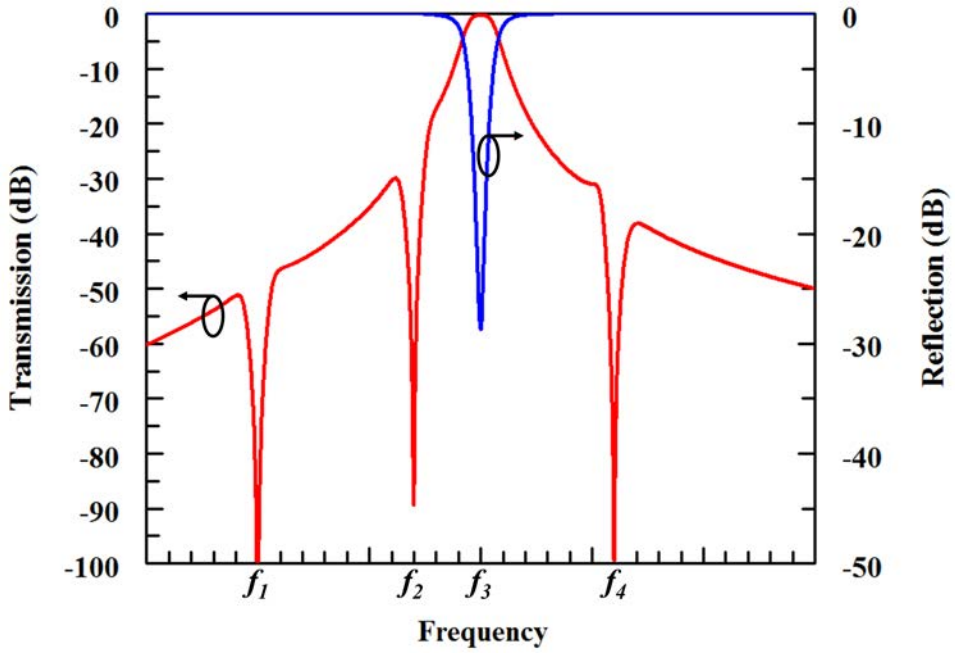

Figure 1.1: Example of a filter cascade with two nulls below and one null above the passband.

filtering functionality to isolate the desired signals from interfering signals in a spectrally-crowded environment where neither a separate bandpass filter nor a single bandstop filter can provide enough isolation [5]–[8]. Such filtering responses are shown for a filter cascade at two different states in figure 1.1 and figure 1.2. The cascade has a second-order bandpass filter placed in cascade with three second-order bandstop filters. In figure 1.1 the bandpass filter is tuned to f_3 while two bandstop filters are tuned to f_1 and f_2 below the passband and one bandstop filter is tuned to f_4 above the passband. While in figure 1.2 all three bandstop filters are tuned to frequencies above the passband, that is f_1, f_2, and f_4 and the bandpass filter is still tuned to f_3. In both states, all frequencies are tunable, independent and have arbitrary values.

Dynamic spectral access and concurrent transmit-receive radars, broadband radios in the presence of co-site interference, ultra high sensitivity re-

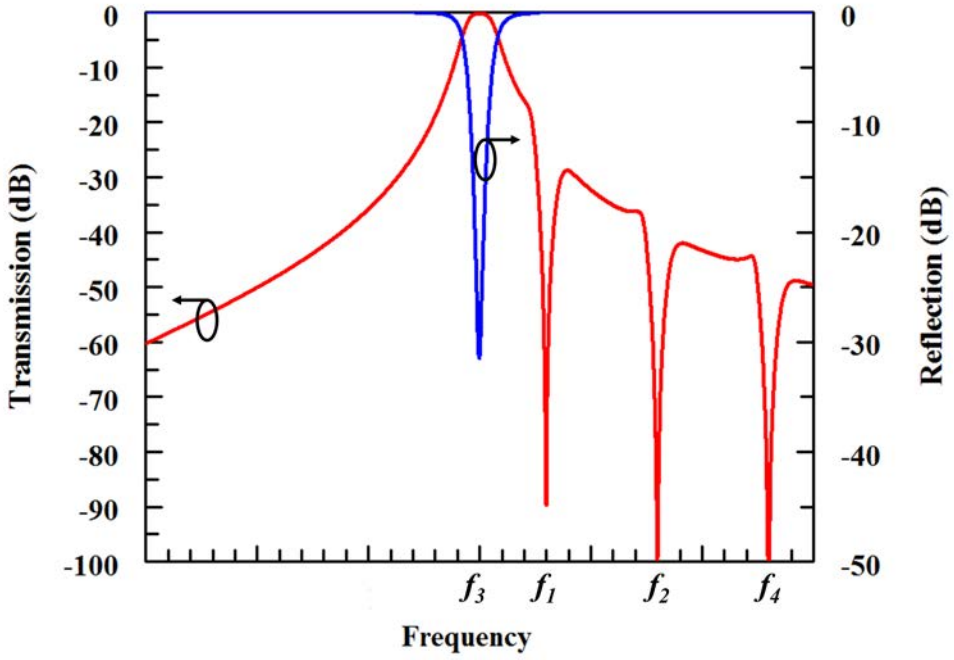

Figure 1.2: Example of a filter cascade with three nulls above the passband.

ceivers, wireless systems with shared-aperture antennas, and spectrum sensing cognitive radios are examples of such systems. Filter cascades have the capability of dynamically relocating transmission zeros around the passband with much less cost, form-factor and complexity of conventional advanced filters with tunable transmission zeros. Therefore, there is a very high interest on the design and development of these state-of-the-art frequency-agile microwave filters for the next generation of adaptive communications and radar systems to enhance the utilization of spectrum by mitigation of interference.

1.2 Microwave Filters from Past to Current

Filters are electric circuits with frequency-dependent characteristics. They are basically used to remove any undesirable-frequency portions of an input sig-

nal and enhance desired ones by providing transmission at frequencies that fall within their passband. Unwanted spurious signals as well as noise make the undesirable-frequency portions of the input signal. Filters utilize energy-storage elements to select or confine the signals within assigned spectral limits. Therefore, they are assumed as the most fundamental signal processing circuits.

Filters have been around mostly in all radio systems since the early stage of electronics industry evolution. These days, they can be found virtually in any RF and microwave communication systems (cellular communications, pagers, satellite communications), wireless data communications (Wi-Fi, Bluetooth), navigation systems (GPS), object detection systems (radars), TV broadcasting, and finally test and measurement systems.

Filter design has been developed gradually along with the advancement of communication technology. Development of filter technology was probably first induced by the introduction of the carrier telephony system in 1910 [9]. Soon, filter technology was officially introduced by independent but simultaneous work of two scientists, one in Germany and the other one in the United States [10]. A filter design method named the *Wagner filter*, was introduced by K. W. Wagner in 1915. Almost at the same time, another design technique, *constant-k filter*, was under development by G. A. Campbell [9]. This technique that got later known as *image parameter* method was developed by O. J. Zobel in the late 1920s [11], [12]. This method was used in low-frequency filters for radio and telephony systems. Later a more modern procedure for filter design called *insertion loss method* was originated by E. L. Norton [12] and then further developed by S. Darlington [11] and W. Cauer [13]. The theory of filter synthesis and design, as the systematic way it is known today,

was mainly studied and developed in the years before and during WWII by the aforementioned scholars and some other pioneers like Mason, Bode, Sykes, Brune, Fano, Lawson, and Richards [10], [12], [14], [15].

A group of researchers including G. L. Matthaei, L. J. E. Young, E. Jones, and S. B. Cohn at Stanford Research Institute did a very extensive study on microwave filters and coupling structure in early 1950s. Their contributions to the development of microwave filter design are still among valuable references on this topic [16]–[20]. By invention of planar microwave structures in the early 50's [21], a variety of new microwave filters were developed [20], [22]. In 1951, Dishal developed a very simple approach for design and tuning of narrow-band filters [23]. He later showed an extension of his method applied to tapped interdigital filters [24]. However, Dishal's method, also known as *K and Q* method, is very general can be applied to many different filter technologies and topologies [25]. Soon, the filter design technology, which was initially bounded to lumped components, got expanded to coaxial and waveguide resonator filters. This was direct result of the advancement of the newly known distributed elements and the broad advances in the microwave materials. The Development of ceramic materials as well as the introduction of microstrip technology also played an important role in the emergence of new types of microwave filters namely, planar and dielectric filters.

Until the early 1970s, almost all filter design techniques were based on the extraction of lumped electrical elements from the polynomials that mathematically described the filter's characteristics. This was adequate for the available technologies and required applications of that time. However, in the early 1970s a big revolution in telecommunication systems happened as satellites were used for communication for the first time. The increasing de-

mand for satellite communication services required more frequency spectrum to accommodate the continuous growth in data quantity. Therefore, the frequency band allocated to satellite communication systems was required to be pushed to higher frequency ranges. This in itself helped the development of the available technologies for implementation of microwave components in higher frequency systems. Also, the growing demand for satellite telecommunication services meant crowding of the available spectrum, which put more stringent requirements on the specifications of channel filters in terms of in-band linearity and out-of-band selectivity [26]. To address these new demands, two significant advancements took place during that time period: (1) the development of techniques for incorporating transmission zeros (TZs) [27], [28] and group delay features in microwave filter; (2) the development of dual-mode technology for waveguide filters. This innovation was in response to very stringent requirements specified for the space-borne microwave filters and was accomplished in two parts. The development of a new method called *coupling matrix method* and a design method for realizing dual-mode waveguide filters with inherent cross-coupling and without complex coupling elements were parts of this advancement [29]–[32]. The introduction of the folded cross-coupled microwave filters enabled designers to implement inter-resonator coupling besides the usual mainline coupling between sequential resonators [33].

Nowadays, filter design and analysis have been revolutionized by recent advances in computer-aided design (CAD) tools especially full-wave electromagnetic (EM) simulators. Meanwhile rapid advances in fabrication technologies such as high-temperature superconductors (HTS), low-temperature co-fired ceramics (LTCC), monolithic microwave-integrated circuit (MMIC), microelectromechanical system (MEMS), substrate-integrated waveguides (SIWs),

and micro-machining technologies, as well as the introduction of novel and artificial materials such as liquid crystal polymers (LCP), ferroelectrics, and metamaterials, have stimulated the rapid development of RF/microwave filter design. Availability of advanced circuit/EM simulators as well as rapid prototyping machines has also contributed to the accelerated development of microwave filter design and fabrication.

1.2.1 Substrate-Integrated-Waveguide Technology

With the everyday development of wireless communications services, satellite applications, and multifunction radar systems low-cost, small-profile, high-performance, and mass-producible microwave components with more functionality and ability of integration with the rest of the system are highly desirable. However, designers are often required to make a compromise between these conflicting requirements. This means that they need to sacrifice some features to get some more important ones. Because simultaneous satisfaction of all design criteria is rather difficult or even technically impossible. For example, to have a filter with higher selectivity the order of the filter, should be increased. However, this in turn will result in a higher insertion loss. Insertion loss, return loss, bandwidth, selectivity, ultimate rejection, tunability, linearity, tuning range, and power handling are just a few basic properties associated with the design of a filter which are usually in conflict.

Although the introduction of planar microwave structures caused revolutionary advances in microwave technology, by addressing most of the above-mentioned requirements, the introduction of SIW technology in 2001 [34] completed the full integration of non-planar and planar microwave circuits and systems. SIW technology can be considered as a hybridization of planar and

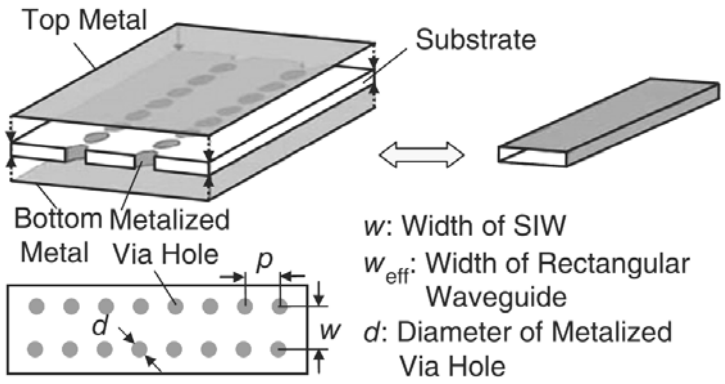

Figure 1.3: Structure of a simple SIW and its equivalent rectangular waveguide (from [35]).

non-planar structures that presents the best compromise in terms of all design aspects. Using this technology almost any non-planar structure can be implemented into a planar form, which results in ease of integration and compatibility with other planar circuits. Thanks to the rapid development of low-cost planar processing and microfabrication techniques, including printed circuit board (PCB) and LTCC, implementation of SIW structures has been made easy.

A basic structure of a typical SIW is shown in figure 1.3. This structure consists of a pair of periodic plated via arrays with specific spacing that well confines EM fields. Similar to conventional metallic waveguides, the SIW structure only supports the propagation of quasi-transverse electric (TE) modes. Transverse magnetic (TM) modes, if be excited, will immediately vanish because of discontinuous side walls that prevent longitudinal current flow. This makes the SIW structure very favorable for bandpass filter design because certain modes that are responsible for out-of-band parasitic responses can be avoided [35].

The region of interest for the proper operation of the SIW is a function of

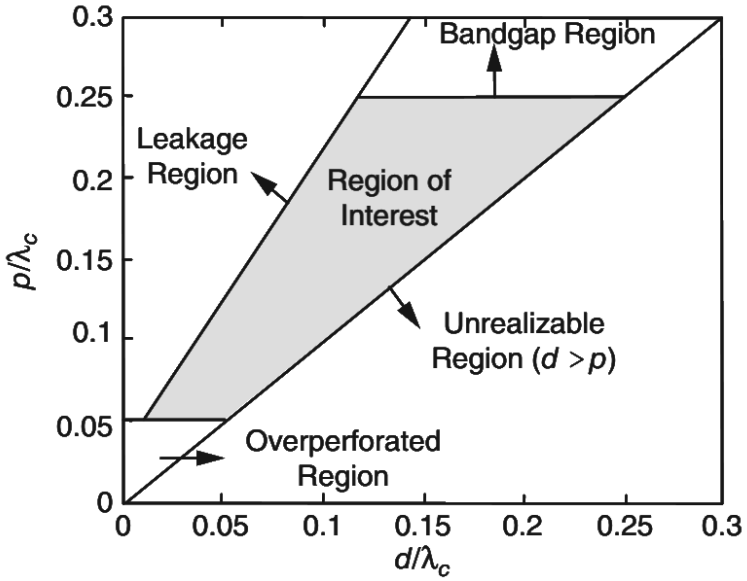

Figure 1.4: The frequency region of interest for the SIW operation (from [36]).

vias diameter (d) and pitch (p), the spacing between adjacent via holes, relative to guided wavelength λ_C. This region is depicted in figure 1.4 [36]. Therefore, d and p should be selected appropriately so that bandgap effects and leakage loss over the entire bandwidth of interest are avoided. The frequency region of interest for TE_{10} mode is defined by the following set of basic but empirical design rules [36]:

$$p > d \tag{1.1a}$$

$$p/\lambda_c < 0.25 \tag{1.1b}$$

$$a_1/k_0 < 1 \times 10^{-4} \tag{1.1c}$$

$$p/\lambda_c > 0.05 \tag{1.1d}$$

where a_1 is the total loss and k_0 is the wave number in free space. Equation (1.1a) guarantees that the circuit is physically realizable while (1.1b) is

used to avoid any bandgap effect in the operating bandwidth of TE_{10} and other related modes. The leakage loss will be negligible if the condition in (1.1c) is met. A more stringent condition for negligible leakage losses is defined as $p \leqslant 2d$. Finally, (1.1d) is a mechanical condition that limits the number of vias to less than of 20% of the wavelength to keep the mechanical rigidity of the board.

In the TE_{10}-mode frequency region of interest, the effective width (w_{eff}) of the equivalent dielectric-filled rectangular metallic waveguide, which has the same cutoff frequency and dispersion properties, can be approximately found from [37]

$$w_{eff} = w - \frac{d^2}{0.95p} \tag{1.2}$$

as long as p is sufficiently small. In (1.2) w is the width of the SIW shown in (1.3). More accurate expressions for the the effective width of the equivalent waveguide can be found in literature [38], [39]. Although these basic design rules provide a good guideline for the designer, usually full-wave field simulations and optimizations are required to validate and tune the SIW circuit. This is often the case for special structures like high-Q, narrowband, and millimeter-wave components.

Because the fields are primarily confined within the geometry, SIW structures are not subject to radiation loss. Therefore, the main loss contributors of SIW structures are dielectric and conductor losses. In general, the total loss is directly proportional to frequency. Therefore, when frequency increases the structure becomes lossier. The increase in loss is also related to surface roughness, decrease in substrate thickness, and the electrical and mechanical quality of metal plating which become more crucial in higher frequencies. The

Table 1.1: Comparison of the Q-factor of a SIW transmission line with respect to that of 50-Ω microstrip line, and a standard rectangular metallic waveguide all at Ka-band (from [37]).

Properties	**Microstrip[1]**	**SIW[2]**	**Waveguide**
Quality Factor	42	462	4613
[1]Substrate: $\epsilon_r = 2.33,\ tan(\delta) = 5 \times 10^{-4},\ h = 10$ mils, copper foil [2]Width=200 mils			

total loss determines the quality factor of the transmission line. A comparison of typical quality factor for a SIW transmission line, a 50-Ω microstrip line, and a standard rectangular metallic waveguide, all operating in Ka-band, is shown in Table 1.1 [35]. It can be seen that the quality factor of the SIW is significantly larger than that of the microstrip line, but it is still lower than that of the standard waveguide. However, it should be noted that the waveguide is a bulky and costly structure and both SIW and microstrip lines are low-cost planar structures.

The other attractive features of SIW structures that makes them a very popular technology for development of microwave components, in general, and filter design, in particular, can be seen in figure 1.5 [36]. This figure compares various microwave resonators in terms of the basic merit parameters. Since the unloaded quality factor for each category is a function of the resonator configuration, excitation, and operating mode therefore, a very wide range for the unloaded quality factor in each category has been reported. It can be seen that when high selectivity is required waveguide and dielectric resonators are the best choices. Their size, weight, and cost, however, are the most limiting factors that prevent them from being used in many applications. On the other hand, microstrip and stripline resonators provide the least cost and size

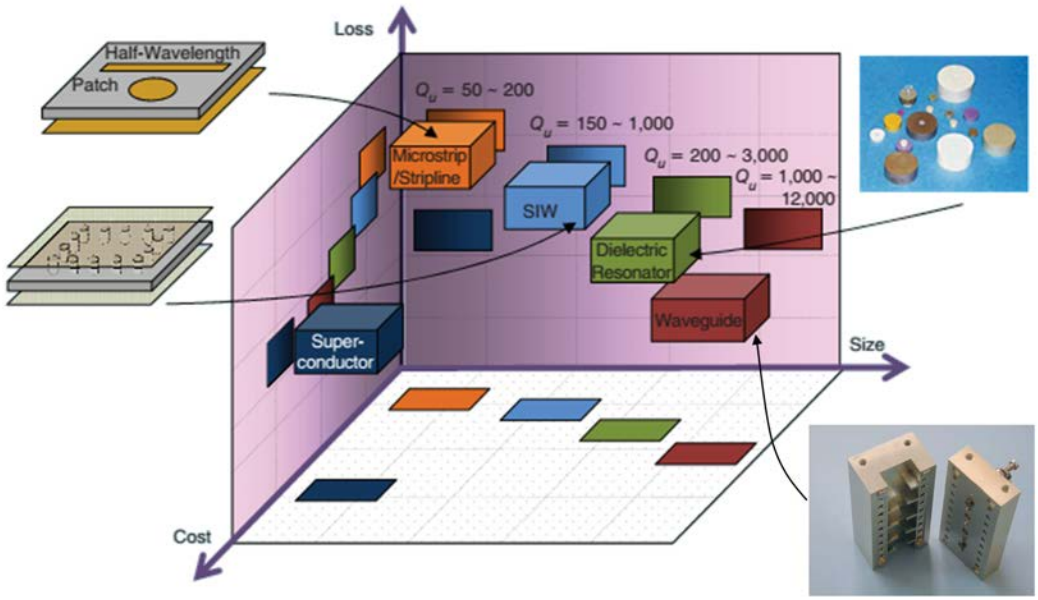

Figure 1.5: Comparison of various microwave resonators in terms of loss, cost, size, and typical quality factor (from [35]).

compared to other technologies, although their quality factor is fundamentally limited by their losses. Finally, it can be seen that SIW technology can fill the technological gap between these non-planar and planar structures by simply combining the best features of both older technologies. SIW technology offers high-quality factors close to those of non-planar structures with size- and cost- related advantages of the planar circuits. This discussion clearly reveals that SIW structures provide perfect trade-off between loss, size and cost for future low-cost, small-profile, high-performance designs with the ability of integration.

Since the introduction of SIW structures, a variety of passive and active microwave components such as antennas, directional couplers, filters, oscillators, and power amplifiers have been developed using this technology [40]. The other feature of SIW structures, that turn them to a very popular technology for current and future microwave systems, is their flexibility in frequency-agile

components designs. Due to low loss, good isolation, high quality factor, and tunability feature of SIW structures, they are very good candidates for tunable and reconfigurable microwave cavity filters. Adaptable filters are promising substitutes for filter banks and multi-band filters in software-defined (SD) and cognitive radios (CRs). Until now, different techniques as well as various tuning mechanisms have been investigated for designing tunable and reconfigurable SIW filters. A comprehensive review of SIW filter design methods including tunable and frequency-agile filters have been presented in [35], [40]–[42].

1.2.2 Evanescent-Mode Cavity Resonators

Waveguides can not be used below their cutoff frequency for guiding waves. In fact, the propagation constant in waveguides below the cutoff frequency is a real value which results in rapid attenuation of waves [43]. Therefore, waves below cutoff frequency are said to be evanescent. However, it is well known that by loading waveguides, they can be used to create microwave filters below their cutoff frequency [20]. The microwave resonators operating below the cutoff frequency of the forming waveguide, are referred to as evanescent-mode or re-entrant cavity resonators [44].

Introducing of an obstacle like conductive re-entrant post inside waveguide cavity resonators, is a common way of loading them. The conductive post loads the cavity by an effective shunt capacitor. The amount of the loading capacitor determines the resonant frequency of the cavity and can be used for frequency tuning of the resonator. The capacitive post concentrates the electric-field above the conductive post without greatly affecting of the magnetic-field distribution. The confinement of the electric-field above the

post increases the tuning sensitivity of the resonator. The capacitive loading also results in a significant decrease in the resonant frequency of the structure without having much impact on the unloaded quality factor of the resonator. Therefore, this method can be used for size reduction of air-filled cavities for a specific resonant frequency without greatly sacrificing the unloaded Q. In order to understand this behavior, consider a air-filled cylindrical cavity resonator operating in its first resonating mode. In this resonator, when the height (d) of structure is smaller than its diameter ($2a$), the first dominant mode is TM_{010} mode, which its resonant frequency is expressed as [45]

$$f_{TM_{010}} = \frac{2.405}{2\pi a\sqrt{\mu_0\epsilon_0}} \tag{1.3}$$

Also, the unloaded Q of the cavity resonator can be found from [45]

$$Q = \frac{1.202\eta}{R_s(1+\frac{a}{d})} \tag{1.4a}$$

$$R_s = \sqrt{\frac{\pi f\mu_0}{\sigma}} \tag{1.4b}$$

where η is the dielectric (free space here) intrinsic impedance, R_s is surface resistance of the cavity walls, and σ is the conductivity of the metallic walls. These equations can be used to calculate the dimensions of cylindrical cavity resonators. In order to design a cavity operating at 3.5 GHz with Q of around 4000, a and d are required to be 32.9 mm and 5.3 mm, respectively. However, if the same cavity is loaded with a metallic post with diameter of 3.8 mm and an air gap of 47 μm so that the same resonant frequency and Q be maintained, a and d can be reduced to 6.85 mm and 3.2 mm, respectively. These values

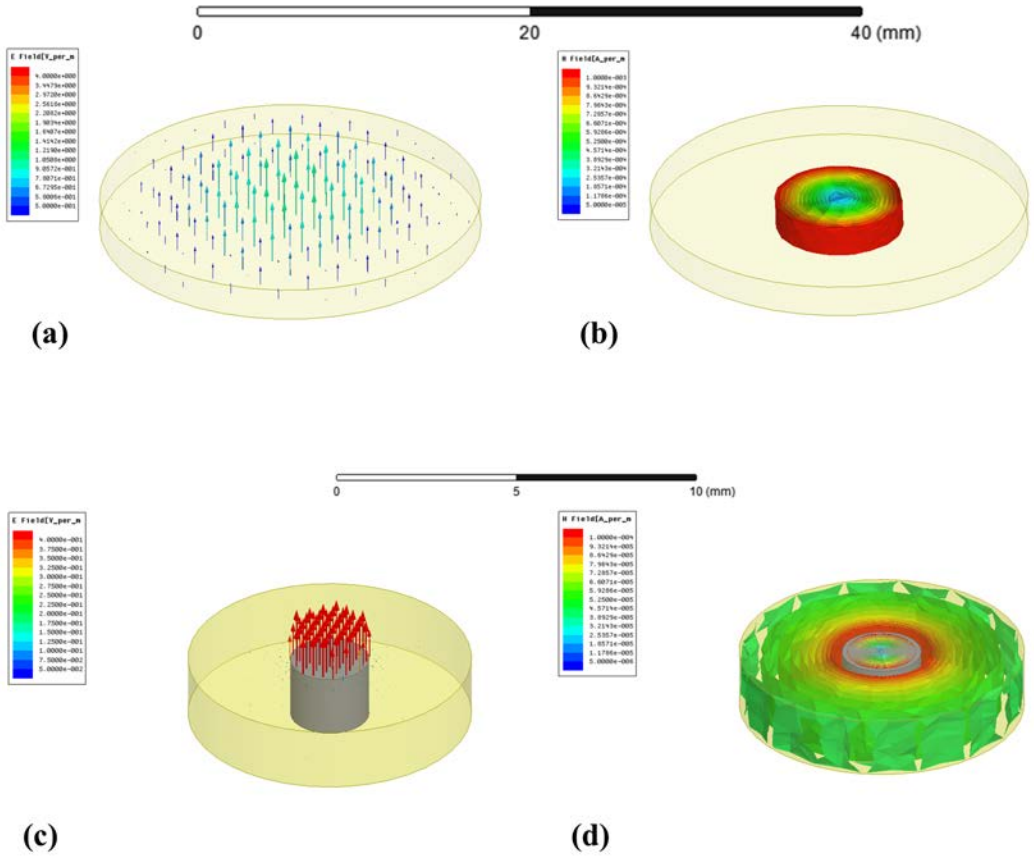

Figure 1.6: Fields distribution in a regular and an evanescent-mode cylindrical cavity resonators for the first mode, (a) E-field in regular cylindrical cavity resonator, (b) H-field in regular cylindrical cavity resonator, (c) E-field in evanescent-mode cylindrical cavity resonator, and (d) H-field in evanescent-mode cylindrical cavity resonator.

show a significant reduction in the size and hence the volume of the resonator (from 18.02 to 0.47 cm^3). This feature is very desirable in miniaturization of microwave cavity filters. Figure 1.6 compares the fields distribution and size of these two cavity resonators. It should be noted that a drawing scale of 4 was used in this illustration.

The first engineering application of evanescent-mode cavity resonators goes back to late 40's when they were used in Klystrons [46]. Waveguides, operating below cutoff frequency, were first called *subcritical* waveguide resonators

in mid 50's by Lebedev and Guttsait [47]. Imperfect waveguides and ghost modes were the other names that were used to refer to evanescent-mode resonators and the waves inside them, respectively [48]. Later in 1971, Craven and Mok used them for the first time in microwave filter design [49]. This first design was corrected and extended by Snyder in 1977 where the theory of direct-coupled cavity filters was used to design more advanced microwave filters using evanescent-mode cavity resonators [50]. More recently, these resonators have attracted a lot of interest for realizing miniaturized low-loss, high-Q, tunable filters for frequency-agile applications thanks to microfabrication techniques [51]–[53]. The conceptual example of an evanescent-mode cavity tunable waveguide filter designed based on the direct-coupled cavity filter method is shown in figure 1.7. As mentioned before, to tune the filter, the loading capacitors need to be changed. In figure 1.7, mechanical deflection of the top wall in the cavities is used to change the loading capacitors in order to tune the filter. Piezoelectric actuators are suitable candidates for providing the required mechanical displacement.

These filters have been demonstrated with quality factors on the order of 1,000 and beyond octave-frequency tuning ranges [52]. Additional benefits include small size and weight, large spurious-free response, and potential for monolithic integration. Because of these advantages, different adaptable and reconfigurable microwave filters with a variety of functionalities have been designed and fabricated using these resonators [52].

1.3 Motivation

According to research conducted by the Pew Research Center, in 2013 cell phones were being used by 91% of adults in the United States [54]. This re-

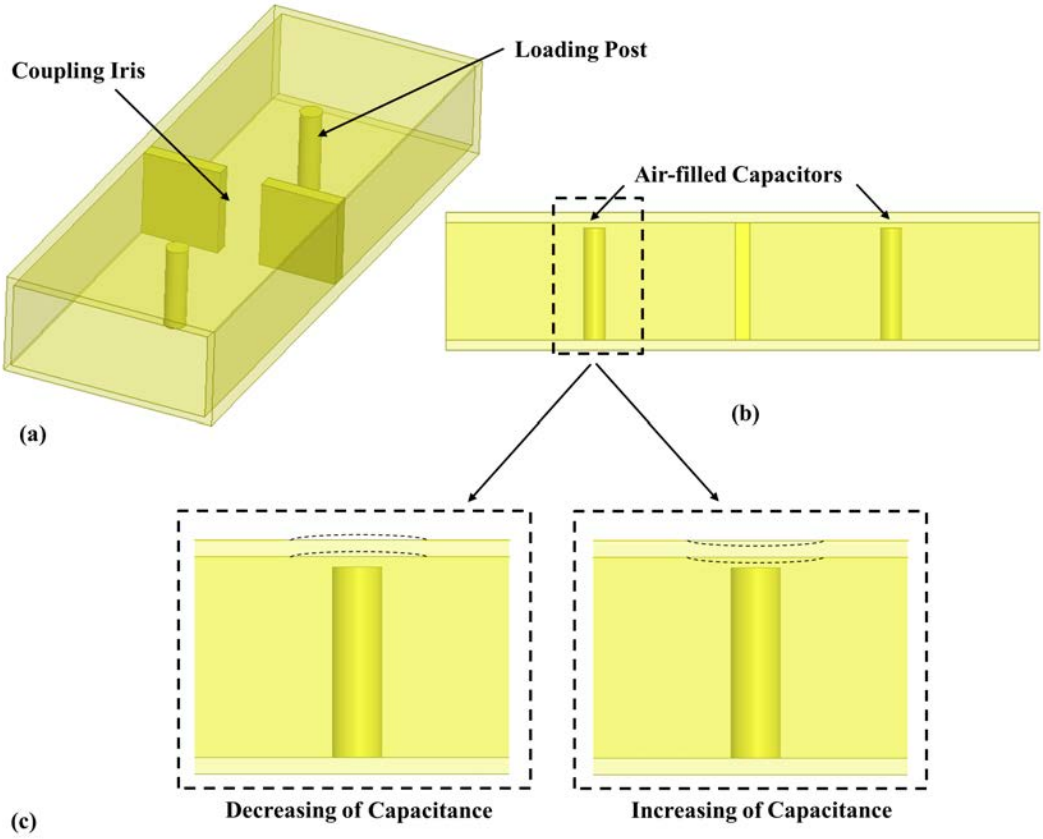

Figure 1.7: Tunable evanescent-mode cavity filter, (a) structure of a evanescent-mode rectangular waveguide filter, (b) side view emphasizing capacitive loading of the cavities, and (c) concept of frequency tuning.

search also shows that 56% of U.S. adults use a smartphone while this value was 35% in 2011 as illustrated in figure 1.8 [55]. Experts believe that such a huge growth in the number of wireless broadband services is alarming considering the looming spectrum crisis [56]. Although the US President National Broadband Plan of 2010 tries to alleviate this issue by mandating the reallocation of 500 MHz of Federal and non-federal spectrum to wireless broadband applications, the wireless technology evolves at a rate that it will outgrow the newly allocated spectrum quickly. Therefore, dynamic spectrum access (DSA) has been suggested as a more permanent remedy [57] and [58]. DSA acts as a

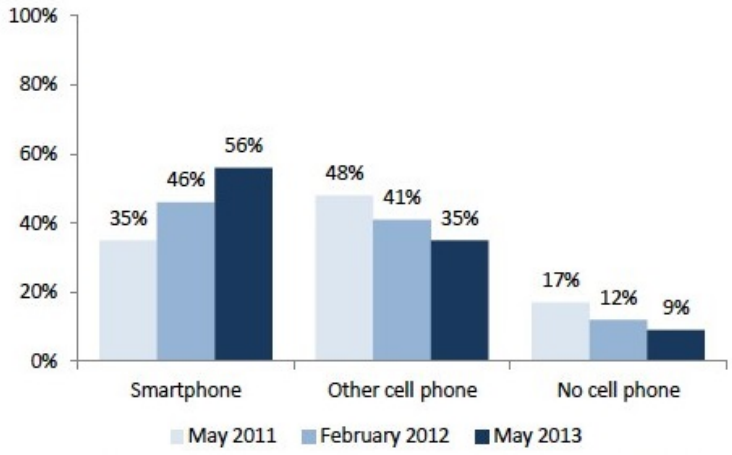

Figure 1.8: Changes in smartphone ownership of US adults between 2011 and 2013 (from [55]).

sharing protocol for real time spectrum assignment in the future. Therefore, frequency-flexibility and cognitive operation are the required features of the future spectrum users.

Unfortunately, current radar systems will not fit into this future environment due to their fundamental limitations including fixed operating frequencies, high power radiation, and power leakage into neighboring bands. Spectral spreading into neighboring frequency bands interferes with other users. Current radar systems have been shown to cause failure of wireless communications because of this issue [56]. High power radiation as well as non-linearity of radar transmitters are a significant source of spectral regrowth. Non-linearity is direct result from the current trend of pushing high-power RF circuits into a more efficient mode. Non-linear behavior of RF circuits causes intermodulation of in-band frequency components, which eventually spread the energy of the transmitting signal to outside of the allotted band. Figure 1.9 shows an example of the spreading spectrum issue. Measured constellations of a digitally-modulated received signal in a wireless communication system, used

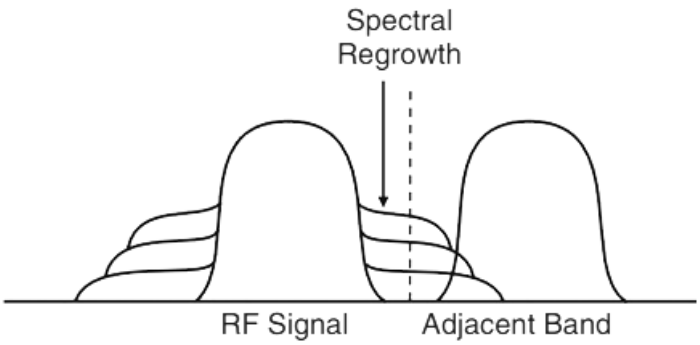

Figure 1.9: An example of spectral regrowth into adjacent band (from [56]).

in an experiment involving a nearby radar system, are shown in figure 1.10. In figure 1.10(a) the constellation of a 64-quadrature amplitude modulation (QAM) received signal in a communication system is shown when it operates without a radar present. The symbols in the constellation distributed uniformly and thus, all symbols are detected correctly. Figure 1.10(b) shows that the constellation is severely degraded and many of the transmitted symbols are incorrectly detected, when a radar is operating in a neighboring frequency band. In fact, due the power leakage of the radar into the frequency band used by the wireless communication system, the low noise amplifier of the communication system is saturated causing the received symbols to be inaccurately detected. Therefore, to avoid this issue, radars are forced to abide by spectral masks provided by government spectrum allocation agencies. A typical radar signal along with the spectral mask defined by the Radar Spectrum Engineering Criteria (RSEC), provided by the National Telecommunications Information Administration (NTIA), is shown in figure 1.11. Due to aforementioned spectrum crisis, everyday radars are facing more stringent allocations, which reach the technical limitations of current systems.

As proposed in [59] and [60], cognitive radars can be considered as a po-

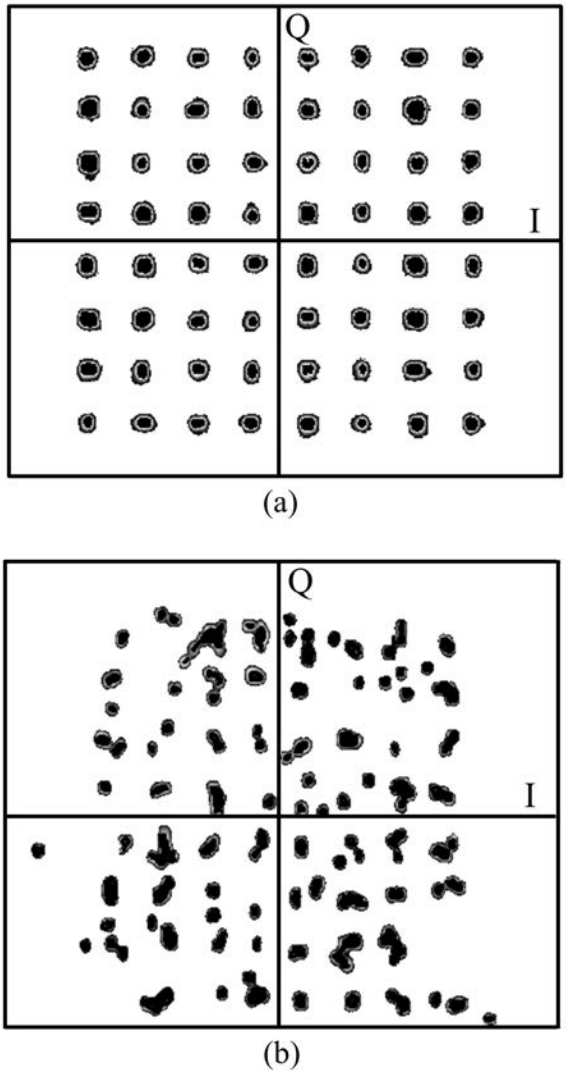

Figure 1.10: Constellation for a 64-QAM received signal of a wireless communication system, (a) without radar interference, (b) with the interference from a radar operating in a neighboring frequency band (modified from [56]).

tential solution to this spectrum issue. A cognitive radar has been defined as a thinking radar that senses and adjusts to its environment. In a cognitive radar the operating frequency, waveform, modulation, and other properties are adjusted according to the surrounding environment including the target and other spectrum users. Cognitive radars are not only very desirable in military-based applications but are good radiating systems in crowded spec-

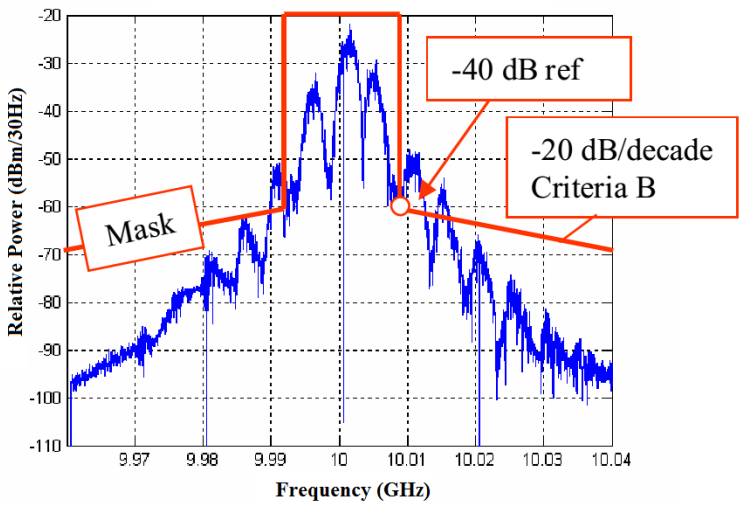

Figure 1.11: A typical radar channel and its spectral mask (from [61]).

trum environments. To be able to adjust, cognitive radars must be reconfigurable [60]. Future cognitive radars should be able to adapt and optimize their performance in real time.

This idea has opened up very interesting research areas in the design and development of reconfigurable circuits for future radars. One area of particular interest is reconfigurable radar systems with simultaneous transmit and receive capabilities. Using simultaneous transmit and receive, full-duplex wireless communication using the same frequency and a single antenna is possible. This is accomplished by providing a high degree of isolation between the transmit and receive chains. Crowded spectrum issues can be alleviated by allowing operation at the same frequency channel rather than using separated channels. Ideally, simultaneous transmit and receive can double the capacity of current wireless systems. The main challenge in implementing systems with this capability is providing sufficient isolation between the receiver and high power transmitters. One possible way to achieve the required isolation is to use sep-

arate antennas, while it is desirable to use a shared antenna for both transmit and receive. This adds flexibility to the system and minimizes the system cost.

Full-duplex systems that use separate antennas for simultaneous transmit and receive, utilize diplexers to achieve separation between the signals. However, when a shared antenna is used for simultaneous transmit and receive, the conventional approach is to use an RF circulator. Current ferroelectric circulators can only achieve about 20 dB of isolation over wide frequency ranges. Active electronic circulators, with higher isolation, are available but they suffer from low power handling capabilities. Until the ideal simultaneous transmit and receive systems are technically possible, another type of simultaneous transmit and receive system can be implemented using multiple closely-separated channels.

In such systems, the transmitter represents a significant in-band interference for the received signals from a previous pulse, where the received signal strength is typically multiple orders of magnitude weaker than the transmitted signal strength. Therefore, in order to operate a radar system in a simultaneous transmit and receive mode, tunable and reconfigurable filters with both bandpass and bandstop functionalities are required. In such a system the transmitter operates at a few different frequencies in such a way that the transmitter filter is tuned to other frequencies after a radar pulse at a specific frequency has been transmitted. The filters on the receive portion of the radar would be operating in an inverse mode compared to the transmitter by placing a bandstop filter at the frequency of the current transmit and a bandpass filter at the receive frequency of the previous pulse. Obviously, frequency-agile filters are vital components in these radar systems. In general, development of frequency-agile microwave circuits will be necessary to build next generation

of microwave systems for the future spectrum.

1.4 Research Objective

In this dissertation, an integrated microwave bandpass-bandstop filter cascade for radar systems with simultaneous transmit and receive is designed. Such a radar system requires two filter cascades. Each cascade will be used on a separate frequency-agile transceiver, but they will be synchronized to provide simultaneously a deep isolation region at one frequency for receive and a high power tolerant passband at an adjacent frequency. Figure 1.12 shows a simple block diagram of the radar front-end. In this radar, frequency-agile bandpass-bandstop filter cascades are used instead of the traditional bandpass filters. When the receiver is waiting for the return of the previous pulses at f_2, the transmitter is sending new pulses at f_1. Therefore, to avoid saturation of the LNA in the receiver, due to high power simultaneous transmission at neighboring frequency, the receiver cascade implements a notch at the current transmitting frequency, (f_1), while tuning the passband to the receiving frequency (f_2). At the same time, the transmitter cascade provides a low insertion loss path for transmission by tuning its bandpass filter to f_1 and reduces the spectral contamination at f_2, by placing a notch at this frequency.

The filter cascade consists of a second-order tunable bandpass and a second-order tunable bandstop filter. The resonators used for these filters have independent operation so that any pole of either the bandpass or the bandstop filter can be tuned to any frequency within the frequency tuning range of the resonators.

The design goal for the filter cascade are continuous frequency tuning ratio of 1:1.2 in S-band from 3.0 to 3.6 GHz. The filters will be designed to have a

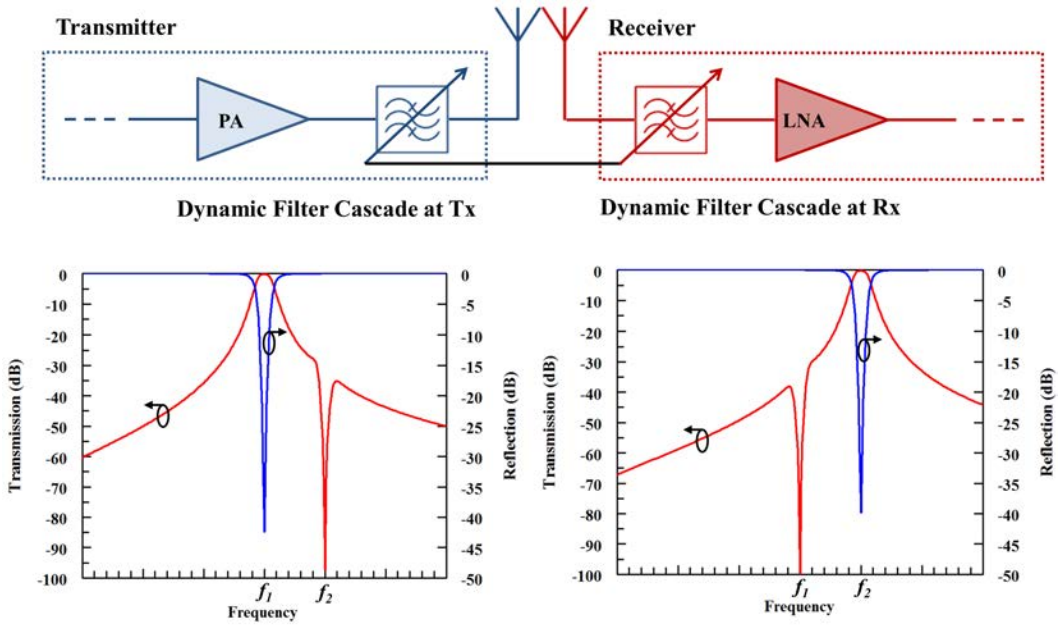

Figure 1.12: Simplified block diagram of the transceiver frond-end in a simultaneous transmit receive radar. Frequency responses of the transmitter and the receiver filter cascades are shown for the current transmission at f_1 and reception at f_2.

few percent fractional bandwidth across the tuning range while maintaining a passband insertion loss of less than 1.5 dB. The desired matching conditions are a better return loss than 10 dB at the bandpass center frequency. The bandstop filter will be designed to provide up to 80 dB of isolation for notch frequencies as close as 10% away from the center of the bandpass filter. The filter cascade will be capable of handling at least 44 dBm (25 Watts) across the entire tuning range.

1.5 Outline of the Dissertation

This dissertation is devoted to substrate-integrated, evanescent-mode, tunable cavity bandpass-bandstop filter cascade. Therefore, the primary focus will be on design, synthesis and fabrication of bandpass filter, bandstop filter,

and bandpass-bandstop filter cascade using this technology. To this end, following the Introduction, Chapter 2 provides a brief overview of filter theory fundamentals, which will be used in the rest of the dissertation. Concepts like transfer function, characteristic polynomials, and lowpass prototype will be covered. The required techniques for the physical implementation of microwave filter based on the synthesis method are described. Also, coupling matrix theory is introduced as an alternative to element extraction method for filter synthesis.

Chapter 3 starts with detailed modeling, characterization, and design of evanescent-mode tunable cavity resonators. First, a general review of the fundamental parameters for the design of evanescent-mode tunable cavity resonators is given. It is followed by the design of a substrate-integrated, evanescent-mode, tunable cavity resonator with a tuning range of (1:1.52) and minimum Q of 600. This resonator is used throughout of this work as a unit cell for design and implementation of all filters. After that, the idea of an active, substrate-integrated, evanescent-mode, tunable cavity resonator is introduced. This chapter will continue by providing detailed design methods for both narrow-band and wide-band bandpass filters. Finally, a discussion on power handling issues and prediction of power handling in this type of filter is given.

Chapter 4 first reviews the conventional method of microwave bandstop filter design. Then, it is shown that how a substrate-integrated, evanescent-mode, tunable cavity resonator bandstop filter can be designed using this method. It is discussed why the bandstop filter designed using the conventional method is not suitable for integration with a bandpass filter. A novel concept for designing single layer, substrate-integrated, evanescent-mode, tun-

able cavity resonator bandstop filters is then presented. A novel coupling matrix synthesis method for this type of bandstop filter is shown. Phase cancellation, through combining two bandpass filters, is used to derive the coupling matrix. It is shown that, classical coupling mechanisms, typically utilized to implement bandpass filters, can be used to design and realize bandstop filters. Using this method, bandstop filters can be designed without source-to-load coupling, which is crucial when integrating substrate-integrated, evanescent-mode, tunable cavity bandstop and bandpass filters.

Chapter 5 studies the integration methods of bandpass and bandstop filters. First, a direct coupling matrix synthesis method for design of a bandpass-bandstop filter cascade is presented. Other techniques used for designing the filter cascade are also reviewed and their drawbacks are discussed. Then, a new single layer, substrate-integrated, bandpass-bandstop filter cascade, based on the previously demonstrated bandpass and bandstop filters is presented. The modular design approach used to design the cascade allows quick construction of the cascade coupling matrix by directly cascading the synthesized coupling matrices of bandpass and bandstop filters. To demonstrate the concept, a state-of-the-art filter cascade with continuous tuning range from 3.0 to 3.6 GHz, insertion loss as low as 0.9 dB, and isolation as high as 100 dB is shown. Eventually, a system-level analysis of the benefits of using the cascade in a communications system is carried out.

Chapter 6 addresses the concept of automatic tuning of evanescent-mode cavity resonator filters. To make this technology ready for widespread commercial use, having an automatic control system for tuning of the filters is critical. The non-linear and non-repeatable behavior of the piezoelectric actuators besides the high sensitivity of the resonator to the gap size, as well as

environmental effects like temperature and vibration, necessitates a feedback control loop be used for automatic tuning of the filter. Such a configuration, including the required hardware and algorithm required for characterization of the filters, is provided in this chapter.

Chapter 7 concludes the dissertation by providing a summary of the work. The significance and contribution of this work is itemized in this chapter. Suggestions on the future directions of the research are also provided.

A new property of Butterworth lowpass prototype filters is also the topic of Appendix A. Using this property insertion loss of a Butterworth filter can be calculated quickly by hand. The required fabrication steps for the implementation of substrate-integrated, evanescent-mode, tunable cavity resonators and filters will be covered in Appendix B. Appendix C presents the list of the abbreviations used in this dissertations and Appendix D provides the summary of publications resulted from this research.

Whereas the majority of the work presented in this dissertation is attributed to the author, some of the design concepts and fabrication techniques were contributed by Sattar Atash-bahar, William Wilson, C. Justin Smith, David Noel, Jonathan Christian and Dr. Hjalti H. Sigmarsson.

Chapter 2

Microwave Filter Design Fundamentals

Today, most microwave filter designs are accomplished with computer-aided design tools based on the *insertion loss* method. Filter design using this method consists of prescribing a desired frequency response for the filter, in terms of signal attenuation characteristics, when the filter is inserted between input and output ports. As opposed to the *image parameter* method, which does not have any methodical way of designing the filter, the *insertion loss* method has a systematic way to synthesize any desired frequency response including bandpass, bandstop, and phase characteristics. In this method, different design tradeoffs between insertion loss, cutoff slope, or linear phase response are available in order to achieve desired filter characteristics. In addition, at the expense of increasing the filter order, the designer can improve the filter performance in a straightforward manner [14]. The classic procedure for filter design using the *insertion loss* method consists of multiple steps:

1. Design of a lumped element lowpass filter with a normalized source impedance of $R_s = 1\ \Omega$ and a cutoff frequency of $\omega_c = 1$ rad/sec, known as the lowpass prototype.

2. Impedance scaling to obtain the desired source and load impedances.

3. Frequency scaling and transformation to convert the lowpass response to any desired bandpass, bandstop, or highpass response with any arbitrary cutoff frequency or bandwidth.

4. Filter implementation. In case of RF and microwave filters, this consists of the use of different techniques to convert the lumped elements to distributed elements suitable for the technology which will be used for realizing the microwave filter.

The procedure for calculating the values of the lumped element components in the prototype filter (the first step above) involves generating polynomials that represent the filter transfer and reflection functions. It has been shown for passive, lossless, two-port networks that the transfer and reflection functions are rational in s (the normalized complex frequency defined as $s = \sigma + j\Omega$) with real coefficients [62]. Then, an element extraction method is used to extract the element values from the polynomials. While the network is formed element by element using this method, the order of polynomials is decreased until the coefficients of the polynomials are all zero or some constants. When this occurs, the network is considered to be completely synthesized. Based on the specific topology of the network being synthesized and the available components in the realization techniques, various extraction schemes have been developed [63].

An alternative to the element extraction method is network synthesis using the *coupling matrix* method. The *coupling matrix* method is a simple mathematical tool for representing the filter network. There is a one-to-one correspondence between every physical components of the filter and the elements of the *coupling matrix*. This interesting feature of this method turns it into a versatile tool for designing, modeling, tuning, analyzing, and diagnosing

microwave filters. This method can accommodate non-ideal, real-world effects in filter analysis while the initial steps of the filter design consider ideal lossless, dispersionless, and frequency-independent components. The other important feature of this method is the capability of reconfiguring the structure into a different coupling arrangement using matrix similarity transforms, which can result in a simpler filter implementation. As opposed to the classical element extraction method that requires the design of the filter to be completely redone for each different topology, the *coupling matrix* for various topologies can be obtained simply using matrix operations. This method can also be used to design more advanced microwave filter responses, such as asymmetric filtering characteristics, dual or multiple band filters, and tunable microwave filters, which all have become very important in modern wireless telecommunication systems as well as in radar applications.

As discussed here, although microwave filters may be realized using different technologies, the fundamental circuit network theory for all filters remains the same. Therefore, this chapter is devoted to various network theories for the design of microwave filters.

2.1 Characterization of Lowpass Prototype

A lowpass prototype of order N can be represented by a general doubly-terminated linear lossless two-port network shown in figure 2.1. From general filter theory and the definition of the generalized scattering parameters, the network reflection coefficient, $\rho\ (s)$, and transmission coefficient, $t(s)$, can be expressed respectively as [64]

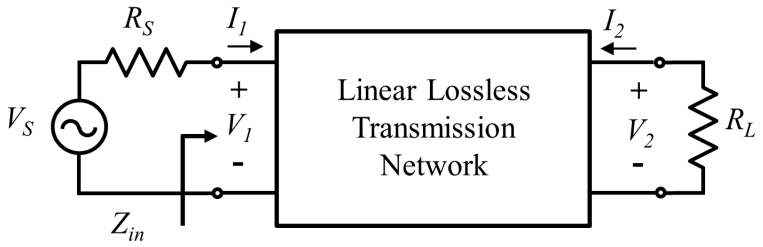

Figure 2.1: Doubly-terminated linear lossless two-port network.

$$\rho(s) = \frac{1}{\varepsilon_R}\frac{F(s)}{E(s)} \tag{2.1a}$$

$$t(s) = \frac{1}{\varepsilon}\frac{P(s)}{E(s)} \tag{2.1b}$$

where $E(s)$, $F(s)$, and $P(s)$ are polynomials in terms of s and are known as characteristics polynomials. In (2.1a) ε_R and ε are real constant values that have been defined to normalize the highest-degree coefficients of the polynomials to unity. This guarantees that the maximum amplitude of the filter in the passband is also normalized to one. ε_R and ε are usually referred to as the ripple constant and ripple factor, respectively.

In general, the Nth-order filter can have at most N finite-frequency transmission zeros. Therefore, $E(s)$ and $F(s)$ are Nth degree polynomials and $P(s)$, which contains N_{fz} finite-frequency transmission zeros, is of degree N_{fz}. For the network to be a realizable, N_{fz} must be less than or equal to N.

The conservation of the energy in the lossless network expresses that the reflected power plus the transmitted power delivered to the load must be equal

to the available power. Therefore,

$$|\rho(s)|^2 + |t(s)|^2 = 1 \tag{2.2}$$

by inserting of the definitions of $\rho(s)$ and $t(s)$ from (2.1a) and (2.1b), we have

$$\left|\frac{1}{\varepsilon_R}\frac{F(s)}{E(s)}\right|^2 + \left|\frac{1}{\varepsilon}\frac{P(s)}{E(s)}\right|^2 = 1 \tag{2.3}$$

or

$$\frac{|F(s)|^2}{{\varepsilon_R}^2} + \frac{|P(s)|^2}{\varepsilon^2} = |E(s)|^2. \tag{2.4}$$

This equation can be used to find the third polynomial when the other two are known.

When the number of finite transmission zeros is less than the order of the filter, that is $N_{fz} < N$, the filter has $(N - N_{fz})$ transmission zeros at infinities. Therefore, no power is transmitted to the load at infinite frequency and, due to the conservation of energy, all power should be reflected back to the source. In other words

$$|\rho(s)|\Big|_{s=\pm j\infty} = 1 \tag{2.5}$$

Referring back to (2.1a) and remembering that the highest-degree coefficients of the Nth-order polynomials $F(s)$ and $E(s)$ are unity, it can be concluded that when $n_z < N$ the constant ε_R should be one.

When $N = n_z$, the polynomial $P(s)$ is also an Nth-degree polynomial, and therefore, the attenuation at $s = \pm j\infty$ is finite. In this case, known as *fully-canonical*, evaluation of (2.4) at infinity reveals the relationship between ε and

ε_R as

$$\frac{|F(s)|^2}{{\varepsilon_R}^2}\bigg|_{s=\pm j\infty} + \frac{|P(s)|^2}{\varepsilon^2}\bigg|_{s=\pm j\infty} = |E(s)|^2\bigg|_{s=\pm j\infty} \tag{2.6a}$$

or

$$\frac{1}{{\varepsilon_R}^2} + \frac{1}{\varepsilon^2} = 1 \ . \tag{2.6b}$$

The transmission loss and reflection loss, in terms of decibel, are defined as

$$A = 10\log\frac{1}{|t(s)|^2}\bigg|_{s=j\Omega} \text{ dB} \tag{2.7a}$$

$$R = 10\log\frac{1}{|\rho(s)|^2}\bigg|_{s=j\Omega} \text{ dB} \ . \tag{2.7b}$$

The transmission loss and reflection loss are often termed the attenuation and the return loss, respectively. Using (2.2), they can be linked together as

$$A = -10\log(1 - 10^{-\frac{R}{10}}) \text{ dB} \tag{2.8a}$$

$$R = -10\log(1 - 10^{-\frac{A}{10}}) \text{ dB} \ . \tag{2.8b}$$

The ratio of the transmitted power to the available power from the source can be found from (2.1b) as

$$|t(s)|^2 = \frac{1}{\varepsilon^2}\frac{|P(s)|^2}{|E(s)|^2} \tag{2.9}$$

substituting $|E(s)|^2$ in (2.9) from (2.4) yields

$$|t(s)|^2 = \frac{1}{1 + \dfrac{\varepsilon^2}{{\varepsilon_R}^2} \dfrac{|F(s)|^2}{|P(s)|^2}} \tag{2.10}$$

The ratio $\dfrac{F(s)}{P(s)}$ is called the characteristic function, $K(s)$, of a lossless prototype filter. If we assume that the filter at frequency Ω_1 in the passband, has a known attenuation of A_1 dB, then (2.10) can be used to find the constant ε in terms of ε_R as

$$|t(j\Omega_1)|^2 = 10^{-\frac{A_1}{10}} = \frac{1}{1 + \dfrac{\varepsilon^2}{{\varepsilon_R}^2} |K(j\Omega_1)|^2} \tag{2.11}$$

or simply

$$\varepsilon = \varepsilon_R \sqrt{(10^{\frac{A_1}{10}} - 1) \frac{1}{|K(j\Omega_1)|^2}} \tag{2.12}$$

Similar expression can be found in terms of the filter return loss, that is R_1, at Ω_1,

$$\varepsilon = \varepsilon_R \sqrt{\frac{1}{10^{\frac{R_1}{10}} - 1} \frac{1}{|K(j\Omega_1)|^2}} \tag{2.13}$$

R_1 is related to the attenuation A_1 using (2.8b). Finally, by combining (2.13) and (2.6b) in the case of fully-canonical filters, ε is expressed as

$$\varepsilon = \sqrt{1 + (10^{\frac{R_1}{10}} - 1)|K(j\Omega_1)|^2} \tag{2.14}$$

For normalized lowpass filter prototypes, Ω_1 is referred to as the cutoff fre-

quency and is normally chosen to be unity. In fully-canonical case ε_R is slightly greater than unity.

2.1.1 Characteristic Polynomials for Different Prototype Frequency Responses

In filter synthesis, the polynomials $P(s)$ and $F(s)$ are found from their roots. The roots of these polynomials are determined based on the specifications of the filter. As mentioned before, when $P(s)$ and $F(s)$ and the constants are known, the polynomial $E(s)$ can be obtained from (2.4). In general, the polynomials should meet the following properties:

1. $E(s)$ is a strict Hurwitz polynomial; hence all of its roots must lie in the left half of the s-plane.

2. $F(s)$ may or may not be a Hurwitz polynomial. $F(s)$ is a pure odd or a pure even polynomial. However, all of its coefficients are real. As a result, its roots must be real, form conjugate complex pairs, or locate at the origin (multiple roots at the origin are possible). The roots of $F(s)$ are called *reflection zeros* since at these frequencies no power is reflected, and therefore, filter loss is zero.

3. $P(s)$ is a pure, even polynomials and has real coefficients. Its roots can occur as conjugate pairs on the imaginary axis, as conjugate pairs on the real axis, or finally as a complex quad in the s-plane. Conjugate pair roots on the imaginary axis happen at frequencies with zero power transmission or infinite loss. Therefore, they are called *transmission zeros* or *attenuation poles*. The other types of roots represent linear

phase response. Filters with such roots are called *non-minimum phase* filters.

Therefore, assigning all the reflection zeros of the filter to the $j\omega$ axis in the passband and all the transmission zeros to the $j\omega$ axis in the high attenuation region of the filter response, guarantees that filter has low loss in its passband and high loss in its stopband. Sometimes, however, having non-$j\omega$-axis zeros in $P(s)$ can be used as a compromise between having a more linear phase response at the cost of lower attenuation in the stopband.

A doubly terminated lowpass prototype can be categorized into two different filter types in terms of its transmission zeros positions:

1. If all the attenuation poles occur at infinity (or simply if the filter does not have any finite transmission zeros), the filter is known as an *all-pole* filter. In such a filter, the attenuation increases monotonically beyond the passband and the filter response is characterized by the form of the polynomial $F(s)$, because in such a filter $P(s) = 1$. In general, $F(s)$ can be either in the form of

$$F(s) \rightarrow s^n \tag{2.15a}$$

or

$$F(s) \rightarrow s^m(s^2 + {a_1}^2)(s^2 + {a_2}^2)... \tag{2.15b}$$

In the first form, all the reflection zeros occur at the origin and the transfer response of the filter will exhibit a maximally flat behavior in the passband. This type of filtering function is known as a *Butterworth* (maximally-flat) response. The amplitude response of a 4th-order But-

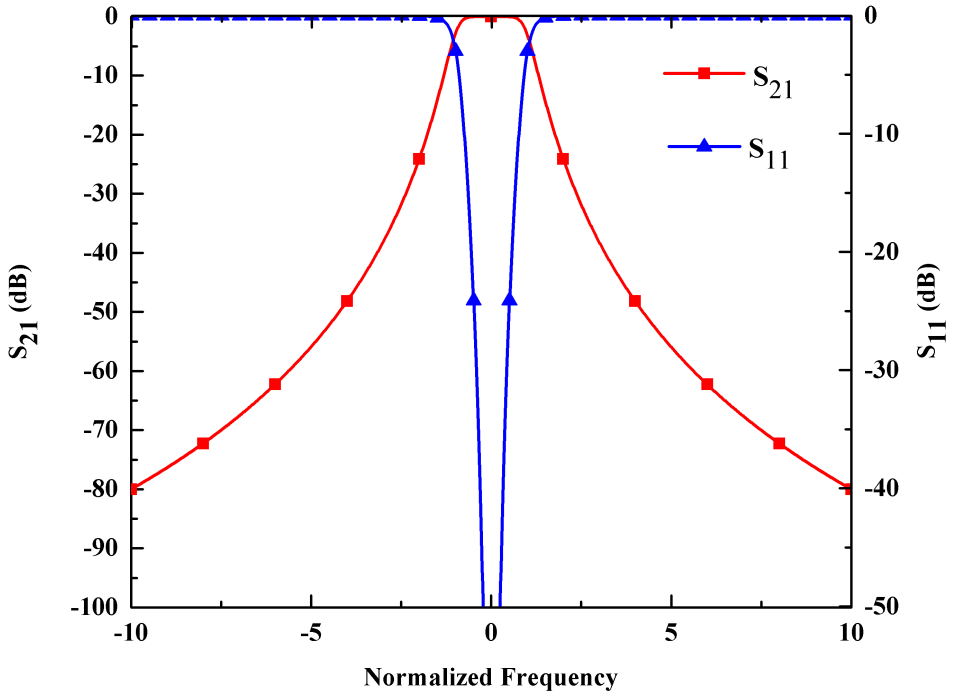

Figure 2.2: Frequency response of a 4th-order Butterworth prototype filter.

terworth filter with 3 dB attenuation at unity corner frequency is shown in figure 2.2.

The second form, however, is more general and can have some zeros at the origin and some at finite frequencies. In a special case, when there are maximum permissible peaks in the passband with an equi-ripple response, the filtering function is known as a *Chebyshev* (equi-ripple) response. In this case, for odd-order filters $m = 1$ and for even-order filters $m = 0$. The amplitude response of a 4th- and a 5th-order Chebyshev filter, with 20 dB of equi-ripple return loss in passband, are shown in figure 2.3 and figure 2.4, respectively.

It has been shown that all-pole filters can be synthesized and implemented using ladder networks [62], [63]. There exist explicit closed form formulas for calculating the element values for these networks in the case

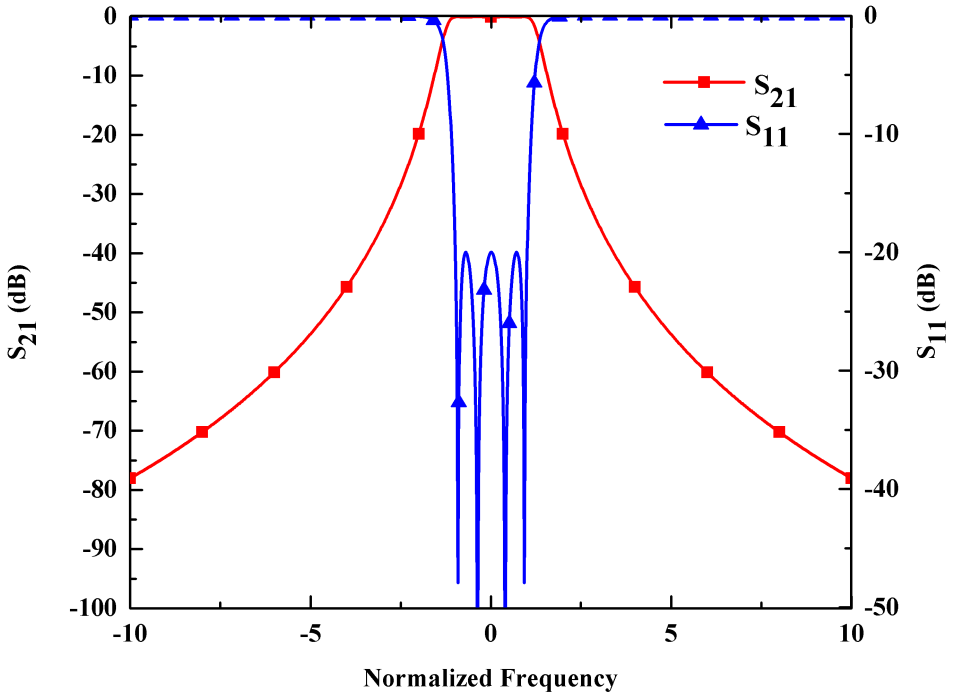

Figure 2.3: Frequency response of a 4th-order Chebyshev prototype filter.

of classic Butterworth and Chebyshev responses. In addition, the element values for these types of filters have been tabulated and presented in literature [10], [20].

2. In the second type of the lowpass prototype, the filter has finite transmission zeros (TZs). Introduction of TZs increases the selectivity of the amplitude response of the filter at the expense of a reduced wideband amplitude response in the stopband. Such a filter is characterized by the following polynomials

$$P(s) \rightarrow (s^2 + {b_1}^2)(s^2 + {b_2}^2)... \tag{2.16a}$$

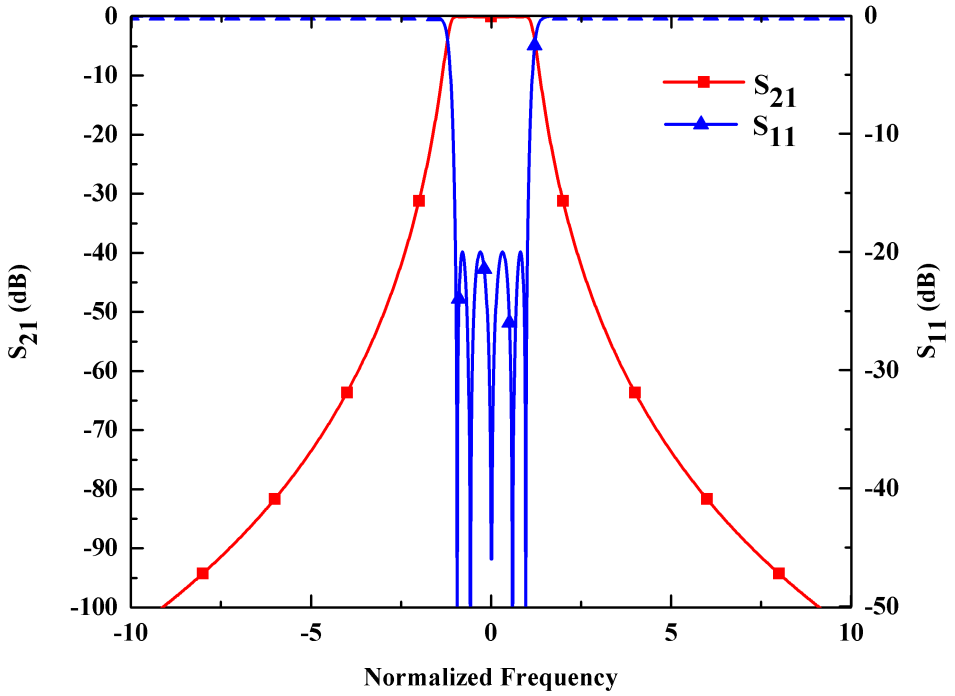

Figure 2.4: Frequency response of a 5th-order Chebyshev prototype filter.

and

$$F(s) \rightarrow s^m(s^2 + {a_1}^2)(s^2 + {a_2}^2)... \tag{2.16b}$$

Generalized Chebyshev and Elliptic filters are two examples of filters with finite TZs.

According to what has been discussed so far, the transfer and reflection functions of a passive linear lossless network are expressed by the ratio of two positive real polynomials. These positive real polynomials have real coefficients. The roots of such polynomials result in an even or odd symmetry about zero frequency for the amplitude and phase response of the network. Therefore, an asymmetric response, with respect to the zero frequency, cannot be achieved using such polynomials. The introduction of constant reactances, known as frequency-independent reactive (FIR) elements, results in a frequency response

that is no longer symmetric with respect to the zero frequency. In such a case, the coefficients of the characteristic polynomials are complex and the poles and zeros have asymmetric distributions in the complex s-plane. Therefore, such polynomials are not positive real anymore; instead they are positive functions [63]. Positive functions exhibit specific properties that guarantee physical realizability of the real asymmetric bandpass filters created using the lowpass prototypes. These properties are very similar to that of positive real functions and originate from the law of conservation of energy. The principal differences are:

1. For the positive real functions, the impedance, $Z(s)$, or admittance, $Y(s)$, functions consist of polynomials with real and positive coefficients. For the positive functions, the polynomials have complex coefficients.

2. $Z(s)$ or $Y(s)$ has poles and zeros in the form of complex conjugate pairs for the positive real functions. There is no such a constraint for the positive functions.

3. The zeros of $P(s)$ for an asymmetric filter must occur either on the imaginary axis or as pairs symmetrically located with respect to the imaginary axis. It is not required that such zeros form complex conjugate pairs.

4. All zeros of $F(s)$ for an asymmetric filter must occur on the imaginary axis, but they are not required to be distributed symmetrically around the frequency origin.

5. $E(s)$ is a positive function with complex coefficients. All of its zeros must be located in the left half side of s plane.

More details about different types of filters in term of calculations of the polynomials and the location of the poles and zeros can be found in filter theory literature [64], [65].

2.2 Lowpass Ladder Prototype

Once the characteristic polynomials and the constants for any desired filtering response have been found, they can be used to form the reflection function of the filter. In the next step, the driving point input impedance (or admittance) of the filter is found from the reflection function using

$$\rho(s) = \frac{Z_{in} - R_s}{Z_{in} + R_s} = \frac{z_{in} - 1}{z_{in} + 1} \tag{2.17}$$

where z_{in} is the input impedance normalized to source impedance, R_s. The final step is to synthesize the input impedance $Z_{in}(s)$ as an electrical network. There are several different electrical networks that can create a given input impedance. In the case of all-pole filters, the network can be synthesized and implemented using ladder networks. In the general case, the elements of the ladder are found by performing successive polynomial divisions. This process is quite well known and is found in most of filter and network synthesis literature [62]–[64]. The results of such a synthesis technique for the all-pole ladder prototypes with normalized cutoff frequency of 1 rad/s, starting with either a shunt or a series element, are shown in figure 2.5. In this figure, g_0 and g_{N+1} are also normalized source and load resistances or conductances. g_0 is the source resistance in figure 2.5(a) or source conductance in figure 2.5(b). g_{N+1} is also the load resistance if the previous element is a shunt capacitor or the load conductance if the previous element is a series inductor.

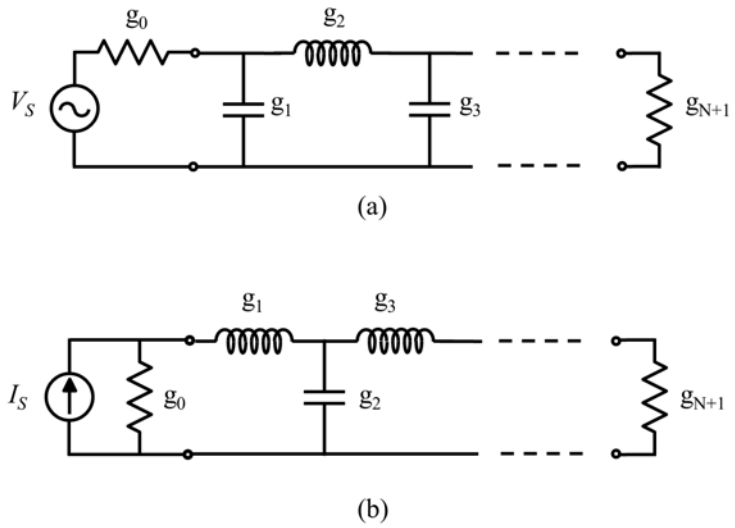

Figure 2.5: Lumped element ladder lowpass prototype, (a) starting with a shunt element, (b) starting with a series element.

Although historically, the values of the elements in the ladder prototype for all-pole filters have been calculated and tabulated [10], [20], there are closed-form expressions for these values in the case of Butterworth and Chebyshev filters [14], [20]. For Butterworth prototypes,

$$g_0 = g_{N+1} = 1\ \Omega \tag{2.18a}$$

$$g_k = 2\ \sin\left(\frac{(2k-1)\pi}{2N}\right) \qquad \text{for } k = 1, 2, 3, ..., N \tag{2.18b}$$

where g_k represents the value of either a series inductor or a shunt capacitor. Similarly, for Chebyshev prototypes,

$$g_0 = 1\ \Omega \tag{2.19a}$$

$$g_1 = \frac{2}{\eta} \sin \frac{\pi}{2N} \tag{2.19b}$$

$$g_k g_{k+1} = \frac{4 \sin\left[(2k-1)\pi/2N\right] \sin\left[(2k+1)\pi/2N\right]}{\eta^2 + \sin^2(k\pi/N)} \qquad \text{for } k = 1, 2, 3, ..., (N-1) \tag{2.19c}$$

$$g_{N+1} = \begin{cases} 1\ \Omega & \text{for } N \text{ odd} \\ \left(\varepsilon + \sqrt{1+\varepsilon^2}\right)^2 \text{ or } \dfrac{1}{\left(\varepsilon + \sqrt{1+\varepsilon^2}\right)^2} & \text{for } N \text{ even} \end{cases} \tag{2.19d}$$

where η is defined as

$$\eta = \sinh\left(\frac{1}{N} \sinh^{-1} \frac{1}{\varepsilon}\right) \tag{2.20}$$

in which ε is the ripple factor and can be found from (2.13), remembering that for regular Chebyshev filters ε_R is unity. The choice of g_{N+1} in (2.19d) is also dependent on the value of the reflection function at zero frequency. An interesting point to note here is that the source resistor and load resistor are only equal for odd-order filters. For an even-order Chebyshev filter the load resistor is a function of the filter ripple. In practice it is generally desirable to have identical source and load resistances, and therefore, implementations of lumped element Chebyshev filters are nearly always restricted to odd orders. However, this limitation can be addressed using electromagnetic coupling. After the normalized prototype filter has been obtained, it can be scaled in terms of impedance and frequency, and converted to give highpass, bandpass, or bandstop characteristics. For example, to obtain a filter with a source re-

sistance of R_0, all the impedances of the prototype should be multiplied by R_0. Thus, if showing impedance scaled quantities with primed variables, the new filter component values are given by

$$L' = R_0 L \tag{2.21a}$$

$$C' = \frac{C}{R_0} \tag{2.21b}$$

$$R'_S = R_0 \tag{2.21c}$$

$$R'_S = R_0 R_L \tag{2.21d}$$

where L, C, and R_L are the component values for the original prototype. In order to derive bandpass and bandstop filters from the lowpass prototype the following frequency transformations are used,

$$\omega \leftarrow \frac{1}{\Delta}\left(\frac{\omega}{\omega_0} - \frac{\omega_0}{\omega}\right) \qquad \text{for bandpass} \tag{2.22}$$

and

$$\omega \leftarrow -\Delta\left(\frac{\omega}{\omega_0} - \frac{\omega_0}{\omega}\right)^{-1} \qquad \text{for bandstop} \tag{2.23}$$

where ω_0 is the filter center frequency, ω_1 and ω_2 are the passband corner frequencies and Δ is the fractional bandwidth. These quantities are related to

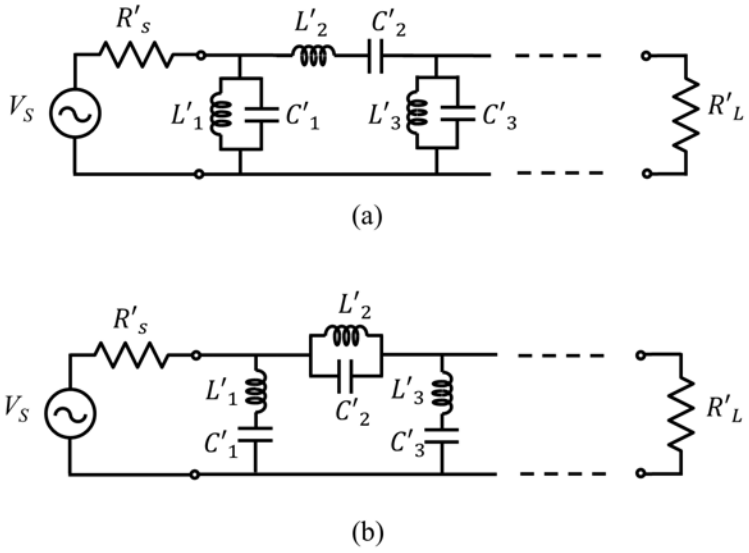

Figure 2.6: Lumped element ladder lowpass prototype, (a) bandpass filter, (b) bandstop filter.

each other using,

$$\omega_0 = \sqrt{\omega_1 \omega_2} \tag{2.24a}$$

$$\Delta = \frac{\omega_2 - \omega_1}{\omega_0} \tag{2.24b}$$

Typical transformed bandpass and bandstop filters with shunt starting resonators are shown in figure 2.6. The bandpass transform converts a series inductor, L_k, to a series LC resonator with element values of

$$L'_k = \frac{L_k}{\omega_0 \Delta} \tag{2.25a}$$

$$C'_k = \frac{\Delta}{\omega_0 L_k} \tag{2.25b}$$

and a shunt capacitor, C_k, to a shunt LC resonators with element values of

$$L'_k = \frac{\Delta}{\omega_0 C_k} \tag{2.25c}$$

$$C'_k = \frac{C_k}{\omega_0 \Delta} \tag{2.25d}$$

Series resonators represent low impedance circuits at resonance in the series arms and parallel resonators exhibit high impedance behavior at resonance in the shunt arms. All series and parallel resonators have the same resonant frequency of ω_0. Similarly, the bandstop transform converts a series inductor, L_k, to a parallel LC resonator with element values of

$$L'_k = \frac{L_k \Delta}{\omega_0} \tag{2.26a}$$

$$C'_k = \frac{1}{\omega_0 L_k \Delta} \tag{2.26b}$$

and a shunt capacitor, C_k, to a series LC resonators with element values of

$$L'_k = \frac{1}{\omega_0 C_k \Delta} \tag{2.26c}$$

$$C'_k = \frac{C_k \Delta}{\omega_0} \tag{2.26d}$$

Although all resonators in the transformed filter, either bandpass or bandstop, resonate at the same frequency of ω_0, the value of all capacitors or inductors in these resonators are not the same. Also, in either type of transformed

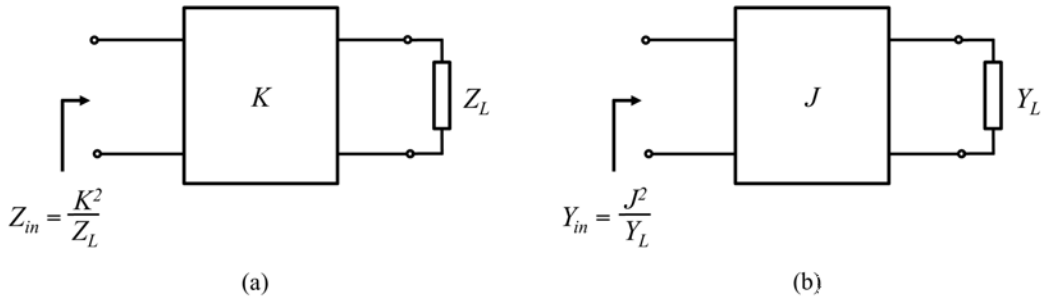

Figure 2.7: Operation of impedance and admittance inverters, (a) K-inverter, (b) J-inverter.

filters both series and parallel resonators are used. However, in the actual implementation of the filters, it is often desirable to use only series or only shunt resonators. Furthermore, it is usually preferable that all the resonators have the same element values. To achieve such requirements, impedance (K) and admittance (J) inverters are used to transform series or shunt reactances to the other type [20]. Figure 2.7 illustrates the principle of the K- and J-inverter operation. The input impedance of an impedance inverter terminated in an impedance Z_L is K^2/Z_L where K is the impedance of the inverter. Similarly, the input admittance of an admittance inverter terminated in an admittance Y_L is J^2/Y_L where this time J is the admittance of the inverter. An impedance or admittance inverter is defined by its ABCD parameters as

$$[ABCD] = \begin{bmatrix} 0 & jK \\ j/K & 0 \end{bmatrix} \qquad \text{K-Inverter} \tag{2.27a}$$

$$[ABCD] = \begin{bmatrix} 0 & j/J \\ jJ & 0 \end{bmatrix} \qquad \text{J-Inverter} \tag{2.27b}$$

From the ABCD matrices, it can be seen that K- and J-inverters are essen-

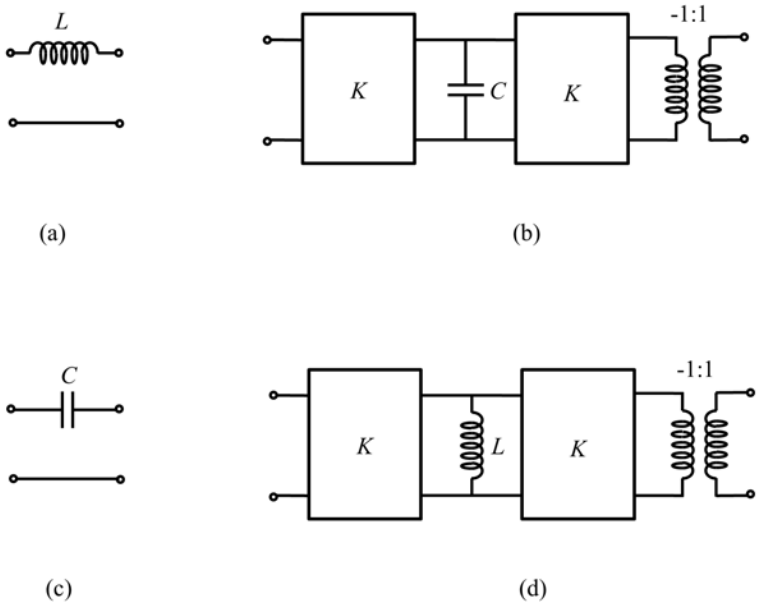

Figure 2.8: Series to shunt conversion of lumped elements using impedance inverters, (a) a series inductor as a two port network, (b) realization of the series inductor using a shunt capacitor, K-inverters, and a negative unity transformer ($C = L/K^2$), (c) a series capacitor as a two port network, and (d) realization of the series capacitor using a shunt inductor, K-inverters, and a negative unity transformer ($L = CK^2$).

tially the same network with just distinction between impedance and admittance inversion. Figure 2.8 shows how, by using a K-inverter, a series reactive element can be transformed into a shunt element. Similarly, a J-inverter can be used to transform a shunt reactive element into a series one.

Using K- and J-inverters, prototype filters can be transformed to consist only of series or shunt reactive elements. For example, the lowpass prototype structure shown in figure 2.5(b) may be converted to a lowpass network implemented using only shunt capacitors as shown in figure 2.9. In this figure, the new element values, such as G_S, G_L, and C_{pi} may be chosen arbitrarily and the filter response will be identical to that of the original prototype, provided that the admittance inverter parameters, $J_{i,i+1}$ are specified as indicated by

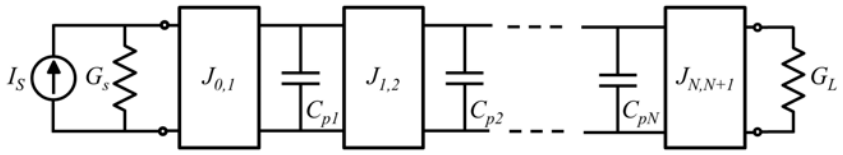

Figure 2.9: Modified lowpass prototype realized with admittance inverters and shunt capacitors.

the following equations [66]:

$$J_{0,1} = \sqrt{\frac{G_S C_{p1}}{g_0 g_1}} \tag{2.28a}$$

$$J_{i,i+1} = \sqrt{\frac{C_{pi} C_{p(i+1)}}{g_i g_{i+1}}} \qquad \text{for } i = 1 \text{ to } (N-1) \tag{2.28b}$$

$$J_{N,N+1} = \sqrt{\frac{G_L C_{pN}}{g_N g_{N+1}}} \tag{2.28c}$$

Regarding the lowpass prototype, interesting and important observations are that:

- Since the negative unity transformers only affect the phase of the transmission coefficient, they may be omitted.
- Although the new element values are chosen arbitrarily, the effect of such a selection is just reflected back in the value of the inverters. In practice, the value of all capacitors, as well as source and load resistances, are selected to be identical.
- Implementation of even-order Chebyshev filters with equal source and load resistances is made possible, when the lowpass prototype is realized

using inverters.

The ideal inverter parameters are frequency invariable, and therefore, the new lowpass prototype can be transformed to other types of filters like bandpass or bandstop structures by applying the element transformations. For instance, as shown in figure 2.10, the lowpass prototype obtained in figure 2.9 can be transformed into a bandpass filter which consists of only shunt-parallel resonators [66]. In this figure, G_S, G_L, and C_{pi} are again chosen arbitrarily while inductors and inverters are found from:

$$J_{0,1} = \sqrt{\frac{\omega_0 \Delta G_S C_{p1}}{\mathrm{g_0 g_1}}} \tag{2.29a}$$

$$J_{i,i+1} = \omega_0 \Delta \sqrt{\frac{C_{pi} C_{p(i+1)}}{\mathrm{g_i g_{i+1}}}} \qquad \text{for } i = 1 \text{ to } (N-1) \tag{2.29b}$$

$$J_{N,N+1} = \sqrt{\frac{\omega_0 \Delta G_L C_{pN}}{\mathrm{g_N g_{N+1}}}} \tag{2.29c}$$

$$L_{pi} = \frac{1}{{\omega_0}^2 C_{pi}} \qquad \text{for } i = 1 \text{ to } (N-1) \tag{2.29d}$$

By replacing the lumped LC resonators in figure 2.10 by distributed circuits, a generalized bandpass prototype using only shunt susceptances and J-inverters can be found [20]. Such a bandpass filter along with its dual form, which consists of only series reactances and K-inverters, are shown in figure 2.11. In figure 2.11(a) the inverter values are found using

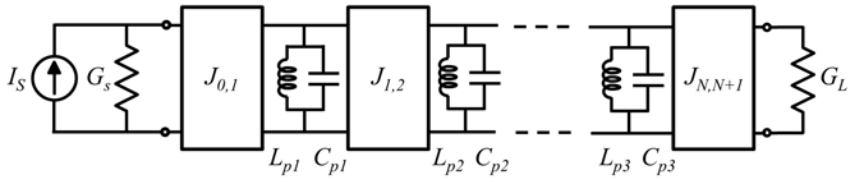

Figure 2.10: Modified bandpass prototype realized with admittance inverters and shunt-parallel resonators.

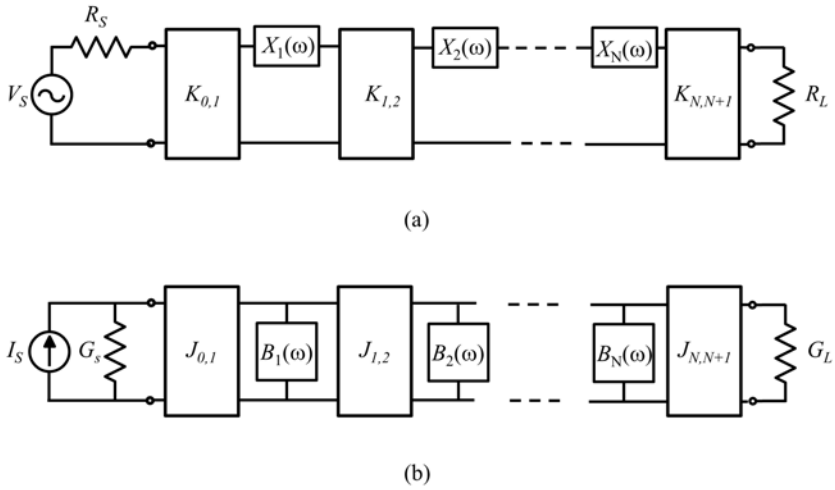

Figure 2.11: Generalized bandpass prototypes, (a) realized with series reactances and impedance inverters, (b) realized with shunt reactances and admittance inverters.

$$K_{0,1} = \sqrt{\frac{x_1 \Delta R_S}{g_0 g_1}} \tag{2.30a}$$

$$K_{i,i+1} = \Delta \sqrt{\frac{x_i x_{i+1}}{g_i g_{i+1}}} \qquad \text{for } i = 1 \text{ to } (N-1) \tag{2.30b}$$

$$K_{N,N+1} = \sqrt{\frac{x_N \Delta R_L}{g_N g_{N+1}}} \tag{2.30c}$$

$$x_i = \frac{\omega_0}{2}\frac{dX_i(\omega)}{d\omega}\bigg|_{\omega=\omega_0} \tag{2.30d}$$

and in figure 2.11(b) the inverter values are found using

$$J_{0,1} = \sqrt{\frac{b_1 \Delta G_S}{g_0 g_1}} \tag{2.31a}$$

$$J_{i,i+1} = \Delta\sqrt{\frac{b_i b_{i+1}}{g_i g_{i+1}}} \qquad \text{for } i = 1 \text{ to } (N-1) \tag{2.31b}$$

$$J_{N,N+1} = \sqrt{\frac{b_N \Delta G_L}{g_N g_{N+1}}} \tag{2.31c}$$

$$b_i = \frac{\omega_0}{2}\frac{dB_i(\omega)}{d\omega}\bigg|_{\omega=\omega_0} \tag{2.31d}$$

where x_i and b_i are referred to as reactance and susceptance slope parameters, respectively.

The series reactances and shunt susceptances in figure 2.11 can be microstrip resonators, microwave cavity resonators, or any other suitable resonant structures. Ideally, these reactances/susceptances should be equal to the lumped element resonators at all frequencies. In practice, however, they approximate the reactances/susceptances of the lumped resonators only only around the resonant frequency. Nevertheless, for narrow-band filters, this is a valid and sufficient approximation. For convenience, the reactances/susceptances of the distributed resonators and their first derivatives, that is the slope parameters, are made equal to their corresponding values in the lumped element

resonators at the center frequency. A lumped element LC series resonator at center frequency, ω_0, has a reactance and a reactance-slope parameter of zero and $\omega_0 L$, respectively. Similarly, a lumped element LC parallel resonator at center frequency, ω_0, has a susceptance and a susceptance-slope parameter of zero and $\omega_0 C$, respectively. These values are helpful in finding the relationship between the generalized bandpass prototypes and their lumped element equivalents.

There are various methods for realizing impedance/admittance inverters. They can be realize either using lumped elements or distributed circuits. Even, mixed circuits, consisting of lumped elements and distributed structures, are possible [66]. A quarter-wavelength transmission line, for example, is one of the simplest forms of an impedance or admittance inverter with an ABCD matrix of the form given in (2.27a) and (2.27b). It is sufficient that in (2.27a) the value of K is selected to be equivalent to the characteristic impedance of the line. Similarly, in (2.27b) the value of J can be made equal to the characteristic admittance of the line. In microwave filters, another common way for realization of impedance/admittance inverters is through proximity coupling of the adjacent resonators, which can be implemented either using inductive or capacitive coupling [66].

Filter design based on the lowpass prototype method is handy for lumped element and planar filters. However, for direct-coupled resonator filters, another design approach is more convenient. Dishal demonstrated that any narrow-band distributed bandpass filter can be uniquely defined by three fundamental parameters [23]. These parameters are: the synchronous resonant frequency of each resonator, ω_0; the coupling coefficients between adjacent resonators, $k_{i,i+1}$; and the singly loaded or external quality factor of the first and

last resonators, Q_{ex}. He also demonstrated that the realized direct-coupled resonator filter can be tuned using knowledge of these fundamental parameters. $k_{i,i+1}$ and Q_{ex} are defined as:

$$Q_{ex1} = \frac{\mathrm{g_0 g_1}}{\Delta} \tag{2.32a}$$

$$k_{i,i+1} = \frac{\Delta}{\sqrt{\mathrm{g_i g_{i+1}}}} \qquad \text{for } i = 1 \text{ to } (N-1) \tag{2.32b}$$

$$Q_{exN} = \frac{\mathrm{g_N g_{N+1}}}{\Delta} \tag{2.32c}$$

Once the required coupling coefficients and external quality factors for a specific design are known, they can be correlated with the physical dimensions of the filter. To this end, Dishal's method can be utilized to generate two design curves. The first design curve is usually for coupling as a function of one of the crucial physical dimensions in the filter. This curve, for example, is usually extracted for the distance or the width of an iris between two adjacent resonators, each tuned to the center frequency. The second design curve maps the external quality factor to another important physical dimension in the filter, like the position of the tap point for the first/last resonator. In the early days of the filter design, these curves were extracted using measured values from experimental hardware, while currently they are primarily calculated using computer simulations.

The *split-pole* technique is a general method that can be used to find the coupling coefficient between two resonators. The concept of the splitting the resonant poles in a coupled-resonator filter is shown in figure 2.12. This figure

shows two coupled resonators, both resonating at $f_0 = \omega_0/2\pi$, that are weakly coupled to the input and output ports. The weak coupling of the resonators to ports guarantees that in this analysis the effects of reactive loading from the ports are minimized and negligible. If the transfer frequency response of the network, is plotted a double peak response is obtained. In fact, as illustrated in figure 2.12, due to interaction between the coupled resonators, the resonant modes degenerate and the frequencies split. If there is no coupling between the two resonators, i.e. $k_{i,i+1} = 0$, the resonant frequencies of the resonators are identical. To assure that the weak coupling condition is met, the peaks of the frequency response should be below -20 dB and the null between the two peaks should be at least -30 dB. The locations of the split peaks f_a and f_b can be used to calculate the coupling coefficient k using [66]

$$k = \frac{{f_b}^2 - {f_a}^2}{{f_b}^2 + {f_a}^2} \tag{2.33}$$

When two coupling mechanisms (for example both electric- and magnetic-field coupling) exist between the resonators, the resulting coupling is called the mixed coupling, and can be found from the superposition of both coupling mechanisms. However, in these mixed coupling situations, the superposition can result in two types of effects, either constructive or deconstructive. In general the coupling coefficient between two coupled resonators can be found from [66] regardless of whether the coupling mechanism is electric, magnetic, or mixed.

$$k = \pm\frac{1}{2}\left(\frac{f_{02}}{f_{01}} + \frac{f_{01}}{f_{02}}\right)\sqrt{\left(\frac{f_b^2 - f_a^2}{f_b^2 + f_a^2}\right)^2 - \left(\frac{f_{02}^2 - f_{01}^2}{f_{02}^2 + f_{01}^2}\right)^2} \tag{2.34}$$

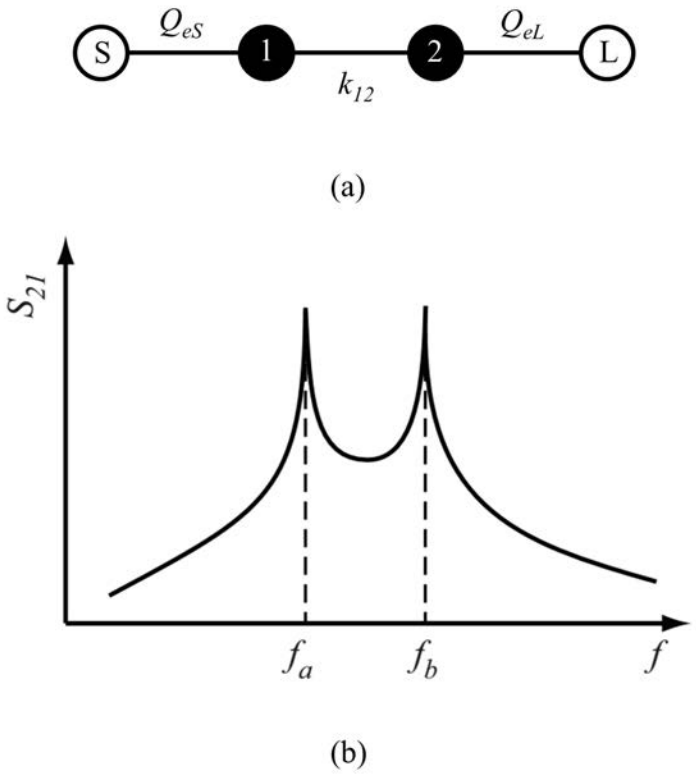

Figure 2.12: Concept of split-pole due to inter-resonator coupling, (a) weakly-coupled structure formed to extract the coupling coefficient between adjacent resonators, (b) an example transfer function for two weakly-coupled resonators.

where f_{01} and f_{02} are the corresponding resonant frequency of the resonator 1 and 2 and f_{p1} and f_{p2} are the same splitting modes shown in figure 2.12. The sign of coupling depends on the physical coupling structure of the coupled resonators, and in general the meaning of positive or negative coupling is relative. If one particular coupling is referred to as a positive coupling, then the coupling that has the opposite phase response will be referred to as negative coupling. Checking the direction of movement for each resonator in the presence of coupling, is another way to find the relative sign of two different coupling mechanisms. If the frequency shifts of f_a or f_b, with respect to their individual uncoupled resonant frequencies, are in the same direction, the

resulting coupling coefficients will have the same signs, if not they will have opposite signs.

Several methods have been proposed to determine the external coupling factor of a coupled resonator in literature [67]. In order to find the effect of an external port on the resonator, the loading effects of the other resonators should be eliminated. Therefore, a single terminated resonator is usually considered as shown in figure 2.13(a). Sometimes, in practice, when the isolation of a single resonator from the rest of the structure is not possible, all the other resonators are short circuited. This is a very useful method for tuning of a coupled-resonator filter. It has been shown that for a singly terminated resonator, the external quality factor of the resonator is linked to the phase of the reflection function at the excitation port using [66]

$$Q_e = \frac{\omega_0}{\Delta\omega_{\pm 90^o}} \tag{2.35}$$

where the definition of $\Delta\omega_{\pm 90^o}$ is shown in figure 2.13(b).

Alternatively, it has been shown that the external quality factor may be extracted from the reflection delay of S_{11} at resonance [68] using

$$Q_e = \frac{\omega_0 \tau_{S_{11}}(\omega_0)}{4} \tag{2.36}$$

where $\tau_{S_{11}}(\omega_0)$, shown in figure 2.13(c), is defined as,

$$\tau_{S_{11}}(\omega_0) = \left.\frac{\partial(\angle S_{11})}{\partial\omega}\right|_{\omega=\omega_0} \tag{2.37}$$

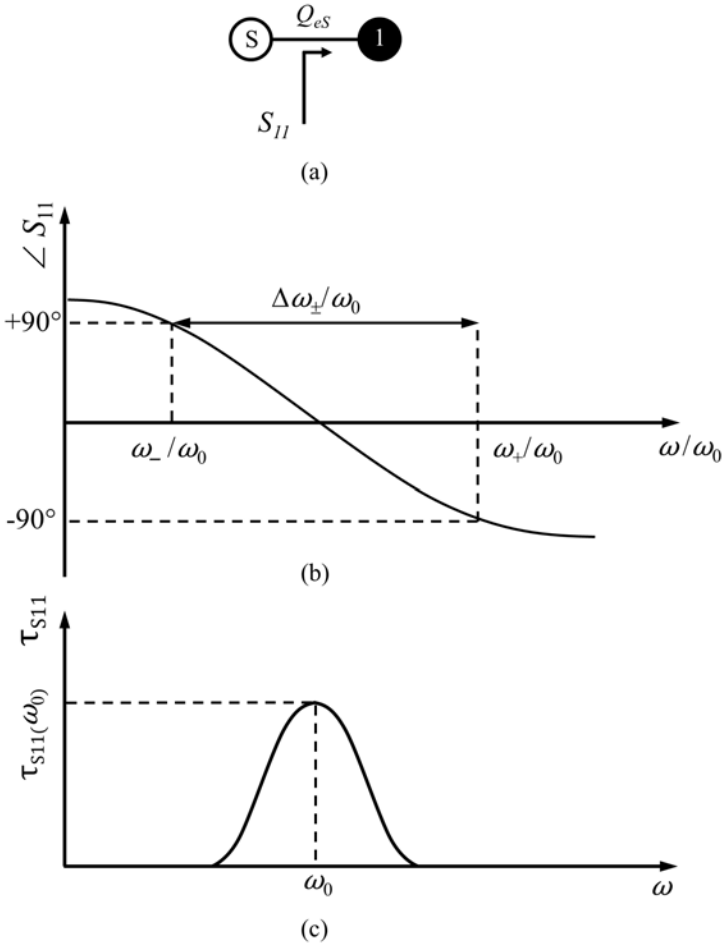

Figure 2.13: Extraction of external coupling, (a) Singly terminated resonator, (b) typical variation of the phase of the reflection function.

2.3 Coupling Matrix

Modeling microwave filters using the coupling matrix method, which is an alternative to the element extraction method, is a particularly useful technique. Applying matrix operation such as inversion, similarity transformation, and partitioning can simplify the synthesis, reconfiguration, simulation, and diagnosis of filters. As mentioned before, there is a one-to-one correspondence between the filter components and the matrix elements, allowing the designer to account for the effect of the electrical characteristics (such as quality factor

or dispersion property) of each element.

The coupling matrix concept was first introduced by A. E. Atia and A. E. Williams in the early 1970s where it was applied to the design of dual-mode, symmetric, waveguide, microwave filters [29]–[32]. The basic circuit model used in [32] was the bandpass prototype shown in figure 2.14. The network is a generalized, multi-coupled, resonator filter that consists of a cascade of lumped element series resonators. Each resonator is consists of a capacitor of 1 Farad in series with the self-inductances of the main-line transformers of 1 Henry within each loop. This gives a center frequency of 1 rad/sec and the coupling mechanisms are normalized to give a bandwidth of 1 rad/sec. The resonators are inter-coupled through the transformers. In addition, every loop is theoretically coupled to every other loop through mutual coupling between the mainline transformers. This circuit supports symmetric frequency characteristics. To more closely model a general microwave filter some modifications to this network must be done. First, the self-inductances of the mainline transformers are separated out and represented as individual inductors in each loop. FIR elements are also included in each loop enabling representation of asymmetric characteristics. Also, since the coupling elements are frequency-invariant, the following modifications can transform the network to a lowpass prototype [64].

- All mutual inductive coupling mechanisms are replaced by inverters with the same value as the mutual coupling of each transformer.

- The value of the series capacitances in each loop are set at infinity. This transforms the bandpass network to a lowpass prototype with cutoff frequencies at $\omega = \pm 1$ rad/sec.

The lowpass prototype has a suitable form for synthesis through element ex-

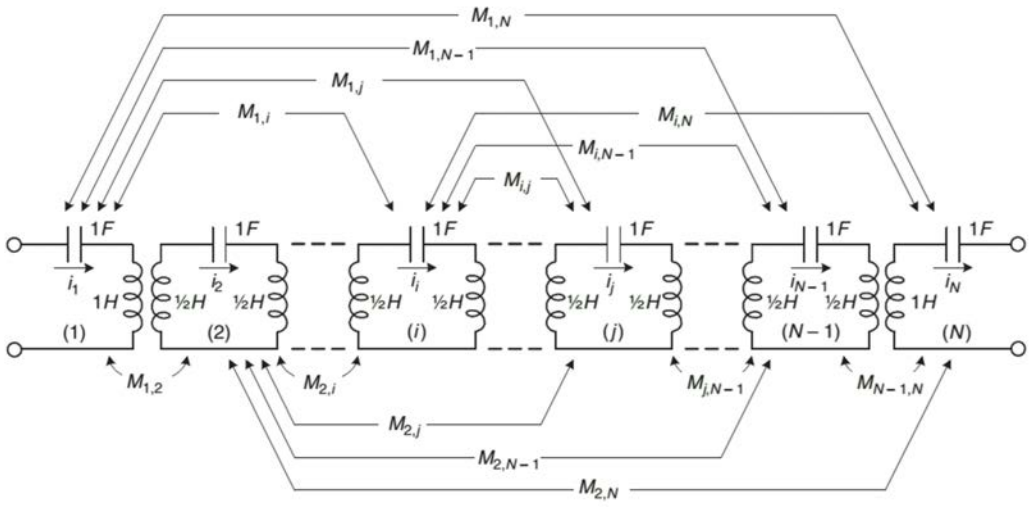

Figure 2.14: Classical, multi-coupled resonator, bandpass filter, prototype (from [26]).

traction method from polynomials. However, the synthesis procedure in the lowpass or bandpass domain results in the same values for the elements and the filter analysis yields the same insertion loss and attenuation response in both domains. Both networks can be represented by an $N \times N$ coupling matrix. The matrix contains the values of all couplings: mainline couplings and cross-couplings. Since the networks are passive and reciprocal, the matrix is symmetrical about its principal diagonal. Due to the inclusion of FIRs, the lowpass prototype coupling matrix can exhibit asymmetric characteristics. The values of the FIRs (usually called self-coupling) are entered along the diagonal of the coupling matrix and represent a frequency shift in the transformed equivalent bandpass prototype. A mesh analysis of the two-port lowpass network yields N linear equations that can be expressed using the following matrix equation [64]

$$[v_S] = [z'] \cdot [i] \tag{2.38}$$

where $[v_S]$ is the voltage source exciting the network at the input port and $[z']$ is the impedance matrix of the network including its terminations. Therefore, it can be decomposed into three $N \times N$ matrices

$$[z'] = [j\mathbf{M} + s\mathbf{I} + \mathbf{R}] \tag{2.39}$$

where $\mathbf{I}$ is the $N \times N$ identity matrix, $\mathbf{R}$ is an $N \times N$ matrix with all entries zero except that $R_{1,1} = R_S$ and $R_{N,N} = R_L$, and $\mathbf{M}$ is the main coupling matrix and contains the values of the mutual coupling between the nodes of the network. The entries on the main diagonal represent the value of the FIR elements at each node or self-couplings, ($M_{i,i} = B_i$). The coupling between sequentially numbered nodes ($M_{i,i+1}$) are entered just beside of self-coupling elements and are referred to as mainline coupling. All other couplings between the non-sequentially numbered nodes, known as cross coupling, are entered at other positions [69]. Since the network is passive and reciprocal $M_{i,j} = M_{j,i}$.

The impedance matrix can be divided into purely resistive and purely reactive parts by

$$[z'] = \mathbf{R} + [j\mathbf{M} + s\mathbf{I}] = \mathbf{R} + [z] \tag{2.40}$$

where $[z]$ represents a purely reactive network exited by a voltage source with internal impedance of R_S and loaded by R_L, shown in figure 2.15(a). Since the source and load resistors are usually nonzero, they can be normalized to unite values by introducing impedance inverters $M_{S1} = \sqrt{R_L}$ and $M_{NL} = \sqrt{R_S}$ at the source and load side of the network, respectively. Now, the network represented by $[z]$, as well as the two sources and load inverters, can be converted to a dual network with shunt resonators and admittance inverters as

coupling elements. The dual admittance network $[y]$, shown in figure 2.15(b), consists of an $N \times N$ matrix with an extra row at the top and bottom and one extra column on each side. The dual $[y]$ matrix is commonly known as an $(N+2) \times (N+2)$ coupling matrix. However, as shown in figure 2.15(c), the matrix may be again converted to a dual impedance matrix with series resonators and impedance inverters as coupling elements. The $(N+2) \times (N+2)$ coupling matrices, either impedance or admittance type, have the same element values as their mainline and cross-coupling entries. Figure 2.16 and figure 2.17 show the final $(N+2) \times (N+2)$ network and the corresponding coupling matrix, respectively. As can be seen, the $(N+2) \times (N+2)$ coupling matrix not only includes the direct source-load coupling, it also accommodates all possible couplings between the source and load and other internal nodes within the primary $N \times N$ matrix.

In the previous analysis, it was assumed that the resonators are all lossless, and therefore, their unloaded quality factors, Q_u, are infinity. However, for bandpass filters, the effect of the unloaded quality factor of the resonator can be taken into account by offsetting the normalized complex frequency, s, by a positive real factor δ, which is defined as $\delta = f_0/(BW \cdot Q_u)$, where f_0 is the center frequency and BW is the filter bandwidth [64]. The reflection and transfer functions of a filter, which are usually are referred to as S_{11} and S_{21}, respectively, can be found from the coupling matrix of the filter [20]:

$$S_{11} = 1 - 2\mathbf{A}^{-1}_{1,1} \tag{2.41a}$$

$$S_{21} = 2\mathbf{A}^{-1}_{N+2,1} \tag{2.41b}$$

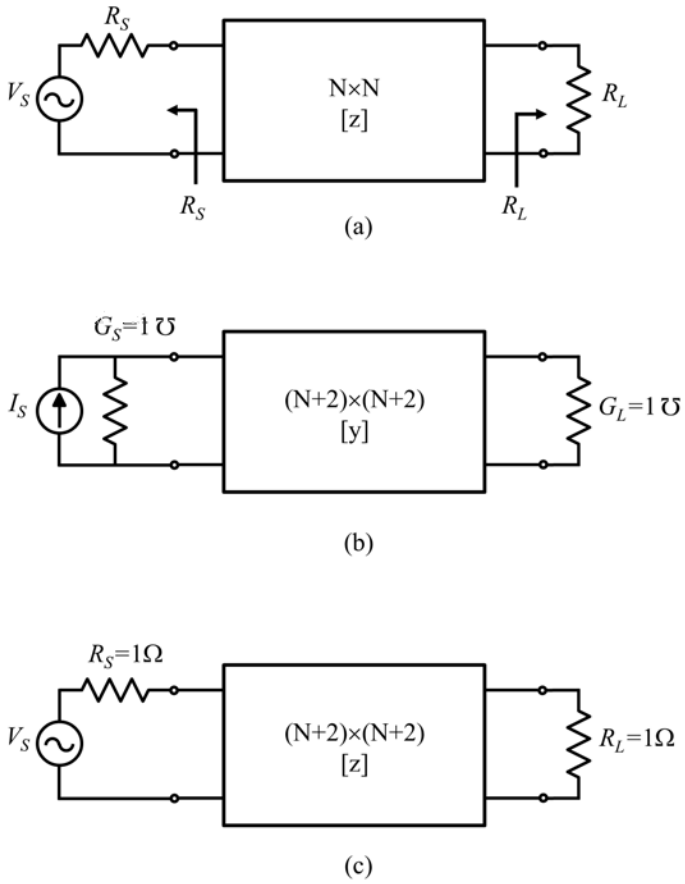

Figure 2.15: Configurations of the input/output circuits for $N\times N$ and $(N+2)\times(N+2)$ coupling matrices, (a) the series resonator multi-coupled lowpass prototype represented by an $N\times N$ coupling matrix and port terminations of R_S and R_L, (b) the parallel resonator multi-coupled lowpass prototype represented by an $(N+2)\times(N+2)$ coupling matrix and normalized port terminations of G_S and G_L (detailed configuration of the circuit is shown in figure 2.16, and (c) dual network of (b) representing series resonator multi-coupled lowpass prototype as an $(N+2)\times(N+2)$ coupling matrix with normalized port terminations of R_S and R_L.

where $\mathbf{A}$ is defined as

$$\mathbf{A} = [j\mathbf{M} + s\mathbf{U} + \mathbf{Q}] \tag{2.42}$$

in which $\mathbf{U}$ is similar to the $(N+2)\times(N+2)$ identity matrix except that $U_{1,1} = U_{N+2,N+2} = 0$, $\mathbf{Q}$ is a $(N+2)\times(N+2)$ matrix whose only nonzero

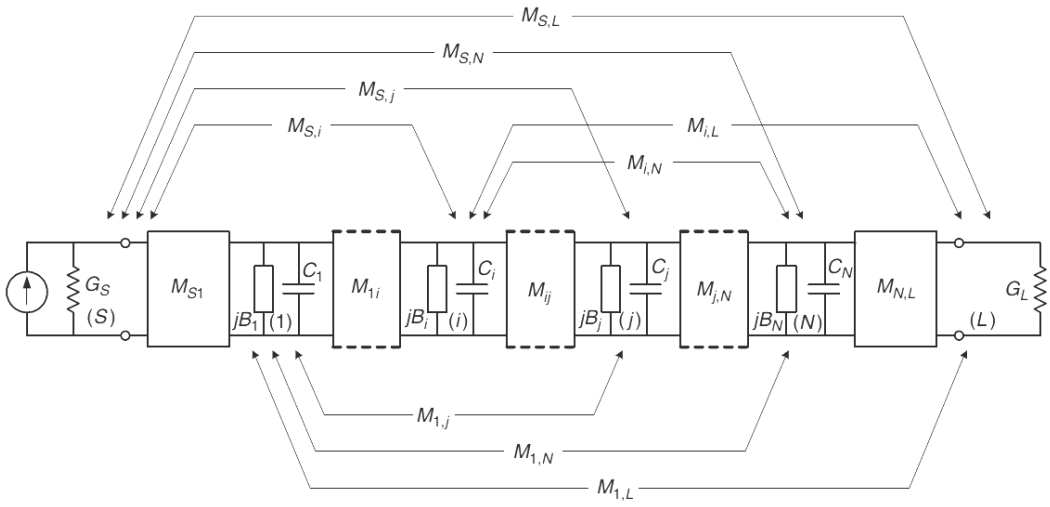

Figure 2.16: Modified multi-coupled resonator lowpass prototype including FIRs and admittance inverters (from [26]).

	S	1	2	...	N	L
S	M_{SS}	M_{S1}	M_{S2}	...	M_{SN}	M_{SL}
1	M_{1S}	M_{11}	M_{12}	...	M_{1N}	M_{1L}
2	M_{2S}	M_{12}	M_{13}	...	M_{1N}	M_{1L}
...	...	...	...	...	...	...
N	M_{NS}	M_{N1}	M_{N2}	...	M_{NN}	M_{NL}
L	M_{LS}	M_{L1}	M_{L2}	...	M_{LN}	M_{LL}

Figure 2.17: General form of a $(N+2) \times (N+2)$ coupling matrix with all possible cross-couplings. The gray core matrix indicates the $N \times N$ coupling matrix.

entries are $Q_{1,1} = Q_{N+2,N+2} = 1$, and $\mathbf{M}$ is the main $(N+2) \times (N+2)$ coupling matrix.

Although the coupling matrix mathematically describes all the existing couplings between the resonators in a specific filter, it is more convenient to graphically show the available couplings between the resonators. There-

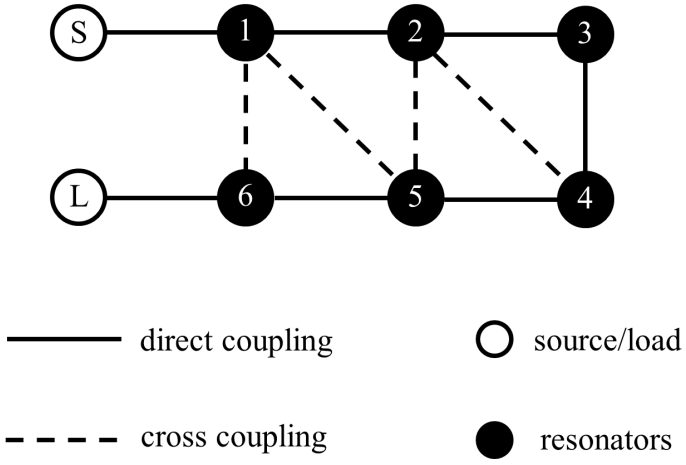

Figure 2.18: A typical coupling-routing diagram with both direct and cross coupling.

fore, a diagram named coupling-routing diagram is employed to graphically summarize all the couplings among the resonators. The coupling-routing diagram provides a convenient insight into the coupling configuration of the filter. An example of coupling-routing diagram for a typical 6th-order filter along with the conventional definition of the diagram elements is shown in figure 2.18. This coupling-routing diagram shows multiple direct couplings between consecutively-numbered resonators and the cross couplings between non-consecutively-numbered resonators. The coupling-routing diagram can be utilized to illustrate the relative phase shifts of multiple signal paths. This is helpful in understanding how transmission zeros are produced.

Filter synthesis using the coupling matrix method can be performed either with the $N \times N$ coupling matrix along with the port resistances, or with the $(N+2) \times (N+2)$ coupling matrix. Both analytic methods and optimization methods are available for this type of synthesis. In analytic methods, the filter is synthesized by equating the coefficients of the polynomials from (2.1b)

to those in (2.41b). Various direct and in-direct synthesis methods, for both bandpass and bandstop prototypes with different coupling-routing diagrams, have been proposed in literature [64], [70]. The synthesis process can also be executed by using optimization methods [64], [71]–[73]. It has been shown for all-pole filters that the coupling matrix contains only mainline couplings and for an Nth-order lowpass prototype can be readily found from the following matrix [74]:

$$M = \begin{bmatrix} 0 & m_{01} & 0 & 0 & \dots & 0 & 0 \\ m_{10} & 0 & m_{12} & 0 & \dots & 0 & 0 \\ 0 & m_{21} & 0 & m_{23} & \dots & 0 & 0 \\ \vdots & \vdots & \vdots & \vdots & \ddots & \vdots & \vdots \\ 0 & 0 & 0 & 0 & \dots & 0 & m_{N,N+1} \\ 0 & 0 & 0 & 0 & \dots & m_{N+1,N} & 0 \end{bmatrix} \tag{2.43}$$

where

$$m_{i,j} = \frac{1}{\sqrt{\mathrm{g_i g_j}}} \qquad \text{for } i = 0, 1, ..., N \text{ and } j = i + 1 \tag{2.44}$$

and $\mathrm{g_i}$ represents the lowpass prototype element values. In fact, since no transmission zeros exist in the frequency response of an all-pole filter, there is no cross-coupling between the resonators. Also, for symmetric responses, all-pole filters in particular, all resonators have the same resonant frequency. Such a filter is a synchronously tuned circuit, and therefore, all FIR elements have zero values, which means that all diagonal entries of the coupling matrix are also zero.

Chapter 3

Substrate-Integrated, Evanescent-Mode Cavity Bandpass Filter Design

3.1 Introduction

The first step in the design of a tunable microwave filter is the choice of a proper resonator. Since the loss in coupled-resonator filters is inversely proportional to the bandwidth of the filter and the resonator quality factor [17], in narrow band applications the loss requirement is the most dominant factor affecting the resonator choice. Although waveguide and dielectric resonators have been shown to have the highest unloaded quality factors, among available RF/microwave resonators, their large form factors and low frequency tuning ranges limit their usage significantly. Recently, evanescent-mode cavity resonators have been shown to be promising in realizing widely tunable filters with high Q_u, and hence low insertion loss [51], [53], [75]. In this chapter, the use of evanescent-mode cavity resonators for making low-profile tunable RF/Microwave filters with high Q_u is presented. Specifically, a design method for both narrowband and wideband tunable filters in the range of 3.0 to 3.6 GHz with fractional bandwidth of 2% to 40% is shown. To this end, the modeling methodology and trade-offs in evanescent-mode cavity resonator

design is first discussed. A design technique for active evanescent-mode cavity resonators is also discussed. Finally, measurements and discussions of the fabricated tunable resonators are provided.

3.2 Evanescent-Mode Cavity Resonators Modeling

Resonant frequency and quality factor are the most important characteristics of a resonator. For a specific resonator, these characteristics can be found from either analytical solutions of the field distribution inside the cavity, for the case of resonators with simple geometries, or numerical simulation for resonators with more complex geometries. Evanescent-mode cavity resonators have been well-studied in the literature and analytical solutions, for example, for cylindrical evanescent-mode cavity have been derived [46], [76], [77]. It has been shown that the resonant characteristics of evanescent-mode cavities are functions of the cavity size, the post size and the gap between the conductive post and the cavity top. By increasing the equivalent shunt capacitance, which is achieved by decreasing of the gap size, the resonant frequency and quality factor of the cavity are lowered.

A cylindrical evanescent-mode cavity resonator along with the fields distribution inside a sample cavity with $a = 1.9$ mm, $b = 6.85$ mm, and $h = 3.175$ mm found from a full wave electromagnetic simulation performed using ANSYS HFSS, (Finite Element Method (FEM) EM solver) is shown in figure 3.1. It can be seen that the electric-field has a nearly uniform distribution between the post top and the cavity top, which suggests that the region above the post can be modeled by a lumped capacitor. Also, the magnetic-field has a uniform toroidal distribution around the post. This distribution suggests that the post and sidewall of the cavity can be modeled by a shorted-circuited,

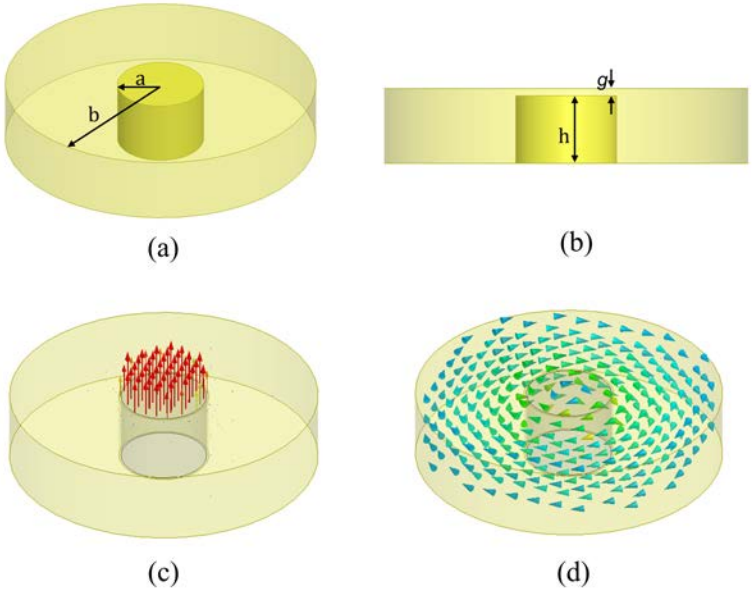

Figure 3.1: A cylindrical evanescent-mode cavity, (a) structure, (b) fields distribution.

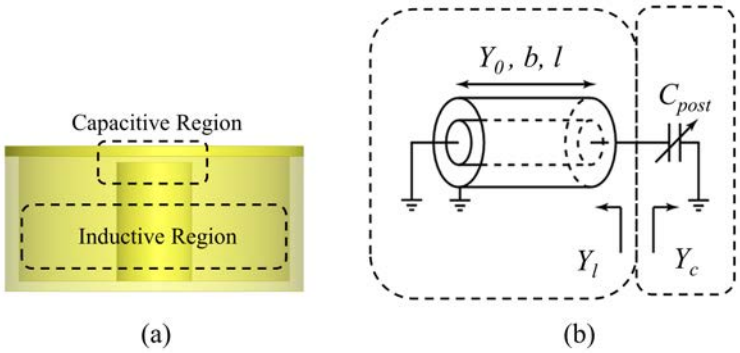

Figure 3.2: Model for highly-loaded, evanescent-mode cavity resonator based on the quasi-static approximation, (a) dominant field regions, (b) equivalent circuit.

electrically-small, coaxial line, which represents an effective inductor. Therefore, the quasi-static model and the equivalent circuit shown in figure 3.2 can be used to characterize the resonator.

At the resonant frequency,

$$Y_c + Y_l = 0 \tag{3.1a}$$

$$j2\pi f_0 C_{post} - jY_0 \cot(\beta l) = 0 \tag{3.1b}$$

$$2\pi f_0 C_{post} = Y_0 \cot\left(\frac{2\pi f_0}{v_p}\right) l \tag{3.1c}$$

where f_0 is the resonant frequency, l is the coaxial line length, C_{post} is the effective capacitance of the post, v_p is the phase velocity in the coaxial line, and Y_0 is the characteristic admittance of the line, which is a function of the post and cavity diameters. If the value of the capacitor is known, (3.1c) can be solved numerically to find the resonant frequency of the structure. In [78] and [79], C_{post} was found using a parallel-plate capacitance formulation as a first order approximation. When l is small enough (3.1c) can be simplified. For an air filled coaxial line, it is simplified to,

$$f_0 = \frac{c_0}{\pi\sqrt{2a^2 \frac{l}{g} \ln\left(\frac{b}{a}\right)}} \tag{3.2}$$

where c_0 is the speed of light in free space. The length of the coaxial line is usually assumed to be equal to the post height. However, in [46] it has been

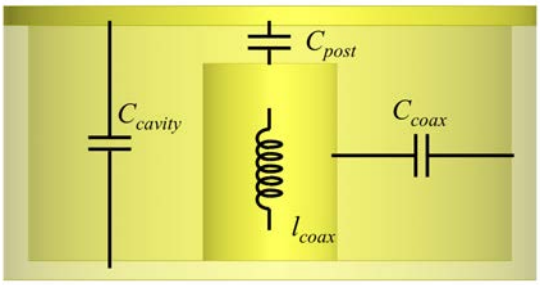

Figure 3.3: Lumped element model for a highly-loaded, evanescent-mode cavity resonator.

approximated with the total height of the cavity, that is $l = h + g$. Therefore,

$$f_0 = \frac{c_0}{\pi\sqrt{2a^2\frac{h+g}{g}\ln\left(\frac{b}{a}\right)}} \tag{3.3}$$

The resonant frequency of a cylindrical evanescent-mode cavity resonator can also be found from the lumped element resonator model shown in figure 3.3. In the simplest form of this model, all elements are assumed to be connected in parallel. Therefore,

$$C_{tot} = C_{post} + C_{cavity} + C_{coax} \tag{3.4a}$$

$$f_0 = \frac{1}{2\pi\sqrt{L_{coax}C_{tot}}} \tag{3.4b}$$

where C_{post} and C_{cavity} are the capacitors formed between the post and the cavity top, and the cavity top and bottom. They can be estimated using parallel plate capacitor model. C_{coax} and L_{coax} are the coaxial line equivalent

circuit parameters per unit length [14]. In the case of air-filled cavity,

$$C_{post} = \epsilon_0 \left(\frac{A_{post-top}}{g} \right) \tag{3.5a}$$

$$C_{cavity} = \epsilon_0 \left(\frac{A_{cavity-top} - A_{post-top}}{h+g} \right) \tag{3.5b}$$

$$C_{coax} = \frac{2\pi\epsilon_0}{\ln(\frac{b}{a})} h \tag{3.5c}$$

$$L_{coax} = \frac{\mu_0}{2\pi} \ln(\frac{b}{a}) h \tag{3.5d}$$

However, for more accurate modeling the effect of the fringing field capacitance C_{ff}, mainly formed between the post and cavity top not directly above the post, must be taken into consideration. [80] has provided estimates of the C_{ff} of a circular structure. Numerical simulation can also be used to extract the approximate value of C_{ff} based on empirical curve fitting. Also, a more accurate expression for the resonant frequency of an air-filled evanescent-mode cavity resonator, based on Green's function analysis, has been presented in [44] as

$$f_0 = \frac{c_0}{2\pi \sqrt{a(h+g)\ln\left(\frac{b}{a}\right)\left[\frac{a}{2g} - \frac{2}{\pi}\ln\left(\frac{0.736g}{\sqrt{(h+g)^2 + (b^2-a^2)}}\right)\right]}} \tag{3.6}$$

Figure 3.4 compares the resonant frequency of a typical resonator found from the various methods discussed here. In this figure, the relationship

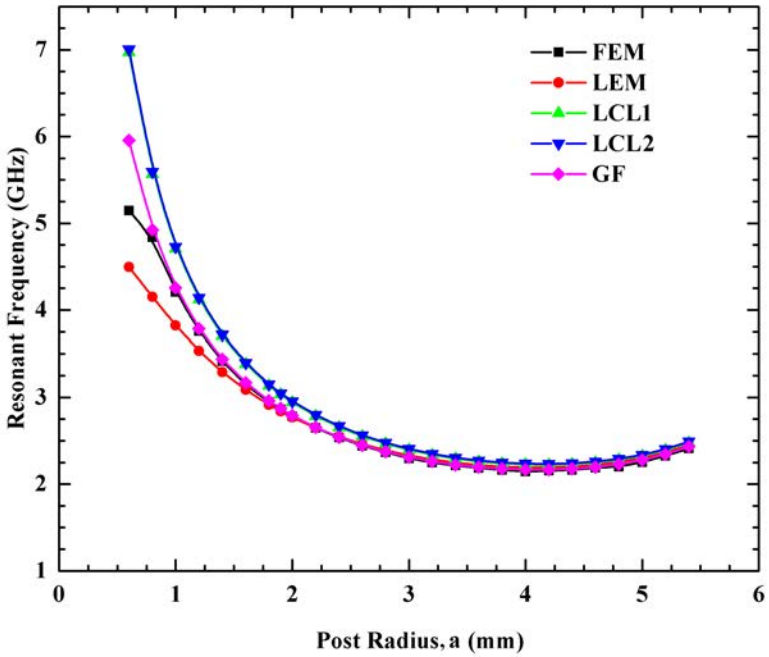

Figure 3.4: A comparison of the resonant frequency versus post radius for a sample air-filled evanescent-mode cavity with $g = 30$ μm, $b = 6.85$ mm, and $h = 3.175$ mm. FEM: Finite Element Method HFSS, LEM: Lumped Element Model from (3.4b), LCL1: Loaded Coaxial Line from (3.2), LCL2: Loaded Coaxial Line from (3.3), GF: Green's function method from (3.6).

between f_0 and the post radius, a, for a resonator with cavity radius of $b = 6.85$ mm, and height of $h = 3.175$ mm for a fixed gap size of $g = 30$ μm has been plotted. As a reference, the result from numerical FEM analysis, found from HFSS, has also been included in this graph. The Green's function method provides the most accurate results although the results from the other methods, especially for larger post radii, are all accurate enough for most of practical applications.

The relationship between the resonant frequency and the the post height can be plotted from any of the provided expressions to calculate the resonant frequency. Figure 3.5 shows the resonant frequency of the same sample resonator with three different post sizes plotted as a function of post radius found from (3.4b). It can be seen that for any post size, the resonant frequency has a

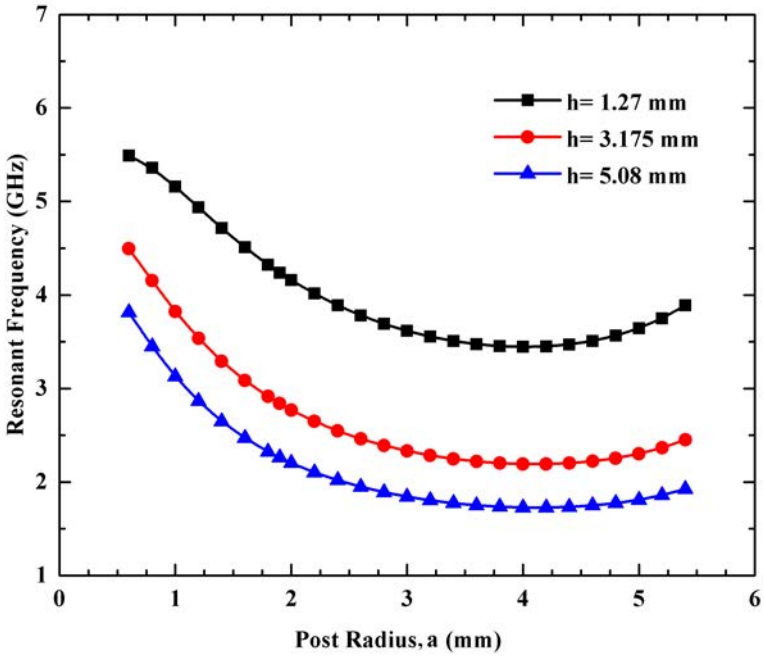

Figure 3.5: Resonant frequency versus post radius for a sample air filled resonator cavity with $g = 30$ μm, $b = 6.85$ mm.

minimum. This suggests that care must be taken during the design of tunable filters as the minimum tuning frequency can be limited by the post height.

The quality factor of an evanescent-mode cavity resonator can also be found using the model shown in figure 3.2 as [81],

$$\frac{1}{Q_u} = \frac{1}{Q_{coax}} + \frac{1}{Q_{ppc}} \tag{3.7a}$$

$$Q_{coax} = \frac{2\eta \ln(\frac{b}{a})\,\omega\sqrt{\mu\epsilon}}{R_S\left(\frac{1}{a} + \frac{1}{b}\right)} \tag{3.7b}$$

$$Q_{ppc} = \frac{\omega\mu h}{2R_S} \tag{3.7c}$$

where R_S is the surface resistance of the metallic walls in the coaxial line and η is the free space intrinsic impedance. Therefore,

$$Q_u = \frac{\omega\mu}{R_S}\left[\frac{\left(\frac{1}{a}+\frac{1}{b}\right)}{\ln\left(\frac{b}{a}\right)}+\frac{2}{h}\right]^{-1} \tag{3.8}$$

An approximated closed-form expression for the calculation of the quality factor has also been provided in [46],

$$Q_u = \frac{2(h+g)}{\delta}\left[\frac{\ln\left(\frac{b}{a}\right)}{2\ln\left(\frac{b}{a}\right)+(h+g)\left(\frac{1}{a}+\frac{1}{b}\right)}\right] \tag{3.9}$$

in which δ is the skin depth of the metallic walls in the cavity. A plot of Q versus post radius, for a fixed b and g calculated from (3.8), is shown in figure 3.6.

It can be seen that, the resonant frequency and the quality factor, for a fixed cavity radius, depend on both the gap and the post radius. Therefore, for a fixed resonant frequency, when post radius is changed, the gap size must change accordingly to compensate for the change in the resonant frequency. This is important for calculating the quality factor. If the fringing fields inside an evanescent-mode cavity resonators is neglected, the maximum Q_u, for a given frequency, happens when $\frac{b}{a} = 3.59$. However, this behavior is not seen in figure 3.6. It seems that for different gap sizes, the maximum Q_u is achieved at different post radii. To clarify this issue, the relationship between the resonator Q_u and the post radius for the sample resonator, tuned to a fixed frequency, has been illustrated in figure 3.7. To extract the required data

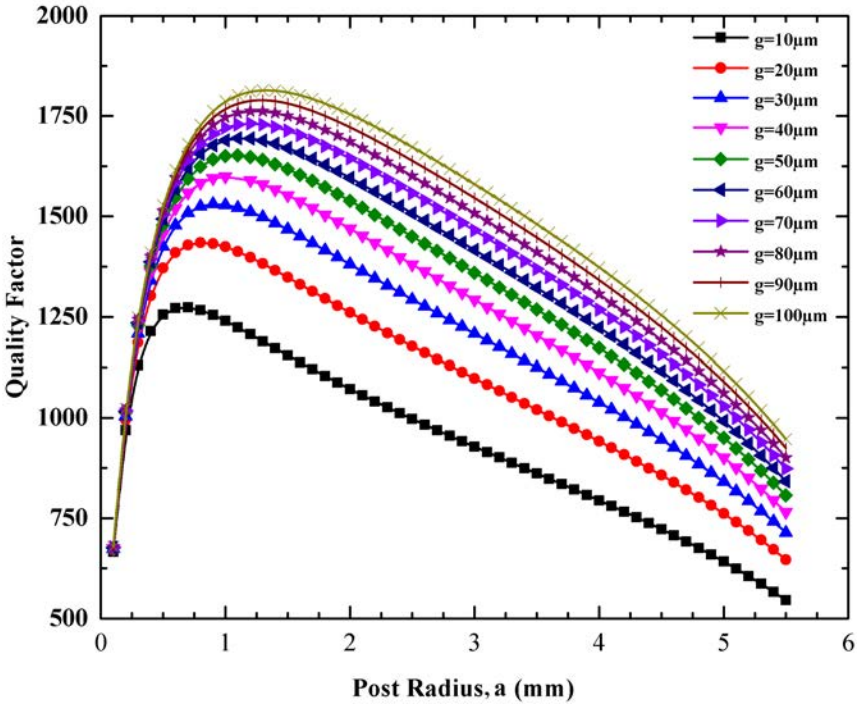

Figure 3.6: Quality factor versus post radius for a sample air-filled resonator cavity with $b = 6.85$ mm, and $h = 3.175$ mm and g as a parameter.

for this plot, when the cavity radius was swept, the gap size was adjusted to keep the resonance frequency constant. For this example, the maximum Q_u happens for $a = 1.9$ mm, which is equivalent to $\frac{b}{a} = \frac{6.85}{1.9} = 3.59$.

Equations (3.8) and (3.9) suggest that Q_u is directly proportional to g. The $Q_u - g$ curve, for different post radii in a typical resonator, shown in figure 3.8, also confirms the behavior. Therefore, a higher absolute g value seems like the natural choice for increasing of the quality factor. However, it should be remembered that when g is increased the frequency also increases. Variation of both resonant frequency and quality factor for versus g is shown in figure 3.9.

Finally, a comparison between (3.8) and (3.9), as well as the results found from FEM analysis, is shown in figure 3.10. In this figure, numerical simulation results are provided for two different cases: one when only the post top is

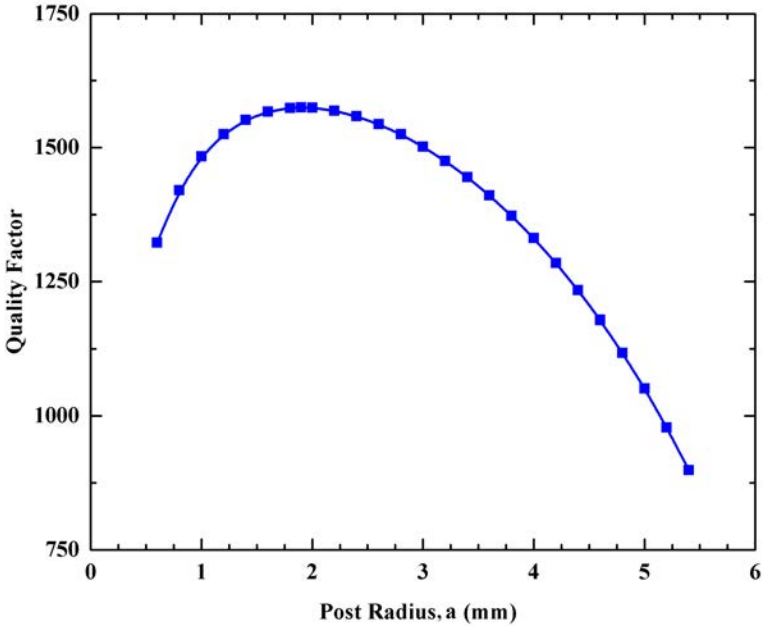

Figure 3.7: Quality factor versus post radius for a sample air-filled resonator cavity $b = 6.85$ mm, and $h = 3.175$ mm for a fixed resonant frequency of 3.6 GHz.

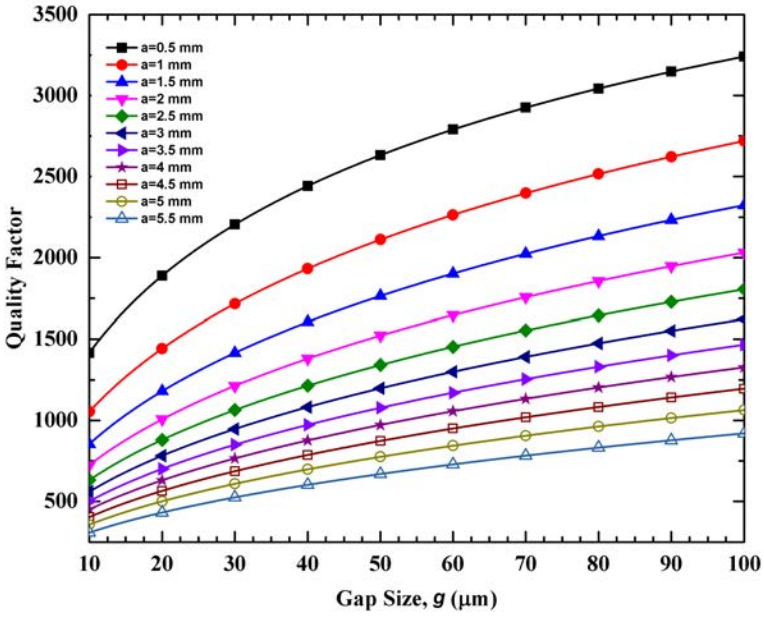

Figure 3.8: Variation in quality factor for a sample air-filled resonator cavity versus gap size with $b = 6.85$ mm, and $h = 3.175$ mm and a as a parameter.

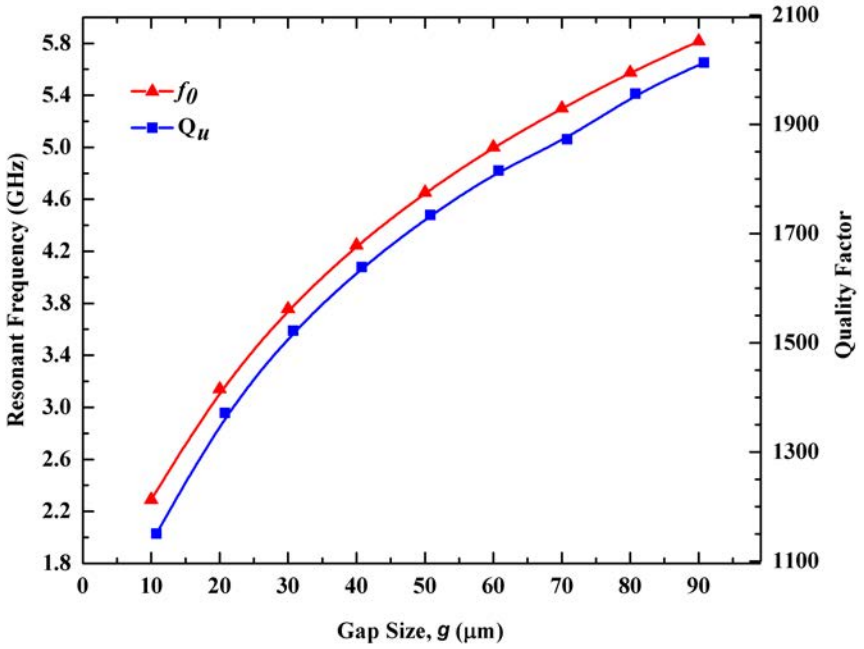

Figure 3.9: Variation of resonant frequency and quality factor for a sample air-filled resonator cavity versus gap size with $b = 6.85$ mm, and $h = 3.175$ mm.

assumed to be a perfect electric conductor and the rest of cavity surface is assumed to be covered with copper. In case two, besides the post top, the cavity top is also modeled as a perfect electric conductor. Because most of the conductive loss happens in the region above the post, this new assumption significantly increases the quality factor.

In summary, the critical parameters in evanescent-mode cavity resonator design are: post radius a, cavity radius b, post height h, and gap size g. The resonant frequency and the quality factor of the resonator are linked to all these parameters. Although full wave analysis is required to fine tune the resonator characteristics, closed form expressions presented in this section provide a very good starting point to evaluate the resonator parameters so that they meet all the design requirements. Increasing the post height will decrease the resonant frequency. While increasing the gap size increases both the resonant frequency and the quality factor of the resonator. In order to get a wider tuning ratio, the

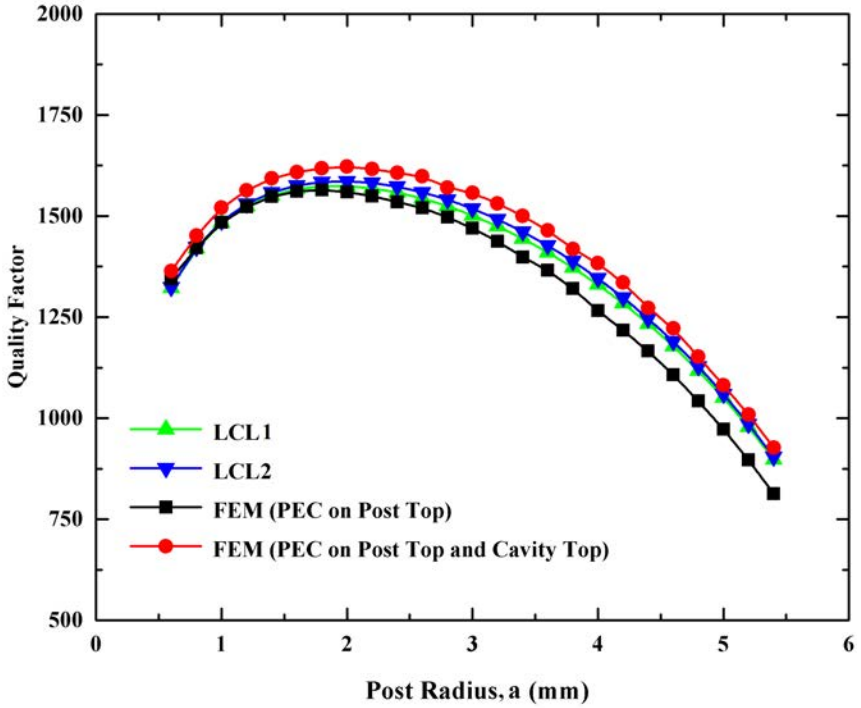

Figure 3.10: A comparison of the quality factor versus post radius found from different techniques for a sample air-filled resonator cavity with $b = 6.85$ mm, and $h = 3.175$ mm at a fixed resonant frequency of 3.6 GHz. FEM: Finite Element Method form HFSS, LCL1: Loaded Coaxial Line from (3.8), LCL2: Loaded Coaxial Line from (3.9)

initial capacitive gap, g_0, must be small. This increases the tuning sensitivity. For a given frequency range, it is therefore desirable to use capacitive post of a smaller diameter so that g_0 can be reduced. Also, it was shown that for a fixed frequency the highest quality factor occurs for $b/a = 3.59$. Therefore a, b, g, and h should be selected so that the resonator covers the desired frequency range with enough tuning sensitivity, while maintaining the highest possible quality factor in order to reduce the loss. At the same time, having a large post size is desirable to increase the power handling of the resonator. These selections must be logical from a fabrication point of view, because in reality, besides all design parameters, manufacturing concerns also places some constraints on the design.

3.2.1 Substrate-Integrated, Evanescent-Mode, Cavity Resonator Design

In order to demonstrate the proposed concepts, a tunable evanescent-mode cavity resonator is designed for the 3.0 to 3.6 GHz range. Traditionally, evanescent-mode cavities have been machined out of a solid piece of metal. On the other hand, substrate-integrated, evanescent-mode, cavity resonators are directly implemented inside a high frequency printed circuit board (PCB) substrate with low loss tangent. This provides the capability of integration with other system components on the same board, as well as avoiding the high weight and bulky size of traditional metallic resonators.

Figure 3.11 shows the basic structure of a cylindrical integrated evanescent-mode cavity resonator. Copper plated vias are used to form both the post and cavity wall. The spacing between vias are selected to be $\lambda_g/20$, at lowest desired frequency, which meets the design guidelines presented in section 1.2.1. The stack-up of the layers is also shown in figure 3.12. Bottom conductive layer is a standard PCB bottom copper-cladding layer, but the top conductive layer is a thin copper foil laminated on top of the substrate using a patterned assembly adhesive. This top layer forms a suspended diaphragm and the opening in the adhesive layer forms an airgap on top of post. The filter is tuned across the desired tuning frequency range by displacement of this diaphragm, which results in the change in the loading capacitance. A disk-shaped two-layer piezoelectric device is mounted on top of the structure and is used to actuate the diaphragm. Shorted grounded coplanar waveguides (GCPW), milled on the bottom conductive layer, are used as the input and output feeding structures. The external coupling is achieved through coupling of the transverse magnetic-field of the shorted GCPW with the toroidal magnetic-field of the

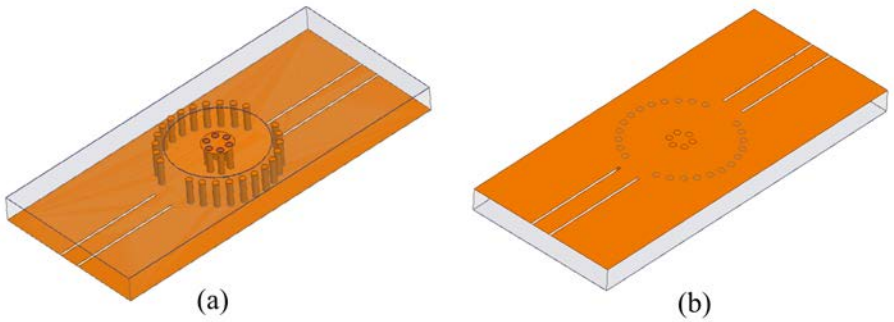

Figure 3.11: Basic structure of the substrate-integrated, evanescent-mode, cavity resonator, (a) top view with copper diaphragm removed for illustration purpose, (b) bottom view.

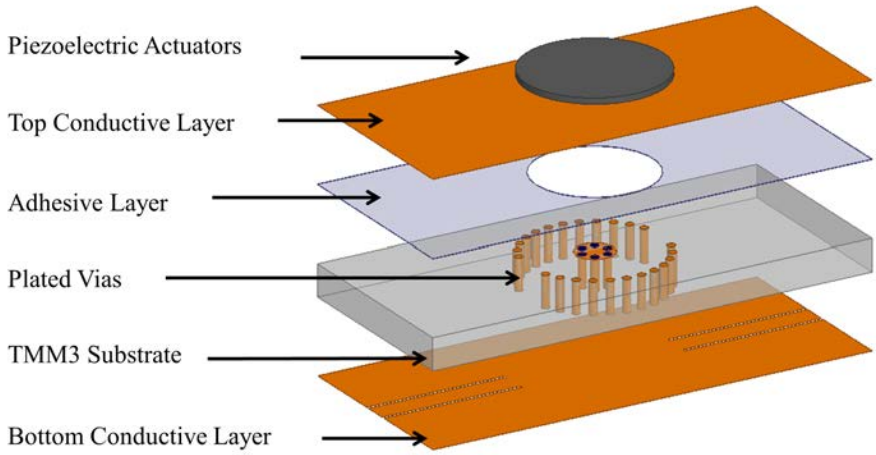

Figure 3.12: Stack-up of the layers in the substrate-integrated, evanescent-mode, cavity resonator.

cavity.

Besides the important design parameters discussed in the previous section, some manufacturing constraints such as standard available sizes of the required materials, force some initial selections. The important practical points that should be considered in the design of the resonator are:

– In PCB fabrication techniques, material stacks will experience some thermal processing. Therefore, a very important factor in the PCB material

selection is the coefficient of thermal expansion (CTE). Significant CTE mismatch between the PCB material and the metals used during the electroplating process (copper in our case), can contribute to lamination failure. In this work, Thermoset Microwave Material (TMM) from Rogers Corp has been selected as the substrate which has a CTE very closely matched to copper (CTE of TMM3 equals to 15 ppm/°K in XY direction and that of copper is 16.5 ppm/°K). This will increase the reliability of plated-through holes and minimize the chance of the copper diaphragm buckling.

– Skin depth, δ, is the determining factor in the selection of copper-cladding thickness, T, for the PCBs. The skin depth for copper at minimum desired frequency (i.e. 3.0 GHz) is 1.2 μm. Therefore, commercial PCB copper thicknesses of 17 and 35 μm, will not have any significant effect on the resonator behavior.

– Based on the past experience, TMM3 ($\epsilon_r = 3.27$ and loss tangent of 0.002) with thickness of 125 mil (3.175 mm), and copper cladding thickness of 17.5 μm has been selected. In addition, from figure 3.5 it can be seen that for a typical resonator, with $b = 6.85$ mm, and $g = 30$ μm, thinner boards do not cover the frequency range of interest.

– In the design approach used in this work, the thickness of the adhesive layer, used for copper membrane lamination, determines the size of the initial gap. Sheet adhesives are commercially available with a variety of thicknesses ranging from 10 to 100 μm. Here, DuPont Pyralux LF0200, with a thickness of 51 μm was selected.

– The nominal free-free displacement of the chosen piezoelectric disk actua-

tor, PSI-5A4E from PIEZO SYSTEMS, is ±19.1 μm when the actuation voltage is swept from -180 V to +180 V. Therefore, the resonator should be designed in a such a way that this amount of displacement should be sufficient to tune the resonator across the frequency range from 3.0 to 3.6 GHz. For this work, disk actuators with a diameter of 0.5 in (12.7 mm) have been chosen.

– Finally, the minimum value for the resonator Q can be found from the maximum allowed insertion loss of the filters. In this work, the maximum insertion loss for the bandpass filter is assumed to be 1.0 dB. In Appendix A, it will be shown that the insertion loss of coupled resonators, Butterworth, bandpass filter is found from

$$L_0 = \frac{8.686}{\Delta Q_u \sin\left(\frac{\pi}{2N}\right)} \quad \text{dB} \tag{3.10}$$

Therefore, for the second-order bandpass filter with smallest fractional bandwidth, i.e. 2%, the minimum unloaded quality factor of the cavity should be 610.

– For having the best diaphragm flexibility, the thickness of top conductive layer should be kept as low as possible. A 25 μm copper foil (from Basic Copper) has been shown to be promising.

Eventually, a substrate-integrated, evanescent-mode, cavity resonator covering frequencies from 3.0 to 3.6 GHz was designed as a vehicle to demonstrate the validity of the above guidelines. The dimensions of the designed resonator are shown in figure 3.13. Table 3.1 also summarizes the resonator design parameters. HFSS simulation results for the designed resonator are depicted in figure 3.14. The unloaded quality factor can be extracted from the loaded

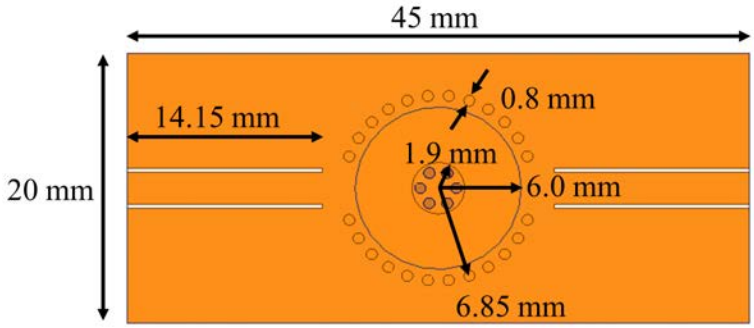

Figure 3.13: Dimension of the designed substrate-integrated, evanescent-mode, cavity resonator.

quality factor. For a weakly coupled resonator, the unloaded quality factor can be found from

$$Q_u = \frac{Q_l}{1 - |S_{21}|} \tag{3.11a}$$

and

$$Q_l = \frac{f_0}{\Delta f_{3dB}} \ . \tag{3.11b}$$

Simulation results shows the resonator covers the frequency range of 3.0 to 3.6 GHz while unloaded quality factor ranges from 757 (for 2.91 GHz) to 809

Table 3.1: Resonator design parameters

Design Parameters	**Value**
Post Radius (a)	1.9 mm
Cavity Radius (b)	6.85 mm
Substrate Height (h)	3.175 mm
Initial Gap Size (g_0)	51 μm
Gap Variation (Δg)	30 μm
PCB Copper Cladding Thickness (T)	17.5 μm
Via Diameter (r_v)	0.8 mm

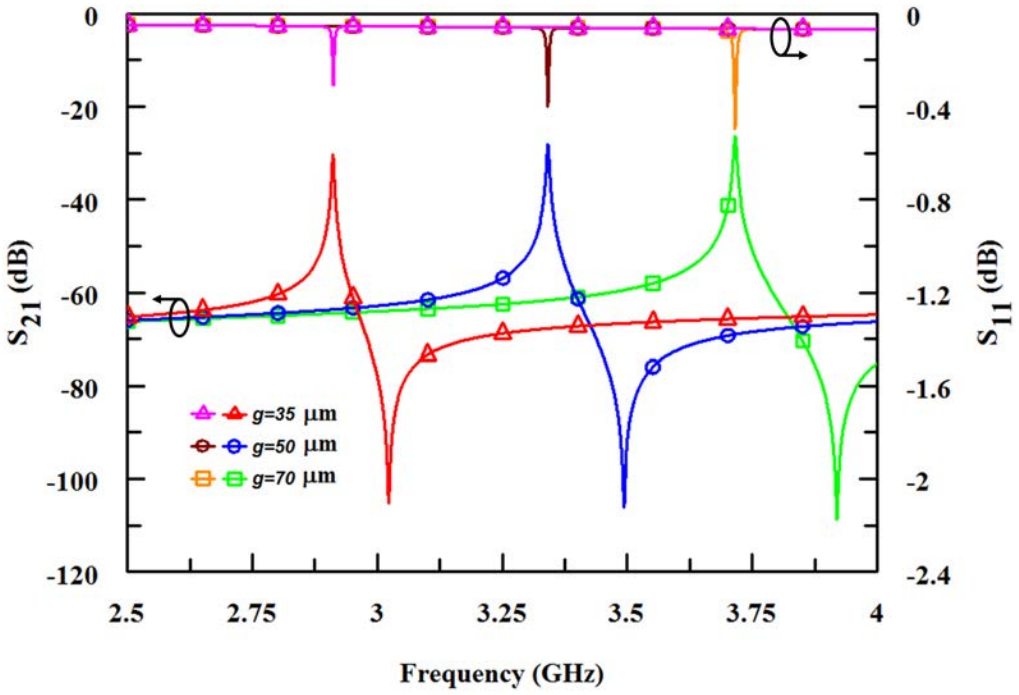

Figure 3.14: Simulated frequency response of the designed substrate-integrated, evanescent-mode, cavity resonator.

(for 3.72 GHz). Therefore, based on the designed resonator, few prototypes were built. The fabrication procedure is presented in Appendix B. The resonators, after soldering of the SMA connectors and attaching the piezoelectric actuators, were tested. A picture of the fabricated resonators, and the test setup are shown in figure 3.15 and figure 3.16, respectively. Agilent Technologies network analyzer, N5225A, calibrated from 2.0 GHz to 6.0 GHz with 4001 points and a resolution bandwidth of 2.0 kHz using an E-Cal module, was used to measure the resonators. A Keithley Instruments 2400 source-meter was used to bias the piezoelectric actuators.

The test results for a sample resonator are provided in figure 3.17, showing the achieved total frequency tuning. The fabricated resonator covers a wider range of frequencies than is needed for this work. For a better comparison to

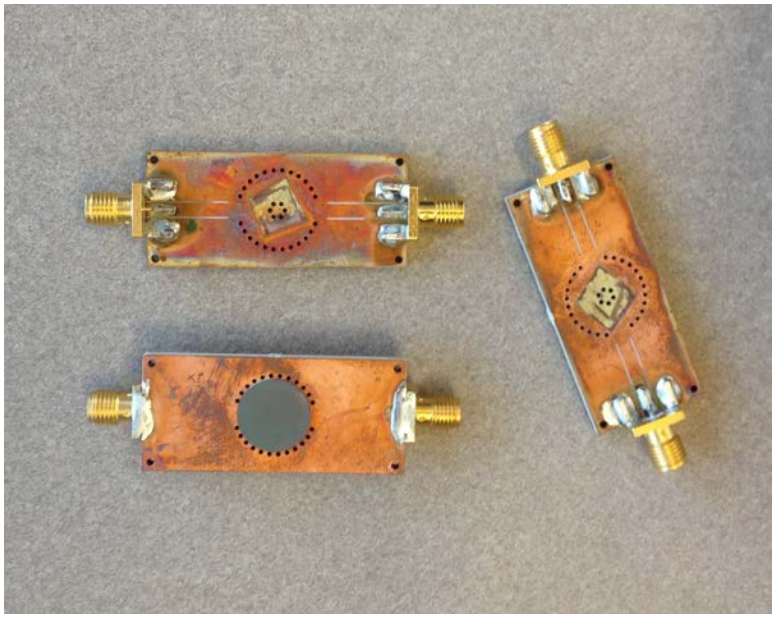

Figure 3.15: A picture of the fabricated substrate-integrated, evanescent-mode, cavity resonators with SMA connectors and piezoelectric actuators attached.

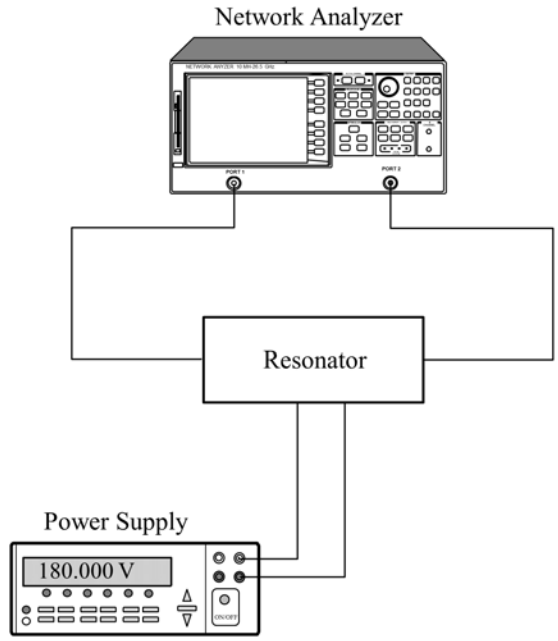

Figure 3.16: Test setup used for measurement of the substrate-integrated, evanescent-mode, cavity resonators.

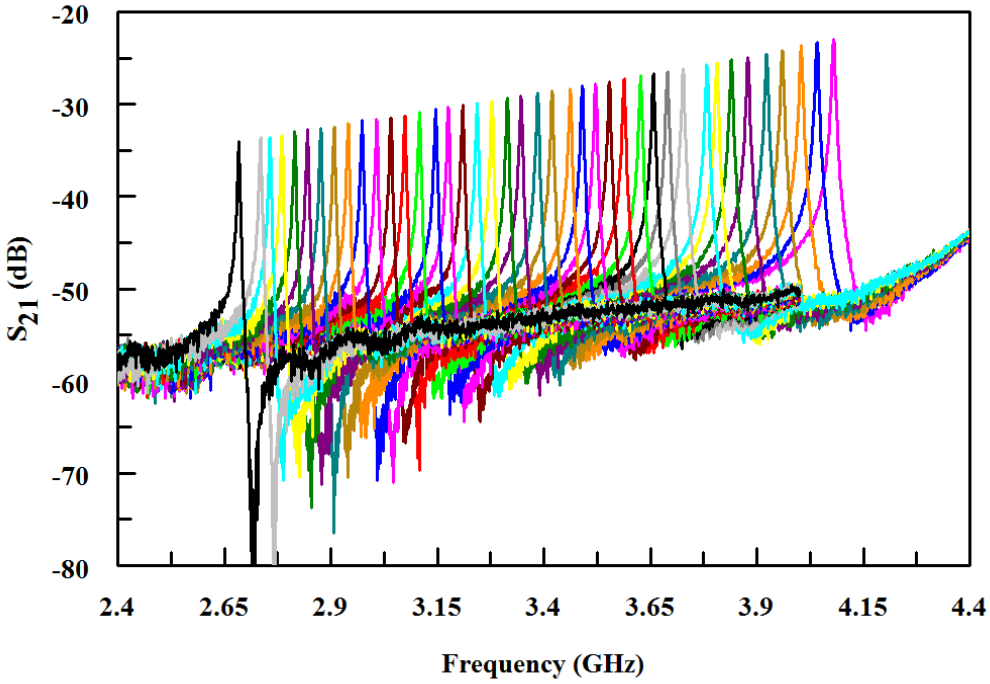

Figure 3.17: Measured results showing wide tuning range of a sample fabricated, substrate-integrated, evanescent-mode, cavity resonators.

figure 3.14, the measured results for three tuned frequencies are shown in figure 3.18. Measured unloaded quality factor of the sample resonator, depicted in figure 3.19, shows a variation from 600 (at 2.91 GHz) to 639 (at 3.73 GHz), which is almost 21% less than the simulated quality factor. This result was expected because in simulation, all metal objects were assumed to be ideal copper with conductivity of $\sigma = 5.8\times10^7$ S/m and zero surface roughness. However, in practice, such conditions cannot be realized. In fact, the copper plating process in the fabrication facility determines both the conductivity and surface roughness of the the plated vias and surfaces. The via drilling process also contributes to the surface roughness.

In figure 3.10, it was shown that the quality factor of the resonator is highly dependent on the conductivity of the conductors in the capacitive region. This

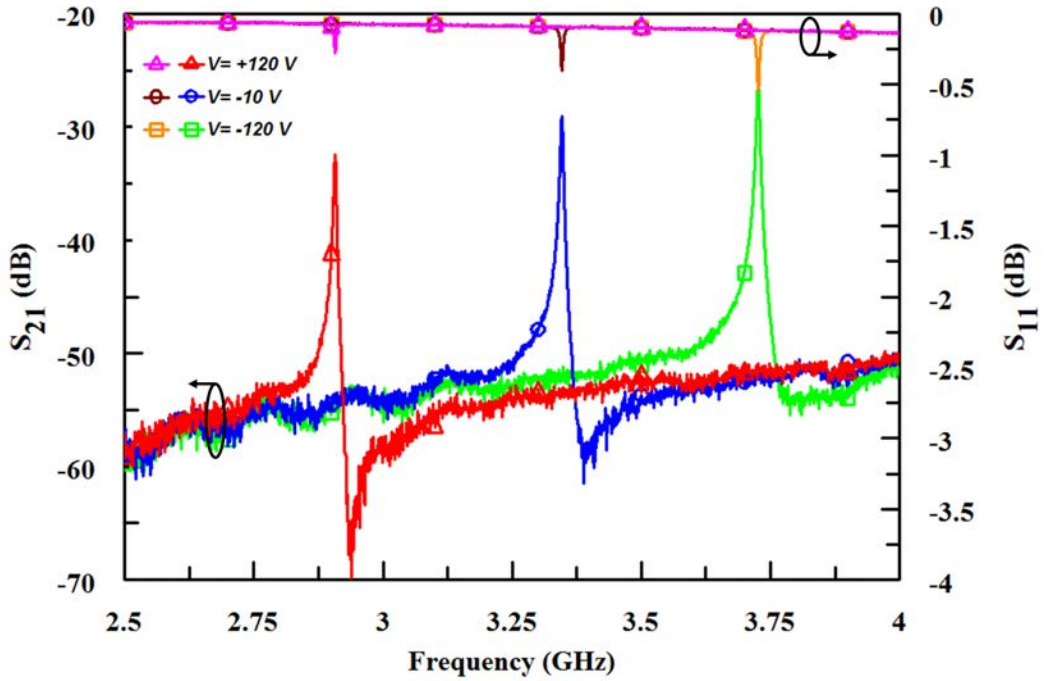

Figure 3.18: Measured frequency response of the designed substrate-integrated, evanescent-mode, cavity resonator.

dependency is due to the concentration of the electric-field in this region where the surface current has its maximum value. Therefore, the conductive loss in this area has the most contribution to the energy loss in the resonator. It has been shown that conductors with surface roughness can be modeled as conductors with lower conductivity [82], [83]. Therefore, the resonator model was again simulated in HFSS, but this time with a varying conductivity for the metallic objects. The result of the simulation at 3.2 GHz is shown in figure 3.20. Comparison of the quality factor from the measurement and simulation, when the conductivity was swept, shows that the effective conductivity of the plated copper in the fabrication facility is around 60% of that of ideal copper. Therefore, when the conductivity of all metallic objects in the simulation is decreased to $\sigma_{eff} = 3.5 \times 10^7$ S/m, the simulated quality factor matches the measurement. It should be noted that for proper modeling and evaluation

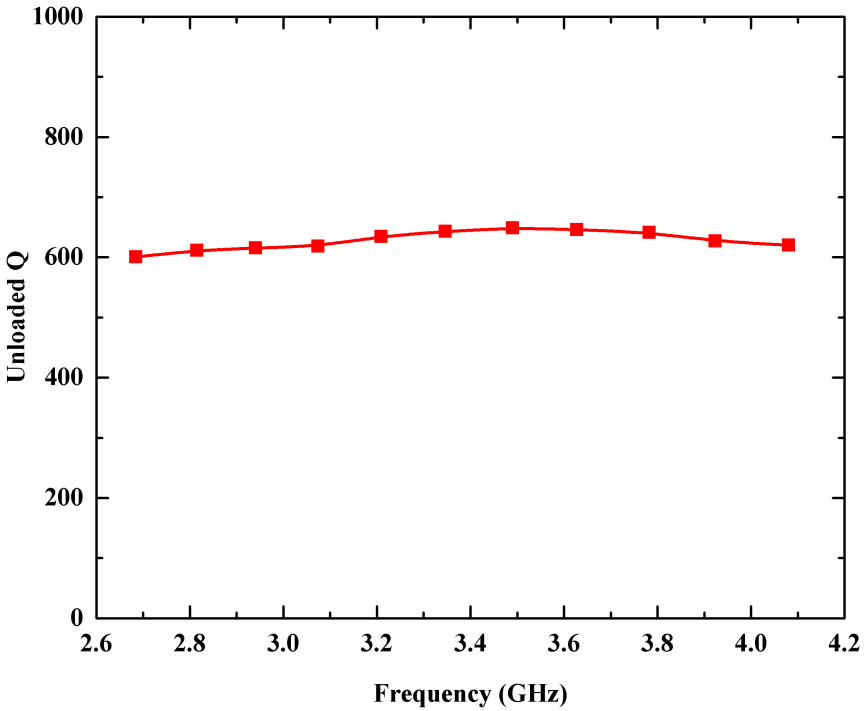

Figure 3.19: Measured unloaded quality factor of the designed substrate-integrated, evanescent-mode, cavity resonator versus frequency.

of the quality of plating, this procedure should be repeated for each fabrication facility.

Since the quality factor in the resonator is also a function of dielectric loss, it is quite reasonable to decrease the loss tangent of the dielectric material, for designing resonators with higher Qs. In the implementation of substrate-integrated, evanescent-mode, cavity resonators, the loss tangent of the dielectric material depends on the selection of the PCB material. Since the dielectric loss tangent is not the only crucial factor in the selection of the PCB, removal of the dielectric inside the cavity seems to be a logical choice. This action brings the quality factor of the resonator close to that of air-filled cavities. HFSS eigen-mode simulations for regular evanescent-mode cavities with copper conductivity of $\sigma_{eff} = 3.5 \times 10^7$ S/m, show that the quality factor of the resonator can be improved by 22% (from 863 to 1052) at 3.5 GHz

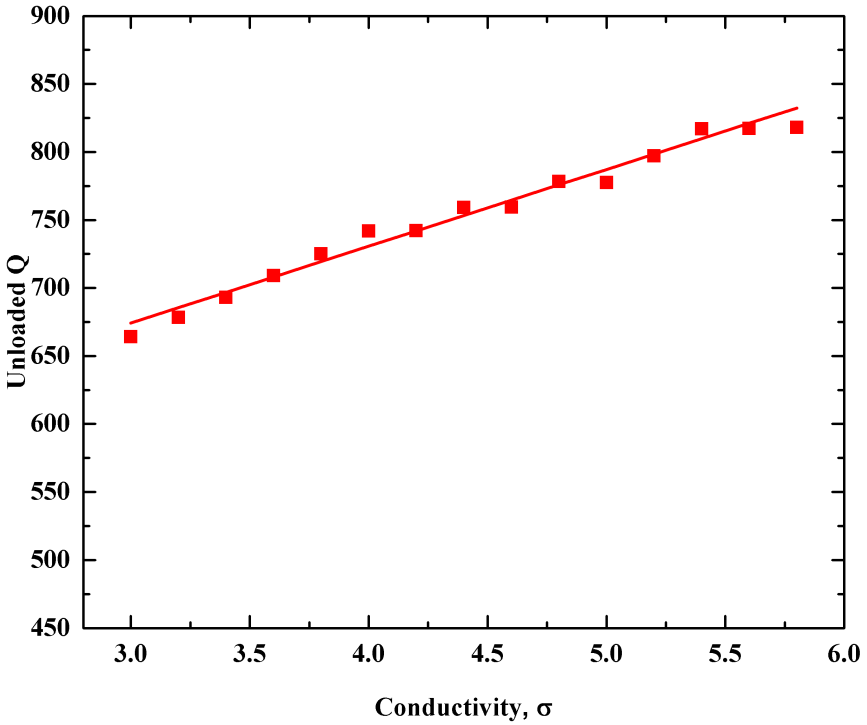

Figure 3.20: Variation of the quality factor for the designed resonator versus the conductivity of the metallic objects.

when the TMM3 dielectric material is removed from the cavity. It should be noted that the removal of the dielectric from the cavity will also shift the resonant frequency. Therefore, for a valid comparison, it is required that the gap size need to be adjusted. A driven-mode HFSS simulation of two sample substrate-integrated, evanescent-mode, resonators, one with dielectric and the other with air-core, shows an improvement of 19.5% (from 651 to 778) in the quality factor of the resonator at 3.2 GHz. However, because the removal of the dielectric material from the cavities adds two extra milling steps to the fabrication process, the dielectric-filled cavities were selected for the rest of this work. It should be noted that previous measured results confirm that the dielectric-filled cavities meet the minimum required quality factor for the maximum allowed filter loss. Pictures of a sample air-filled substrate-integrated,

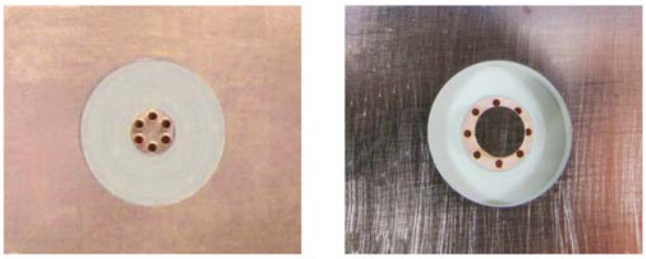

(a) (b)

Figure 3.21: Pictures of the fabricated substrate-integrated, evanescent-mode, cavities, (a) dielectric-filled, (b) air-filled

evanescent-mode, cavity along with a sample dielectric-filled cavity are shown in figure 3.21.

Another way of improving the quality factor is through compensation of the resonator loss by injecting RF power into it. This is the way an active resonator is designed.

3.2.2 Active Resonators

The current trend of rapid advancement in modern wireless communication services, satellite applications, and radar systems imposes a big challenge on future spectrum management due to overcrowding in popular frequency bands. This requires increased operational agility in the next generation of wireless and radar systems. This agility will enable cognitive adjustments in order to meet the requirements of future dynamic spectral environments. Cognitive Radios (CR) and Software Defined Radios (SDR) [84] combined with reconfigurable hardware components have the ability of providing the desired level of agility. Among all active and passive reconfigurable components, design of reconfigurable filters is still very challenging. For example, adding reconfigurability to filters results in higher insertion loss. This directly results in higher noise figure in receivers and higher power loss in transmitters. Eventually this

degrades the system performance in which the reconfigurable filter is utilized. As a result, extensive research has been conducted over the past decades on different aspects of filter reconfigurability such as frequency tuning [85], [86], bandwidth control [87], [88], and shape control [89], [90]. Besides these various reconfigurability features, improvement of the quality factor of the resonators, as a way of reducing filter loss, has always been one of the research goals. As discussed before, a promising technology for realizing low loss filters with wide tuning range is based on substrate-integrated, evanescent-mode, cavity resonators [51], [53].

Alternatively, the insertion loss can be compensated for by adding gain to the filter. Recently, a method for insertion loss compensation in a defected ground structure (DGS), fixed-frequency resonator was demonstrated by using a negative resistance circuit [91]. Negative resistance circuits have been combined with varactor-tuned evanescent-mode resonators for realizing low phase-noise voltage–controlled oscillators [92]. However, in [92], the intrinsic high quality factor of the evanescent-mode cavity resonator was utilized to improve the phase-noise of the oscillator and high-Q RF-MEMS varactors were proposed to increase the quality factor of the resonator.

The idea used in [91] can be applied to a substrate-integrated, evanescent-mode, cavity resonator to design an active tunable resonator with gain and higher quality factor. The gain and improvement in Q are provided through coupling of a negative resistance into the resonator, which compensates for the resonator loss and effectively increases its quality factor. Adding the negative resistance circuit to the resonator does not change its symmetry and reciprocity. This substrate-integrated, evanescent-mode, cavity resonator with wide tunability range, high loaded Q, and gain is a promising building block

for future reconfigurable filter arrays with built-in loss compensation. The structure of the active, tunable, substrate-integrated, evanescent-mode, cavity resonator and its equivalent circuit are shown in figure 3.22. This is the same resonator that was designed in the previous section with one exception. In this design, the resonator can not be weakly coupled to the ports. Doing so, would trap the injected power from the negative resistance circuit inside the cavity and turn it into an oscillator. In fact, the resonator is strongly coupled to three ports, the passive RF input and output ports and the active circuit port. The RF ports provide a doubly terminated resonator while the negative resistance circuit is coupled to the resonator through the third port for loss compensation. The cavity resonator and the active circuit are designed separately and implemented in different layers. They are connected using the third (active) port in the resonator full wave simulation. Co-simulation of the EM structure and negative circuit is used to complete the design. In order to estimate the resonator tuning range and quality factor, the structure is modeled in HFSS. It is expected that due to loading effect imposed by the negative resistance circuit, not only the Q is improved but also the tuning range is shifted to lower frequencies. Since the reference plane for the input impedance of the active circuit is defined at the edge of the resonator board, the EM simulation includes the transmission line connecting the third port of the resonator to the active circuit board.

The designed negative resistance circuit as well as its simulated input impedance are shown in figure 3.23 and figure 3.24. In order to realize the negative resistance, the emitter of the bipolar transistor is grounded using a transmission line. The extracted three port S-parameters from the EM simulation are used in National Instruments AWR for co-simulation of the resonator

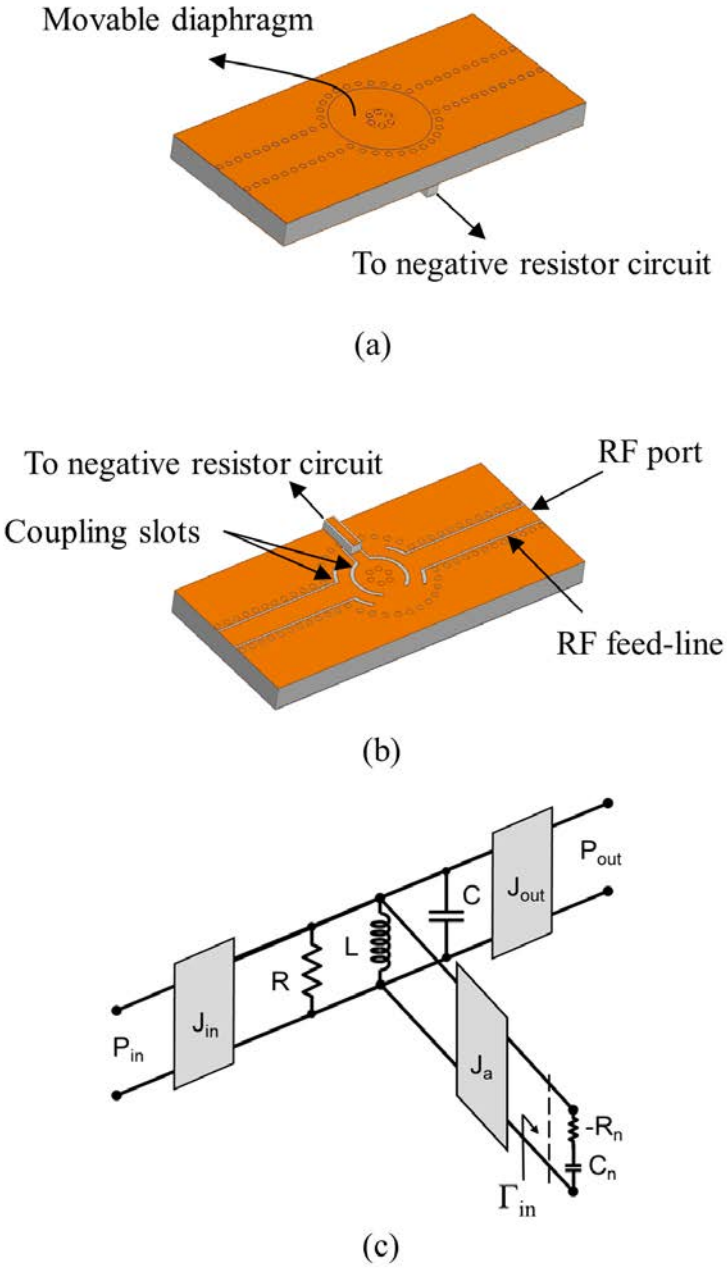

Figure 3.22: The structure of a tunable, substrate-integrated, evanescent-mode, cavity resonator with three ports (a) top view, (b) bottom view, and (c) equivalent circuit showing the negative resistance reference plane with a dashed line.

and the active circuit. This allows for optimization of the circuit values for gain, frequency tuning range, and quality factor. In general, the active circuit is designed in such a way that it provides a negative resistance that is equivalent to the real part of the input impedance seen at the third port of the EM structure. Additionally, if the absolute value of the negative resistance is larger than the real part of the EM structure input impedance, gain can be introduced in the resonator. Increasing the gain brings the circuit poles closer to the imaginary axis and the circuit will be on the verge of oscillating. Therefore, there exists a tradeoff between the achievable gain and stability. However, stability is the most challenging aspect of the negative resistance design. Although passive evanescent-mode cavity resonators have been shown promising to provide more than octave tuning ranges [93], wideband stability is one of the constraints when designing active evanescent-mode cavity resonators with a wide frequency tuning range. When the resonator is tuned, the input impedance seen by the active resonator changes, which directly affects the circuit stability. Therefore, in order to achieve widely tunable, active resonators, extensive broadband stability analysis must be performed during the negative resistance circuit design. Any oscillation, even outside the desired frequency band, alters the quiescent point of the transistor, pushing the transistor from the desired linear operating range into the non-linear range and thus changing the realized value of the negative resistance in-band. The stability analysis is performed by checking whether the oscillation condition is met at the active resonator reference plane, where the reference plane has been defined in figure 3.22(c).

Based on the design procedure presented above, the resonator and the active circuit have been fabricated separately and then soldered together. The

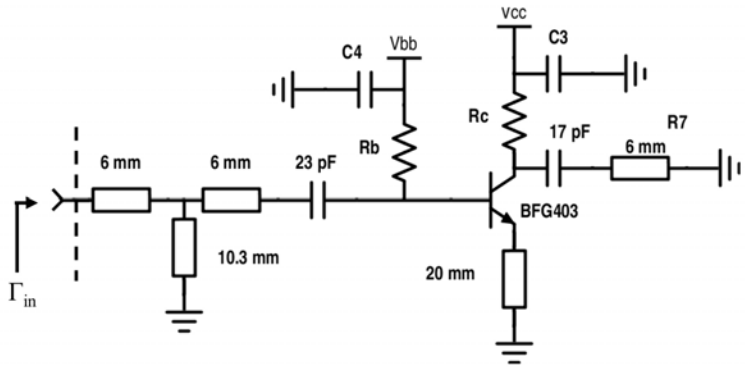

Figure 3.23: Schematic of the negative resistance circuit. Width of all transmission lines are 0.8 mm.

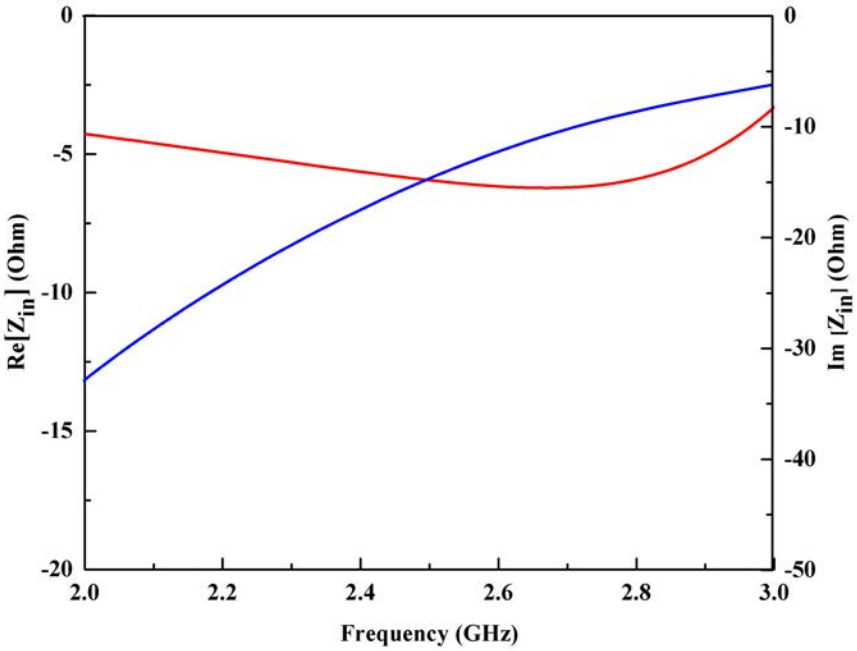

Figure 3.24: Simulated real and imaginary part of the input impedance of the negative resistance circuit.

fabricated active resonator is shown in figure 3.25. The negative resistance circuit was fabricated on Rogers RO3006 with dielectric constant of 6.15 and a thickness of 1.28 mm. The negative resistance circuit was realized using BFG403w Bipolar Junction Transistor (BJT) from NXP biased at VCE=1V and IC=1.3 mA. High-Q surface mount capacitors from Johanson Technology

Inc. were also used in the circuit implementation. The resonator performance was measured using the same test setup presented in figure 3.16. Figure 3.26 shows the tuning range of the fabricated active resonator. The measured gain and loaded quality factor of the resonator versus frequency are shown in figure 3.27. The loaded quality factor has been calculated using (3.11b). The measured gain ranges from 0.74 dB to 1.58 dB in the 2.259 to 2.963 GHz frequency range and the Q_L is from 217 to 253. It is important to notice that the measured Q_L includes the loading effect of the input and output ports. The loss introduced by the ports reduces the resonator overall quality factor. This means that the unloaded quality factor of the resonator is higher than the measured Q_L. Methods of how to quantify effective unloaded quality factors for active resonators have not been provided in the literature yet. However, for having a better idea about the amount of loading imposed by the ports on the resonator, the previous passive, substrate-integrated, evanescent-mode, cavity resonator has been changed to include this loading effect. A driven-mode simulation in HFSS shows that the circular coupling slots used to strongly couple ports to the resonator decrease the cavity quality factor to 40 to 60 for the same frequency range which is almost 20% of the quality factor reported for the active resonator. A comparison between the measured transmission response of the strongly-coupled resonator without and with the active circuit is also depicted in figure 3.28. This figure shows that the unbiased negative resistance circuit does not significantly degrade the quality factor and loss of the resonator. However, the biased negative resistance circuit improves the Q_L and gain of the resonator. A comparison between the HFSS-NI AWR co-simulation result and the measured response at 2.8 GHz is shown in figure 3.29. From this figure, it can be seen that improvement of Q is higher than the

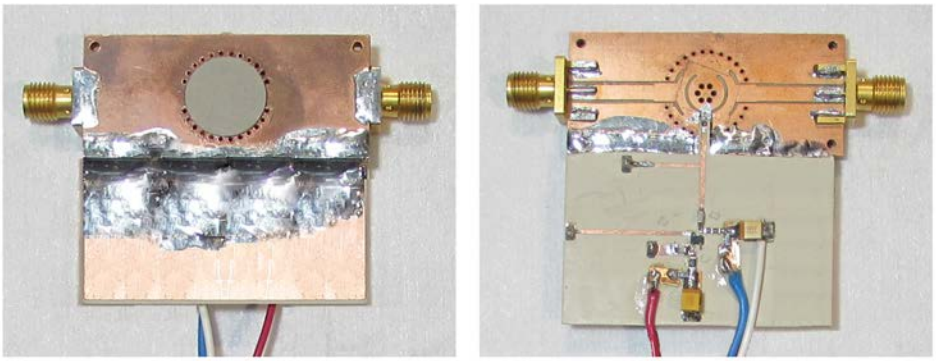

(a) (b)

Figure 3.25: Fabricated tunable active resonator, (a) piezoelectric actuator attached on top of resonator, (b) the negative resistance circuit coupled to the third port of the resonator.

simulation. A reason for this observation is that the fabricated circuit was slightly tweaked during testing to optimize the stability and gain which has not been reflected back in the simulation. Furthermore, figure 3.30 shows that both reciprocity and symmetry of the resonator are maintained. This is a result of the symmetric coupling of the negative resistance into the tunable resonator. This property is crucial for higher-order active filter designs. In summary, the designed active, tunable, substrate-integrated, evanescent-mode, cavity resonator presents 1 dB of gain across 700 MHz of the frequency tuning range (2.259 to 2.963 GHz) and a measured loaded quality factor of 217 to 253. Due to the reciprocity and symmetry of the active resonator, higher order filters can be designed using regular filter design methodology. Overall, this design and implementation of active resonator provides an important step for realizing a wide range of reconfigurable filters that will be included in the next generation of spectrally-agile wireless systems.

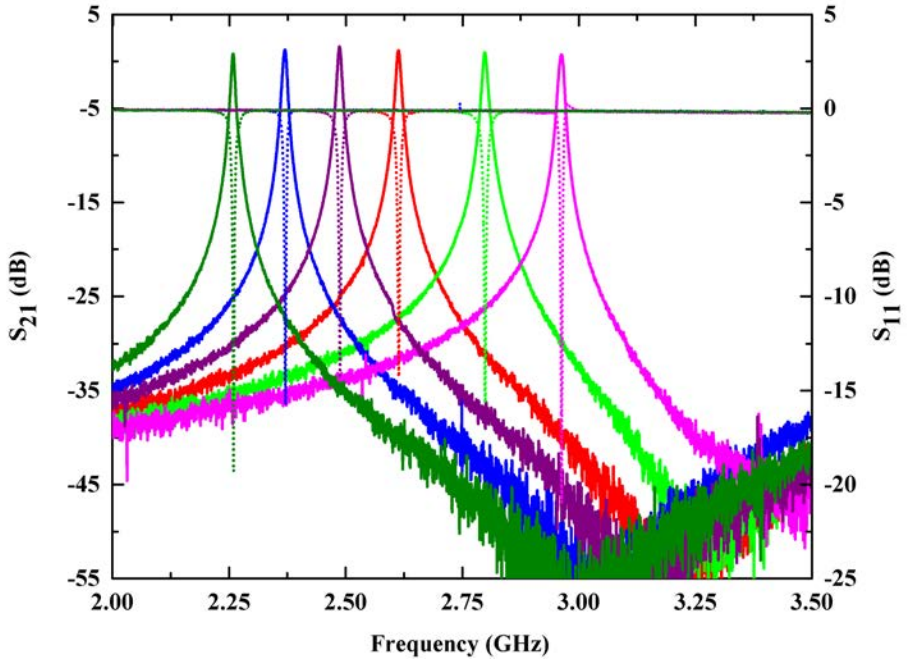

Figure 3.26: Measured S-parameters of the active tunable resonator showing gain tuned from 2.259 GHz to 2.963 GHz.

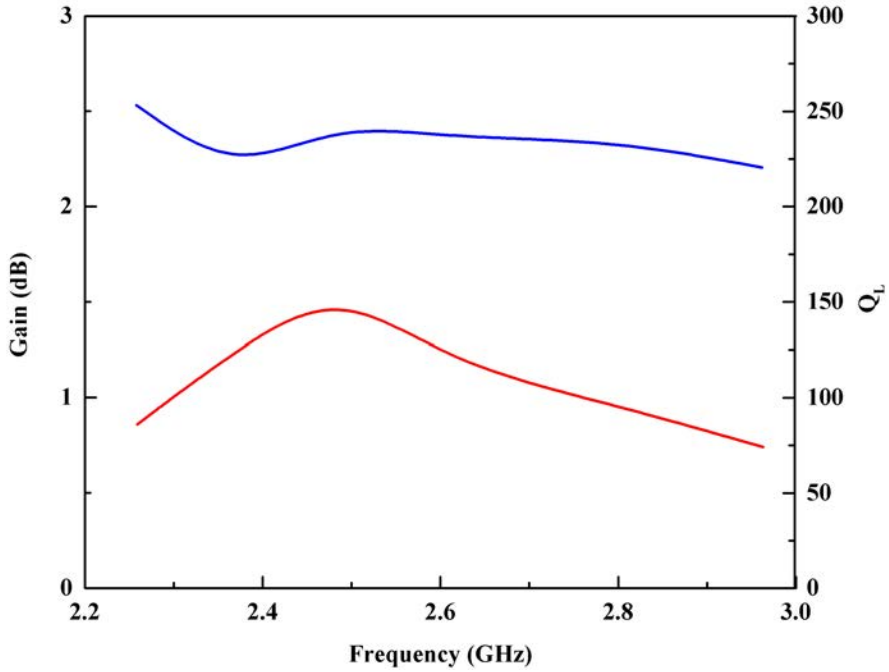

Figure 3.27: Measured gain and loaded quality factor of the active resonator versus frequency.

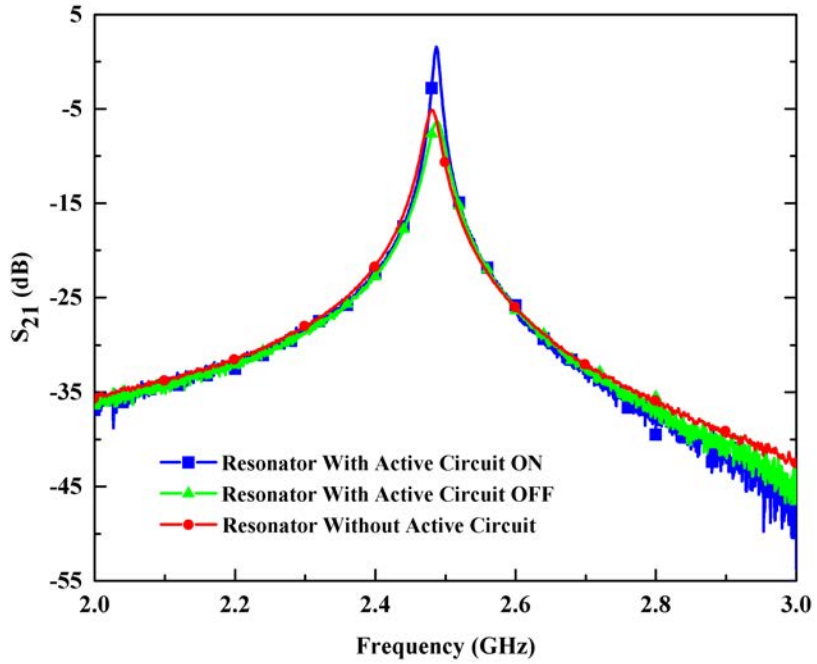

Figure 3.28: Comparison between the measured transmission response of the strongly-coupled resonator without and with the active circuit both biased and unbiased.

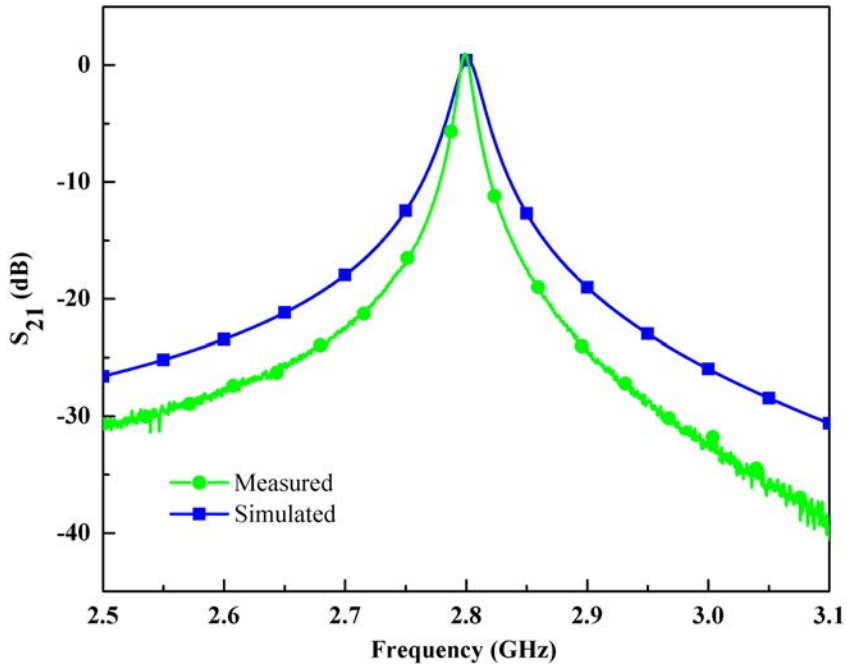

Figure 3.29: Comparison of the simulated and measured transmission response of the active resonator.

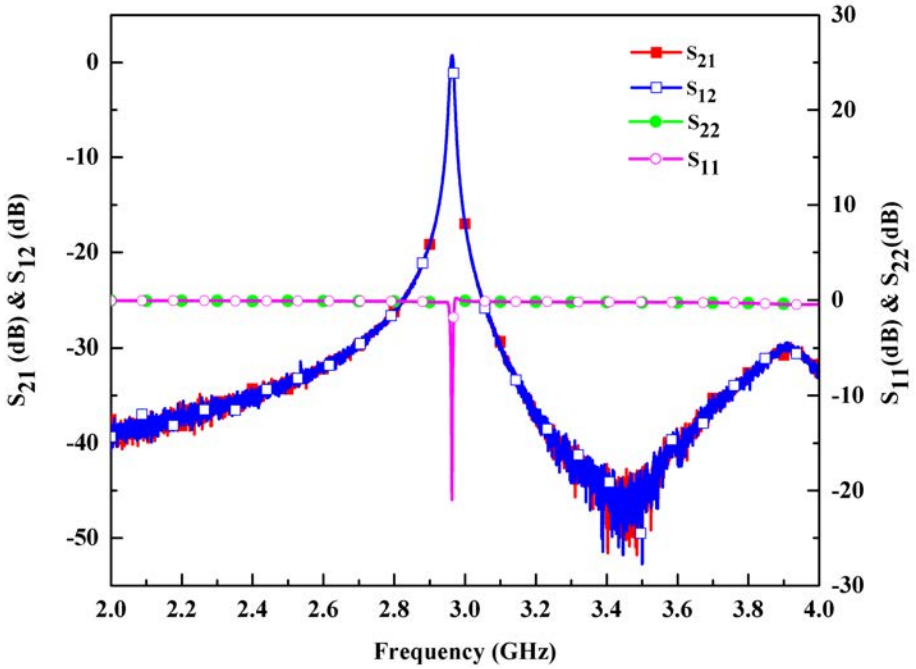

Figure 3.30: Forward and reverse S-parameters of the tunable active resonator showing that the device is both symmetric and reciprocal.

3.3 Narrow-band Bandpass Filter Design

Second order, tunable, Butterworth bandpass filters, with 2% and 4% fractional-bandwidths, covering the range from 3.0 to 3.6 GHz are designed as a technology demonstrator. Higher order filters can also be designed using the approach outlined in this section. Figure 3.31(a) shows the normalized lowpass prototype in which the element values are found from (2.18a) and (2.18b) as

$$g_0 = g_3 = 1\ \Omega \tag{3.12a}$$

$$g_1 = 2\ \sin\left(\frac{\pi}{4}\right) = 1.4142 \tag{3.12b}$$

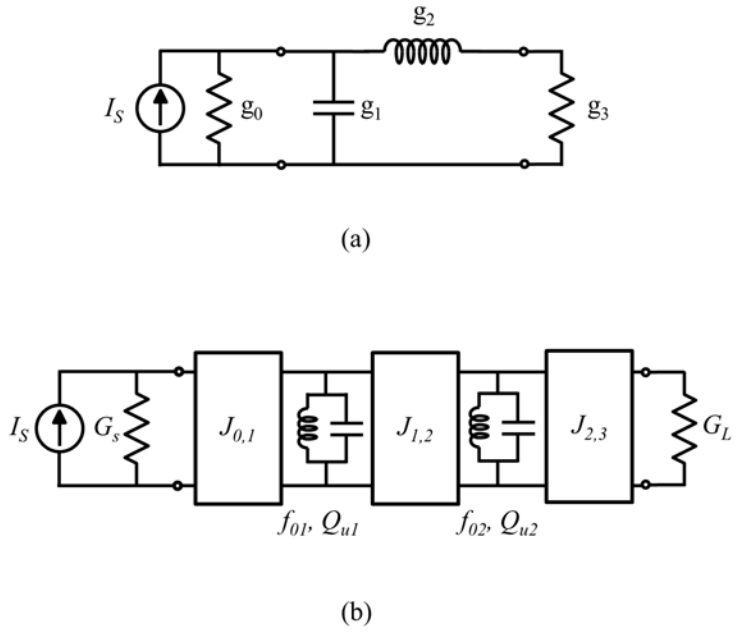

Figure 3.31: A second order Butterworth lowpass filter, (a) realization using lumped elements, (b) realization using admittance inverters.

$$g_2 = 2 \sin\left(\frac{3\pi}{4}\right) = 1.4142 \tag{3.12c}$$

According to what has been presented in section 2.2, frequency and impedance scaling as well as lumped-element-to-inverter and lowpass-to-bandpass transformations are used to convert a lowpass prototype to a direct-coupled bandpass filter shown in figure 3.31(b). In this figure, f_{01} and f_{02} are the synchronous resonant frequencies of the resonators and are found from the geometrical mean of the minimum and maximum frequencies of the tuning range, that is $\sqrt{3.0 \text{ GHz} \times 3.6 \text{ GHz}} = 3.286$ GHz. Q_{u1} and Q_{u2} are the unloaded quality factor of the resonators. These values are selected as the minimum permissible quality factor of 610, which results in the maximum allowed insertion loss. The values of the admittance inverters can be found from (2.29a) to (2.29d). For example, the 2%-fractional-bandwidth filter with shunt capacitors of 1 pF

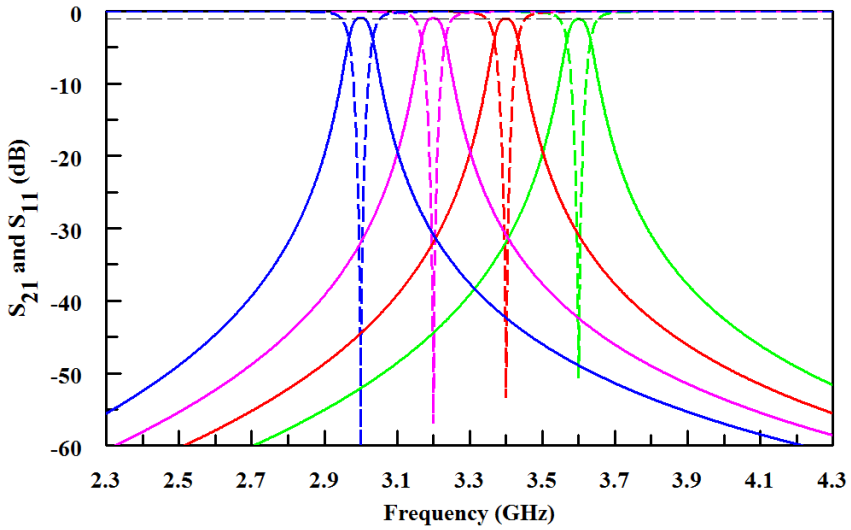

Figure 3.32: Frequency response of the second order Butterworth lowpass filter found from circuit simulation tuned from 3.0 to 3.6 GHz.

and port admittances of $G_S = G_L = 0.02$ ℧, has $J_{01} = J_{01} = 2.422$ m℧ and $J_{23} = 0.2919$ m℧. The circuit-simulated frequency response of the designed bandpass filter, tuned from 3.0 to 3.6 GHz, is depicted in figure 3.32. The coupling values, calculated for the center frequency, provide almost a perfect design for the whole tuning ratio of 1.2:1. In this figure, the 1-dB maximum allowed insertion loss has been emphasized with a dashed line.

To extract the physical dimensions of the filter, the external quality factor (Q_{ex}) and the inter-resonator coupling (k_{12}) need to be carefully designed. The values of the required Q_{ex} and k_{12} can be calculated from (2.32a) to (2.32c) as,

$$Q_{ex1} = \frac{g_0 g_1}{\Delta} = 70.71 \tag{3.13a}$$

$$k_{1,2} = \frac{\Delta}{\sqrt{g_1 g_2}} = 0.0168 \tag{3.13b}$$

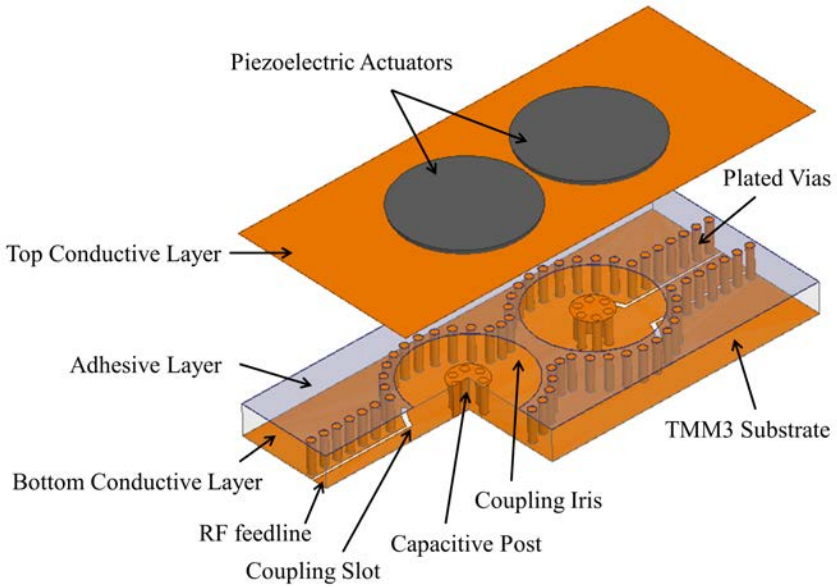

Figure 3.33: Basic structure of the second order substrate-integrated, evanescent-mode, cavity bandpass filter

$$Q_{ex2} = \frac{g_2 g_3}{\Delta} = 70.71 \tag{3.13c}$$

Figure 3.33 shows the basic structure of the second order bandpass filter modeled in HFSS. The full-wave simulation is used to correlate Q_e and k_{12} with the dimensions of the external and internal coupling structures. Similar to the resonator design, shorted GCPW lines are used as the input and output feed structures. However, in order to increase the amount of external coupling, semi-circle slots were also added to the end of the GPCW lines. The interaction between the magnetic-field of the slots and the magnetic-field of the first mode of the resonator increases the coupling. The inter-resonator coupling strength is controlled by the coupling iris formed by plated vias between the resonators.

Q_e is primarily determined by the length of the shorted GCPW feed lines (l_t), the width of the slots (w_S), and the sector angle defining the slots (γ). The

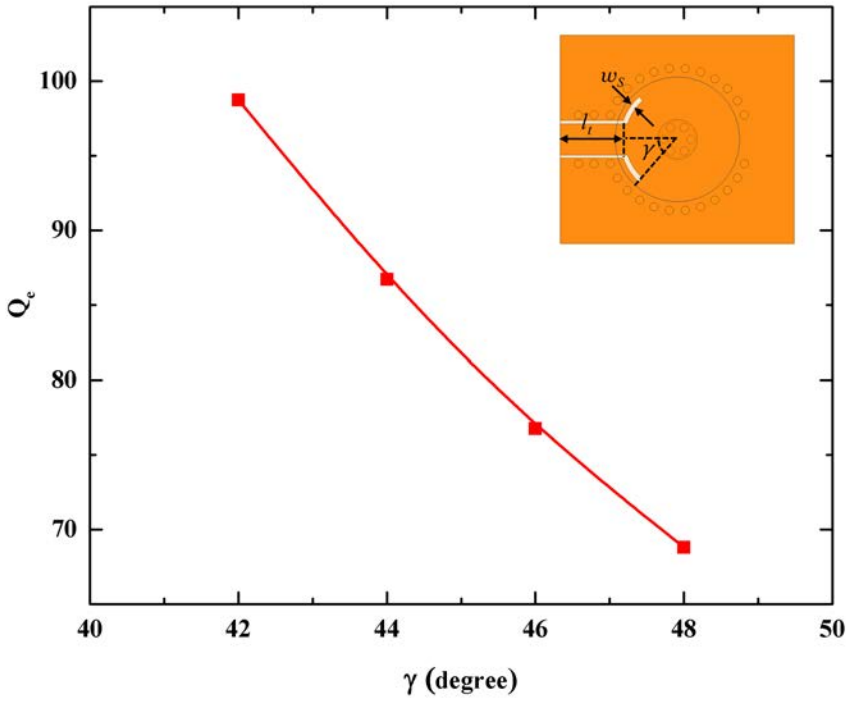

Figure 3.34: Simulated relationship between Q_e and γ for fixed values of l_t and w_S.

inter-resonator coupling coefficient k_{12} is determined by the spacing between the resonators (s_R) and the opening width of the coupling iris w_I. Reflection delay and split-pole techniques, described in section 2.2, were used to extract the required values of these parameters. Figure 3.34 shows the simulated relationship between Q_e and γ for fixed-length, GCPW feed lines and a fixed slot width, and figure 3.35 illustrates the simulated relationship between k_{12} and w_i for a fixed spacing between the resonators. The dimensions of the final design are listed in Table 3.2.

The same procedure is used to design a 4%-fractional-bandwidth, band-pass filter. The only difference is that the values of the external and internal couplings and their corresponding dimensions are different. Table 3.3 provides the dimensions of the final design for this filter.

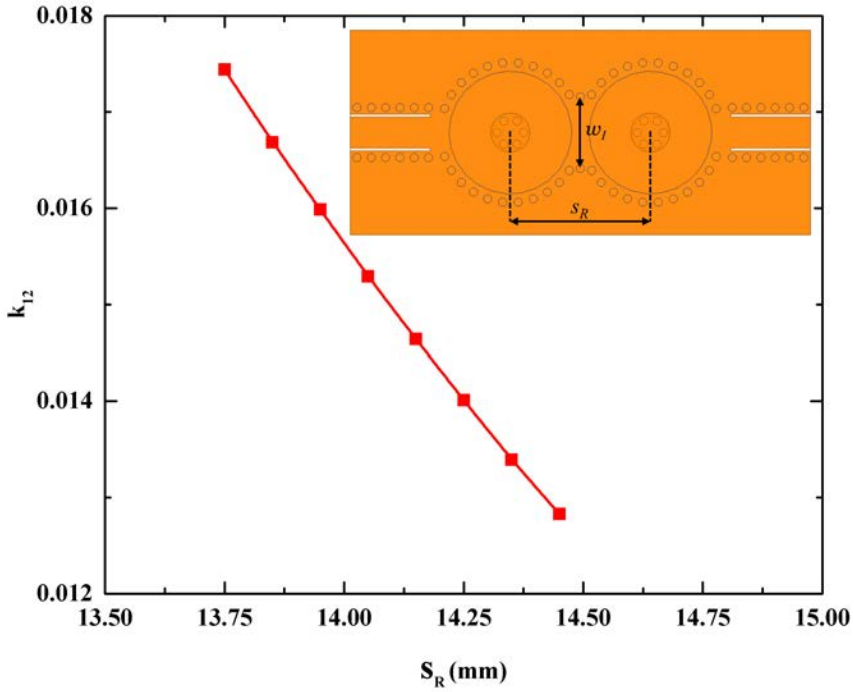

Figure 3.35: Simulated relationship between k_{12} and w_i for a fixed value of s_R.

Table 3.2: 2%-fractional-bandwidth bandpass filter design parameters

Design Parameters	**Value**
Slot Angle (γ)	46 °
GCPW Length (l_t)	10.8 mm
Slot width (w_S)	0.5 mm
Resonators Spacing (s_R)	13.7 mm
Iris Width (w_I)	7.0 mm

Table 3.3: 4%-fractional-bandwidth bandpass filter design parameters

Design Parameters	**Value**
Slot Angle (γ)	58 °
GCPW Length (l_t)	10.8 mm
Slot width (w_S)	0.5 mm
Resonators Spacing (s_R)	13.2 mm
Iris Width (w_I)	9.4 mm

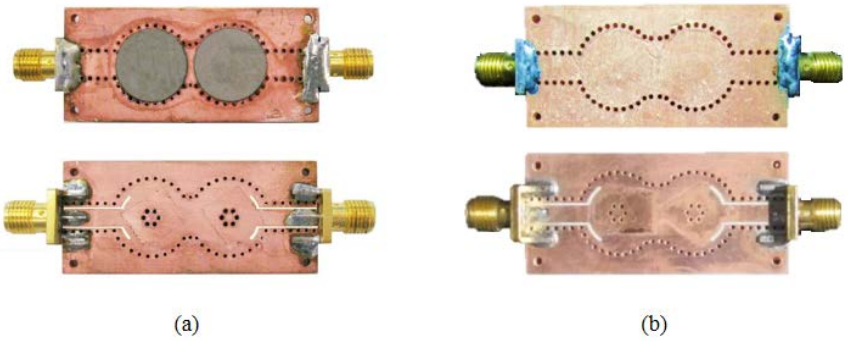

Figure 3.36: Picture of the fabricated tunable bandpass filters, (a) 2%-fractional-bandwidth filter after piezoelectric actuator attachment, (b) 4%-fractional-bandwidth filter prior to piezoelectric actuator attachment.

3.3.1 Bandpass Filters Measurement

The filters are fabricated using the process presented in Appendix B. For each filter, two piezoelectric disk actuators are assembled on top of the two evanescent-mode cavity resonators. Figure 3.36 shows the fabricated, tunable, evanescent-mode cavity filters. Figures 3.37 and 3.38 show the measured tuning response of the fabricated filters. The test setup is the same as what has been shown in figure 3.16, except that two separate power supplies are used to tune the resonators of the filter. In tuning the center frequency of the filters, the two bias voltages need to be individually adjusted. Due to fabrication and assembly tolerances, these two bias voltages are slightly different. Both filters readily cover the whole design tuning range of 3.0 to 3.6 GHz.

Figures 3.39 and 3.40 compare the simulated and measured insertion loss and bandwidth of the filters. A very good agreement is observed. It should be noted that the measured insertion losses include SMA connector losses. Finally, a comparison of the circuit simulation, EM simulation, and measurement for the 4%-fractional-bandwidth tunable filter tuned at 3.3 GHz is depicted in figure 3.41. This figure shows accuracy of the modeling, design procedure,

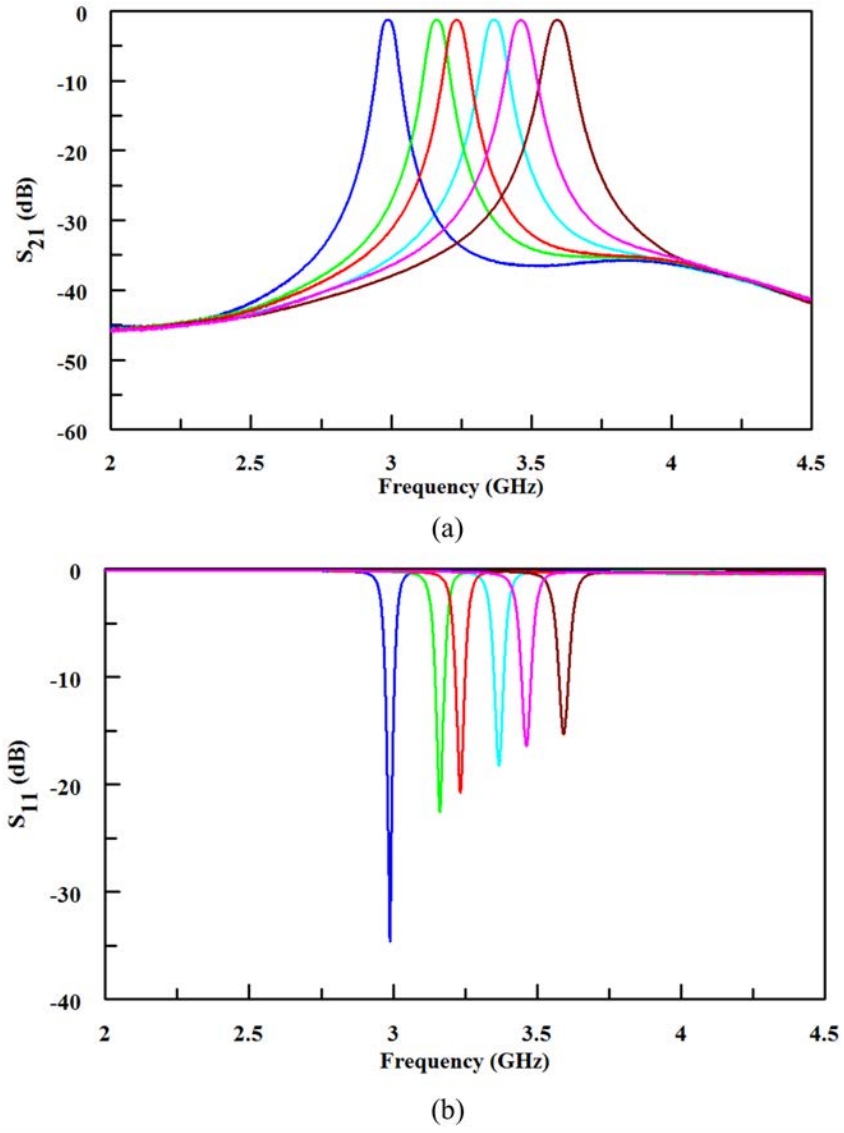

Figure 3.37: Measured frequency response of the 2%-fractional-bandwidth tunable filter, (a) S_{21}, (b) S_{11}.

and fabrication process.

3.4 Wide-band Bandpass Filter Design

Although the method discussed in the previous section was basically designed for narrowband filters (bandwidth of less than 10%), it can be extended to

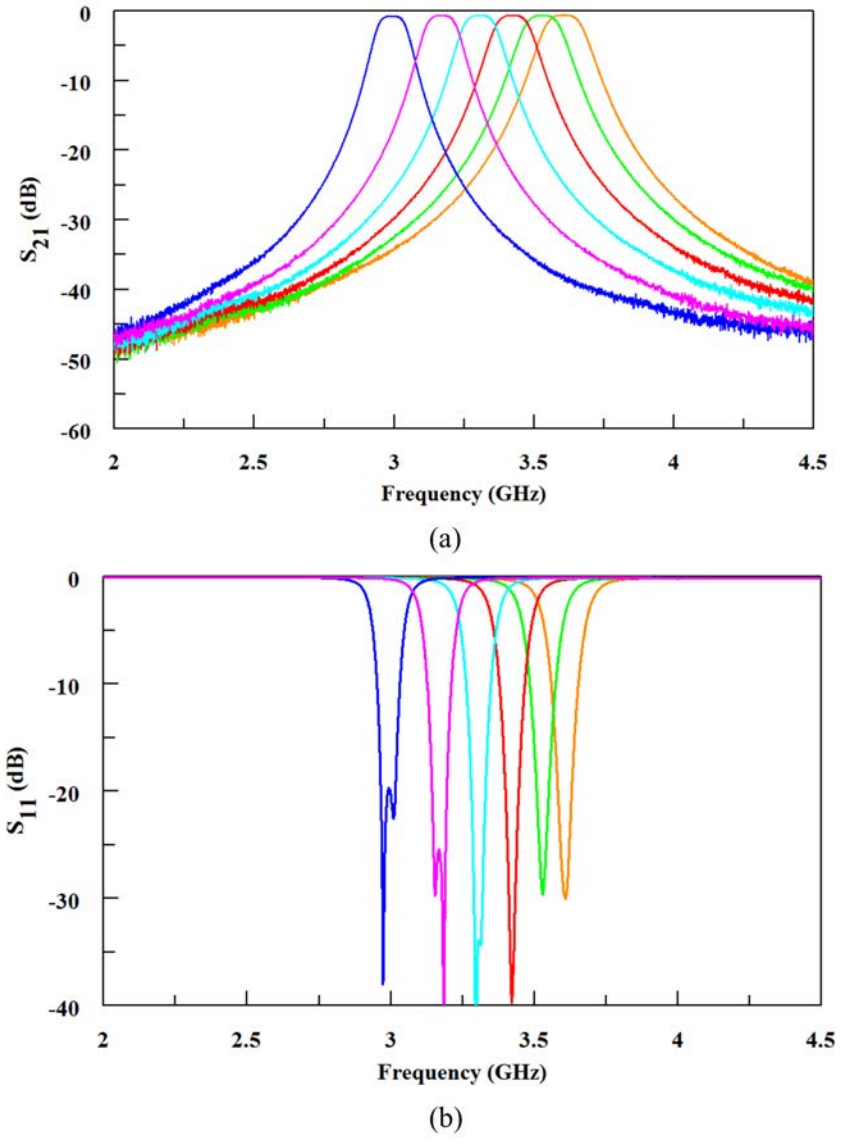

Figure 3.38: Measured frequency response of the 4%-fractional-bandwidth tunable filter, (a) S_{21}, (b) S_{11}.

allow for the design of wideband, evanescent-mode, cavity bandpass filters. In general, there are two main limitations in the design of wideband microwave filters using the direct-coupled method. First, the design method developed in section 2.2 assumes frequency-independent coupling structures, whereas in the real world such elements do not exist. Although in narrowband applications, the coupling structures can be approximately considered to be frequency in-

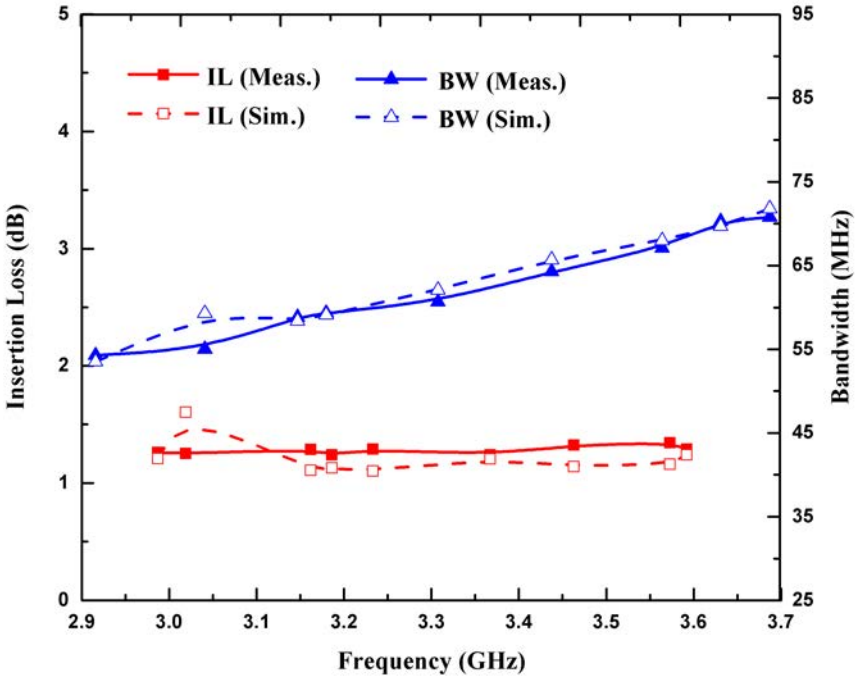

Figure 3.39: Comparison of the simulated and measured insertion loss and bandwidth for the 2%-fractional-bandwidth tunable filter.

dependent, the change of coupling with frequency in wideband filters causes deviation from the ideal design. This problem is not limited to wideband filters. In fact, the same issue occurs in narrowband tunable bandpass filters with wide tuning ranges. This issue, however, can be addressed using various coupling-compensation techniques [51], [94], [95]. In these techniques, usually two different coupling schemes are simultaneously utilized where the change of coupling with frequency due to the first scheme, is compensated with the opposite behavior of the second one. This technique provides almost frequency-independent coupling.

The second issue is, regardless the variable behavior of the coupling mechanisms in wideband applications, that there are physical limitations to the achievable bandwidth that commonly-used coupling structures can provide. For example, inter-resonator coupling through magnetic iris coupling is a very

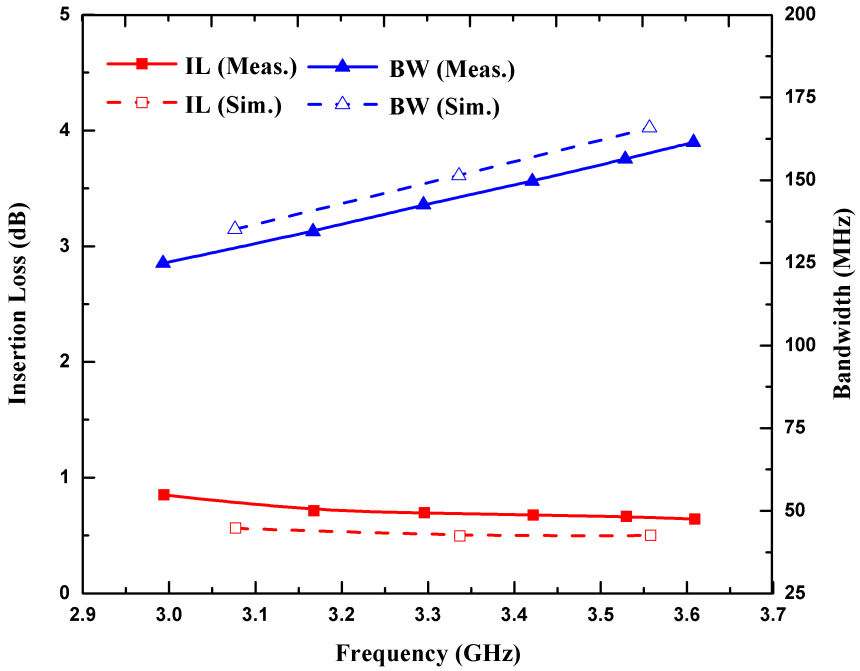

Figure 3.40: Comparison of the simulated and measured insertion loss and bandwidth for the 4%-fractional-bandwidth tunable filter.

common way for designing of narrowband microwave filters. In the previous section, it was seen that the amount of coupling can be controlled using the width of the iris between the resonators and the spacing between them. However, increasing the magnetic-field coupling via widening of the the iris has a practical upper bound. In fact, when the width of the iris exceeds the resonators width, the increase in the coupling is not efficient anymore. The spacing between the resonators has also a lower limit dictated by the diameter of the piezoelectric actuators, provided that they are required to be mounted on the same layer. In addition, widening of the iris as well as shortening the spacing between the resonator increase the risk of the exciting other modes. Similar problems are associated with the external magnetic-field coupling through the slots. For example, when the slots become larger, the radiation from them adds more loss to the resonator and therefore, the Q of

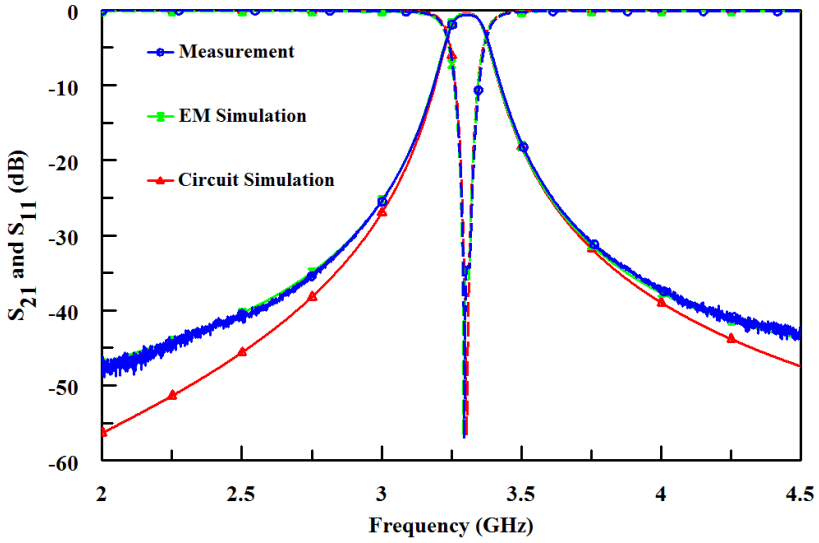

Figure 3.41: Comparison of the 4%-fractional-bandwidth tunable filter frequency responses found from the circuit simulation, EM simulation, and measurement.

the resonator is reduced. Also, larger slots perturb the current path on the ground plane, and hence disturb the distribution of the fields inside the cavity. These physical-geometry-related limitations are often a side-effect of confining either the electric- or magnetic-field in order to increase the frequency sensitivity of the resonator structure. Therefore, achieving the appropriate coupling mechanism for broadband coupling using specific filter technologies still requires investigation. In this section, a novel structure for broadband coupling in substrate-integrated, evanescent-mode, cavity filters is presented. Figure 3.42 shows the structure of the second order wideband bandpass filter. In order to increase the external coupling, direct tapping to the center post of the cavity is used in addition to the magnetic-field coupling from the GCPW feed line. The internal coupling is similarly increased by using the same type of direct tapping in addition to a traditional inductive magnetic iris.

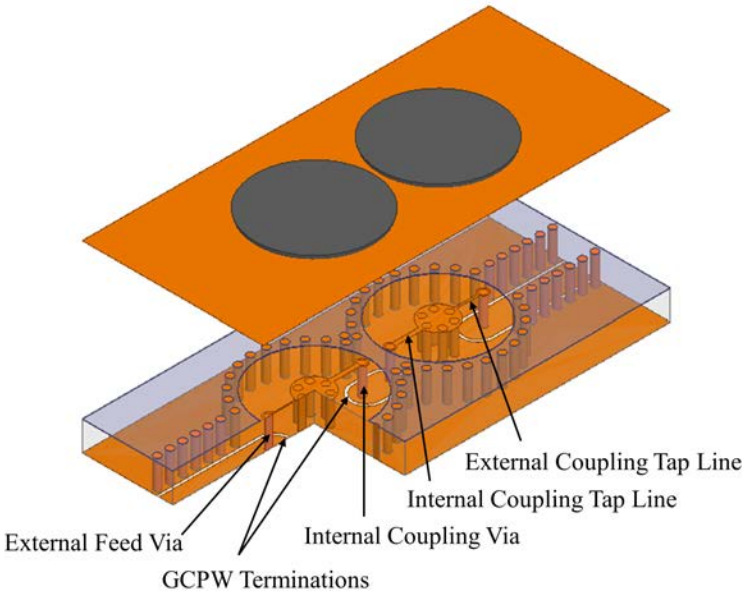

Figure 3.42: Structure of the second order, substrate-integrated, evanescent-mode cavity, wideband, bandpass filter.

3.4.1 Wideband Coupling Implementation and Filter Measurement

Aperture coupling (slots coupling) has been widely used for realizing external coupling of substrate-integrated, evanescent-mode, cavity filters both for bandpass and bandstop operation. In bandpass filters, the apertures are usually used in combination with a short circuit termination of a transmission line to couple the signal into the resonators [96]. In the case of bandstop filters, the apertures are commonly incorporated as defects in the ground plane of a microstrip line acting as the through line between the source and the load [5]. In both cases, the aperture provides a magnetic-field coupling between the transmission line and the first mode of the resonator [5]. However, the achievable coupling strength, using these previously-demonstrated aperture coupling methods, is limited since the magnetic-field is distributed over the entire cav-

ity. A method for confining the magnetic-field, by bringing the lower part of the center post closer to the outer walls of the cavity, resulted in increased coupling strength and external Qs on the order of 50 were demonstrated in an evanescent-mode cavity bandstop filter [97]. From (2.32a) to (2.32c), it can be seen that, filters with wider bandwidth require stronger inter-resonator couplings as well as smaller external Qs.

An alternative method for providing high external coupling is using a U-shape transmission line that is routed through the cavity instead of the aperture. This method is capable of providing external Qs down to around 40 [98]. However, for realizing very wide bandpass filters, even stronger external coupling is required. For example, for a second order Butterworth filter with 40% fractional bandwidth the required external Q is 3.53, which is an order of magnitude lower than what has previously been reported. Since the electric-field is primarily confined between the top of the cavity and the center post, tapping directly into the electric-field, using a tap-line technique, will result in coupling levels that are suitable for wideband filters.

When designing a tap-line coupling structure, the position of the tap is a critical parameter for providing the required coupling strength. However, in the method presented here, the tap point is considered to be fixed to the top of the post where the maximum electric-field confinement is located. The reason for this design choice is to reduce the number of fabrication steps and limit the structure to two metal layers. This keeps the fabrication method compatible with the method used for the narrowband filters. However, this reduces the degrees of freedom in the design as the height of the tap cannot be used to adjust the external coupling. The primary design parameters used in the proposed design are the position and diameter of the feeding via that pro-

vides the connection from the GCPW feeding line to the tap-line. Additional design parameters that can be adjusted are the width of tap-line, the relative position of the coplanar waveguide termination with respect to the feed via position, and the coplanar waveguide spacing and gap size. The proposed external coupling structure is emphasized in figure 3.43 using dashed lines. In figure 3.44, the result of an HFSS full-wave simulation for the external quality factor variation in terms of the external feed via distance, l_{fe}, is shown. Additionally, the achievable fractional bandwidth as a function of l_{fe} is depicted in the same figure.

Similarly, the same design principles are applied in order to realize stronger internal coupling. This way the bandwidth limitations of the conventional magnetic-field iris coupling, can be overcome. One significant difference between the external and the internal coupling mechanisms when direct tapping is used, is that the iris provides a greater contribution to the overall coupling than the feed lines in the case of internal coupling. The design parameters in this case are the same as for the external coupling with the addition of the width of the coupling iris and the spacing between the resonators. The same limitations apply for this design methodology regarding the fixed tap-line height. The internal coupling mechanism is emphasized by the dotted line in figure 3.43. Examples of the achievable coupling coefficient, k_{12}, and fractional bandwidth as a function of the internal feed via distance, l_{fi}, are shown in figure 3.45. Similar curves can be generated for the other design parameters for characterizing both the external and the internal couplings.

To demonstrate the wide bandwidth capability of the proposed coupling structure, a second order, Butterworth,bandpass filter with a fractional bandwidth of 38% at 3.3 GHz, with the same tuning range from 3.0 to 3.6 GHz,

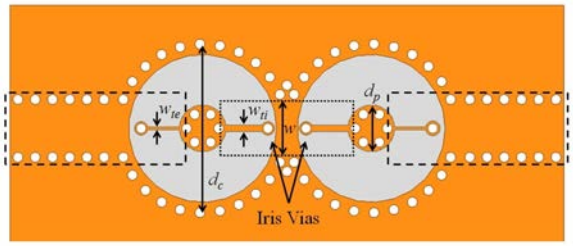

(a)

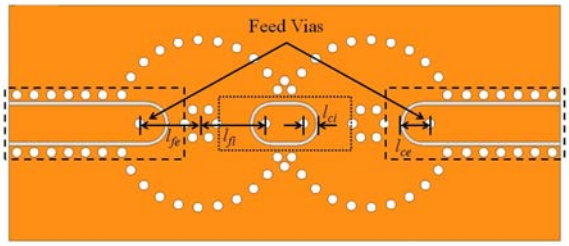

(b)

Figure 3.43: Layout of the proposed wideband bandpass filter with emphasized external and internal coupling sections with dashes and dotted lines, respectively, (a) top layer, (b) bottom layer.

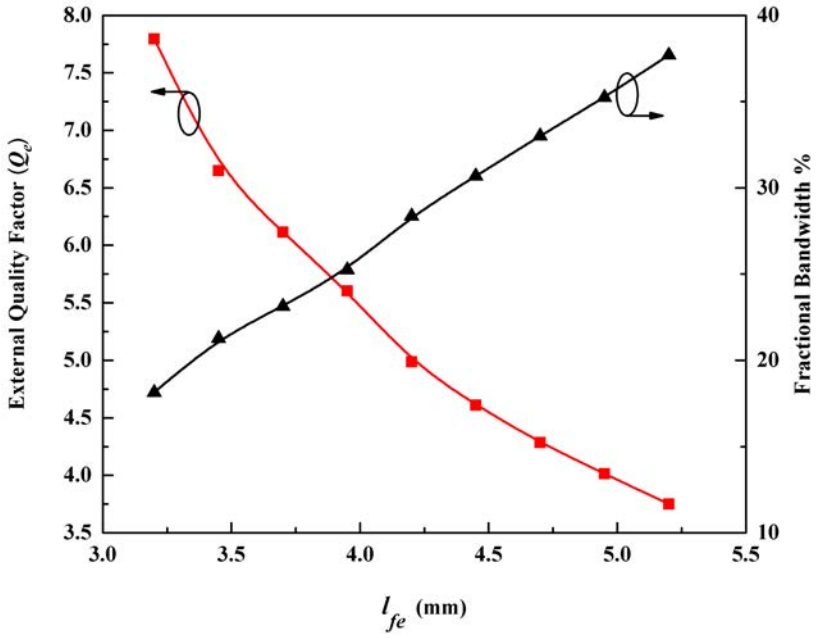

Figure 3.44: Simulated external Q of the proposed wideband filter structure at 3.3 GHz as a function of the external feed via position. The other design variables are kept fixed as shown in Table 3.4.

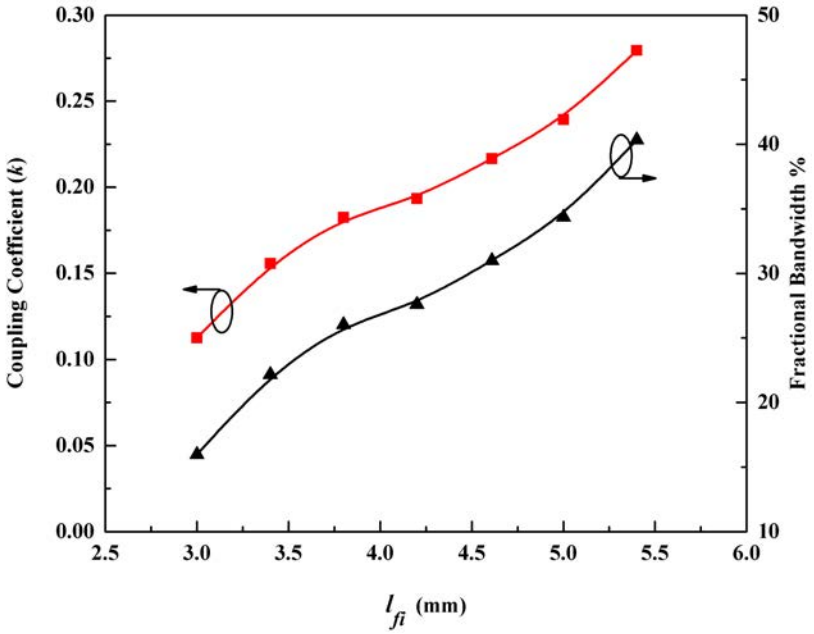

Figure 3.45: Simulated coupling coefficient of the proposed wideband filter structure at 3.3 GHz as a function of the internal feed via position. The other design variables are kept fixed as shown in Table 3.4.

is designed. The external and internal coupling sections are designed separately and combined to form the complete filter. To achieve 38% fractional bandwidth, the required external feed via distance is selected to be 5 mm, as can be seen in figure 3.44. From figure 3.45, the corresponding internal feed via distance, for this bandwidth, needs to be 5.3 mm, if the iris width is kept at 7 mm. The filter primary dimensions are listed in Table 3.4. The filter is implemented in the same Rogers TMM3 microwave laminate. The rest of design characteristics such as board thickness and gap size are the same as the narrowband filters designed in the previous section.

The same traditional circuit board fabrication process and test setup, as used before, is utilized to implement and measure the filter. A photo of the fabricated filter is shown in figure 3.46. The test results are presented in figures 3.47 to 3.49.

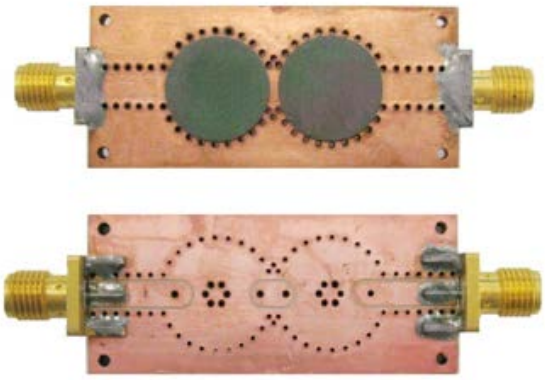

Figure 3.46: Picture of the fabricated, 38%-fractional-bandwidth, tunable bandpass filter, (a) top view, (b) bottom view.

Figure 3.47 shows the measured response of the filter while it was tuned over the desired frequency range. The measured response exhibits an insertion loss as low as 0.4 dB while tuned across the range from 2.91 to 3.80 GHz. The 3-dB bandwidth varied from 1.018 to 1.411 GHz. This is equivalent to a fractional bandwidth of 35% to 37.2%. Also, a comparison between the simulation and the measurement at 3.35 GHz is shown in figure 3.48. The measured and simulated insertion loss and bandwidth are also compared in figure 3.49. A good agreement is seen between the results which confirms the wide bandwidth

Table 3.4: The fabricated 38%-fractional-bandwidth tunable bandpass filter primary dimensions

Substrate Thickness	3.175 mm	
Post Diameter (d_p)	3.8 mm	
Cavity Diameter (d_c)	13.7 mm	
Iris Width (w)	7 mm	
-	Internal (i)	External (e)
Tap-line Width (w_t)	0.5 mm	0.25 mm
Feed Via Diameter (d_f)	0.8 mm	0.8 mm
Feed Via Distance (l_f)	5.3 mm	5 mm
CPWG Term. Length (l_c)	1.15 mm	2.25 mm

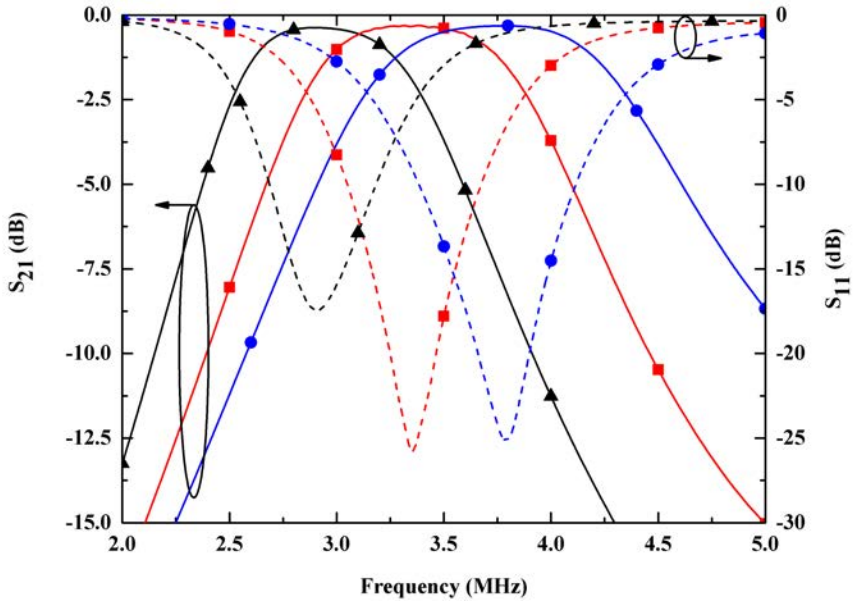

Figure 3.47: Measured S-parameters of the 38%-fractional-bandwidth, tunable, bandpass filter as it is tuned from 2.91 to 3.80 GHz.

capability of the proposed structure. The insertion loss is slightly higher in the measurement than the simulation but the measurement includes the loss from the SMA edge mounted connectors. Also, the narrower bandwidth contributes to the increase in loss. The difference in bandwidth can be attributed to the non-planar movement of the top copper as the piezoelectric transducers are operated as well as from the assembly and fabrication tolerances.

In general, a combination of electric- and magnetic-field coupling, for both external and internal coupling, can be used in the wideband implementation of the substrate-integrated, evanescent-mode, cavity bandpass filters. Fractional bandwidths on the order of 40% are demonstrated to be feasible using this methodology. This design can be extended to higher order designs as both the internal and external coupling can be tailored to a wide range of coupling coefficients. As an application of wideband bandpass filter, in the next chapter it will be seen how this substrate-integrated, evanescent-mode cavity, wideband,

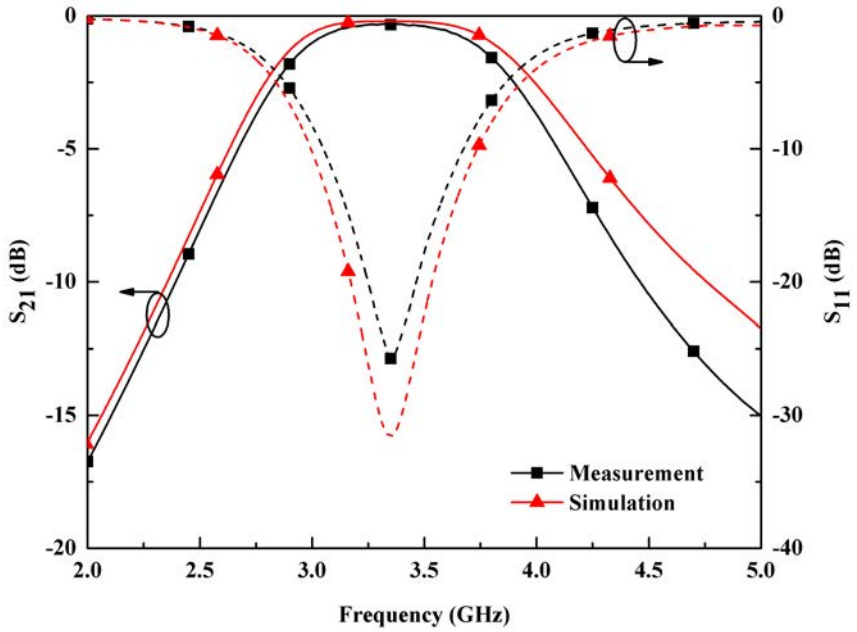

Figure 3.48: Comparison between the measured and simulated results for the 38%-fractional-bandwidth, tunable, bandpass filter.

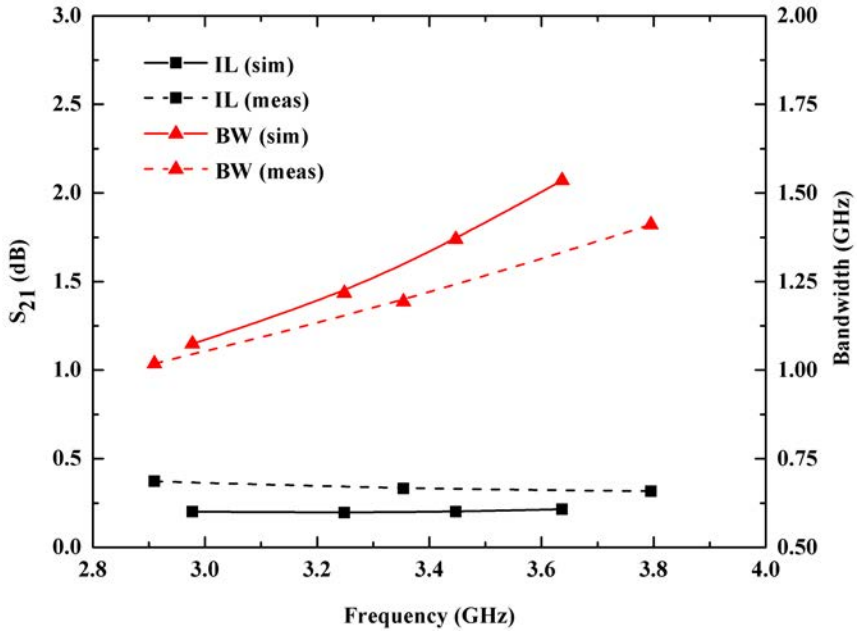

Figure 3.49: Simulated and measured insertion loss and bandwidth of the 38%-fractional-bandwidth tunable bandpass filter.

bandpass filter can be used to design a single substrate bandstop filter.

3.5 Power Handling Issues in Evanescent-mode Cavity Filters

As the frequency spectrum is getting increasingly crowded, more narrowband bandpass filters will be required. This tends to increase the power density of filters. Therefore, modern microwave filter designs for wireless and radar applications demand better estimation of power handling capabilities [99]. The need for reduced volume and mass, also increases the difficulty of the filter design from a power handling capabilities perspective.

Most of the available technologies for implementing tunable and reconfigurable filters, such as ferroelectric thin films, microelectromechanical systems (MEMS), and substrate-integrated, evanescent-mode cavity, suffer from either low power handling or poor intermodulation performance at high operating powers [100], [101]. Although this is acceptable for low power receive applications, in order for any of these techniques to be feasible for widely distributed commercialization, they must be able to work on transmitters as well. Therefore, in order to realize tunable and reconfigurable filters for such systems, the power handling will need to be improved significantly. Consequently, the main power handling issues that can occur in an evanescent-mode cavity-based device need to be analyzed to be able to achieve maximum power handling capabilities of these devices.

In general, several factors limit the power handling capabilities of RF/microwave filters, including

- multipaction breakdown,
- ionization breakdown,
- thermal-related high-power breakdown,

– device non-linearities,

– and self-biasing.

Multipaction is an RF vacuum-related breakdown mechanism. Multipaction happens when the free electron space charges between two surfaces grow continuously. The electrons accelerate under the intensity of the applied field and bombard the walls which causes continuous release of secondary electrons. This phenomena should be considered for the RF components designed for operations in space or under vacuum [99].

In contrast, ionization breakdown is an RF-gas breakdown phenomenon under which an initially low electron density in the gas increases abruptly. When ionization breakdown occurs the avalanche-like increase in the number of electrons turns an isolating gas into conducting plasma. Ionization breakdown happens at higher pressures than multipaction and therefore ground-based components must be designed considering such a breakdown [99].

Due to different loss mechanisms in RF/microwave filters, they may dissipate a substantial amount of power. This power dissipation leads to an overall temperature rise and forming of local hot spots inside the filter. Temperature rise, either due to self-heating from power dissipation or heat from the ambient environment, is a major factor contributing to the aging of filter structures in terms of the quality of substrate material, frequency drift and/or detuning effect due to physical and dimensional changes of the filters and substrate permittivity changes, and finally, structural stresses that affect the reliability of the filter. In SIW filters where both conductive and dielectric losses contribute to the generation of heat, thermal-related breakdown study is important. An SIW filter, with a good thermally-engineered design, guarantees an acceptable increase and distribution in temperature [102]–[105]. An approach for analyz-

ing the power handling capability of SIW filters can be found in [42], which has been developed based on the general approach presented in [99] for different RF/microwave filters.

Like all electronic devices, non-linearity is another common power-related issue in tunable and reconfigurable filters. Device non-linearities result in the generation of unwanted amplitude modulation of signals. This behavior is usually referred to as intermodulation distortion (IMD), and it introduces excessive in-channel and cross-channel interferences. The main sources of non-linearities in tunable and reconfigurable filters are the control devices like solid state varactors, PIN diodes, or RF-MEMS devices; although passive intermodulation, which is largely a workmanship-related issue and is related to the device production, can also cause it [100], [101], [106].

Self-biasing refers to actuation of movable micro-structures by a quasi-electrostatic attractive force from RF signal power [107]. There are two forces acting on the cavity top, the DC actuation force and the force from the RF signal. In evanescent-mode cavities, at a certain RF power level, the attractive force from the RF signal counteracts the DC biasing force and pulls the top of the cavity towards the capacitive loading post, changing the capacitance and therefore the center frequency of the resonator. This can cause non-linearity effects such as frequency response distortion and intermodulation. To optimize the power handling such non-linearities must be taken into account. A preliminary study of modeling this effect for an evanescent-mode cavity has been previously shown for MEMS actuators [108], [109]. In the case of the piezoelectric actuator being mounted on a laminated copper layer, the stiffness of that stack will reduce the effect of self-biasing on the device and it is not expected that any such effects will distort the RF signal.

Ionization breakdown of the air in the capacitive gap between the loading post and the top of the cavity is of great concern in designing evanescent-mode cavity filters. Typically 90% of the electric-field energy is stored in the air gap [52]. The confinement of the electric-field in this region results in high field intensity, which can result in ionization breakdown of the air dielectric. Analytical expressions for the breakdown threshold of the electric-field in small gap geometries, in the range of few millimeters, have been investigated [99]. Gas discharge and breakdown are traditionally understood with the Paschen law in which a relationship between breakdown voltage and pressure for static fields is presented. However, due to field emission and gas ionization the macroscopic Paschen law is not valid for smaller gaps (in the range of micrometers). Therefore, a modified Paschen law, that linearly relates breakdown voltage to gap size, must be used. Although, a wide variety of experimental efforts have validated these observations for static fields [101], breakdown due to RF fields has not been widely investigated. Published experiments about RF-gas discharge for gaps in the millimeter range agree with the available theory. However, a limited number of studies for micro/nanogaps at these frequencies have been conducted [101], [110]. Therefore, additional studies are needed to fully understand these phenomena.

3.5.1 Prediction of Power Handling

Power handling of a distributed filter is dependent on the distribution of electromagnetic fields inside the EM structure. Therefore, to predict the power handling of a filter, knowledge of the fields or the stored and dissipated energy inside the filter is required. This might be done using full-wave analysis of the filter structure or via equivalent circuit models. Eventually, comparing

of the maximum electric-field with the breakdown threshold or the generated heat with the glass transition temperature can be used to predict the power handling of the filter [42] and [99]. However, three-dimensional full-wave EM analysis of the filters, although possible, is a very time-consuming process. This analysis for high-Q and narrowband filters, in which the filter performance is extremely sensitive to the filter dimensions, is a very demanding task. For substrate-integrated, evanescent-mode cavity filters with large aspect ratios (usually the gap size is in the micrometer range, while other filter dimensions are in the millimeter range) and high sensitivity to the gap sizes, such an analysis does not seem to be practical. Therefore, for power handling analysis of these structures, other methods that requires less emphasis on full-wave EM analysis are preferred [99].

In [109] and [111], electromechanical non-linearity behavior in MEMS- and piezoelectric-actuated, substrate-integrated, evanescent-mode, cavity filters have been studied, respectively. More recently, in [112] and [110] gas breakdown and power handling in a microwave, tunable, evanescent-mode cavity resonator was experimentally studied. It was also discussed that in atmospheric pressure, gas breakdown due to electron-induced ionization and secondary electron emission is the dominant breakdown mechanism in these type of resonators where the gap size is larger 10 μm. However, prediction of power handling in a tunable, substrate-integrated, evanescent-mode, cavity filter has not been investigated [52].

This section presents a step-by-step systematic procedure for accurately modeling a tunable, high-Q, substrate-integrated, evanescent-mode bandpass filters, for predicting the power handling. A circuit-EM co-design approach is used for this purpose as follows:

1. The the resonator is first modeled using an eigen-mode simulation in a full-wave EM solver, like HFSS, where the maximum electric-field in the resonator as well as the unloaded quality factor is extracted. The resonator dimensions can readily be fine tuned, as eigen-mode analysis is much faster than driven-mode simulation. The calculated quality factor of the resonator, is used to accurately model the resonator in the circuit simulator. Since, the majority of the electric-field in the resonator is confined to the air gap, the quality factor of the resonator is mostly determined by the dissipation of energy in the air rather than the dielectric. The quality factor of the resonator is also highly dependent on the conductivity of the conductors in the air gap where the surface current has its maximum value. In order to simultaneously increase the accuracy and speed of the simulation, the EM simulator should be set to increase the number of cells in the air gap as compared to any other portion of the structure. Also, the occurrences of local numerical fluctuations should always be checked and avoided. Although the total stored energy in a lossless filter is just a function of the filter group delay [113], in a lossy filter the total stored energy, as well as the stored energy in each resonator, is also dependent on the quality factor of the resonator. Therefore, in order to accurately predict the power handling of the filter, the accuracy of the simulated quality factor in the EM simulator is crucial. This requires the accurate extraction of the effective metal conductivity for the plating facility as described in 3.2.1. In order to find the maximum electric-field in the resonator, the resonator excitation is scaled so that the total stored energy in the resonator is 1 nJ. The maximum electric-field in this situation is referred to as normalized

maximum electric-field ($E_{max-norm}$).

2. Based on the required coupling values obtained from filter synthesis, the filter is directly modeled in a circuit simulator in bandpass domain. Similar to what has been presented in 2.2, in the direct-coupled bandpass filter model, resonators are modeled using parallel RLC circuits (series resonators are also possible). The value of capacitors are chosen arbitrarily as long as they resonates with the inductors at the right frequency. It was mentioned in Chapter 2 that, the effect of arbitrarily selection of the capacitors is compensated by the value of inverters for every predetermined frequency response. The quality factor, found from the EM simulation, is utilized to model the loss in the resonators while the coupling values, calculated using filter synthesis, are used to model the lossless admittance inverters. Nodal admittance analysis of this model, which is linked to the filter coupling matrix, yields the frequency response and the stored energy in each resonator of the filter. In order to find the stored energy, the generator voltage is set to $\sqrt{8R_s}$, where R_s is the source resistance. This excites the filter with one Watt of available power from the source. The stored energy in each resonator, at any frequency (f), can be found from

$$W_{stored} = \frac{1}{4} C_i V_i^2 \left(1 + (\frac{f_0}{f})^2\right) \tag{3.14}$$

where f_0 is the resonant frequency and C_i and V_i are the nodal capacitance and voltage, respectively.

3. Finally, the maximum stored energy ($W_{stored-max}$) is found from the above analysis. Based on the filter order and configuration, $W_{stored-max}$

can happen in any resonator. Eventually, the power handling of the filter is found by comparing the air breakdown threshold ($E_{breakdown}$) with $E_{max-norm}$ scaled by $W_{stored-max}$ using

$$P_{max} = (\frac{E_{breakdown}}{E_{max-norm}})^2 \times \frac{1}{W_{stored-max}} \tag{3.15}$$

where the value of $E_{breakdown}$ for air gaps in the micrometer range has been found to be 7.9 V/μm at atmospheric pressure [112].

To verify the proposed analysis approach, the power handling of the 4%-fractional-bandwidth, second-order, Butterworth, bandpass filter is measured and compared to the predicted value. The power handling calculation is performed at 3.0 GHz, where the filter has the smallest gap size, the narrowest bandwidth and the highest group delay. This results in the highest stored energy in the resonators and represents the worst case in the power handling calculation. The eigen-mode simulation in HFSS gives a value of 627 for the unloaded quality factor of the resonator at 3.0 GHz which is in good agreement with the previous measured value of 615. The model in figure 3.31(b) is utilized for the nodal admittance analysis. The nodal voltage and stored energy in each resonator for a capacitance of 1 pF are shown in figure 3.50. Voltage magnification is clearly seen in this figure, which is common for narrow-band, high-Q, bandpass filters. It is also seen that due to the loss of resonators, the total stored energy is not equivalent to the filter group delay. For this case, $W_{stored-max}$ is found to be 2.55 nJ.

The electric-field distribution inside the resonator, normalized for a total stored energy of 1 nJ, found from eigen-mode simulation in HFSS, is shown in figure 3.51. When the vias are modeled as solid rods $E_{max-norm}$ is 0.813 V/μm, while when the vias are modeled as tubes $E_{max-norm}$ is increased to 1.02 V/μm,

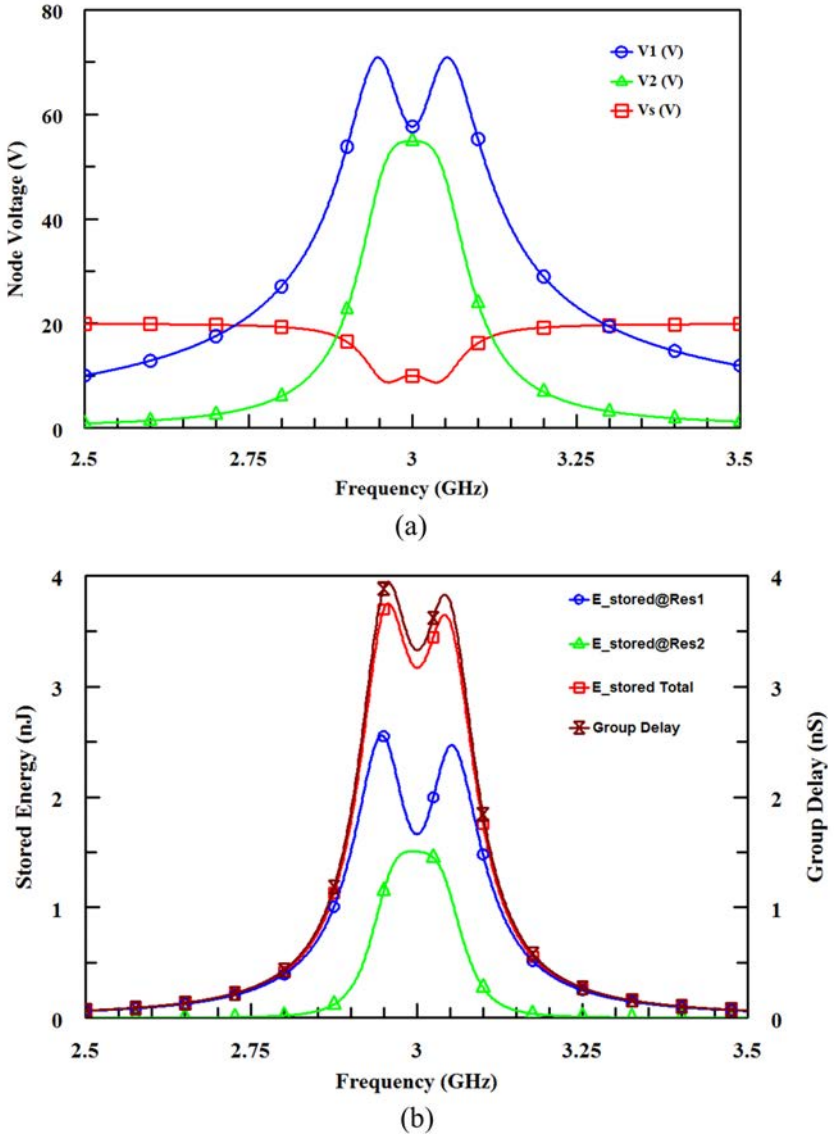

Figure 3.50: Admittance nodal analysis results, (a) nodal voltages, (b) stored energy of the resonators.

which reduces the expected power handling of the filter. The increase in the peak of the electric-field in the latter case, is due to current crowding around via holes. Therefore, the power handling of the filter can be found using (3.14) to be between

$$(\frac{7.9}{0.813})^2 \times \frac{1}{2.55} = 37\ Watts \equiv 45.7\ \text{dBm}$$

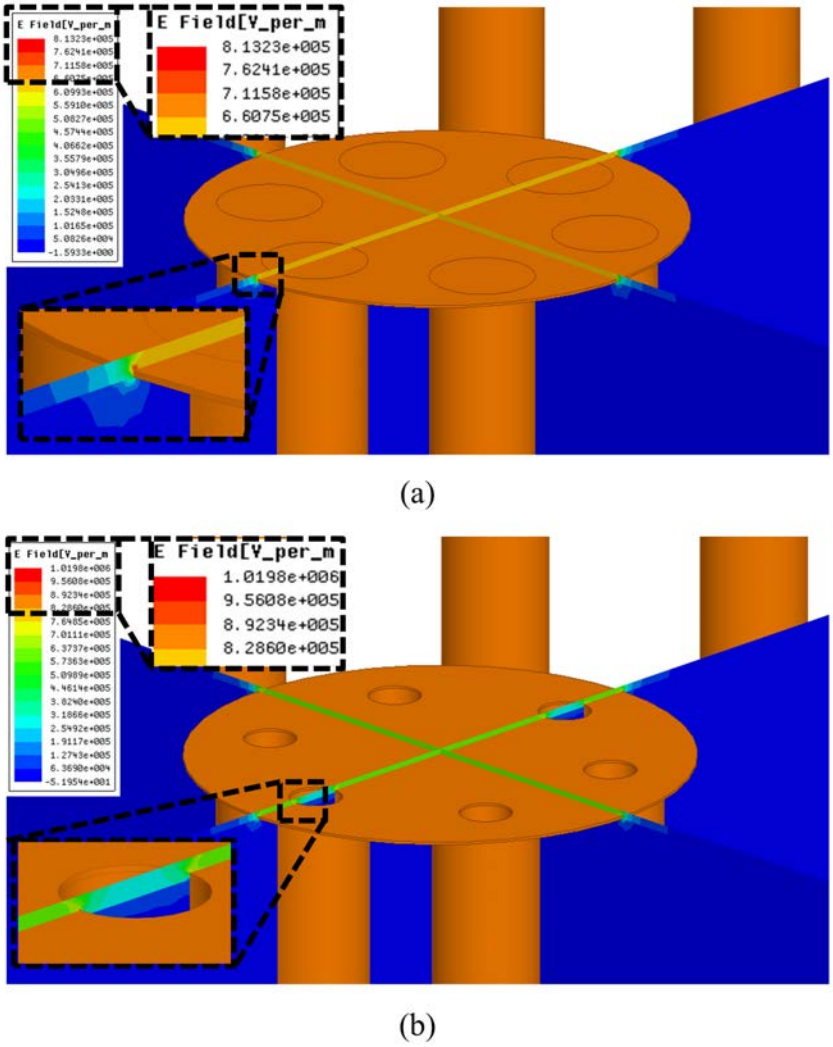

Figure 3.51: Distribution of electric-field inside the cavity shown on two perpendicular planes, (a) vias modeled as rods, (b) vias modeled as tubes.

and

$$(\frac{7.9}{1.02})^2 \times \frac{1}{2.55} = 23.5\ Watts \equiv 43.7\ \text{dBm}.$$

The power handling of the fabricated filter was measured using the setup shown in figure 3.52. In this setup, consisting of a chain of a few RF components, isolators are used to minimize mismatch between the components and

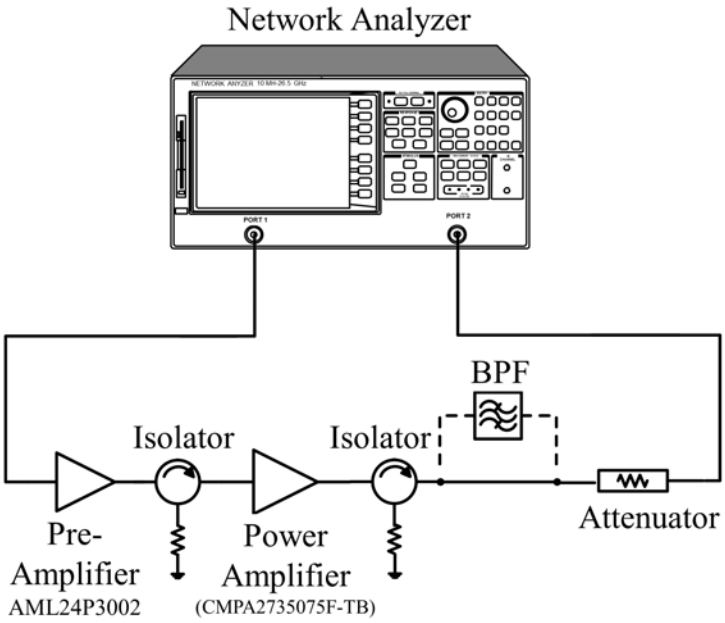

Figure 3.52: Test setup used to measure power handling of the bandpass filter. The input power to the filter is first calculated when the filter is not in the chain.

the attenuator is utilized to protect the network analyzer. Before inserting the bandpass filter into the chain, the exact attenuation of the attenuator and the total gain of the chain for different input powers are measured and saved. These values are used to calculate the actual input power to the bandpass filter. During the test, the input power is gradually increased until air breakdown is observed. Therefore, the input power to the filter is counted as the filter power handling capability.

The test result for the fabricated filter is shown in Fig. 3.53. At 3.0 GHz the air breakdown happens at 30.9 Watts (44.9 dBm), while filter can handle 26.9 Watts (44.3 dBm) of continuous-wave RF signal. This confirms the accuracy of the predication method. The test results for 3.3 GHz and 3.6 GHz also show that the filter power handling is 28.2 Watts (44.5 dBm) and 30.9 Watts (44.9 dBm), respectively. It is observed that the filter can handle more power

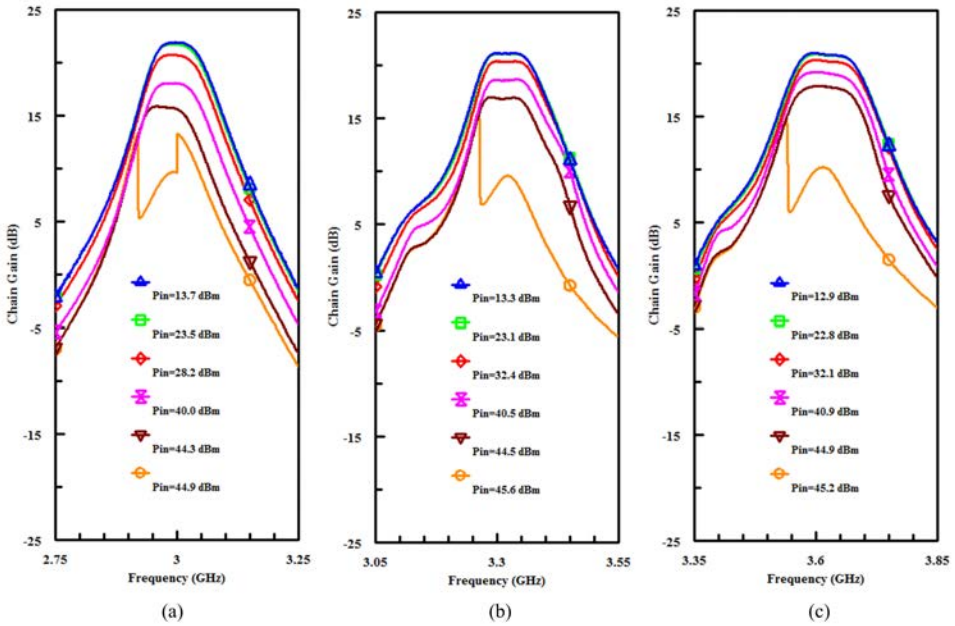

Figure 3.53: Measured power handling of the 4%-fractional-bandwidth, bandpass filter at 3.0, 3.3, and 3.6 GHz.

in higher frequencies because of its wider bandwidth as well as larger gap size. In other words, wider bandwidth reduces the density of the stored energy over frequency, which results in higher power handling. Fabrication tolerances, non-uniformity in the air gap, and sharp edges formed on top of the posts during the fabrication process are assumed as the reasons for the minor discrepancy observed between the predicted and the measurement results. It can be seen that the prediction method matches perfectly with measurement results showing of almost 27 Watts continuous-wave power handling for the 4%-fractional-bandwidth, second-order, Butterworth bandpass filter. The same procedure can be repeated for the 2%- and 38%-fractional-bandwidth, second-order, Butterworth, bandpass filters. Based on a calculation using the above analysis, their power handling capabilities are expected to be 13.5 and 255 Watts, for the 2%- and 38%-fractional-bandwidth filters, respectively.

Chapter 4

Single Layer, Substrate-Integrated, Evanescent-Mode Cavity Bandstop Filter Design

4.1 Introduction

Receivers are usually required to detect very weak signals in the presence of much stronger ones. The strong signal may be a strong adjacent transmitter or even self-interference while operating in simultaneous transmit and receive mode. Unfortunately, the stronger signals can drive the receiver front-end amplifier into compression or saturation, which results in distorting, compressing, masking weaker signals, and desensing the receiver. Bandstop filters are essential devices for selective suppression of a specific narrow band of frequencies in such situations. Bandpass filters are commonly used for such purposes. However, it is not an easy task to design a bandpass filter with an optimized passband characteristics, in terms of low insertion loss and good return loss, and simultaneously a customized level of rejection in the stopband. Lumped element bandstop filters can be readily designed from the lumped element lowpass prototype using the appropriate scaling and transformation as discussed in section 2.2. Although the designed bandstop filter is suitable for lumped element realization, having both parallel and series resonators with different

element values for resonators, limit its application in many actual implementation especially in microwave frequencies where the lumped elements are required to be replaced by distributed structures.

4.2 Conventional Microwave Bandstop Filter Design

Microwave bandstop filters, either static or tunable, have been conventionally designed using a transmission line between the source and load ports. This transmission line is coupled at quarter wavelength (or odd multiples of that) intervals to bandstop resonators (anti-resonators), [114]–[116]. Such a configuration is shown in figure 4.1 where the element values can be directly found from the lowpass prototype [114]. A comparison of these circuits with the general form of direct-coupled resonator filters reveals that the quarter wavelength transmission lines are just impedance or admittance inverters implementing the required couplings between the resonators. A typical, third-order, bandstop filter realized in a rectangular waveguide structure along with the coupling-routing diagram of such structures are shown in figure 4.2.

Bandstop filters designed using this method can be implemented via different technologies including coaxial lines, waveguides, and substrate-integrated waveguides [117], [118]. Although many pioneers have contributed to the design of bandstop filters, direct synthesis of bandstop filters was first presented in [70]. It was shown that Chebyshev (equal-ripple) bandstop filters can be designed using the same folded fully-canonical topology used for the synthesis of generalized Chebyshev (pseudo-elliptic) and elliptic bandpass filters [33], [119]. In the approach that was first noted in [33], the similarities between the resonators of the bandstop filter and those resonators of the extracted-poles, bandpass filter, that realize the transmission zeros, are used to design

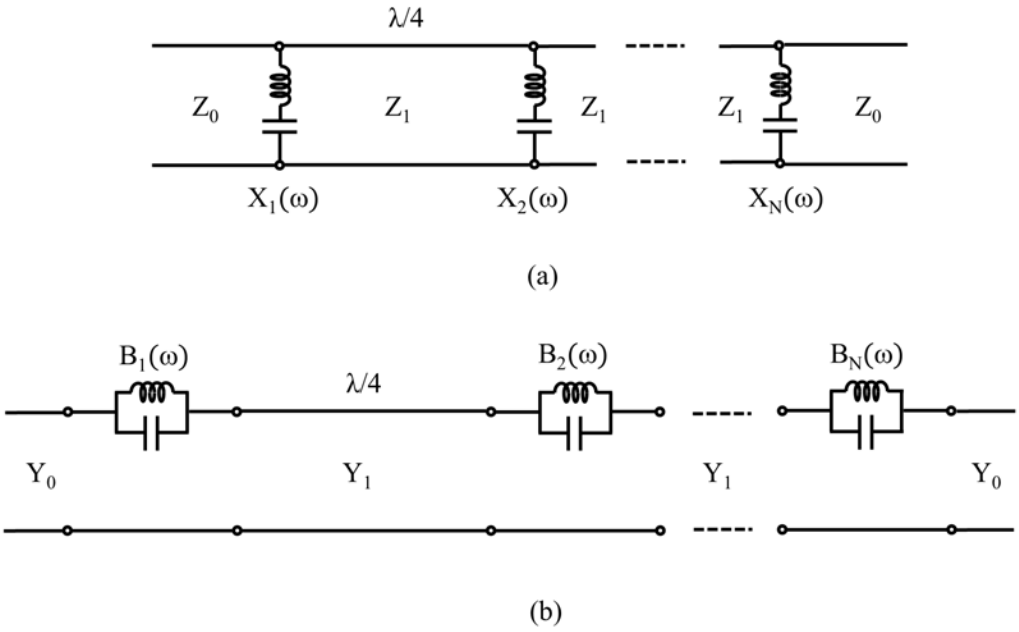

Figure 4.1: Bandstop filter with quarter wavelength couplings, (a) implemented using series resonators in shunt branches, (b) implemented using parallel resonators in series branches.

the bandstop filter. In this method, instead of using the common frequency transformation for synthesizing a bandstop filter from its lowpass prototype, the transfer and reflection functions of the bandpass filter, found from the lowpass prototype, are swapped. Through this synthesis procedure, the return loss characteristic of the bandpass filter in the passband, determines the attenuation level of the bandstop filter in the stopband. Similarly, the transmission characteristic of the bandpass filter in the stopband determines the return loss of the bandstop filter in the passband [120]. Based on the method presented in [70], and due to the use of folded canonical structure in the design of bandstop filter, successive placement of resonators coupled to a main transmission line is not required. Therefore, bandstop filters can be implemented more compactly. Using this method, it is possible to realize up to N reflection zeros for a bandstop filter with N resonators because the folded canonical

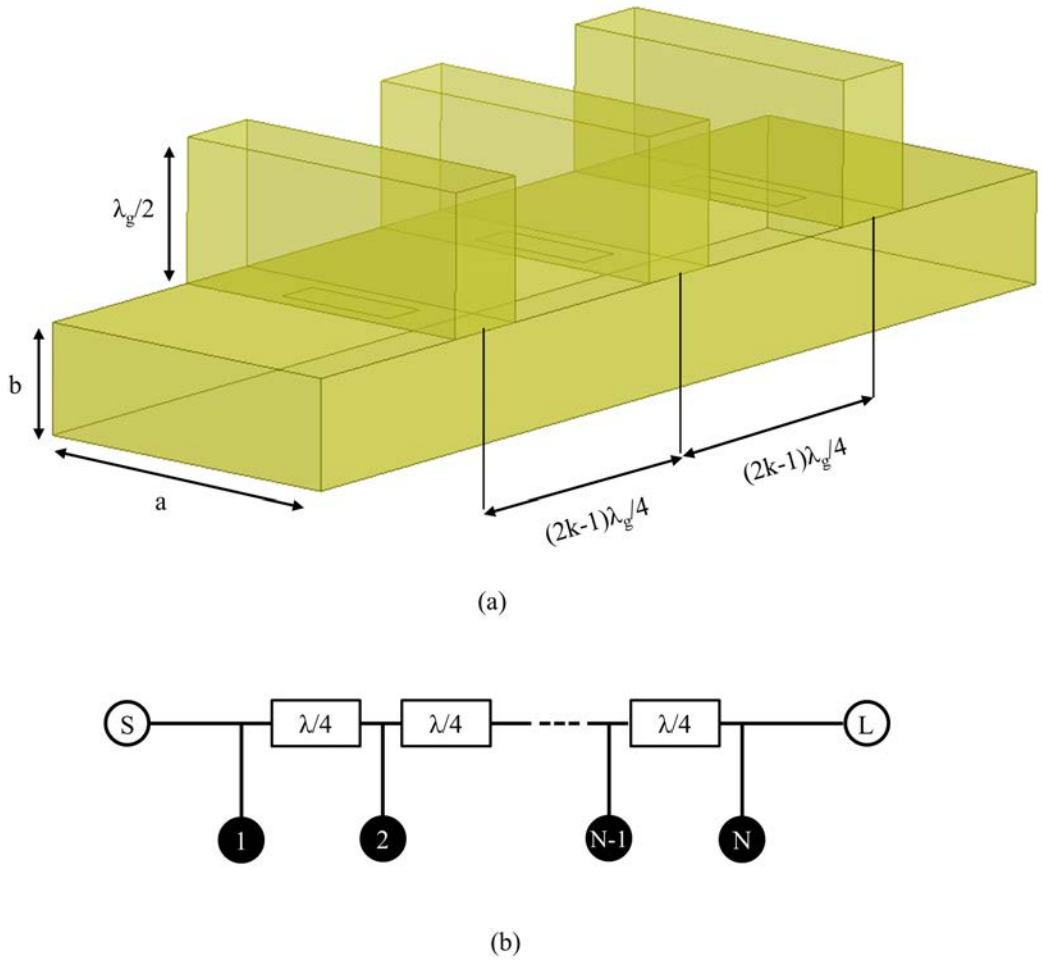

Figure 4.2: Third-order bandstop filter realized in a rectangular waveguide.

structure includes direct source-to-load coupling. The tunable bandstop filter with variable attenuation introduced in [121] also utilizes direct source-to-load coupling. A design method for bandstop filters without source-to-load coupling based on dual-band combline filter transformation was demonstrated in [122]. However, the provided design formulas have been derived for combline structures without showing the synthesis procedure for realizing the coupling matrix.

More recently, evanescent-mode cavity filters were used to design and implement tunable reconfigurable bandstop filters as well as bandpass-bandstop

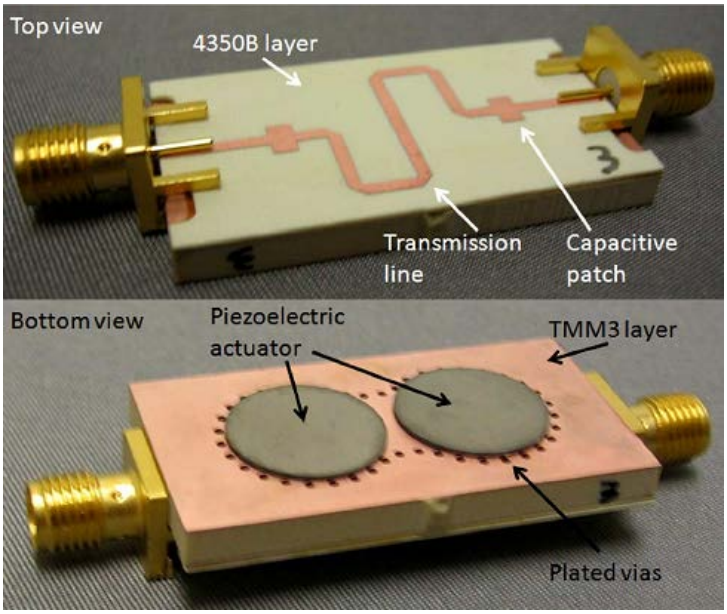

Figure 4.3: Picture of a second-order, substrate-integrated, evanescent-mode cavity, bandstop filter fabricated using two substrates (from [2]).

filter cascades [2], [4]–[6], [97], [98], [123]–[128]. As mentioned previously, the benefits of evanescent-mode cavity filters include high-Q, multi-octave tuning ranges, and low power consumption in actuation circuitry. For these reasons, extensive research has been devoted to the design and development of reconfigurable, evanescent-mode cavity filters. The aforementioned bandstop filters also utilize source-to-load coupling. This source-to-load coupling is implemented using a microstrip transmission line between the filter ports, fabricated on a separate layer and laminated to the back of the cavity substrate, to which the resonators are coupled in a shunt configuration. Figure 4.3 shows a picture of a second-order, substrate-integrated, evanescent-mode cavity, bandstop filter realized using two substrates [2]. The basic single resonator structure, implemented using this technique, is shown in figure 4.4. A magnetic-field coupling slot, in the microstrip line ground plane, is used to couple the feeding microstrip line to the resonator in a shunt configuration.

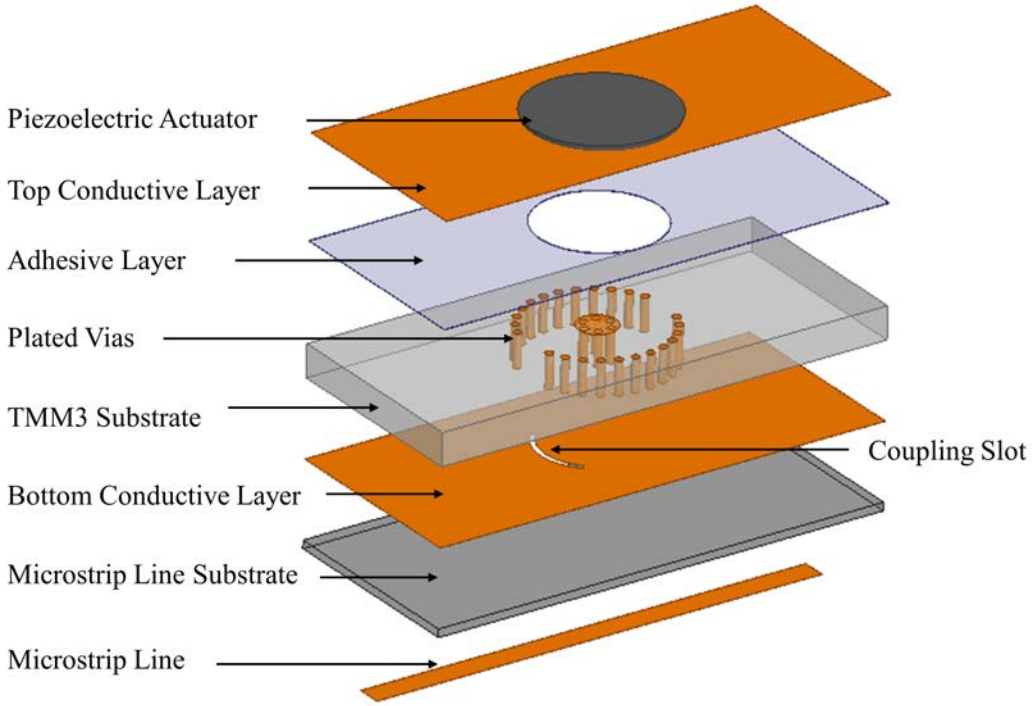

Figure 4.4: Structure of a substrate-integrated, evanescent-mode cavity, resonator in a shunt coupling structure.

The frequency response of this resonator is shown in figure 4.5. In comparison to the response of the resonator in series coupling configuration (figure 3.14), it can be seen that the transmission and reflection responses have been swapped. This confirms that the same resonators can be used to realize both bandpass and bandstop filters. However, for bandpass filters, implemented using the same technology, a series feed is required [5]. Therefore, although the resonators are identical for both bandpass and bandstop filters, due to different coupling schemes, the physical implementation of each filter is different. Thus their integration increases the complexity of the fabrication process, which results in reduced yield.

The following section presents a new coupling matrix synthesis method for designing bandstop filters without source-to-load coupling. To this end, phase

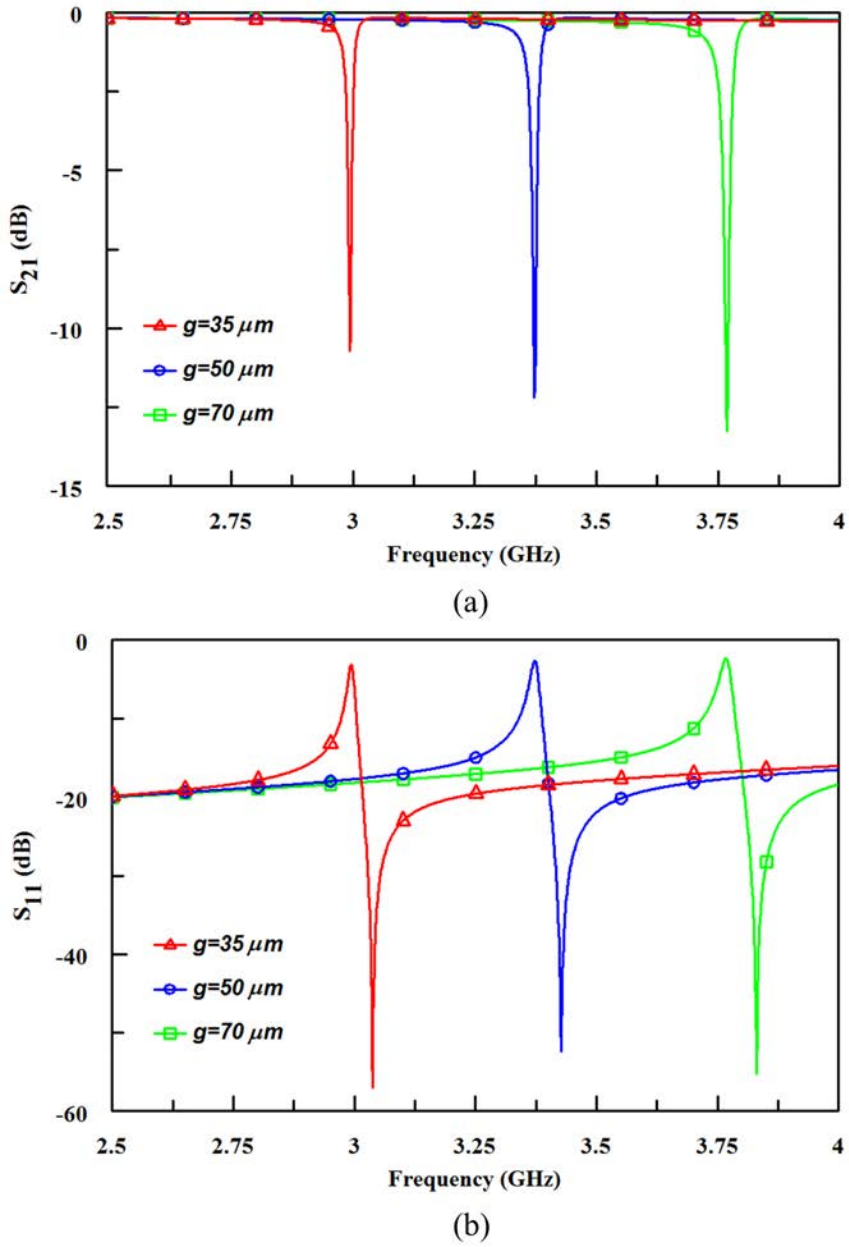

Figure 4.5: Simulated frequency response of a substrate-integrated, evanescent-mode cavity, resonator arranged in shunt coupling configuration to the feeding transmission line, (a) S_{21}, (b) S_{11}.

cancellation is used to provide the notch in the frequency response of the filter. The presented method provides the option of designing and implementing bandstop filters using the same coupling scheme that is used for bandpass fil-

ters. For demonstration, a coupling matrix for a second-order, bandstop filter is derived and examples of single substrate evanescent-mode cavity bandstop filters with different bandwidths are provided to prove the concept. The proposed design method is quite general and can be applied to higher-order filters and implemented in any filter technology.

4.3 Bandstop Filter Design without Source-to-Load Coupling

In order to design a bandstop filter using phase cancellation, two different signal paths with 180° phase shift must be provided between the source and load. The first path behaves like the source-to-load coupling; however, it should not directly connect the source port to the load port. This idea is shown in figure 4.6 for a second-order, bandstop filter. Since every coupling provides a 90° phase shift, the second signal path must pass through two additional couplings so that the two signals are added out of phase at the filter output. This suppresses the signal at the stopband region of the filter response. In addition, the coupling values must be designed in such a way that the two signals have the same magnitude at the filter output to cancel out each other perfectly. The benefit of using this technique is that bandstop filters can be designed and implemented using two bandpass filters. Therefore, the internal and external coupling between the ports and resonators are realized using the same methods as used in bandpass filters. The direct path in the bandstop filter should be a broadband, bandpass filter, while the indirect path is a narrowband bandpass filter. This idea can be extended to any filter order as long as the conditions for the phase and magnitude of the two signals are met. Since the indirect signal path has two resonators and couplings in common

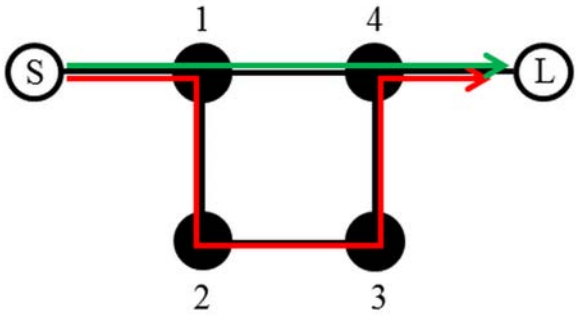

Figure 4.6: Coupling routing diagram for a second-order bandstop filter designed using phase cancellation.

with the direct path, the synthesis method must take this into account. Similar to the implementation in [122], designing an Nth- order bandstop filter using phase cancellation requires 2N resonators, although they use different coupling routing diagrams. Figure 4.7 shows the coupling routing diagram for each case.

To synthesize the coupling values for the bandstop filter, it is first decomposed into two bandpass filters. Figure 4.8 shows the resulting coupling routing diagram for the two bandpass filters. Each bandpass filter has only inline coupling and therefore, its design is not challenging. In section 2.3, it was shown that for such a filter, the coupling values are calculated using

$$m_{i,j} = \frac{1}{\sqrt{\mathrm{g_i g_j}}} \qquad \text{for } i = 0, 1, ..., N \text{ and } j = i + 1 \tag{4.1}$$

where $\mathrm{g_i}$ represents the low-pass normalized prototype element value. Therefore, the coupling matrix of the second- and fourth-order bandpass filters can

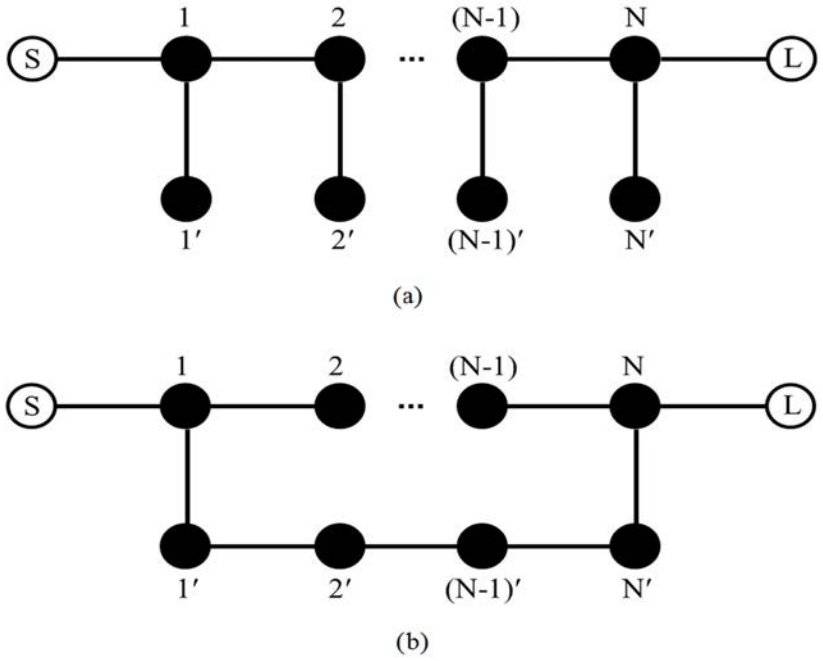

Figure 4.7: Coupling routing diagram for an Nth-order, bandstop filter designed using (a) the method presented in [122], (b) the proposed method in this work.

be found, respectively, as

$$M_1 = \begin{bmatrix} 0 & m_{S1} & 0 & 0 \\ m_{S1} & 0 & m_{14} & 0 \\ 0 & m_{14} & 0 & m_{4L} \\ 0 & 0 & m_{4L} & 0 \end{bmatrix} \tag{4.2}$$

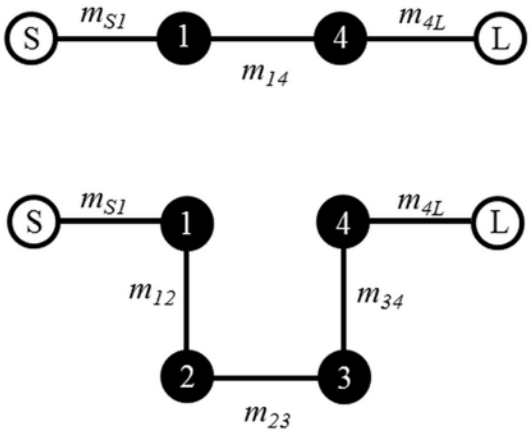

Figure 4.8: Decomposition of a second-order bandstop filter into two bandpass filters.

and

$$M_1 = \begin{bmatrix} 0 & m_{S1} & 0 & 0 & 0 & 0 \\ m_{S1} & 0 & m_{12} & 0 & 0 & 0 \\ 0 & m_{12} & 0 & m_{23} & 0 & 0 \\ 0 & 0 & m_{23} & 0 & m_{34} & 0 \\ 0 & 0 & 0 & m_{34} & 0 & m_{4L} \\ 0 & 0 & 0 & 0 & m_{4L} & 0 \end{bmatrix} \tag{4.3}$$

Assuming symmetric frequency responses for the bandpass filters,

$$m_{S1} = m_{4L} \qquad m_{12} = m_{34} \tag{4.4}$$

The low-pass, normalized prototype can be obtained from any common filter synthesis approximation. In the case of Butterworth filters, for instance, the

coupling matrices can be written as

$$M_3 = \begin{bmatrix} 0 & 0.8409 & 0 & 0 \\ 0.8409 & 0 & 0.7071 & 0 \\ 0 & 0.7071 & 0 & 0.8409 \\ 0 & 0 & 0.8409 & 0 \end{bmatrix} \tag{4.5}$$

and

$$M_4 = \begin{bmatrix} 0 & 1.1430 & 0 & 0 & 0 & 0 \\ 1.1430 & 0 & 0.8409 & 0 & 0 & 0 \\ 0 & 0.8409 & 0 & 0.5412 & 0 & 0 \\ 0 & 0 & 0.5412 & 0 & 0.8409 & 0 \\ 0 & 0 & 0 & 0.9409 & 0 & 1.1430 \\ 0 & 0 & 0 & 0 & 1.1430 & 0 \end{bmatrix} \tag{4.6}$$

When these two filters are recombined, m_{S1} and m_{4L} in the coupling matrices cannot retain their original values. They are forced to be either 0.8409 or 1.1430. This means that either of these filters can be synthesized directly to have the desired response while the other one must be re-synthesized with two predefined external couplings. Otherwise, the response of the filter is distorted. If, for example, the second-order bandpass filter is designed independently, the

coupling matrix of the fourth-order, bandpass filter must be rewritten as

$$M_5 = \begin{bmatrix} 0 & m'_{S1} & 0 & 0 & 0 & 0 \\ m'_{S1} & 0 & m'_{12} & 0 & 0 & 0 \\ 0 & m'_{12} & 0 & m'_{23} & 0 & 0 \\ 0 & 0 & m'_{23} & 0 & m'_{34} & 0 \\ 0 & 0 & 0 & m'_{34} & 0 & m'_{4L} \\ 0 & 0 & 0 & 0 & m'_{4L} & 0 \end{bmatrix} \tag{4.7}$$

where

$$m'_{S1} = m'_{4L} = 0.8409 \tag{4.8}$$

According to 2.41b, $S_{21}(s)$ of this filter can be found using its new coupling matrix as

$$S_{21} = -2j\mathbf{A}^{-1}_{N+2,1} \tag{4.9}$$

where $\mathbf{A}^{-1}_{N+2,1}$ is the $(N+2,1)$ element of the inverse matrix of $\mathbf{A}$ and N is the order of the filter. Matrix $\mathbf{A}$ is defined as

$$A = \mathbf{M} + \omega\mathbf{U} - j\mathbf{Q} \tag{4.10}$$

where $\mathbf{M}$ is the coupling matrix, $\mathbf{U}$ is similar to the $(N+2)\times(N+2)$ identity matrix, except that $[U]_{11} = [U]_{N+2,N+2} = 0$, $\mathbf{Q}$ is the $(N+2)\times(N+2)$ matrix with all entries zeros, except for $[Q]_{11} = [Q]_{N+2,N+2} = 1$, and ω is the frequency variable of the low-pass prototype ($s = j\omega$).

From general filter theory, as it was shown in Chapter 2, the transmission

and reflection functions of a two-port lossless filter network can be written using characteristic polynomials $P(s), F(s)$, and $E(s)$, which are repeated here for the convenience.

$$S_{11}(s) = \frac{1}{\varepsilon_R}\frac{F(s)}{E(s)} \tag{4.11a}$$

$$S_{21}(s) = \frac{1}{\varepsilon}\frac{P(s)}{E(s)} \tag{4.11b}$$

Remembering that ε_R and ε are two constants used to normalize the highest degree coefficients of the polynomials to one. It was shown that ε_R for Butterworth filters is one. The characteristic polynomials are related to each other due to the conservation of energy,

$$|F(s)|^2 + \frac{|P(s)|^2}{\varepsilon^2} = |E(s)|^2 \tag{4.12}$$

Therefore, in the case of a fourth-order, Butterworth, lowpass prototype filter with the corner frequency of $\omega = 1$ rad/s, the transmission function is given as

$$S_{21}(s) = \frac{1}{s^4 + 2.6131s^3 + 3.4142s^2 + 2.6131s + 1} \tag{4.13}$$

Constructing (4.9) using (4.7) and (4.10) shows that M_5 cannot generate a transmission response similar to (4.13) unless frequency scaling is introduced to (4.13). Applying frequency scaling,

$$\omega \leftarrow \frac{\omega}{\omega_c} \tag{4.14}$$

to (4.13), equating (4.13) and (4.9), and finally solving the equations simultaneously will result in

$$m'_{S1} = m'_{4L} = 1.1430\sqrt{\omega_c} \tag{4.15}$$

$$m'_{12} = m'_{34} = 0.8409\omega_c \tag{4.16}$$

$$m'_{23} = 0.5412\omega_c \tag{4.17}$$

Enforcing a predefined external coupling gives the value of ω_c, and hence, the rest of the coupling values. For example, according to (4.5) for $m'_{S1} = m'_{4L} = 0.8409$, (4.15) to (4.17) will give

$$\omega_c = 0.5412 \tag{4.18}$$

$$m'_{12} = m'_{34} = 0.4551 \tag{4.19}$$

and

$$m'_{23} = 0.2992 \tag{4.20}$$

Therefore, the coupling matrix of the fourth-order, Butterworth, bandpass

filter with corner frequency of ω_c rad/s is written as

$$M_6 = \begin{bmatrix} 0 & 0.8409 & 0 & 0 & 0 & 0 \\ 0.8409 & 0 & 0.4551 & 0 & 0 & 0 \\ 0 & 0.4551 & 0 & 0.2929 & 0 & 0 \\ 0 & 0 & 0.2929 & 0 & 0.4551 & 0 \\ 0 & 0 & 0 & 0.4551 & 0 & 0.8409 \\ 0 & 0 & 0 & 0 & 0.8409 & 0 \end{bmatrix} \tag{4.21}$$

Finally, combining (4.5) and (4.21) gives the bandstop filter coupling matrix

$$M_7 = \begin{bmatrix} 0 & 0.8409 & 0 & 0 & 0 & 0 \\ 0.8409 & 0 & 0.4551 & 0 & 0.7071 & 0 \\ 0 & 0.4551 & 0 & 0.2929 & 0 & 0 \\ 0 & 0 & 0.2929 & 0 & 0.4551 & 0 \\ 0 & 0.7071 & 0 & 0.4551 & 0 & 0.8409 \\ 0 & 0 & 0 & 0 & 0.8409 & 0 \end{bmatrix} \tag{4.22}$$

The matrix has an embedded notch with a 3-dB bandwidth of 0.273 rad/s within the passband of a bandpass filter with a 3-dB bandwidth of 1.236 rad/s. It is worth mentioning that if the fourth-order, bandpass filter is synthesized directly and two predefined external couplings are forced on the second-order, bandpass filter, the resulting bandstop filter will have a 3-dB bandwidth of 0.505 rad/s, and it will be embedded in the passband of a bandpass filter with a 3-dB bandwidth of 2.28 rad/s. The coupling matrix of such a bandstop filter is identical to M_4, except that $m_{14} = 1.3064$ instead of zero. Applying an additional frequency scaling to the resulting coupling matrices can be used to

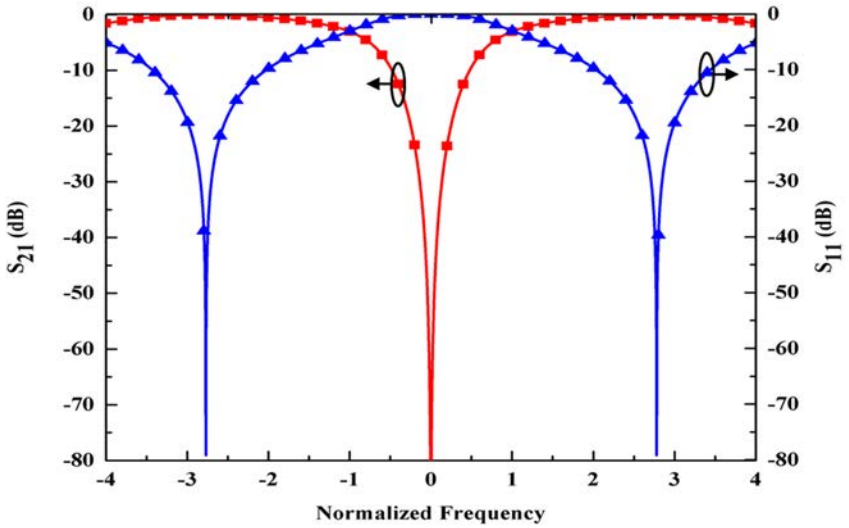

Figure 4.9: Frequency response of the bandstop filter using the proposed topology.

normalize their corner frequencies. The interesting observation is that both methods give the same normalized coupling matrix as

$$M_8 = \begin{bmatrix} 0 & 1.6094 & 0 & 0 & 0 & 0 \\ 1.6094 & 0 & 1.6670 & 0 & 2.5901 & 0 \\ 0 & 1.6670 & 0 & 1.0729 & 0 & 0 \\ 0 & 0 & 1.0729 & 0 & 1.6670 & 0 \\ 0 & 2.5901 & 0 & 1.6670 & 0 & 1.6094 \\ 0 & 0 & 0 & 0 & 1.6094 & 0 \end{bmatrix} \tag{4.23}$$

The frequency response of the final bandstop filter with a normalized 3-dB bandwidth is shown in figure 4.9.

4.3.1 Higher Order Bandstop and Bandpass Filter Synthesis With Predefined Coupling

Extension of the bandstop filter synthesis, using phase cancellation through combing two bandpass filters, requires the synthesis of a bandpass filter with predefined external coupling. Applying a similar procedure to a general bandpass filter of order N results in

$$m'^{2}_{S1} = m'^{2}_{NL} = -\frac{1}{2}\sum_{k=1}^{N} p_k \; . \; \omega_c \tag{4.24}$$

$$m'_{ij} = \omega_c \; . \; m_{ij} \qquad \text{for } i = 1, 2, ..., (N-1) \text{ and } j = i + 1 \tag{4.25}$$

where the prime has been used to express the filter's coupling after the frequency scaling and represents the poles of the filter.

For Butterworth and Chebyshev filters, the poles are expressed, respectively, as

$$p_k = -\sin(\theta_k) + j\cos(\theta_k) \tag{4.26}$$

and

$$p_k = -\eta \, \sin(\theta_k) - j\sqrt{1+\eta^2} \, \cos(\theta_k) \tag{4.27}$$

where θ_k is defined as

$$\theta_k = \frac{(2k-1)\pi}{2N} \qquad \text{for } k = 1, 2, ..., N \tag{4.28}$$

For the Chebyshev filters,

$$\eta = \sinh\left(\frac{1}{N}\sinh^{-1}\frac{1}{\varepsilon}\right) \tag{4.29}$$

where ε is called the ripple factor and is related to the filter passband return loss, L_{Ar} in dB, as

$$\varepsilon = \sqrt{10^{\frac{L_{Ar}}{10}} - 1} \tag{4.30}$$

In Appendix A, it will be shown that for both filter approximations,

$$-\frac{1}{2}\sum_{k=1}^{N} p_k = \frac{1}{\mathrm{g}_1} \tag{4.31}$$

Therefore, (4.24) is written as

$$m'^{2}_{S1} = m'^{2}_{NL} = -\frac{\omega_c}{\mathrm{g}_1} \tag{4.32}$$

which shows how the new corner frequency can be found from the predefined external coupling and the first coefficient of the low-pass prototype. The remaining new coupling coefficients can then be found using (4.25). It is worth noting that (4.25) and (4.32) can also be used to re-calculate the coupling coefficients for a bandpass filter, either in the case of enforcing a predefined internal coupling or frequency scaling of the corner frequency.

It is possible to combine (4.25) and (4.32) in order to eliminate the corner frequency. This results in a relationship between the new coupling coefficients that is independent of the frequency scaling factor. For example, in the case

of a fourth-order, bandpass filter, it can be shown that

$$m'_{23} = \sqrt{\frac{g_2}{g_3}} \frac{m'^2_{12}}{m'^2_{S1}} \tag{4.33}$$

where, for a Butterworth filter (with $g_2 = g_3$), (4.33) can be simplified into

$$m'_{23} = \frac{m'^2_{12}}{m'^2_{S1}} \tag{4.34}$$

This suggests that when m'_{S1} is forced to have a specific value, m'_{12} can be chosen arbitrarily and m'_{23} can be found from (4.34). This provides another degree of freedom to the design that allows for enforcing m'_{12} freely in addition to m'_{S1}. However, such a selection will result in a non-Butterworth bandpass filter. For instance, using (4.34) in the previous example, the coupling matrix of the fourth-order, bandpass filter with enforced $m'_{S1} = 0.8409$ will be

$$M_9 = \begin{bmatrix} 0 & 0.8409 & 0 & 0 & 0 & 0 \\ 0.8409 & 0 & 0.5000 & 0 & 0 & 0 \\ 0 & 0.5000 & 0 & 0.3535 & 0 & 0 \\ 0 & 0 & 0.3535 & 0 & 0.5000 & 0 \\ 0 & 0 & 0 & 0.5000 & 0 & 0.8409 \\ 0 & 0 & 0 & 0 & 0.8409 & 0 \end{bmatrix} \tag{4.35}$$

for $m'_{12} = 0.5$ and will be

$$M_10 = \begin{bmatrix} 0 & 0.8409 & 0 & 0 & 0 & 0 \\ 0.8409 & 0 & 0.4000 & 0 & 0 & 0 \\ 0 & 0.4000 & 0 & 0.2263 & 0 & 0 \\ 0 & 0 & 0.2263 & 0 & 0.4000 & 0 \\ 0 & 0 & 0 & 0.4000 & 0 & 0.8409 \\ 0 & 0 & 0 & 0 & 0.8409 & 0 \end{bmatrix} \tag{4.36}$$

for $m'_{12} = 0.4$. However, as shown in (4.22), the conventional coupling matrix of a fourth-order, Butterworth, bandpass filter with $m'_{S1} = 0.8409$ requires $m'_{12} = 0.4551$. The frequency responses of these filters, after being scaled to have normalized corner frequency, are compared in figure 4.10. The non-Butterworth bandpass filters have a slightly wider (for the case of $m'_{12} = 0.5000 > 0.4551$) or narrower bandwidth (for the case of $m'_{12} = 0.4000 < 0.4551$) and the reflection zeros are not all at $\omega = 0$ rad/s, which means that the passband ripple for the non-Butterworth bandpass filters is nonzero. However, this ripple is quite acceptable for many practical applications.

4.3.2 Single-Layer, Tunable, Substrate-Integrated Evanescent-Mode Cavity Bandstop Filter

In order to verify the proposed theory, two prototype tunable bandstop filters are designed and fabricated using the substrate-integrated, evanescent-mode, cavity filter technology. The same resonators designed in section 3.2.1 are used. Both prototype filters are second-order, frequency-tunable, bandstop filters in the band of 3.0–3.6 GHz. They are designed to provide low passband insertion loss in the tuning range, 10% away from the center frequency. Therefore, the

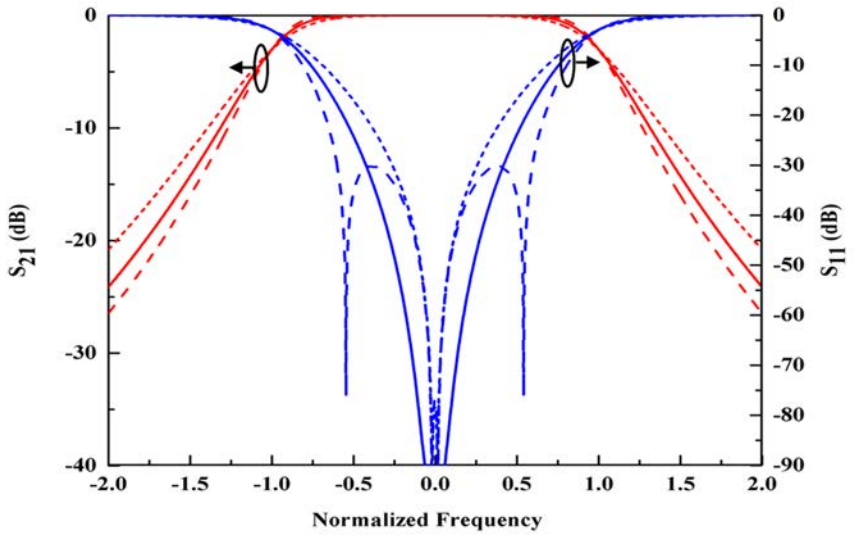

Figure 4.10: Frequency response of a fourth-order bandpass filter, (solid line) Butterworth, (dotted line) non-Butterworth with $m'_{12} = 0.4000$, and (dashed line) non-Butterworth with $m'_{12} = 0.5000$.

passband is from 3.0 to 3.6 GHz and the bandstop filter can be tuned anywhere within this range. The first filter is an extremely narrowband bandstop filter with 10-dB fractional bandwidth of 0.2% and the second one is a narrowband bandstop filter with 10-dB fractional bandwidth of 2.0%. The filters were implemented in a 3.175-mm-thick Rogers TMM3 microwave substrate. The structure of the filters are similar to bandpass filter designed in Chapter 3. Similar to the previously designed bandpass filters, each cavity has a 13.7-mm diameter and a 3.8-mm post formed using 0.8-mm copper-plated vias. The initial air gap was designed to be 51 μm at 3.3 GHz. In order to tune the filters from 3.0 to 3.6 GHz, the gap needs to be changed from 40 to 70 μm, respectively. Piezoelectric actuators (with a diameter of 12.7 mm, a thickness of 0.41 mm, and $\pm$19 μm unloaded vertical movement) from Piezo Systems Inc. are attached using conductive epoxy to the diaphragm external to the cavity above the posts. They are used to provide the required physical displacement.

The bandstop filter consists of two bandpass filters; a wideband bandpass

filter (direct path) that functions like a transmission line between the filter ports, and a narrowband bandpass filter that embeds the notch inside the wideband filter response. Again, similar to [122], the bandwidth of the wide bandpass filter determines the passband of the bandstop filter. Therefore, when a bandstop filter with a very wide passband is required, the bandwidth of the bandpass filter in the direct path must be increased. This limitation can be overcome by tuning of the resonators 1 and 4 to achieve lower insertion loss in the passband of the bandstop filter. Therefore, using an asynchronous tuning mode, tuning of resonators 1 and 4 can be used to compensate for the insertion loss of the bandstop filter in the desired passband, even if the wideband bandpass filter does not have a wide enough bandwidth to create a low-loss path between the ports in the desired tuning range.

Figure 4.11 shows the 2%-fractional-bandwidth, bandstop filter response tuned at 3.6 GHz while the passband insertion loss at 3.0 GHz has been compensated using asynchronous tuning of the resonators in the direct path by a 300-MHz offset from the center frequency. The center frequency of the notch in the bandstop filter is controlled using resonators 2 and 3. An interesting observation in this response is that due to the use of four resonators in the bandstop filter design, four reflection zeros are incorporated in the return loss of the filter. Asynchronous tuning of the resonators can be used to split and change the position of these reflection zeros. This results in a sharper transition from the stopband to the passband of the filter on one side of the stopband. By controlling the location of the poles, a bandstop filter with either a constant absolute bandwidth or a constant fractional bandwidth is achievable. Constant absolute bandwidth was previously reported in [122]. Asynchronous tuning of the resonators can also be utilized for control of the

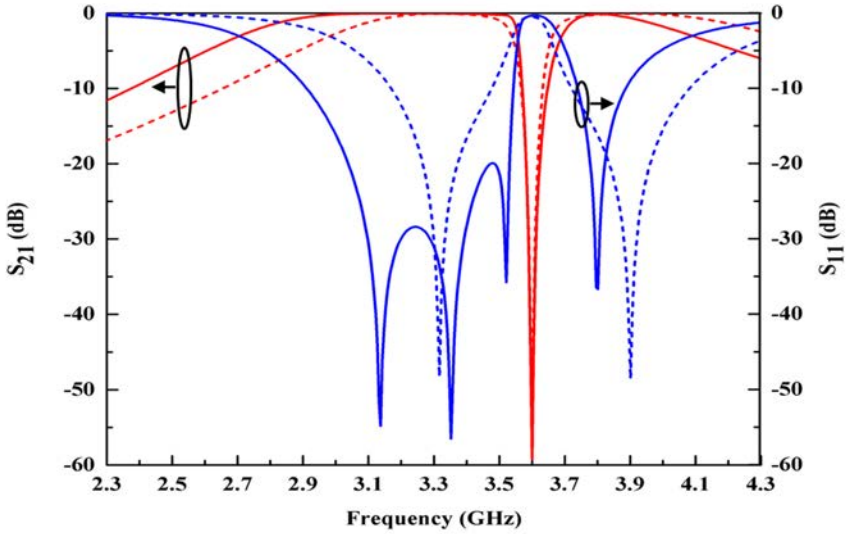

Figure 4.11: Simulated results for compensation of insertion loss in the bandstop filter passband using asynchronous tuning mode. (solid line) After compensation and (dotted line) before compensation.

input phase response of the bandstop filter, which is a very crucial feature for designing filter cascades.

To design the wideband bandpass filter, a mixed electric- and magnetic-field coupling technique is used. For both fabricated prototypes, a bandpass filter with a 3-dB bandwidth of 1.25 GHz at 3.3 GHz is used. The 2-D and 3-D EM models of the bandstop filter, simulated in HFSS, along with the definition of primary dimensions for the case of 2.0%-fractional-bandwidth prototype, are shown in figure 4.12. Table 4.1 summarizes the primary dimensions for this filter. A photograph of the fabricated prototype for the 2.0%-fractional-bandwidth case is shown in figure 4.13. All coupling mechanisms, except the one between resonators 2 and 3, have been implemented using mixed electric- and magnetic-field coupling.

The 0.2%-fractional-bandwidth bandstop filter is also designed and fabricated similarly, except that in this filter, in addition to the coupling between resonators 2 and 3, the coupling between resonators 1 and 2 and also between

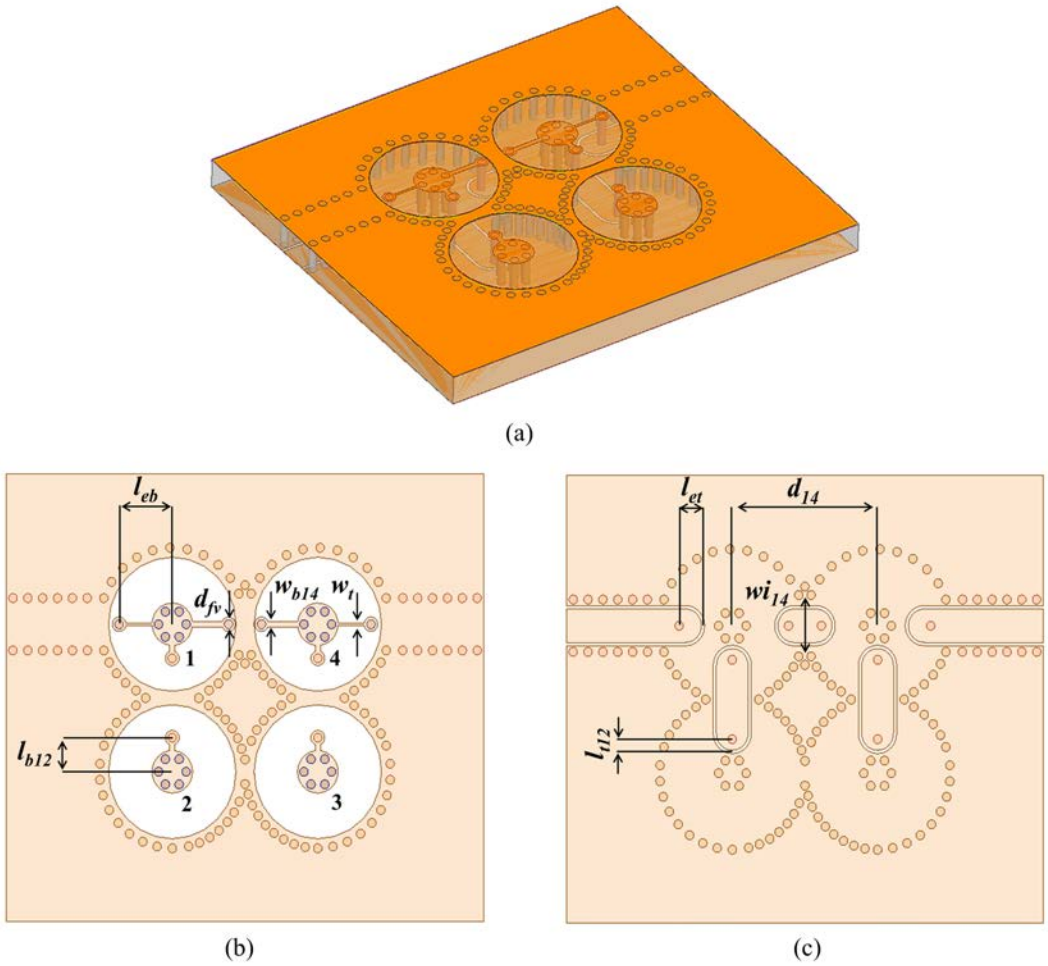

Figure 4.12: Simulated model for the bandstop filter with 10-dB fractional bandwidth of 2.0% at 3.3 GHz. (a) 3-D view, (b) 2-D top view, and (c) 2-D bottom view.

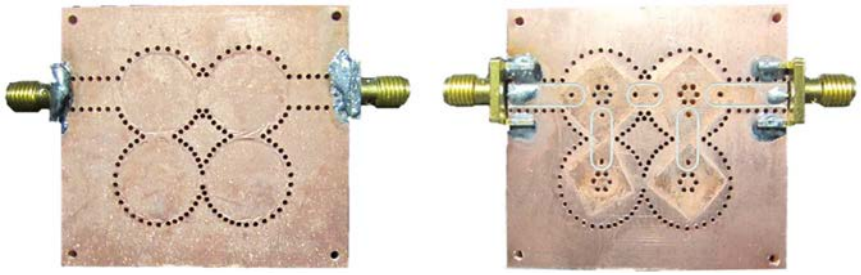

Figure 4.13: Fabricated prototype bandstop filter with 10-dB fractional bandwidth of 2.0% at 3.3 GHz. Filter shown prior to piezoelectric actuator attachment.

Table 4.1: 2.0%-fractional-bandwidth fabricated filter primary dimensions

Design Parameters	**Value**
Iris14 Length $(d_{14} - 2r_o)^{\star}$	0 mm
Iris12 Length $(d_{12} - 2r_o)$	-0.5 mm
Iris23 Length $(d_{23} - 2r_o)$	0 mm
Iris34 Length $(d_{34} - 2r_o)$	-0.5 mm
Iris14 Width (w_{i14})	7.0 mm
Iris12 Width (w_{i12})	5.0 mm
Iris23 Width (w_{i23})	2.2 mm
Iris34 Width (w_{i34})	5.0 mm
Tap-line Width (w_t)	0.25 mm
Bar Width $(w_{b14}, w_{b12}, w_{b23}, w_{b34})$	0.5mm
Feed Via Diameter (d_{fv}) (all vias diameter)	0.8 mm
External Bar Length $(l_{eb})^{\dagger}$	5.0 mm
Bar14 Length (l_{b14})	5.3 mm
Bar12 Length (l_{b12})	3.05 mm
Bar34 Length (l_{b34})	3.05 mm
External GCPW Termination Length $(l_{et})^{*}$	2.25 mm
GCPW Termination14 Length (l_{t14})	1.15 mm
GCPW Termination12 Length (l_{t12})	1.15 mm
GCPW Termination34 Length (l_{t34})	1.15 mm
* d_{xy} is the spacing between the center of resonators and r_o is the cavity radius † All bar lengths are measured from the resonator center to feed via. * The spacing between the center of the semi-circle slot to feed via.	

resonator 3 and 4 are implemented only using magnetic-field coupling. The fabricated 0.2%-fractional-bandwidth prototype is shown in figure 4.14. Different coupling mechanisms between the resonators can be seen by comparing figures 4.13 and 4.14. Additionally, these figures also represent two stages in the fabrication process: 1) prior to attaching the piezoelectric actuators with the laminated copper diaphragm visible and 2) after the piezoelectric actuators attachment.

The coupling matrices for both prototypes were obtained using (4.34) for

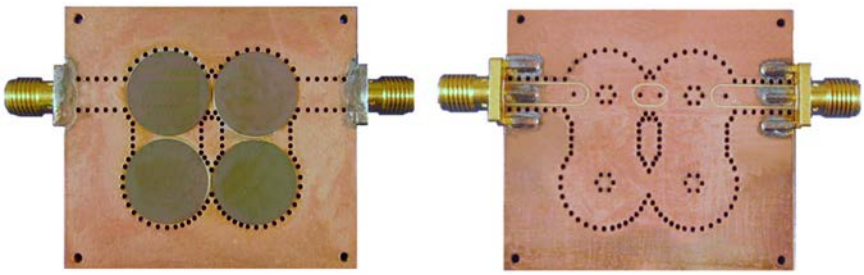

Figure 4.14: Fabricated prototype bandstop filter with 10-dB fractional bandwidth of 0.2% at 3.3 GHz. Filter shown after piezoelectric actuator attachment.

a non-Butterworth filter. For the 0.2%-fractional-bandwidth filter,

$$m'_{S1} = 0.8409, \qquad m'_{12} = 0.0925, \qquad \text{and} \qquad m'_{23} = 0.0121 \tag{4.37}$$

and for the 2.0%-fractional-bandwidth filter

$$m'_{S1} = 0.8409, \qquad m'_{12} = 0.2925, \qquad \text{and} \qquad m'_{23} = 0.1210 \tag{4.38}$$

Weakly coupled cavity resonators are included in the fabrication run in order to characterize the unloaded quality factor. This can be used to include the impact of processing conditions in the EM bandstop filter simulations.

4.3.3 Tunable Bandstop Filter Measurement

The prototype filters were measured using the test setup shown in figure 3.16. For this test, an Agilent Technologies N5222A PNA and four Keithley 2400 Sourcemeters were used. Each power supply was used to bias one of the piezoelectric actuators independently. An unloaded quality factor of 620 at 3.3 GHz was extracted by measuring the transmission response of the weakly coupled cavity resonators. This quality factor value matched well with the

previous experiments and was used in all circuit and full-wave simulations.

Figure 4.15 shows the measured result for the 0.2%-fractional-bandwidth, bandstop filter tuned between 3.0 and 3.6 GHz. When the filter is tuned at 3.0 GHz, the insertion loss from 3.3 to 3.6 GHz ranges from 0.67 to 0.95 dB, respectively. Also when the filter is tuned at 3.6 GHz, the insertion loss from 3.0 to 3.3 GHz ranges from 0.42 to 0.32 dB, respectively. A broader view of the bandstop filter response tuned at 3.3 GHz showing the wideband bandpass filter response is also depicted in figure 4.16. Due to limited bandwidth of the wideband bandpass filter, when the bandstop notch is tuned to one end of the tuning range, the insertion loss of bandstop filter in the other end of the tuning range is increased. Such a case, along with the asynchronous tuning compensation solution, is shown in figure 4.17. The filter has been tuned to 3.0 GHz and the insertion loss at 3.6 GHz has been compensated. This reduces the insertion loss of the filter from 0.95 to 0.29 dB. All the measurements include the loss of two SMA end-launch connectors.

The measured response of the 2%-fractional-bandwidth bandstop filter tuned between 3.0 and 3.6 GHz is shown in figure 4.18. During this measurement, resonators 1 and 4 were synchronously tuned. Figure 4.19 illustrates a comparison between the measured and simulated 10-dB bandwidth of the filter. The measurement exhibits 10-dB bandwidths ranging from 1.92% at 3.0 GHz to 2.04% at 3.6 GHz.

The measured and simulated insertion losses of the bandstop filter, in the passband, 10% away from (above and below) the center frequency of the filter in the desired frequency range from 3.0 to 3.6 GHz, are also shown in figure 4.20. The horizontal axis shows the bandstop center frequency (f_0), while the vertical axes are showing the insertion loss of the filter at $0.9f_0$ and $1.1f_0$.

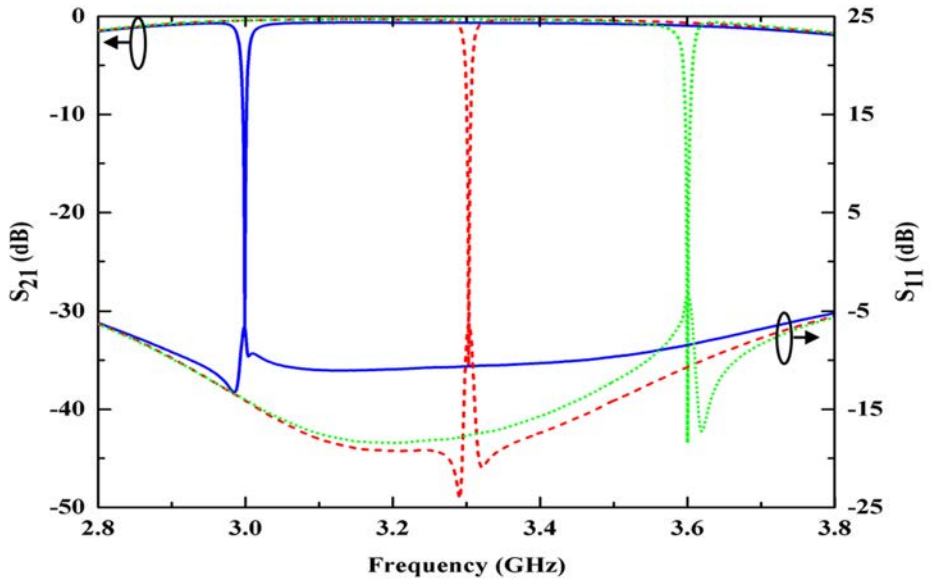

Figure 4.15: Measured response of the 0.2%-fractional-bandwidth bandstop filter tuned between 3.0 and 3.6 GHz.

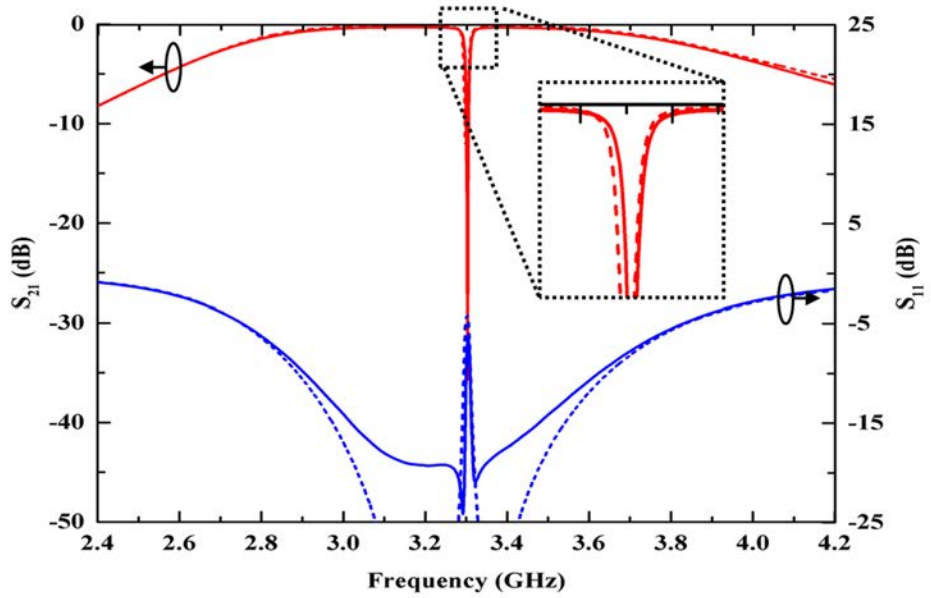

Figure 4.16: Measured versus EM simulated response of the 0.2%-fractional-bandwidth bandstop filter tuned at 3.3 GHz. (solid line) Measurement and (dotted line) simulation.

A passband insertion loss of less than 0.6 dB is guaranteed across the entire range.

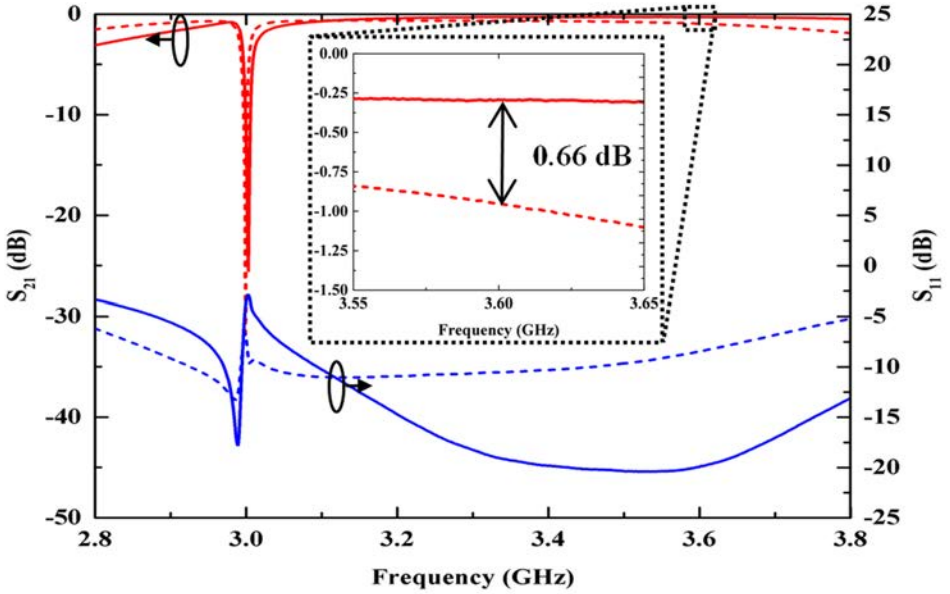

Figure 4.17: Measured result for asynchronous tuning of the 0.2%-fractional-bandwidth bandstop filter tuned at 3.0 GHz to compensate insertion loss at 3.6 GHz. (solid line) After compensation and (dotted line) before compensation.

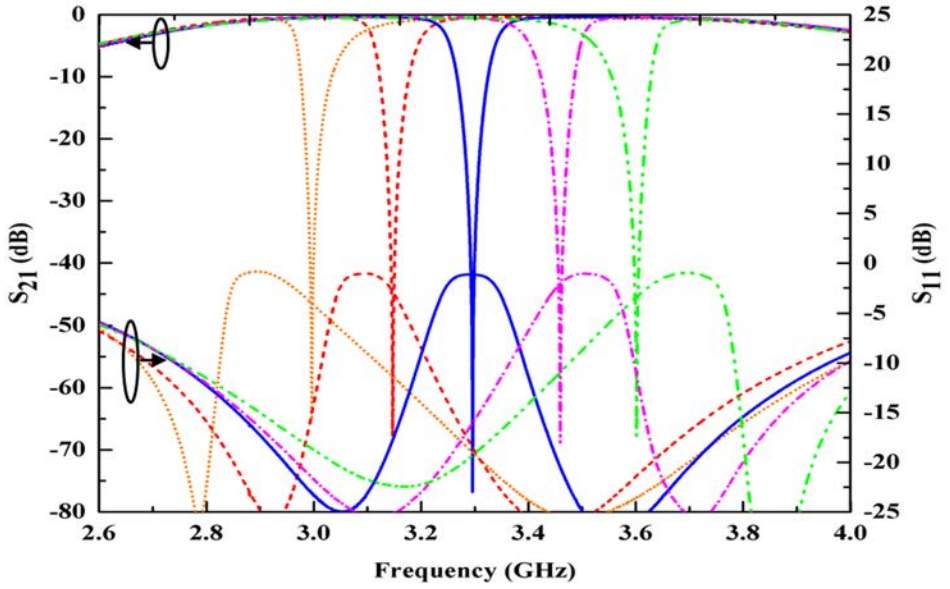

Figure 4.18: Measured response of the 2%-fractional-bandwidth bandstop filter tuned between 3.0 and 3.6 GHz.

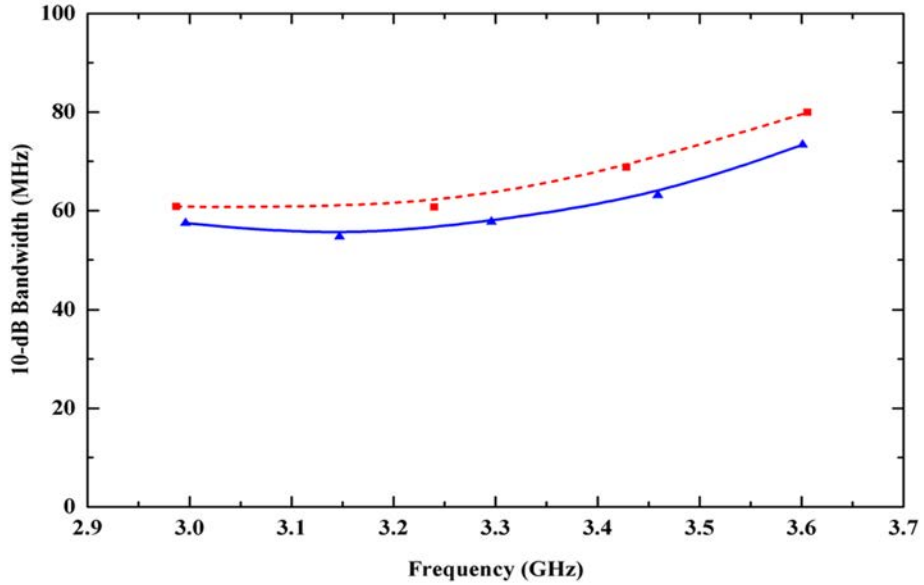

Figure 4.19: Measured versus EM simulated 10-dB bandwidth of the 2%-fractional-bandwidth bandstop filter. (solid line) Measurement and (dotted line) simulation.

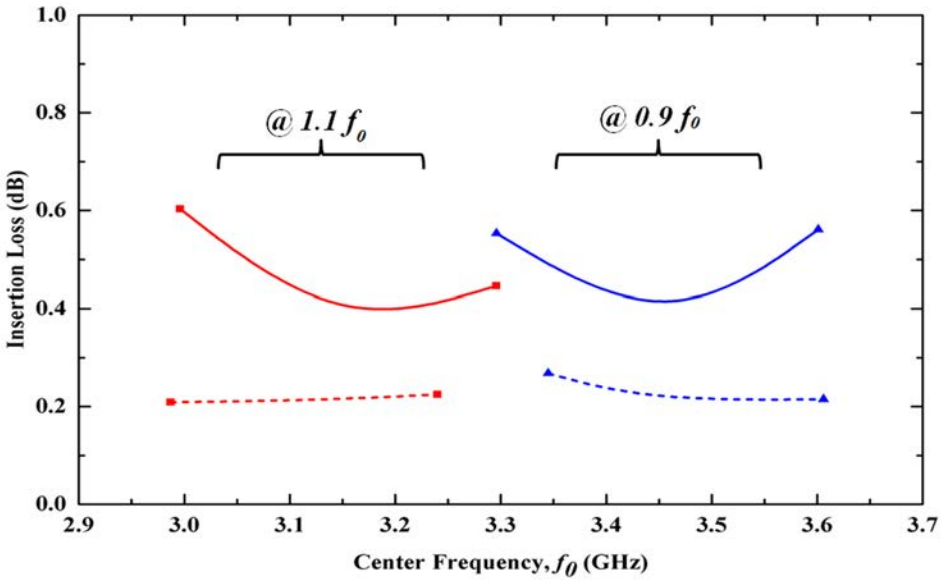

Figure 4.20: Measured versus EM simulated insertion loss of the 2%-fractional-bandwidth bandstop filter at 10% away from the center frequency. (solid line) Measurement and (dotted line) simulation.

In general, there is a good agreement between the measurements and simulations. The slightly higher insertion loss in the measurement can be attributed to the SMA connectors. Also, non-planar movement of the copper membrane on top of cavities and finally fabrication imperfections and tolerances contribute to the slightly narrower bandwidth in comparison to the simulation.

In summary, the theory for a new and elegant synthesis method for bandstop filters has been presented in this chapter. The proposed method utilizes phase cancellation to realize the coupling matrix without source-to-load coupling. Therefore, the same coupling implementation methods used for bandpass filters can be used for designing and implementing bandstop filters. In fact, through the application of this design method, a bandstop filter notch is embedded in the passband of a wideband bandpass filter. The procedure utilizes bandpass filter frequency scaling. This scaling is equivalent to re-synthesis of the coupling matrix when a predefined coupling value is forced into the matrix. The appropriate expressions for calculating the new coupling values are provided. In general, this method can be utilized for scaling coupling matrices with forced values in order to realize filters with practical limitations.

To verify the theory, examples of second-order bandstop filters with 0.2% and 2.0%-fractional-bandwidths in the range of 3.0–3.6 GHz were provided. The prototypes were implemented in single-layer, substrate-integrated, evanescent-mode cavity technology. The proposed design technique eliminates the extra substrate used to form the source-to-load coupling, in previously reported substrate-integrated evanescent-mode cavity bandstop filters. Therefore, bandstop filters can be implemented in the same substrate that is used to realize bandpass filters which gives a compact solution for designing and implementing of filter cascades in substrate-integrated, evanescent-mode cavity technology.

Additionally, asynchronous tuning of the resonators, provides an important feature, not only for insertion loss compensation, but also for control of the input phase response of the bandstop filter. This feature provides a tool for matching bandstop filters to bandpass filters that have been designed individually. Good agreement observed between simulations and measurements confirms the accuracy of the synthesis and design method.

Chapter 5

Bandpass-Bandstop Filter Cascade Design

5.1 Introduction

One of the challenges confronting current and future wireless and microwave systems is spectrum management. Adaptable front-ends, consisting of tunable/reconfigurable filters, can provide dynamic isolation between the desired and interfering signals in a crowded spectrum environment. Concurrent transmit-receive systems, wireless systems in co-site environments, and systems with shared-aperture antennas, are among applications that require a high level of isolation. In these applications, however, conventional bandpass filters or bandstop filters may not be able to provide the required level of isolation, especially when high power transmitters are involved [6]. In such cases, bandpass-bandstop (BP-BS) filter cascades have been shown to be a promising solution. BP-BS filter cascades have the capability of dynamically relocating transmission zeros around the passband. This provides similar functionality as tunable elliptic filters and filters formed by cascaded unit cells or in-line transmission zeros, while maintaining a smaller form factor. Additionally, relocation of the transmission zeros in BP-BS filter cascades does not require manipulating of the inter-resonator coupling coefficients [7], [8].

The idea of a tunable substrate-integrated, high-Q, BP-BS cascade was first introduced in [5] and later developed in [6] and [7]. In the cascades designed in [5]–[7], the bandstop filter uses a different physical structure than the bandpass filter, which requires an extra dielectric layer. Therefore, the filters can not be integrated in a single substrate, which limits the miniaturization of the cascade. Recently, a more integrated cascaded topology was introduced in [8], which utilizes an arbitrary phase-controllable bandstop filter and a complex-load bandpass filter. Although this architecture, when implemented using lumped element components, results in a more compact BP-BS filter cascade, it remains challenging for the miniaturization of substrate-integrated, cascades due to the complex coupling configuration to the output node.

In this chapter, two novel methods for designing BP-BS filter cascades are presented. The first method is based on the direct coupling matrix synthesis of a cascade, while the second one generates the coupling matrix for the cascade through combining the coupling matrices of bandpass and bandstop filters using non-resonating-nodes (NRN). Although the first method results in a compact structure for the cascade, due to requirement of variable coupling, is not suitable for tunable filters. However, the second method allows dynamic tuning of the cascade passband and stopband at any two independent frequencies by tuning the resonators. Using this method, cascades can be designed using direct connection of bandpass and bandstop filters that have been designed independently.

This method is used in a single layer implementation of substrate-integrated, evanescent-mode cavity, tunable filter cascade with fixed couplings. As opposed to the cascades designed in [5]–[7], the proposed method does not include any electrically-long transmission lines between the filters. This eliminates

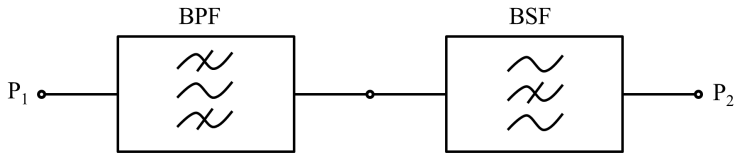

Figure 5.1: Direct connection of a bandpass and a bandstop filter forming a BP-BS filter cascade.

strong frequency dependency in the cascade design enabling the potential of wide tuning range.

5.2 Direct Coupling Matrix Synthesis of BP-BS Filter Cascades

In order to directly synthesize the coupling matrix of BP-BS filter cascades, the rational representation of the filter cascade response, in terms of characteristic polynomials similar to (2.1a) and (2.1b), are required. Assuming a tandem placement of the bandpass filter and the bandstop in the cascade, similar to what is shown in figure 5.1, the two-port reflection and transmission coefficients of the cascade can be written in the form of rational functions using [64],

$$S_{11}^{Cascade} = S_{11}^{BPF} + \frac{S_{12}^{BPF} . S_{11}^{BSF} . S_{21}^{BPF}}{1 - S_{22}^{BPF} . S_{11}^{BSF}} \tag{5.1a}$$

$$S_{12}^{Cascade} = \frac{S_{12}^{BPF} . S_{12}^{BSF}}{1 - S_{22}^{BPF} . S_{11}^{BSF}} \tag{5.1b}$$

$$S_{21}^{Cascade} = \frac{S_{21}^{BPF} . S_{21}^{BSF}}{1 - S_{22}^{BPF} . S_{11}^{BSF}} \tag{5.1c}$$

$$S_{22}^{Cascade} = S_{22}^{BSF} + \frac{S_{21}^{BSF}.\ S_{22}^{BPF}.\ S_{12}^{BSF}}{1 - S_{22}^{BPF}.\ S_{11}^{BSF}} \tag{5.1d}$$

Therefore, when the characteristic polynomials of the bandpass and bandstop filters are known, the cascade can be described in terms of its polynomials, and finally the coupling matrix of the BP-BS filter cascade can be calculated. However, as mentioned in Chapter 2, a bandpass filter and its lowpass prototype have the same coupling matrix. Therefore, it is more convenient to construct the cascade characteristic polynomials in the lowpass domain.

For example, using what has been shown in Chapter 2, for a second order Chebyshev bandpass filter with 20 dB equi-ripple return loss, the lowpass prototype with normalized 20 dB equi-ripple bandwidth at 1 rad/s, can be written as

$$S_{11}^{LPF}(s) = \frac{F^{LPF}(s)}{{\varepsilon_R}^{LPF} E^{LPF}(s)} = \frac{j}{0.201(s^2 + 3s + 5)} \tag{5.2a}$$

$$S_{21}^{LPF}(s) = \frac{P^{LPF}(s)}{\varepsilon^{LPF} E^{LPF}(s)} = \frac{s^2 + 0.5}{(s^2 + 3s + 5)} \tag{5.2b}$$

$$S_{12}^{LPF}(s) = S_{21}^{LPF}(s) \tag{5.2c}$$

$$S_{22}^{LPF}(s) = -S_{11}^{LPF}(s) \tag{5.2d}$$

where in (5.2a) to (5.2d), LPF (lowpass filter) represents the lowpass prototype of the BPF (bandpass filter) in (5.1a) to (5.1d).

For the bandstop filter in (5.1a) to (5.1d), a lowpass prototype is first

synthesized and then is converted to a highpass prototype by swapping its transmission and reflection functions. For a second-order, Butterworth bandstop filter, the highpass prototype with 3-dB normalized bandwidth of 1 rad/s is obtained,

$$S_{11}^{HPF}(s) = \frac{F^{HPF}(s)}{\varepsilon_R{}^{HPF} E^{HPF}(s)} = \frac{js^2}{(s^2 + 1.4142s + 1)} \tag{5.3a}$$

$$S_{21}^{HPF}(s) = \frac{P^{HPF}(s)}{\varepsilon^{HPF} E^{HPF}(s)} = \frac{s^2 + 0.5}{(s^2 + 1.4142s + 1)} \tag{5.3b}$$

$$S_{12}^{HPF}(s) = -S_{21}^{HPF}(s) \tag{5.3c}$$

$$S_{22}^{HPF}(s) = S_{11}^{HPFF}(s) \tag{5.3d}$$

where in (5.3a) to (5.3d) HPF is the highpass prototype of the BSF in (5.1a) to (5.1d).

It is important to notice that for the lowpass prototype $S_{11}^{LPF}(s)$ and $S_{22}^{LPF}(s)$ have 180° phase difference while for the highpass filter this phase difference exist between $S_{21}^{HPF}(s)$ and $S_{12}^{HPF}(s)$. If these phase shifts are neglected in the evaluations of (5.1a) to (5.1d), an unwanted spike in the frequency response of the cascade, around the bandstop filter notch frequency, will occur. This spike is due to mismatch between the filters. To understand the reason for this difference, the two-port network in figure 2.1 is considered. For a passive, lossless, and reciprocal two-port network, the unique unitary conditions require the following relationship between the two-port scattering

parameters [64]

$$\begin{bmatrix} S_{11} & S_{12} \\ S_{21} & S_{22} \end{bmatrix} = \frac{1}{E(s)} \begin{bmatrix} \dfrac{F(s)}{\varepsilon_R} & \dfrac{P(s)}{\varepsilon} \\ \dfrac{P(s)}{\varepsilon} & \dfrac{(-1)^{(N_{fz}+1)} F(s)^*}{\varepsilon_R} \end{bmatrix} \tag{5.4}$$

where N_{fz} is the number of finite-frequency transmission zeros. This relationship for all-pole filters (where there is no finite-frequency transmission zero and all polynomial coefficients are real values) is simplified to

$$\begin{bmatrix} S_{11} & S_{12} \\ S_{21} & S_{22} \end{bmatrix} = \frac{1}{E(s)} \begin{bmatrix} \dfrac{F(s)}{\varepsilon_R} & \dfrac{P(s)}{\varepsilon} \\ \dfrac{P(s)}{\varepsilon} & \dfrac{-F(-s)}{\varepsilon_R} \end{bmatrix} \tag{5.5}$$

Since, the polynomials for the highpass prototype are obtained using swapping the transmission and reflection functions of an original lowpass prototype, then the phase shift between the $S_{11}^{LPF}(s)$ and $S_{22}^{LPF}(s)$ of the lowpass prototype is transferred to the phase shift between $S_{21}^{HPF}(s)$ and $S_{12}^{HPF}(s)$ of the highpass prototype.

By plugging (5.2a) to (5.3d) back to (5.1a) to (5.1d), the rational expressions for the filter cascade response can be found. However, evaluating of (5.1a), due to one additional term compared to (5.1b), will not yield a common denominator for both $S_{11}^{Cascade}(s)$ and $S_{21}^{Cascade}(s)$. But, further investigation shows that the additional term in (5.1a) generates two extra poles exactly at the locations of the two transmission zeros. Therefore, they can be removed without any effect on the frequency response of the cascade. This gives the final polynomial-rational representation of the $S_{11}^{Cascade}(s)$ and $S_{21}^{Cascade}(s)$

with a common denominator. For the previous example, assuming that in the normalized lowpass frequency domain, the lowpass prototype is tuned at $\omega_{BP} = 5$ rad/s and the highpass prototype is tuned at $\omega_{BS} = 20$ rad/s, the reflection and transmission functions can be written as

$$S_{11}^{Cascade}(s) = \frac{F^{Cascade}(s)}{\varepsilon_R{}^{Cascade} E^{Cascade}(s)} \tag{5.6a}$$

$$= \frac{\left(s^4 + (1.4 - 50j)s^3 + (-822.5 - 42.4)s^2 + (-320.5 + 496j)s + (975.55 + 708j)\right)}{0.201\,(s^4 + (4.4 - 50j)s^3 + (-813.8 - 177.4j)s^2 + (-210.81 + 467.39i)s + (753.12 + 655.07j))}$$

$$S_{21}^{Cascade}(s) = \frac{P^{Cascade}(s)}{\varepsilon^{Cascade} E^{Cascade}(s)} \tag{5.6b}$$

$$= \frac{s^2 - 40s - 400}{(s^4 + (4.4 - 50j)s^3 + (-813.8 - 177.4j)s^2 + (-210.81 + 467.39j)s + (753.12 + 655.07j))}$$

It can be seen that the coefficients of the polynomials are not real numbers any more. This is because the cascade response does have not a symmetric frequency response. The frequency response of an ideal synthesized BP-BS cascade, found from this analysis, is shown in figure 5.2.

Next, either the element extraction method or the coupling matrix synthesis method is applied to the rational representation of the filter cascade, in order to complete the synthesis procedure [64]. The coupling matrix of the filter cascade in the above example, arranged in the form of a folded fully-canonical structure, is found to be,

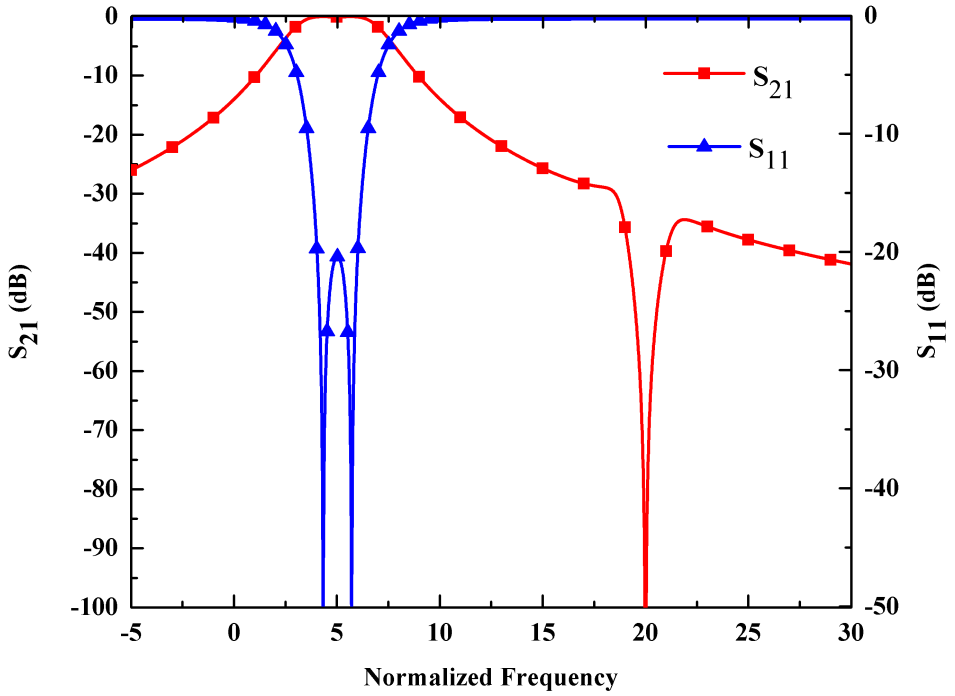

Figure 5.2: Frequency response of a second order Chebyshev bandpass filter cascaded with a second order Butterworth bandstop filter.

$$M_1 = \begin{bmatrix} 0.0000 & 1.2247 & 0.0000 & 0.0000 & 0.0000 & 0.0000 \\ 1.2247 & -5.0000 & 1.1552 & 0.0000 & -1.1897 & 0.0000 \\ 0.0000 & 1.1552 & -12.7208 & 0.0000 & -7.4967 & 0.0000 \\ 0.0000 & 0.0000 & 0.0000 & -20.0000 & 2.0301 & 0.0000 \\ 0.0000 & -1.1897 & -7.4967 & 2.0301 & -12.2792 & 1.7071 \\ 0.0000 & 0.0000 & 0.0000 & 0.0000 & 1.7071 & 0.0000 \end{bmatrix} \tag{5.7}$$

Due to the asymmetric frequency response of the filter cascade, the resonators need to be tuned asynchronously. In this example, if the bandpass filter is tuned to $\omega_{BP} = 10$ rad/sec, the coupling matrix will be changed to,

$$M_1 = \begin{bmatrix} 0.0000 & 1.2247 & 0.0000 & 0.0000 & 0.0000 & 0.0000 \\ 1.2247 & -10.0000 & 1.1552 & 0.0000 & -1.1897 & 0.0000 \\ 0.0000 & 1.1552 & -15.1472 & 0.0000 & -4.9978 & 0.0000 \\ 0.0000 & 0.0000 & 0.0000 & -20.0000 & 2.0301 & 0.0000 \\ 0.0000 & -1.1897 & -4.9978 & 2.0301 & -14.8528 & 1.7071 \\ 0.0000 & 0.0000 & 0.0000 & 0.0000 & 1.7071 & 0.0000 \end{bmatrix} \tag{5.8}$$

In the other case, if the bandpass filter is tuned back again to $\omega_{BP} = 5$ rad/s and the bandstop filter tuned to $\omega_{BS} = 15$ rad/s, the coupling matrix is changed to,

$$M_1 = \begin{bmatrix} 0.0000 & 1.2247 & 0.0000 & 0.0000 & 0.0000 & 0.0000 \\ 1.2247 & -5.0000 & 1.1552 & 0.0000 & -1.1897 & 0.0000 \\ 0.0000 & 1.1552 & -10.1472 & 0.0000 & -4.9978 & 0.0000 \\ 0.0000 & 0.0000 & 0.0000 & -15.0000 & 2.0301 & 0.0000 \\ 0.0000 & -1.1897 & -4.9978 & 2.0301 & -9.8528 & 1.7071 \\ 0.0000 & 0.0000 & 0.0000 & 0.0000 & 1.7071 & 0.0000 \end{bmatrix} \tag{5.9}$$

The coupling-routing diagram of the cascade, extracted from the coupling matrix, is shown in figure 5.3. Investigation of the coupling matrices and the coupling-routing diagram reveals that tunable coupling is neccessary to achieve tunable passband and stopband. In general, some properties of the cascade coupling matrix can be listed as,

- $M_{11} = -\omega_{BP}$
- $M_{33} = -\omega_{BS}$

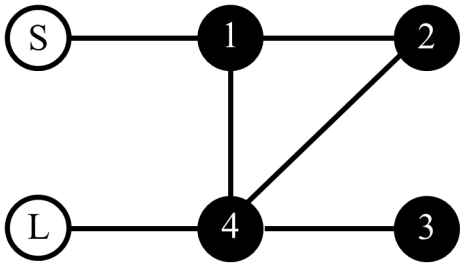

Figure 5.3: Coupling routing diagram of a second order Chebyshev bandpass filter cascaded with a second order Butterworth bandstop filter.

- $M_{22} \approx -\frac{1}{2}(\omega_{BP} + \omega_{BS})$
- $M_{44} \approx -\frac{1}{2}(\omega_{BP} + \omega_{BS})$
- $M_{22} \neq M_{44}$
- $M_{11} + M_{33} = M_{22} + M_{44}$
- $M_{24} = M_{42} \approx \pm\frac{1}{2}|\omega_{BS} - \omega_{BP}|$ with the opposite sign of M_{11}
- $M_{24} + M_{42} \approx -(M_{11} + M_{22} + M_{33} + M_{44})$ when ω_{BP} and ω_{BS} have opposite signs.
- $M_{24} + M_{42} \approx -\frac{1}{4}(M_{11} + M_{22} + M_{33} + M_{44})$ when ω_{BP} and ω_{BS} have the same signs.
- The rest of couplings are fixed and are determined using the specifications of the bandpass and bandstop filters.

This filter cascade utilizes two cross-couplings in order to implement two transmission zeros. The filter cascade uses four resonators and compared to the bandstop filter designed in Chapter 4, that uses four resonators for implementation of a bandstop filter, is assumed to be a compact filter cascade implementation. Also, it does not include any direct source-to-coupling, which

makes the fabrication process much simpler. However, as mentioned above, it needs tunable coupling. The designed cascade requires variable couplings for the sake of frequency tuning. The implementation of variable couplings, especially for wideband applications, is not an easy task. The other problem associated with this design is the number of couplings linked to resonator 4, which again makes the implementation of the filter difficult. Nevertheless, this design may be used for realization of fixed-frequency filter cascades.

5.3 Bandpass-Bandstop Filter Cascade Design Using Non-Resonating-Node

A conventional approach in designing complex filters consists of a modular design, in which separate building blocks are utilized to generate and control specific portions of the desired frequency response [129]. A relatively new building block in modular filter design is called a non-resonating-node (NRN) [130], [131]. NRNs can be utilized to design fully-canonical filters without source-to-load coupling. NRNs facilitate complex filter implementations through cascaded sub-blocks. Inserting NRNs between different building blocks, allows for separate design of the individual elements that are then combined, with minor adjustments to make the final filter.

An NRN is modeled by a shunt frequency invariant susceptance, B_{NRN}, in the lumped element representation of the filter. With this susceptance the level of the inverters between two building blocks can be adjusted in order to facilitate the filter implementation. The value of this susceptance can be zero, in which case the inserted internal inverter between two NRNs is one ($J = 1$), that has a practical advantage in filter realization [130]. This condition can be implemented using a uniform section of transmission line, which is quarter-

wavelength long at the filter center frequency. When the susceptance is not zero, the NRN can be realized using a strongly detuned resonator (either capacitive or inductive), a section below cutoff frequency (iris), or an inductive post. In practice, having a good approximation for the frequency invariant susceptance of the NRN, is required when it varies slowly with frequency.

In general, the extraction of the coupling matrix and the implementation of it, for a network that contains both resonating and non-resonating-nodes, is identical to the standard synthesis and implementation methods that are used for regular coupled-resonator filters. However, one of the benefits of using NRNs in filter design is that it enables modular design of filter coupling matrices, using the coupling matrices of individual building blocks. This technique is used in this section to design a BP-BS cascade.

Figure 5.4 shows three different topologies that can be used to design and implement tunable, substrate-integrated, BP-BS filter cascades. In all three topologies, bandpass and bandstop filters have been designed separately and connected together to form the cascade. The bandstop filters in figure 5.4(a) and figure 5.4(b), similar to conventional designs, contain source-to-load coupling. Therefore, when implemented in substrate-integrated waveguide technology, they require two substrates. As shown in Chapter 4, one of the substrates is utilized for implementing the resonators and the other one is used to realize the source-to-load coupling and simultaneously couple to the resonators. But the bandstop filter in figure 5.4(c) uses the single layer substrate-integrated bandstop filter designed in Chapter 4. The filters as well as the other building blocks in the figure, are highlighted using different colors. The coupling-routing diagram in figure 5.4(a) uses a half-wavelength transmission line between the bandpass and bandstop filters to realize three NRNs [6]. This transmission

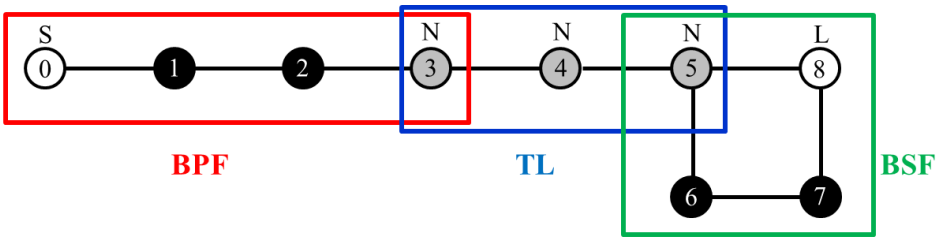

(a)

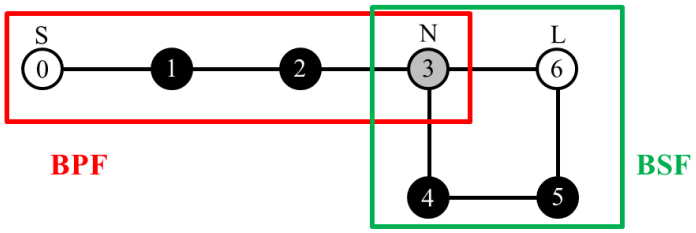

(b)

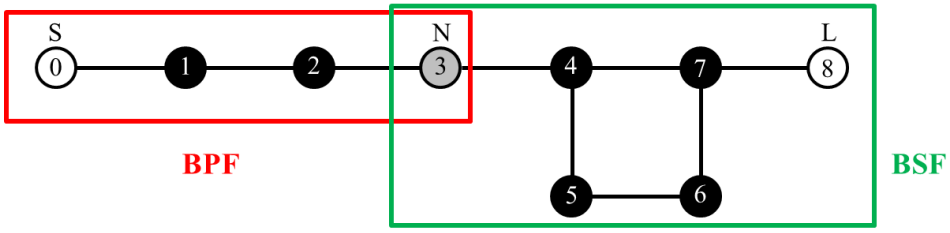

(c)

Figure 5.4: Coupling-routing diagram for three different filter cascades, (a) using three NRNs, (b) using one NRN requiring NRN-to-Load coupling, and (c) using one NRN with no NRN-to-Load coupling.

line not only connects two filters with different physical structures, but is also used to match the two filters. A picture of a typical BP-BS filter cascade, designed and implemented using an inter-filter transmission line in S-band (around 3.0 GHz), is shown in figure 5.5. The filters are connected together using an SMA-to-SMA adapter. Integration of the filters on the same substrate, is a very demanding task. Because, as the coupling-routing diagram of

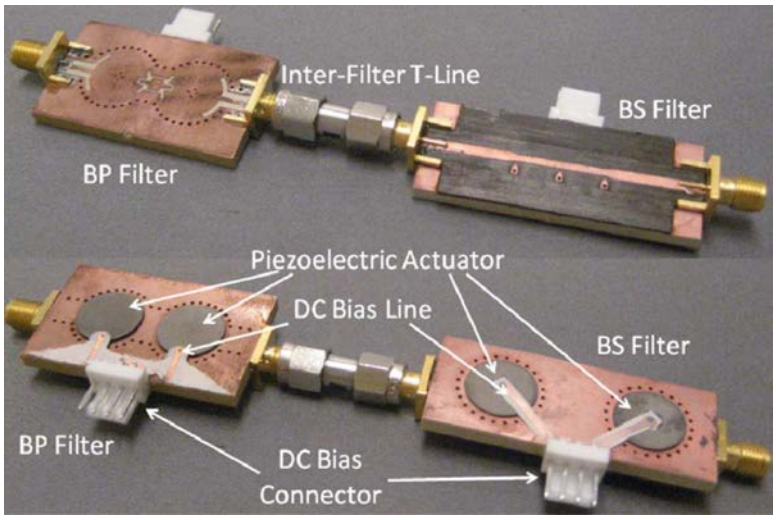

Figure 5.5: Substrate-integrated, evanescent-mode cavity bandpass and band-stop filters connected by an SMA-to-SMA, inter-filter, transmission line (adapter) to form a BP-BS cascade (from [6]).

the cascade shows, it requires coupling between the load and one of the NRNs.

Using this method, re-synthesis of cascade coupling matrices can be achieved by combining individual filter coupling matrices. The coupling matrix for this structure can be written as

$$M_{BP-BS\ (1)} = \begin{bmatrix} 0 & M_{01} & 0 & 0 & 0 & 0 & 0 & 0 & 0 \\ M_{01} & M_{11} & M_{12} & 0 & 0 & 0 & 0 & 0 & 0 \\ 0 & M_{12} & M_{22} & M_{23} & 0 & 0 & 0 & 0 & 0 \\ 0 & 0 & M_{23} & 0 & 1 & 0 & 0 & 0 & 0 \\ 0 & 0 & 0 & 1 & 0 & 1 & 0 & 0 & 0 \\ 0 & 0 & 0 & 0 & 1 & 0 & M_{56} & 0 & M_{58} \\ 0 & 0 & 0 & 0 & 0 & M_{56} & M_{66} & M_{67} & 0 \\ 0 & 0 & 0 & 0 & 0 & 0 & M_{67} & M_{77} & M_{78} \\ 0 & 0 & 0 & 0 & 0 & M_{58} & 0 & M_{78} & 0 \end{bmatrix} \tag{5.10}$$

where the unity elements in the matrix represent the half-wavelength transmission line (which has been decomposed into two quarter-wavelength transmission lines placed in tandem). Modular composition of the coupling matrix can be understood from the color-coded representation of the filter coupling-routing diagram in figure 5.4 and comparing that to the coupling matrix.

However, the frequency dependency of the transmission line results in spurious peaks at certain frequencies, which are due to the parasitic resonances of the transmission line when the bandstop filter is tuned. Additionally, utilizing a half-wavelength transmission line, increases the size of the filter cascade [6].

If one of the NRNs is eliminated, the length of transmission line will be reduced to a quarter of a wavelength. However, this action not only limits the operating frequency range of the cascade, but will also generate unwanted peaks at the operating frequency of the bandstop filter, regardless of the resonant frequency of the bandpass filter. Again, this behavior is the result of the resonance in the inter-filter transmission line terminated by different loads.

Extension of this analysis shows that the generation of the unwanted peaks is not limited to the case of BP-BS cascades; it is also seen in bandpass-bandpass and bandstop-bandstop cascades. In general, the insertion of a quarter wavelength transmission line, between any two filters, severely affects the input/output impedance-phase-relationship between the filters and causes the unwanted spikes in the cascade response.

In order to design a more compact BP-BS filter cascade, with no parasitic resonances, the routing diagram in figure 5.4(b) was introduced in [8]. The cascade is designed by eliminating the electrically-long transmission line and merging the three NRNs using a new coupling-matrix-based approach. The

general form of the coupling matrix for this topology is given by

$$M_{BP-BS\ (2)} = \begin{bmatrix} 0 & M_{01} & 0 & 0 & 0 & 0 & 0 \\ M_{01} & M_{11} & M_{12} & 0 & 0 & 0 & 0 \\ 0 & M_{12} & M_{22} & M_{23} & 0 & 0 & 0 \\ 0 & 0 & M_{23} & 0 & M_{34} & 0 & M_{36} \\ 0 & 0 & 0 & M_{34} & M_{44} & M_{45} & 0 \\ 0 & 0 & 0 & 0 & M_{45} & M_{55} & M_{56} \\ 0 & 0 & 0 & M_{36} & 0 & M_{56} & 0 \end{bmatrix} \tag{5.11}$$

This coupling matrix shows that by eliminating the connection between two NRNs, the benefits of the cascade are maintained and the design method is simplified. Similar to the previous case, the color coding convention, used to represent the filter topology and the coupling matrix, aids in distinguishing between the modular structure of the cascade.

For any pre-determined bandstop filter coupling-routing diagram, several designs with different coupling values can be found that generates the same amplitude-frequency responses with different phase-frequency responses [70]. It was shown in [70] that when the bandpass filter is designed, only a bandstop filter with specific properties, that provides the proper phase-impedance-relationship between the filters, can create a desirable cascade frequency response. A picture of a sample, low-Q, lumped-element, BP-BS filter cascade, implemented using this coupling-routing diagram at UHF band (around 300 MHz), is shown in figure 5.6. It can be seen that a compact BP-BS filter cascade can be achieved when it is implemented using lumped element components.

In general this method requires re-synthesis of the bandpass and bandstop

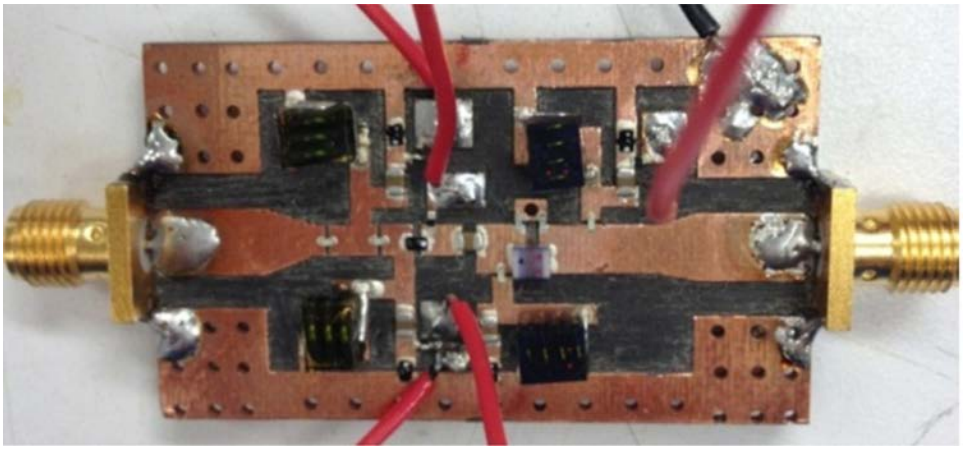

Figure 5.6: Lumped element BP-BS cascade (from [8]).

filters with proper input/output impedance-phase-relationship, which results in simpler and more compact cascades with improved performance compared to the topology in figure 5.4(a) [8]. However, this topology still employs a load-to-NRN coupling that limits the implementation of filter cascades using distributed technology such as substrate-integrated waveguide.

Figure 5.4(c) shows a new cascade topology with a single NRN, but without any direct coupling between the load and the NRN. The bandstop filter in this topology utilizes two extra resonators to provide a second signal path to realize a notch through phase cancellation. More details about the synthesis of the coupling matrix and the design of the bandstop filter has been presented in Chapter 4. A typical coupling matrix for this cascade, shown in (5.12a), is directly constructed from incorporating the coupling matrices of the individual bandpass and bandstop filters.

$$M_{BP-BS\ (3)} = \tag{5.12a}$$

$$
\begin{bmatrix}
0 & 0.8409 & 0 & 0 & 0 & 0 & 0 & 0 & 0 \\
0.8409 & f_{01,BP} & 0.7071 & 0 & 0 & 0 & 0 & 0 & 0 \\
0 & 0.7071 & f_{02,BP} & 0.8409 & 0 & 0 & 0 & 0 & 0 \\
0 & 0 & 0.8409 & 0 & 0.8409\sqrt{\omega_{c,BS}} & 0 & 0 & 0 & 0 \\
0 & 0 & 0 & 0.8409\sqrt{\omega_{c,BS}} & f'_{01,BS} & 0.1720\ \omega_{c,BS} & 0 & 0.7071\ \omega_{c,BS} & 0 \\
0 & 0 & 0 & 0 & 0.1720\ \omega_{c,BS} & f_{01,BS} & 0.0418\ \omega_{c,BS} & 0 & 0 \\
0 & 0 & 0 & 0 & 0 & 0.0418\ \omega_{c,BS} & f_{02,BS} & 0.1720\ \omega_{c,BS} & 0 \\
0 & 0 & 0 & 0 & 0.7071\ \omega_{c,BS} & 0 & 0.1720\ \omega_{c,BS} & f'_{02,BS} & 0.8409\sqrt{\omega_{c,BS}} \\
0 & 0 & 0 & 0 & 0 & 0 & 0 & 0.8409\sqrt{\omega_{c,BS}} & 0
\end{bmatrix}
$$

In this coupling matrix, $\omega_{c,BS}$ is the bandstop corner frequency compared to the normalized bandpass filter and diagonal elements represent the resonant frequencies of the bandpass and bandstop resonators.

In (5.12a), the previously designed bandpass and bandstop filters from Chapter 3 and Chapter 4 were used. Because the coupling matrix does not include any load-to-NRN coupling, both filters can be readily implemented using a single substrate. Ideally, a transmission line with zero-degree electrical length is required to implement a NRN without any frequency dependency. Therefore, the cascade can be formed modularly by bringing the first and last resonators of the bandpass and bandstop filters together. However, by doing this, a new physical coupling is introduced between the resonators that will disrupt the previously designed coupling. Therefore, in practice, an electrically short transmission line –on the order of $\lambda/20$ where λ is the wavelength at the bandstop filter center frequency– must be used to prevent strong interaction between the resonators.

As discussed in [6] and [8], a cascade without a spurious response can be designed only if a proper phase relationship between the two filters is met. In the topology in figure 5.4(c), the extra resonators in the bandstop filter (resonators 4 and 7 in the direct path) are used to control the phase relationship between the filters, while the notch frequency is determined by the other two resonators (resonators 5 and 6 in the indirect path).

Figure 5.7 shows the input/output impedance of both the bandpass and

bandstop filters. The bandpass filter is matched to the system characteristic impedance (50 Ω here), at the center frequency. The output impedance of the bandpass filter is capacitive below the resonant frequency and inductive above the resonant frequency. This implies that different matching conditions, below or above the center frequency, are required. When all four bandstop filter resonators are synchronously tuned, the input impedance of the bandstop filter is effectively a short circuit, seen on the left side of the Smith chart. Tuning the extra resonators in the direct path to a higher or lower frequency, than the notch frequency, results in capacitive and inductive input impedance, respectively. This means that without changing the center frequency of the bandstop filter, its input impedance can be dynamically adjusted to provide the best matching condition between the filters. This is a feature of the bandstop filter that was discussed in Chapter 4, and is called asynchronous tuning mode. The asynchronous tuning of the resonators changes the location of the reflection zeros in the bandstop filter and consequently, can be used for either insertion loss compensation in the passband of bandstop filter or providing the required matching condition for the load, that is the bandpass filter in this case. Therefore, this feature can be used to maintain good matching between the filters over a wide frequency range; enabling cascade designs with minimum mismatch loss and no spurious peaks.

5.3.1 Tunable BP-BS Filter Cascade Measurement

To verify the practical feasibility of the proposed method, a filter cascade in the range from 3.0 to 3.6 GHz was designed and fabricated. To this end, the second-order, Butterworth, bandpass filter, with 4% fractional bandwidth, and the second-order, Butterworth, bandstop filter, with 2% 10-dB fractional

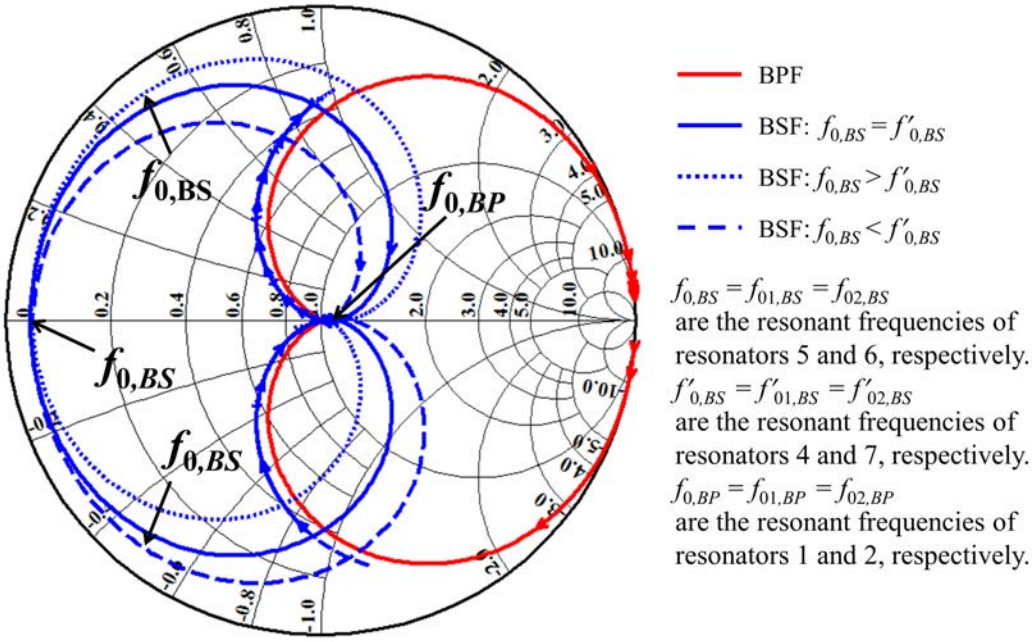

Figure 5.7: Frequency response for the output impedance (S_{22}, red) of the bandpass filter and input impedance (S_{11}, blue) of bandstop in the proposed cascade.

bandwidth, which have been individually designed, are used. Details on the bandpass and bandstop filter designs are found in Chapter 3 and Chapter 4, respectively. The filters are directly connected using a 2.7-mm-long, grounded coplanar waveguide transmission line. This transmission line is smaller than $\lambda/20$ at the highest frequency. The reference planes for the beginning and end of the transmission line (which forms the NRN) were chosen to be at the circumferences of resonators 2 and 4 [130]. Similar to the individual filters, the cascade is also implemented in a Rogers TMM3 substrate with the thickness of 3.175 mm. The layer-by-layer structure of the cascade is shown in figure 5.8. Six piezoelectric actuators are mounted on top of the resonators and are used to tune the filter cascade. A photograph of the fabricated filter cascade is shown in figure 5.9. For quality control purpose a separate weakly-coupled resonator is included in the fabrication run to extract the unloaded quality

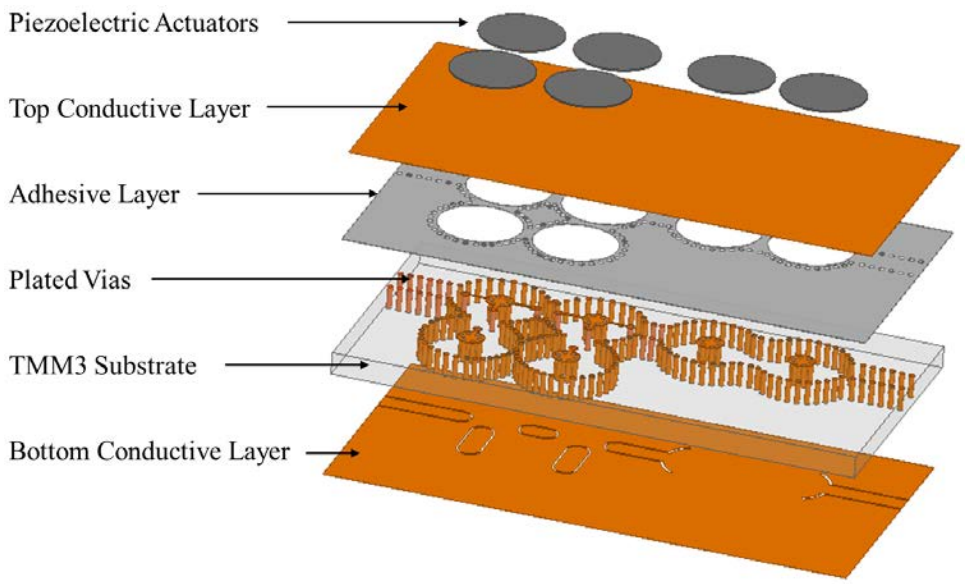

Figure 5.8: Structure of the proposed BP-BS filter cascade, implemented using evanescent-mode cavity resonators in a single substrate.

factor of the resonators. The measurement shows that the resonators have an unloaded quality factor of 620, which is in a good agreement with the previous experiments.

A photograph of the test setup used to measure the fabricated filter cascade is shown in figure 5.10. Figure 5.11 shows the measured response of the cascade tuned to two different states. The measured insertion loss is as low as 0.9 dB in the passband and the rejection is as high as 95 dB in the stopband, which meets the research objectives. The passband return loss, as low as 25 dB, shows that good matching between the filters is achieved. A comparison between the synthesis, the EM simulation (from HFSS), and the measured results is shown in the figure 5.12. All three results are in good agreement.

Measured 20-dB spurious-free range of up to 26.5 GHz is shown in figure 5.13. It can be seen the fabricated BP-BS filter cascade provides a very wide spurious-free range. In figures 5.14(a) to 5.14(d), the most important frequency responses of the cascade are shown, where the passband and stopband

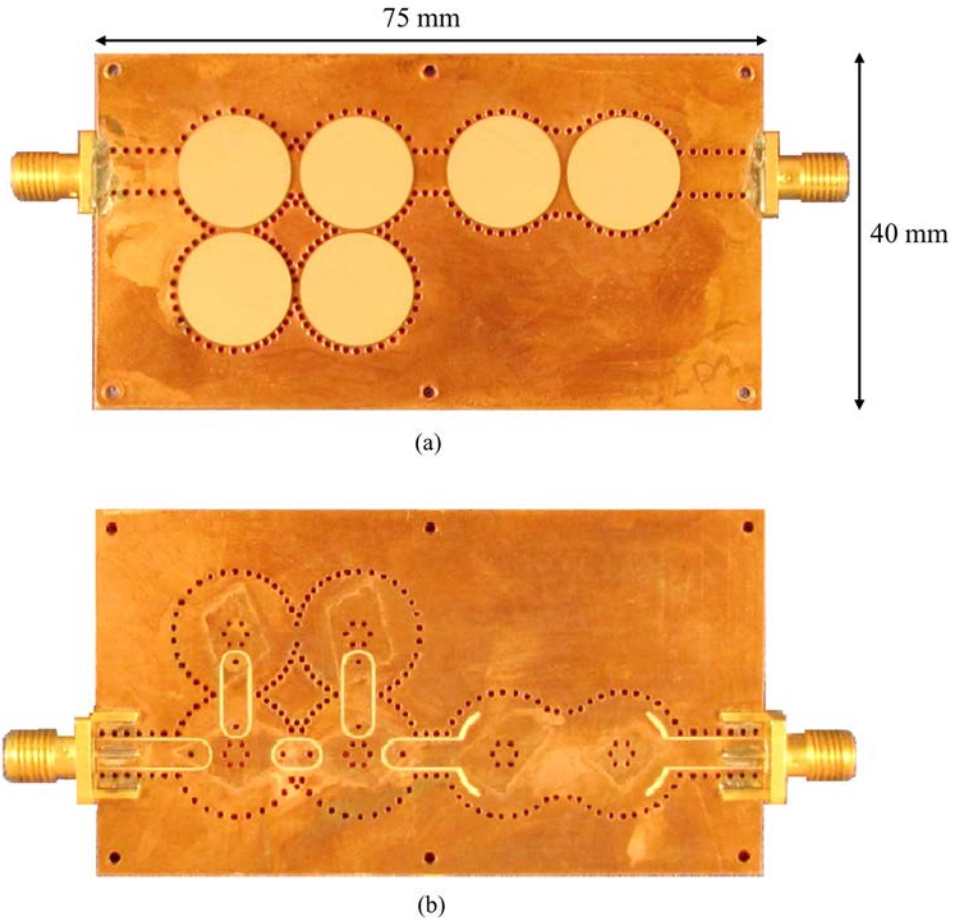

Figure 5.9: Fabricated prototype of the proposed BP-BS filter cascade, (a) top view, (b) bottom view.

are dynamically tuned to any two independent frequencies within the desired frequency range. In figure 5.14(a,b), the bandpass filter is swept within the desired frequency range while the bandstop filter is at a fixed frequency 10% away from the passband. In figure 5.14(a), the passband is placed below the stopband transmission zero, and in figure 5.14(b) the passband is tuned to higher frequencies than the transmission zeros. The same procedure is repeated in figure 5.14(c,d), except that the roles of the bandpass and bandstop filters are interchanged. Isolation as high as 100 dB between the passband and stopband is observed. This figure demonstrate the capabilities of the cascade,

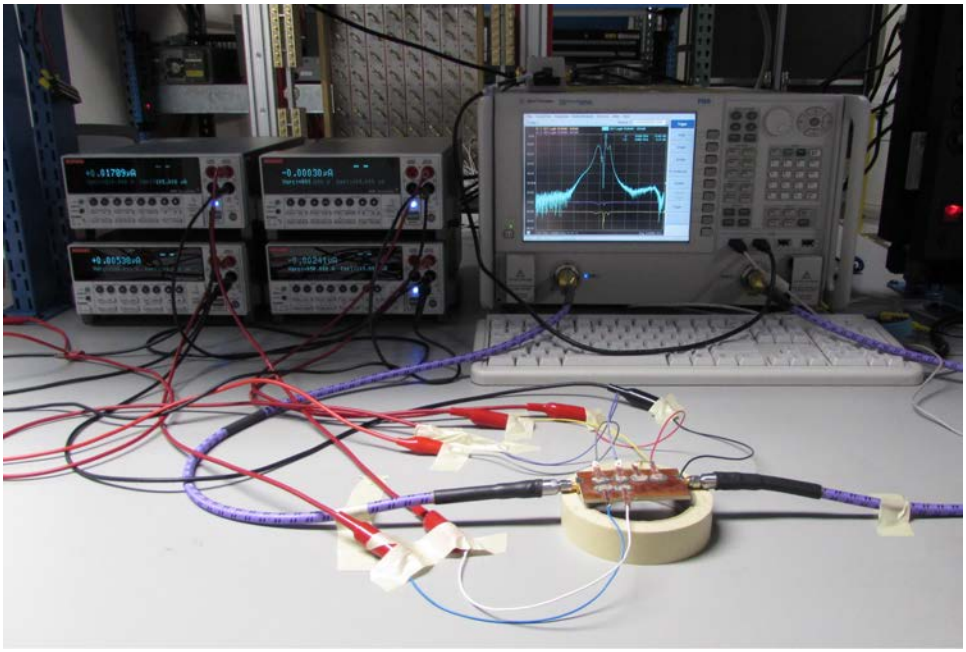

Figure 5.10: A photograph of the test setup used to measure the BP-BS filter cascade.

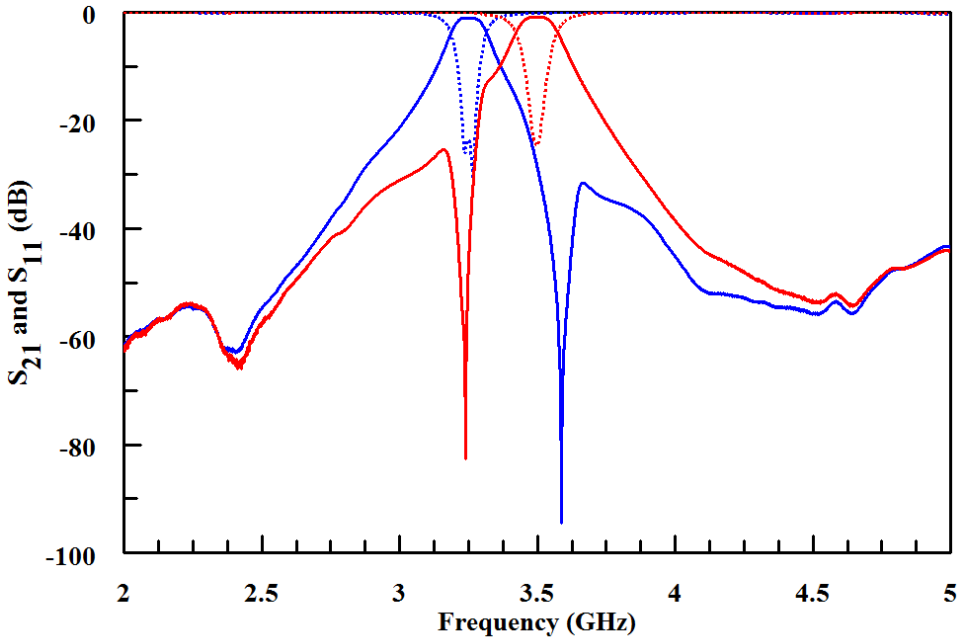

Figure 5.11: Measured frequency response of the proposed BP-BS filter cascade tuned to two different states.

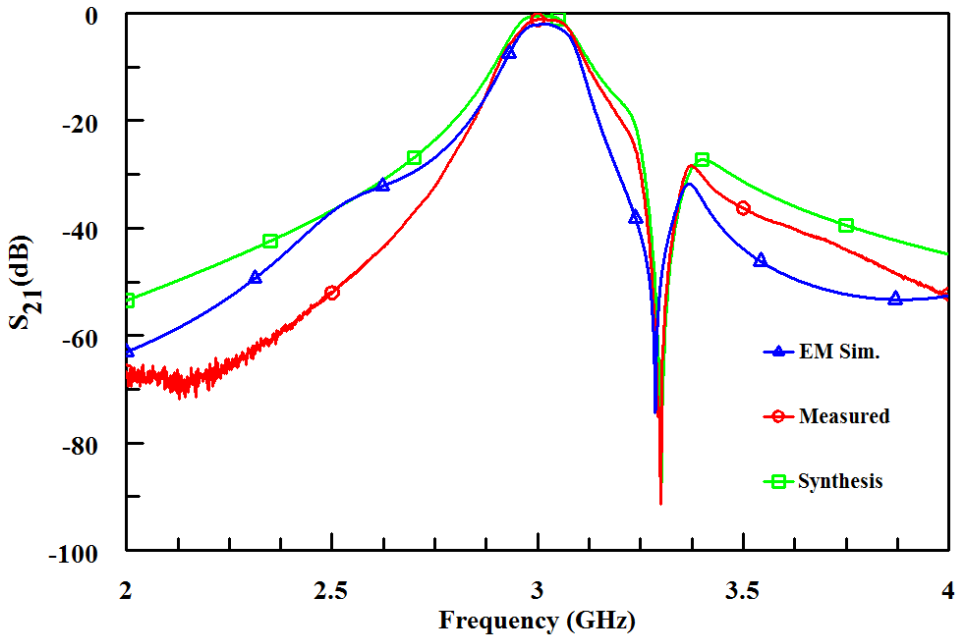

Figure 5.12: Comparison between the BP-BS frequency response results found from synthesis, EM simulation, and measurement.

in terms of providing dynamic relocation of the transmission zeros around the tunable transmission poles.

To increase the selectivity of the bandpass filter, transmission zeros provided by the bandstop filter can be split and be tuned to both sides of the passband. Measured results of that arrangement, with three configurations of transmission zeros, are shown in figure 5.15. This figure shows how the tunable BP-BS filter cascade can be used to arrange the transmission zeros in a psudo-elliptic responses as well as dynamically change their positions to manipulate the rejection of the filter. This flexibility is solely provided by the tuning the resonators without any change in the coupling structures. This feature can not be achieved in elliptic filter unless the coupling structures are variable.

In summary, the proposed filter cascade provides symmetric and asymmetric frequency responses via dynamic relocating of two transmission zeros

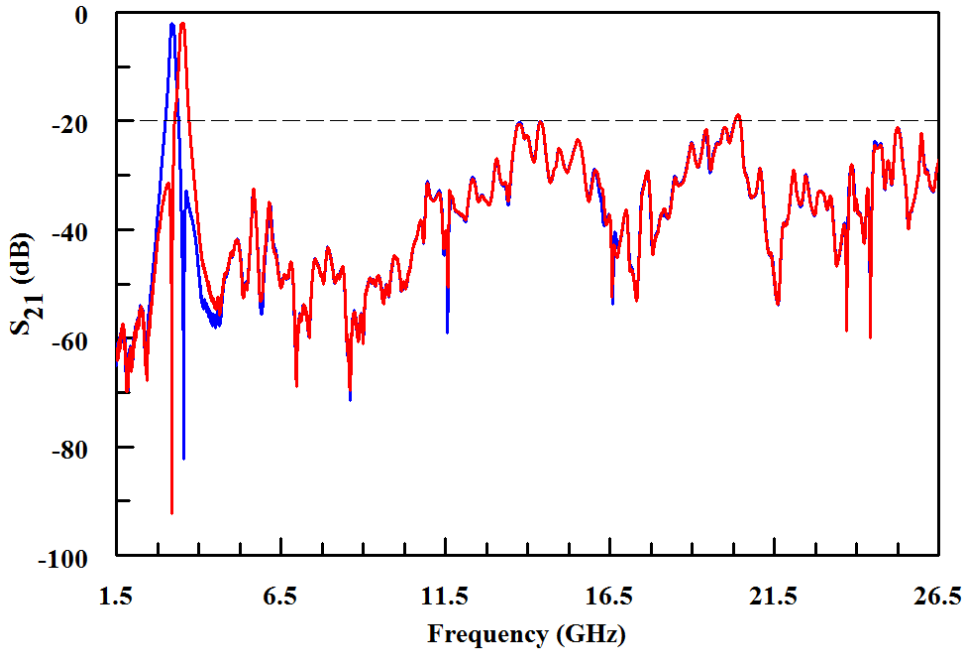

Figure 5.13: Measured wideband frequency response of the BP-BS filter cascade.

around two tunable transmission poles. One of the important features of the proposed method is that the cascade is designed modularly, by direct connection of the previously designed bandpass and bandstop filters, using a non-resonating-node. Additional resonators in the bandstop filter are used to control the phase response of the bandstop filter input impedance, to match the bandpass filter, eliminating any spurious responses. This method does not contain any load-to-NRN coupling and therefore, can be readily used for the implementation of substrate-integrated, filter cascades.

Based on the proposed method, a tunable filter cascade in the range from 3.0 to 3.6 GHz using substrate-integrated, evanescent-mode, cavity resonator is designed, fabricated, and tested as a proof of concept. The BP-BS filter cascade has insertion loss as low as 0.9 dB and isolation up to 100 dB. Measured results are shown to be in good agreement with synthesis and simulation. Due

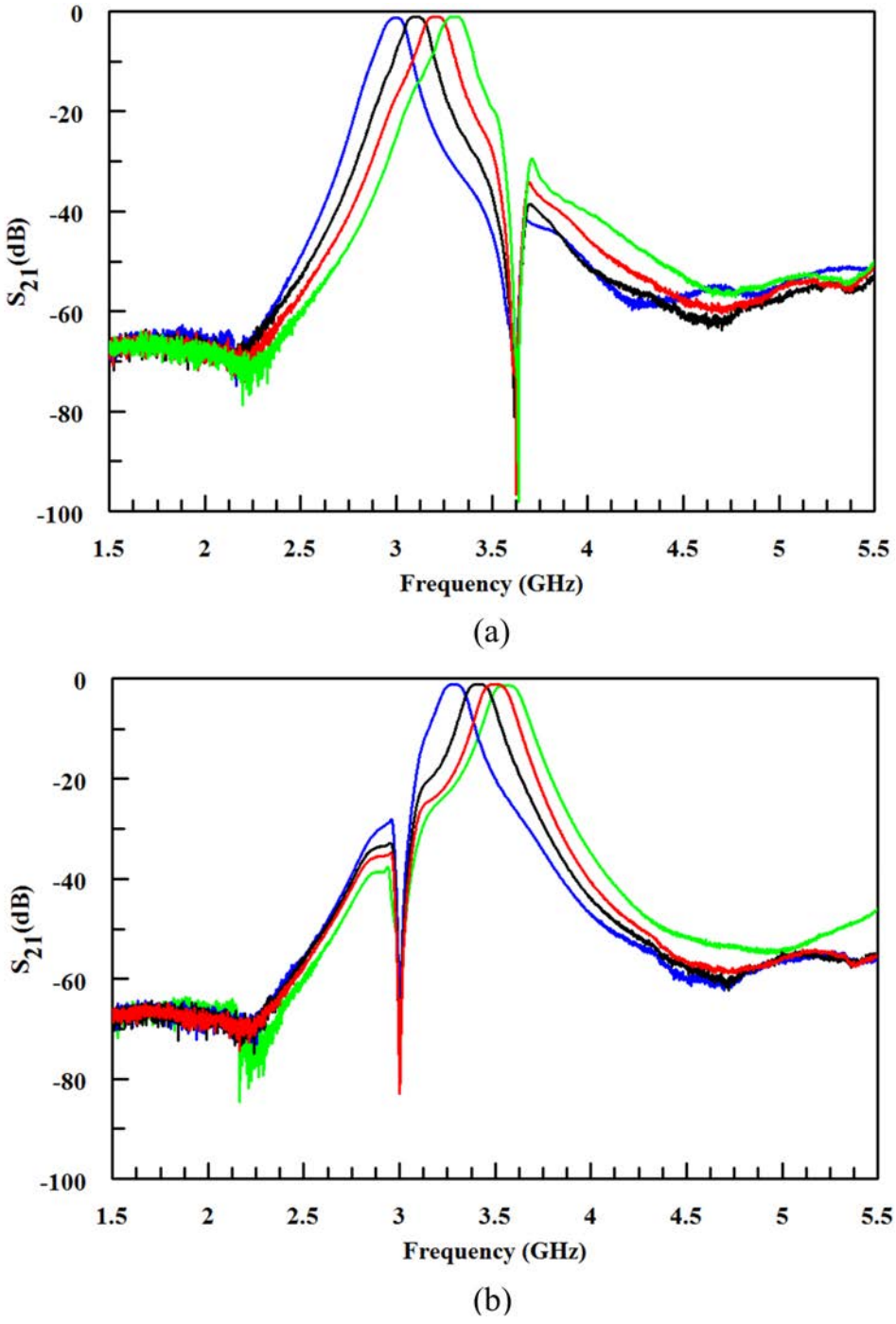

Figure 5.14: Measured frequency response of the BP-BS filter cascade with either passband or stopband being swept, (a) bandstop filter fixed and bandpass filter swept below bandstop filter, (b) bandstop filter fixed and bandpass filter swept above bandstop filter.

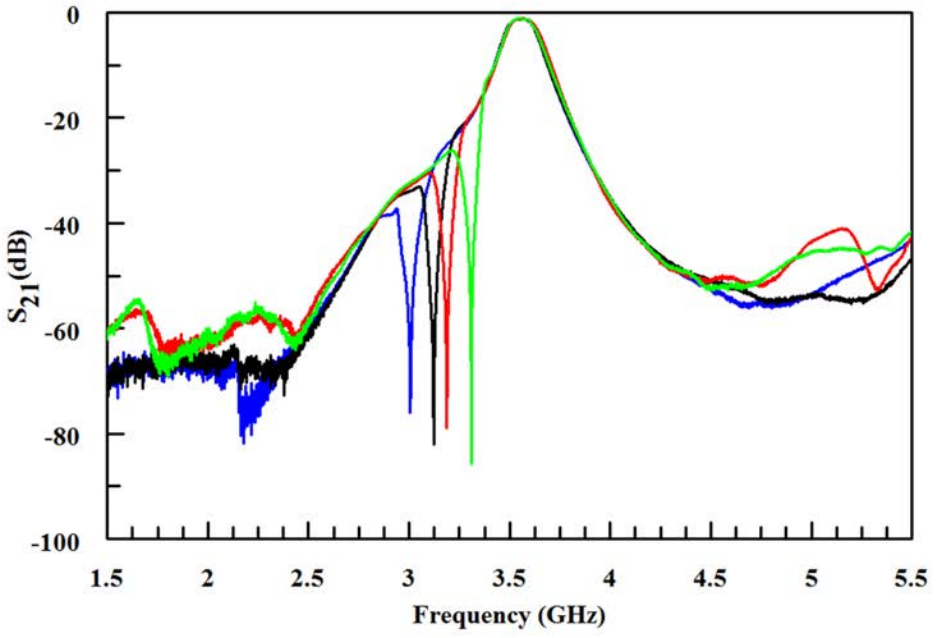

(c)

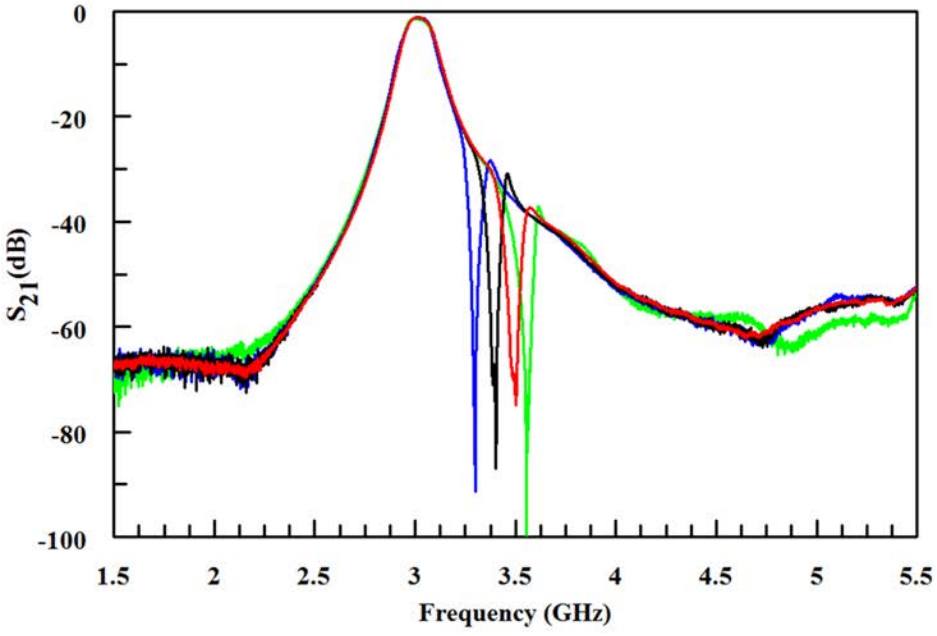

(d)

Figure 5.14: (continued) (c) bandpass filter fixed and bandstop filter swept below bandpass filter, and (d) bandpass filter fixed and bandstop filter swept above bandpass filter.

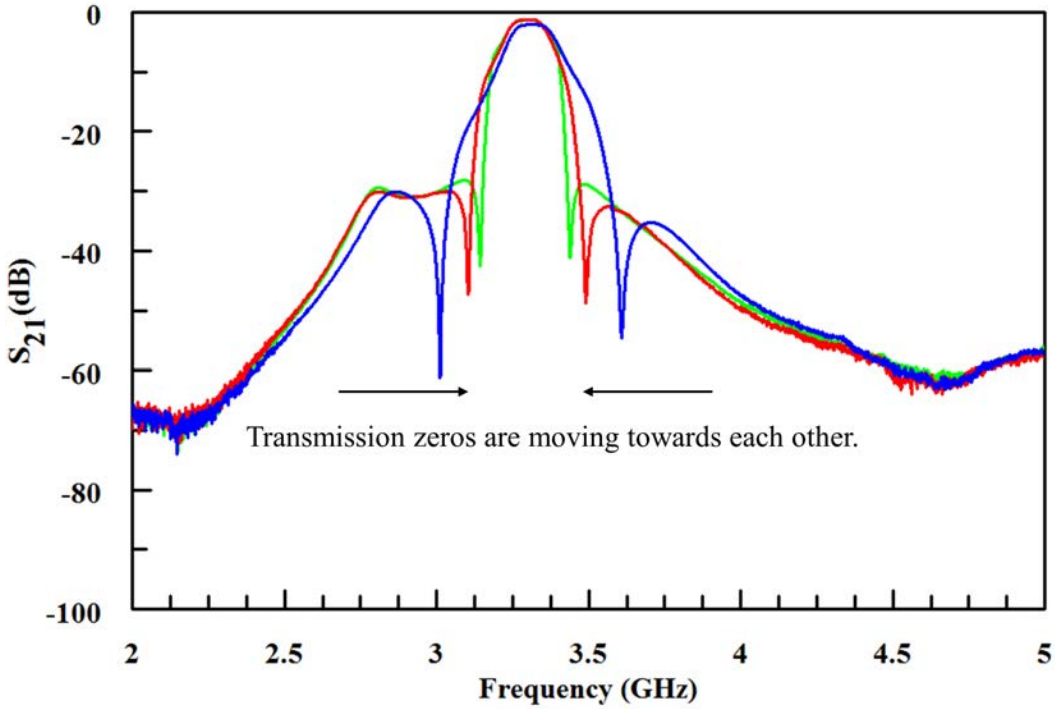

Figure 5.15: Measured BP-BS filter cascade frequency responses with two transmission zeros placed on both sides of the passband providing psudo-elliptic response.

to the used technology, the fabricated filter cascade has a very small profile, low weight, low cost, and capability of integration and mass production, while providing high electrical performance.

The fabricated filter, to the best of the author's knowledge, is the smallest reported BP-BS filter cascade implemented using substrate-integrated, evanescent-mode cavities to date. It represents the state-of-the-art in reconfigurable filtering for current and future communications and radar applications.

5.4 BP-BS Filter Cascade System Test

The final goal is to incorporate BP-BS filter cascades in the front-end of microwave systems such as radar systems with simultaneous transmit-receive or

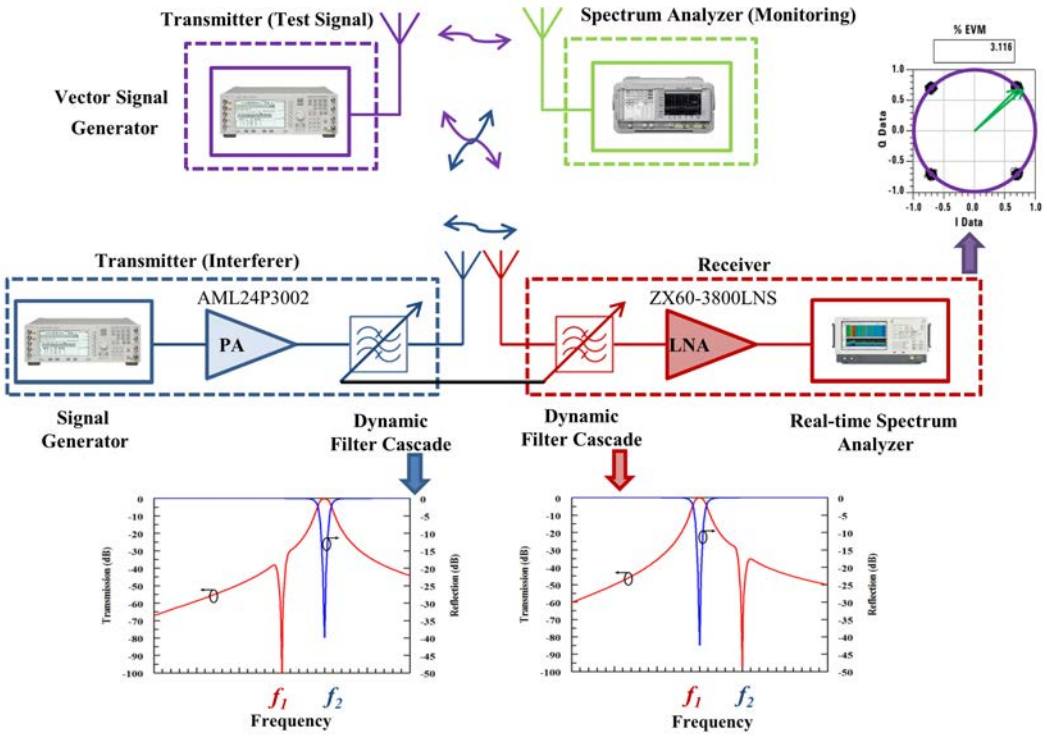

Figure 5.16: System-level test block diagram.

communication systems with co-site interference mitigation. In either case, the leakage from the high power transmitter into the receiver, degrades the system performance. In such applications, a BP-BS filter cascade provides a very deep, tunable null, independent of the tunable transmission passband, using relatively few resonators. In order to evaluate the performance of the designed BP-BS filter cascade in a system level setting, a pair of filter cascades are fabricated and tested. Figure 5.16 shows the block diagram of the system-level test. This test setup emulates the conditions that happen in simultaneous transmit-receive radars or a co-site interference communication systems. The low-level test signal at f_2 is the desired receive signal. This signal can be a weak echo from previous pulse in the simultaneous transmit-receive radar system. However, a strong interfering signal is being radiated at an adjacent channel at f_1. This signal can be a new pulse transmitted by the

radar system. One filter cascades is utilized in the transmitter and another in the receiver. The cascades are synchronized to provide simultaneously a deep isolation region at the receive frequency (f_1) and a high power tolerant pass-band at the adjacent frequency (f_2) for the transmit. Therefore, the cascade in the receiver should provide a low insertion loss path for the received signal at f_1 and simultaneously provide a high rejection for the transmitted signal at f_2. Similarly, the cascade in the transmitter should provide a low insertion loss path for the transmit signal at f_2 and simultaneously reduce the noise level generated at f_1.

In this test, the transmitter is a vector signal generator with an arbitrary output waveform or modulation and the receiver is a real-time spectrum analyzer (RTSA). Different parameters can be used to quantify the impact of including a BP-BS filter cascade in a radio link. In this work, a quadrature phase shift keying (QPSK) signal with symbol rate of 10 MSPS, 40 MHz IQ filter, and raised Nyquist filter with $\alpha = 0.35$, at 3.3 GHz is used as the desired signal. An arbitrary frequency modulated (FM) signal with FM deviation of 8 MHz, FM rate of 1 MHz, and sinusoid signal source at 3.6 GHz is utilized as the interference. The constellation of the digital modulated signal or error vector magnitude (EVM) at the receiver is used to measure the performance of the link. Since in this test both high-power and low-level signals are involved, a second spectrum analyzer is used to monitor and ensure the correctness of the measurements. The key metrics of the power amplifier (PA) are of gain of 30 dB and a 1-dB compression point of 27 dBm. Similarly, the key metrics of the low-noise amplifier (LNA) are a gain of 23.7 dB and a noise figure of 3.1 dB. By using the cascades, a significant improvement, in the signal-to-noise ratio of the link at the presence of interference, is expected.

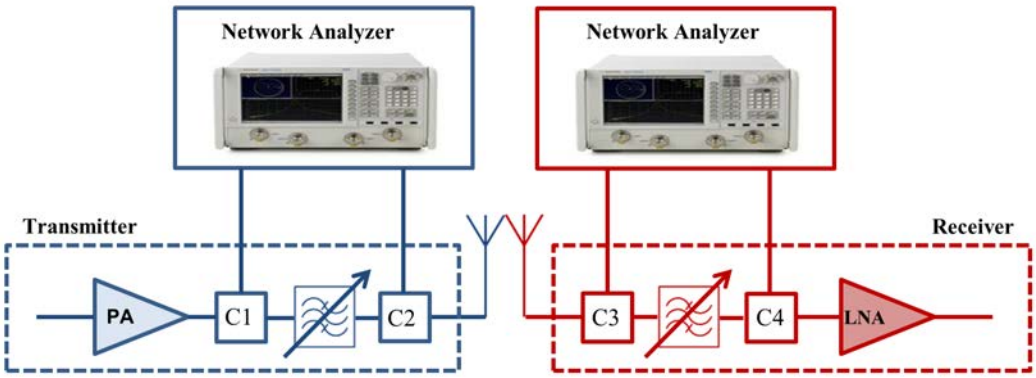

Figure 5.17: Cascade tuning setup in the RF chain.

Tuning the cascades in the chain, is challenging. Therefore, directional couplers are used in the transmitter and receiver chains to simultaneously monitor and tune the cascades as they are operated in the system. The setup block diagram is shown in figure 5.17. To verify the performance of the tuning method, a similar test using the configuration, shown in figure 5.18, using and 4%-fractional-bandwidth bandpass filter was performed. In this configuration 50 Ω terminations were used to emulate the input impedances of the low noise amplifier, power amplifier and antennas. Two 20 dB couplers (Narda 4244-20) were used in the test. The network analyzer along with two couplers in the chain, was first calibrated, and then was used to monitor the response of the filter. A photograph of the test setup is shown figure 5.19. The result confirms that the filters can be tuned using couplers in the system level test.

Four monopole antennas were fabricated and tested. Three of them are used in the system-level test and the fourth is connected to the second spectrum analyzer for independent spectrum monitoring. A platform was also constructed to keep the antennas in a well-controlled configuration. The antennas and platform are shown in figure 5.20. The measurement setup with all the equipment used in this test is shown in figure 5.21.

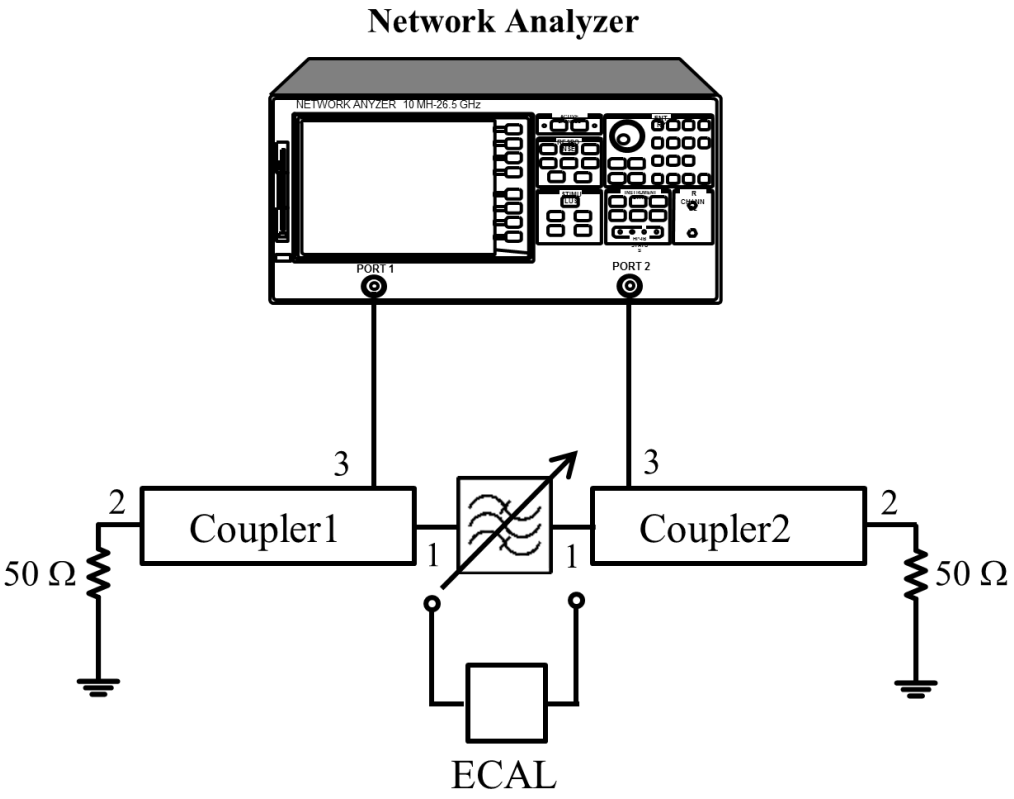

Figure 5.18: Test setup used for verification of the filter tuning method in chain.

5.4.1 Link Recovery

In this test, it is shown how the performance of a communication link is degraded when a neighboring transmitter is radiating at a close-by frequency, while there is no proper filtering in the transmitter chain. BP-BS filter cascade are then used to demonstarte how the link can be recovered.

The first experiment is a control experiment where the receiver noise level at 3.3 GHz is observed with the interfering transmitter turned off. This is represented by the yellow trace in figure 5.22. When the interfering transmitter is turned on, and operating at 3.6 GHz, the receiver noise level is increased, which is shown by the cyan trace in the figure. The increase in observed out-

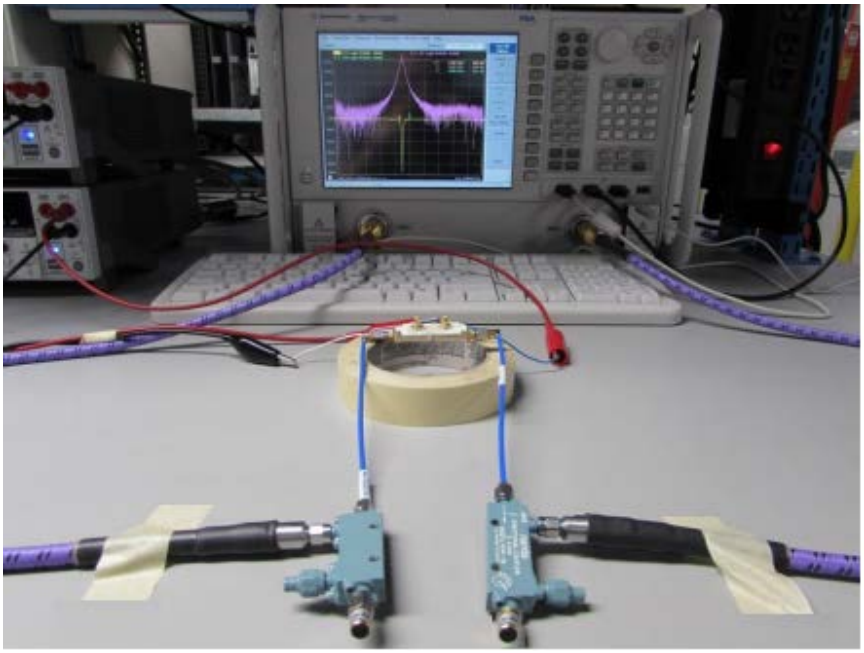

Figure 5.19: Test setup used for tuning of the bandpass filter with directional couplers in the chain.

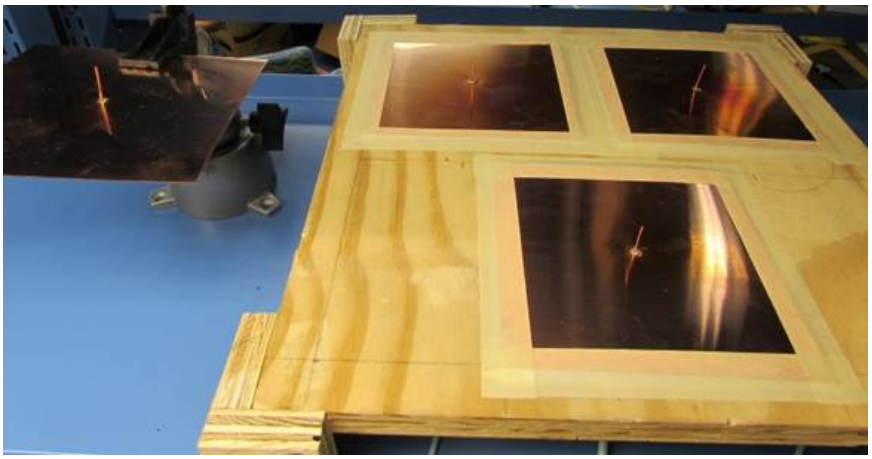

Figure 5.20: Fabricated antennas for the system-level test.

of-band noise is almost 15 dB and it is due to the noise generated by the power amplifier in the interfering transmitter.

In the next step the test signal transmitter at 3.3 GHz, is turned on, while the interferer transmitter is kept off. The received spectrum and EVM of the test signal is captured and shown in figure 5.23. The measured root mean

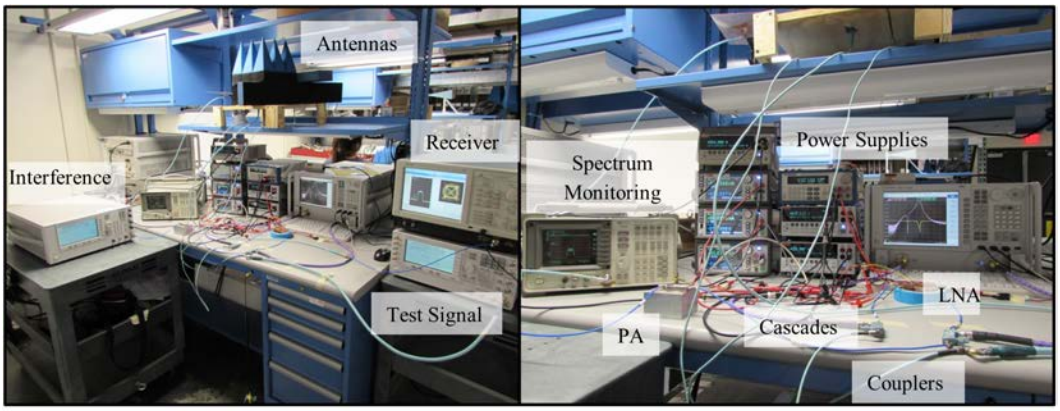

(a) (b)

Figure 5.21: System-level test setup, (a) wide angle showing all the equipments, (b) closer view showing the observed filter cascade response on the network analyzer.

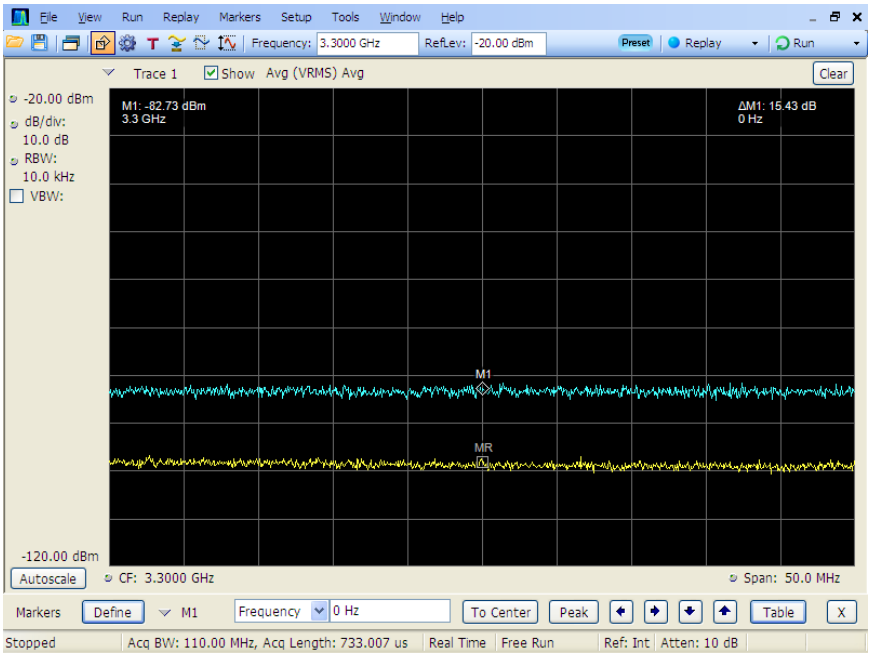

Figure 5.22: Control experiment used to measure noise level without (yellow trace) and with (cyan trace) the interfering transmitter turned on.

square (RMS) EVM is less than 3% with a signal-to-noise ratio greater than 30 dB, which guarantees a high quality data link. When the power amplifier of the interfering transmitter (without the interfering signal being transmitted)

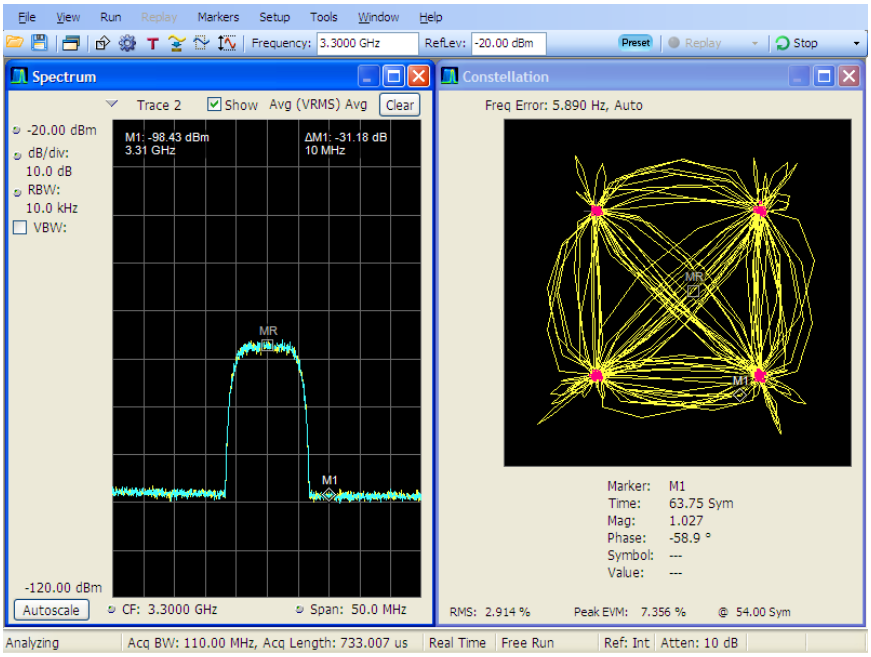

Figure 5.23: Measured received signal and EVM with the test signal transmitter turned on at 3.3 GHz, while the interfering transmitter is off.

is turned on, the received noise level is increased by 15 dB, represented by the cyan trace in figure 5.24, while the yellow trace shows the received signal when no interference is present. It can be seen that the RMS EVM deteriorates down to 16.3%. The constellation now clearly shows a spread in the symbol locations. However, the signal-to-noise ratio is still sufficient to capture the content of the transmitted signal. Figure 5.25 shows what happens when the interfering signal at 3.6 GHz is turned on. The signal level is degraded in addition to the noise increase. The impact on the RMS EVM is significant and it further deteriorates to around 50%. At this point the constellation is severely distorted and the symbol locations cannot be properly extracted resulting in loss of communications.

The communication link can be recovered if bandpass-bandstop filter cascades are brought into the measurement setup. The transmitter noise at 3.3 GHz can be reduced, by placing the first cascade bandstop filter at 3.3 GHz

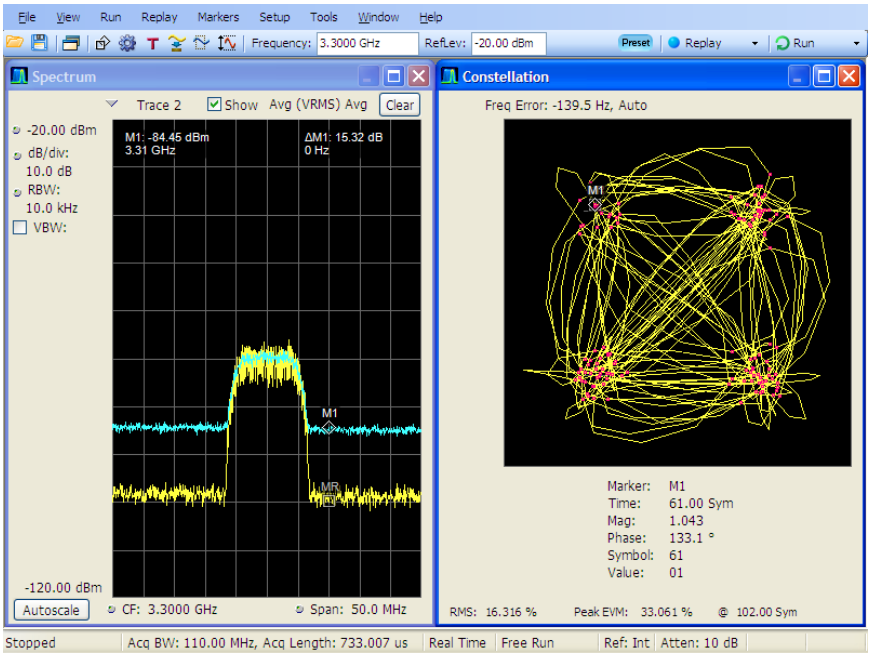

Figure 5.24: Measured received spectrum with the interfering power amplifier turned on but with no interfering signal being transmitted.

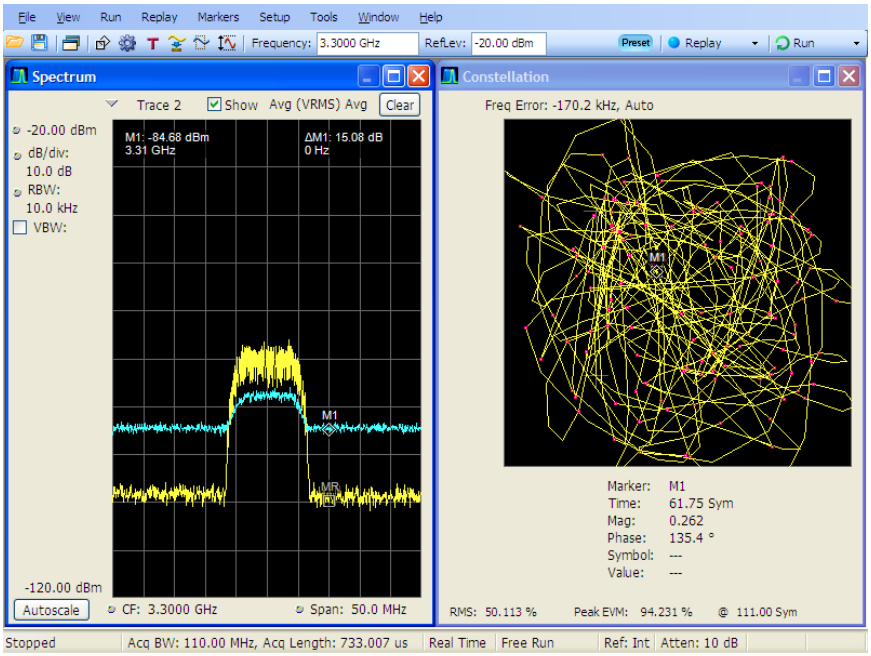

Figure 5.25: Measured received spectrum with the interfering power amplifier turned on and with an interfering signal being transmitted.

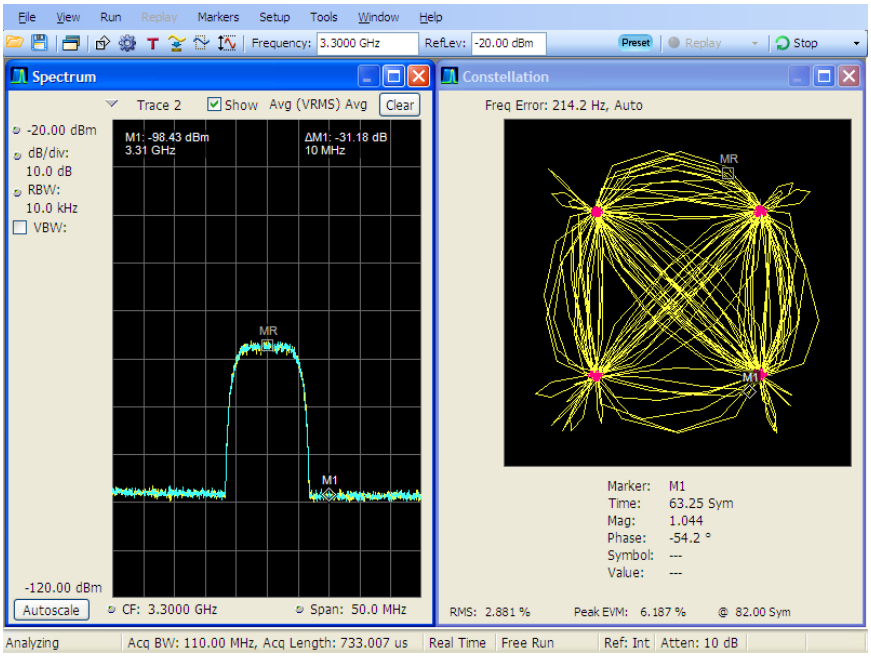

Figure 5.26: Measured received spectrum using a BP-BS filter cascade to clean up the transmitted noise, with the interfering power amplifier turned on, but no interfering signal being transmitted.

and bandpass filter at 3.6 GHz, while simultaneously rejecting the interference at 3.6 GHz by placing the second cascade bandstop filter at 3.6 GHz and the bandpass filter at 3.3 GHz, the quality of service can be greatly improved. Figure 5.26 shows what happens when the interfering power amplifier is on but the interfering signal is turned off (similar to the case shown in figure 5.24). As can be seen from this figure, the RMS EVM is restored and the noise from the power amplifier is cleaned up. If the interfering signal is also turned on (similar to the case shown in figure 5.25), the filter cascades will also clean up the noise in the receive band. The resulting spectrum and constellation can be seen in figure 5.27. The RMS EVM is now better than 5.57%, which is sufficient to restore the communications link.

To further demonstrate the benefits of having a pair of cascades in the system, two additional tests are performed. In the first test, which is referred

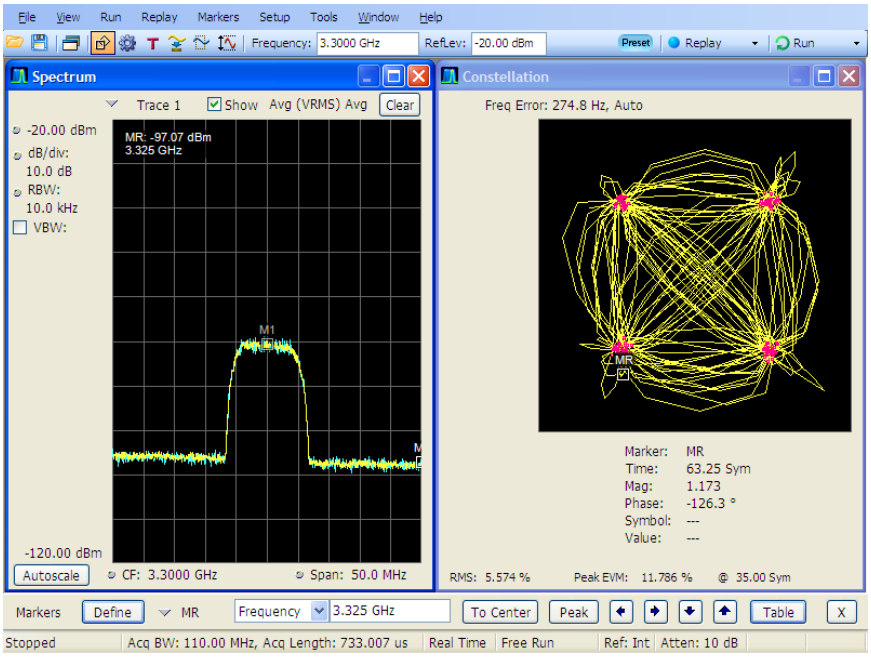

Figure 5.27: Measured received spectrum using two BP-BS filter cascades to clean up the transmitted noise, with the interfering power amplifier turned on, and an interfering signal being transmitted.

to as noise-shaping test, the same test setup is used with some slight alteration. In this test, despite the link recovery test, a high performance regular (not real-time) spectrum analyzer is used. This results is a reduced the noise floor and a wider frequency span. In this test, a demonstration of the recovery of a masked signal by using a filter cascade in the interfering transmitter is presented. In the second test, the effects of the increase in interference power level on the receive LNA will be investigated. It will be demonstrated how the proposed BP-BS filter technology can alleviate these effects beyond what is possible using traditional bandpass filtering on both transmit and receive.

5.4.2 Noise-Shaping

In this test, it is shown that the filter cascade can reduce the noise level of an adjacent interfering transmitter that is masking a desired receive signal.

The cascade allows for signal reception that is impossible with the traditional bandpass filters in the transmitter and receiver hardware. This test is performed for two different cases: one with a narrow-band desired receive signal and the other with a wide-band desired receive signal.

The test results are shown in figures 5.28 and 5.29 for the narrow-band and wide-band desired signals, respectively. In these figures, the original desired signal, without the presence of the masking interference, is shown in blue. The receiver noise floor is around -115 dBm and the peak of desired signal is about -85 dBm in the case of narrow-band signal and about -95 dBm in the case of wide-band signal. This level of desired signal provides a good signal-to-noise ration suitable for a robust communication link. The received spectrumn the presence of the injected interference is shown in green. The noise level is dramatically increased to a level of -60 dBm, and the desired signal is completely masked. Therefore, the link is lost.

The yellow spectrum shows the received noise at receiver, when bandpass filters in the traditional transmit and receive chains are used. However, this technique is not successful in recovering the masked signal. The red spectrum shows how the cascades in the transmitter and receiver chains enable the recovery of the masked signal. This is achieved by shaping the transmitted noise to create a spectral region that allows for reception of weak signals.

Although in this test, BP-BS filter cascades were used in both the interferer transmitter and the receiver, it is clear that the noise shaping is mainly accomplished by the filter cascade in the transmit chain and not in the receive chain. In order to fully demonstrate, the benefits of having filter cascades, both in the transmit chain and the receive chain, another test is performed.

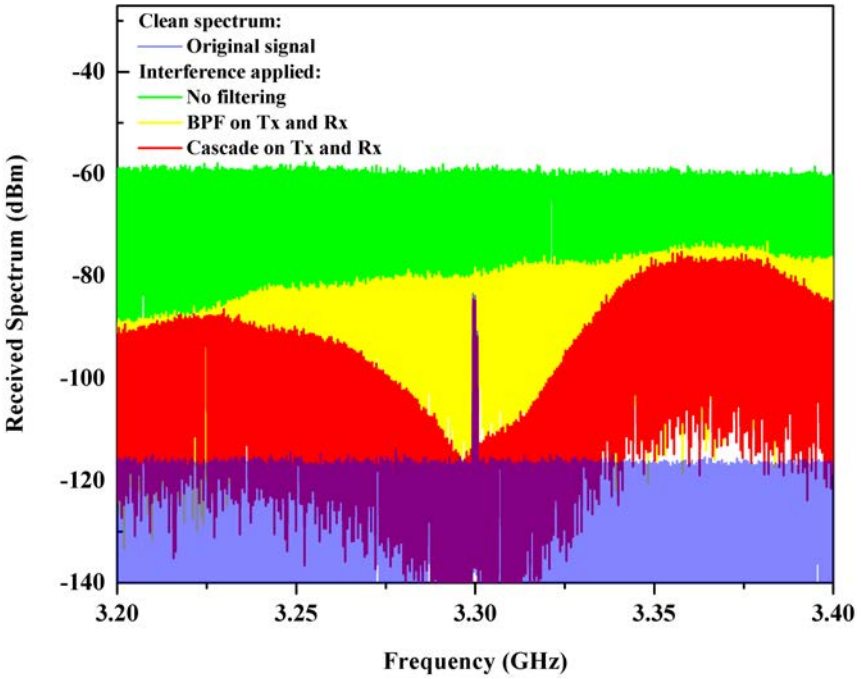

Figure 5.28: Noise shaping using BP-BS filter cascade on both transmitter and receiver for narrow-band desired receive signal.

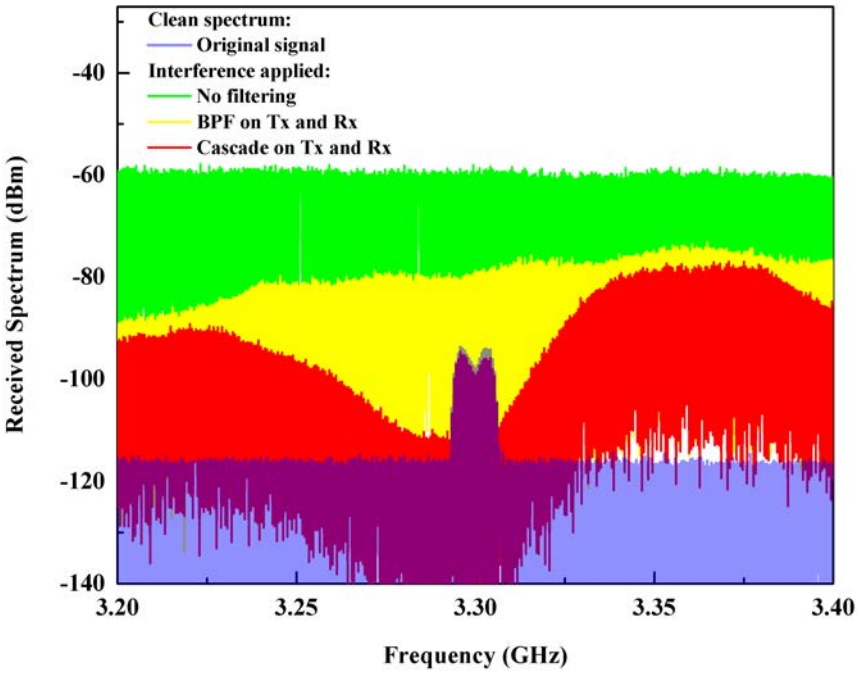

Figure 5.29: Noise shaping using BP-BS filter cascade on both transmitter and receiver for wide-band desired receive signal.

5.4.3 LNA Compression Mitigation

In order to demonstrate the benefits of having a BP-BS filter cascade in the receive chain, the deficiencies of only using a bandpass filter are demonstrated. The test setup is shown in figure 5.30. Additionally, the antennas are replaced with a combiner in order to remove the statistical behavior of the received signal level due to wave propagation effects. This is also important due to FCC regulations. High power radiation has both the potential safety hazards and the potential of interfering with existing spectrum users. Therefore, any interference study, using radiated power, will be limited in terms of available power level.

In the test configuration shown in figure 5.30(a), the power amplifier output level is changed from 2.35 to 28.35 dBm and the resulting change in receive performance is shown in figure 5.31. The impact is a loss of signal strength of around 5.0 dB and an increase in the receiver noise level by 8.5 dB. This is due to compression of the LNA from the high power level received from the interfering signal at 3.6 GHz. Changing the system configuration to include a BP-BS filter cascade in the receiver, as shown in figure 5.30(b), results in a total recovery of the system-level performance. This is clear indication that the LNA is no longer impacted by the interfering signal. The resulting receive spectrum is shown in figure 5.32, for the same power levels as used in the previous test. Not only is the signal level not affected, but also the noise level is maintained at the same level. This shows that the filter cascade in the receive chain can protect the LNA from compression due to high power levels of adjacent signals. Finally, the two test scenarios are directly compared in figure 5.33(a). There is a very significant improvement from including a filter cascade in the receiver chain. This test was repeated for different power levels

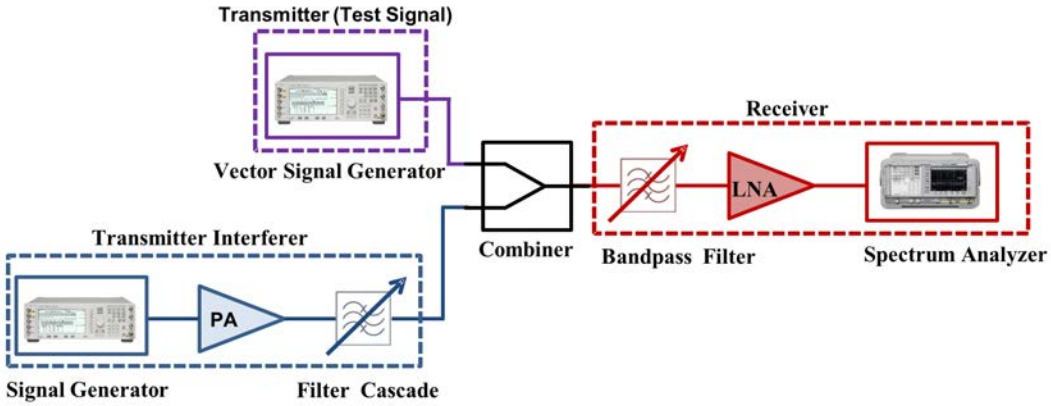

(a)

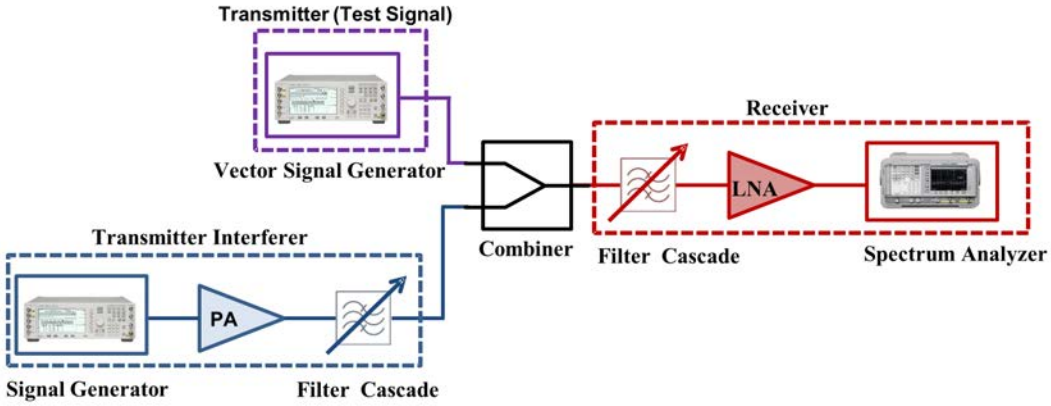

(b)

Figure 5.30: Test configuration with a BP-BS filter cascade in the transmitter and, (a) a bandpass filter in the receiver, (b) a BP-BS filter cascade in the receiver.

between the 2.35 and 28.35 dBm. The signal loss as a function of PA output power is shown in figure 5.33(b). From the slope of the signal loss curve, a rudimentary trend can be extrapolated for higher power levels. It can be seen that for any radar systems with higher output power, the problem will be further magnified. Therefore, having a cascade is absolutely vital for radar systems, operating in simultaneous transmit-receive mode.

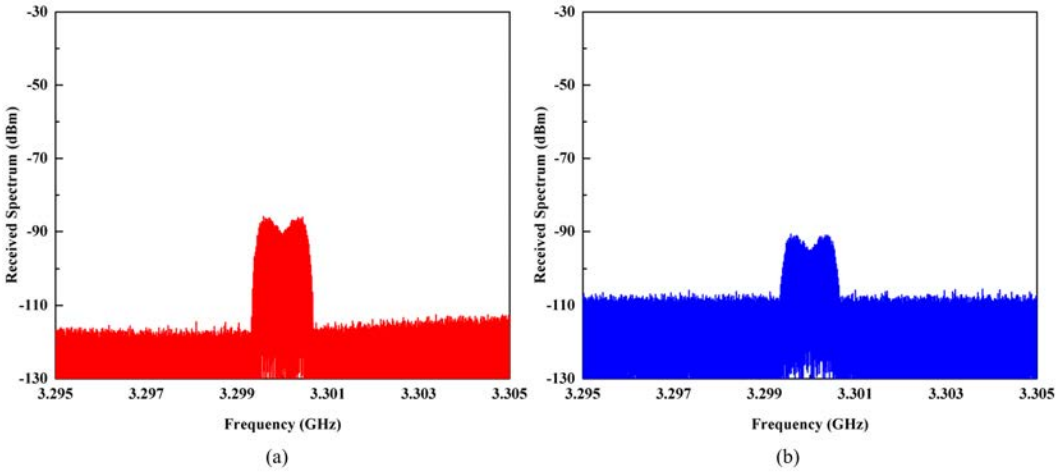

Figure 5.31: Measured receive spectrum for the system-level configuration shown in figure 5.30(a), for demonstrating the impact of the interference on the LNA for two different PA output levels, (a) 2.35 dBm, (b) 28.35 dBm.

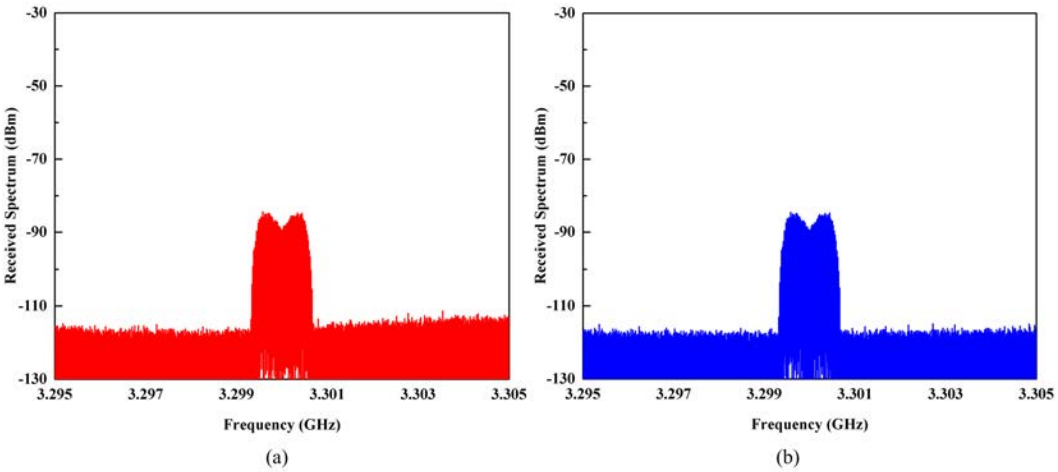

Figure 5.32: Measured receive spectrum for the system-level configuration shown in figure 5.30(b), for demonstrating the impact of the interference on the LNA for two different PA output levels, (a) 2.35 dBm, (b) 28.35 dBm.

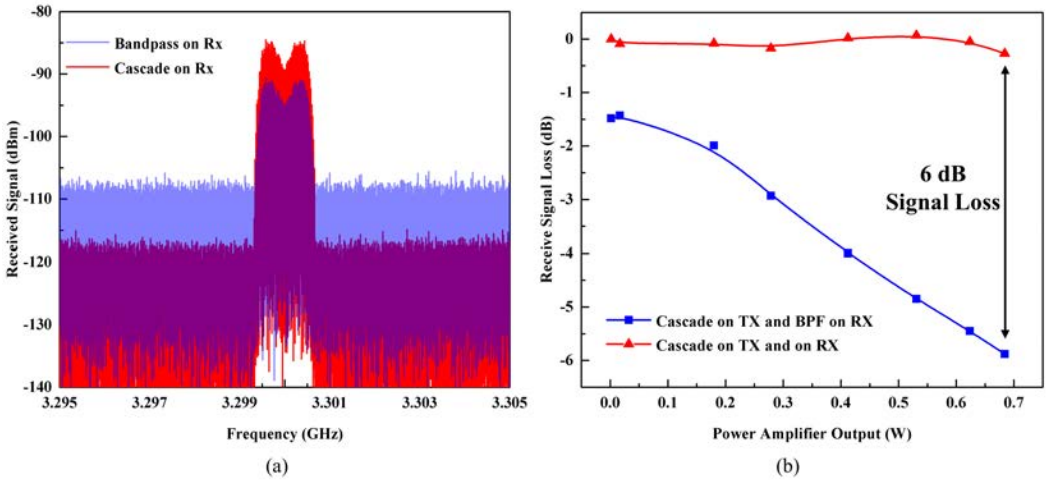

Figure 5.33: Summary of the LNA compression test, (a) direct comparison between the received spectrum having a bandpass filter or a filter cascade on the receiver with a power amplifier output of 28.35 dBm, (b) the signal loss as a function of power amplifier output.

Chapter 6

Automatic Control of Tunable Filters

6.1 Introduction

In Chapter 3, it was shown that the physical structure of the evanescent-mode cavity resonator is designed in such a way that its resonant frequency is very sensitive to the changes in the capacitive gap. A gap size change on the order of few micrometers results in a frequency change on the order of few hundred megahertz. This feature is required for wideband tuning of the resonators. However, this sensitivity can also be viewed as a drawback of these structures in terms of stability. Due to the sensitivity of the resonator to very small changes in the gap size, environmental effects like temperature variation and vibration can lead to a very large change in the resonant frequency, even under a fixed biasing condition. When piezoelectric actuators are used to tune the resonators this issue is further compounded. There are two issues inherent to the piezoelectric actuators that limit their usefulness as a tuning element for loaded evanescent-mode cavity resonators.

1. The actuator deflection exhibits hysteresis effect when the actuation voltage changes in ascending versus descending manner. Therefore, look up tables or open loop controllers cannot be used to perform the frequency

tuning.

2. The CTE of the piezoelectric material is large (4 μm/°C) [132]. Therefore, when the temperature changes a few degrees, it causes significant displacement of the actuator, compared to its total deflection (which is $\pm$19 μm for the 12.7 mm disc actuators used in this work). This results in a large change in the resonant frequency.

In many filter applications a simple, well-trained, open-loop, control system including thermal sensors can be utilized to perform the frequency tuning of the resonators in a stabilized discipline. Frequency control of resonators based on piezoelectric actuators, however, requires a more advanced and sophisticated control circuit. Through temperature cycling of an evanescent-mode cavity resonator, it was experimentally shown that the piezoelectric actuators can be used over a wide temperature range for frequency tuning of the resonators using a closed-loop control system [133].

Therefore, implementation of an automatic frequency tuning system utilizing a closed-loop feedback control circuit is a critical concern that needs to be addressed before substrate-integrated, evanescent-mode, cavity resonators with piezoelectric actuation become ready for widespread commercial usage.

6.2 Conceptual Design

In-circuit/in-situ filter tuning is a crucial need in multi-band and multi-mode radio and radar systems that use tunable filters. However, most of the previously reported methods for tuning these filters, like time-domain transformation of the return loss [134], fuzzy logic-based filter tuning [135], tuning

based on the transmission of a test signal [136], and scalar transmission [137], require direct access to the filter ports. Therefore, they cannot be utilized to tune filters that are in operation. In the above methods, using RF switches the filter is first disconnected from its real system and then is connected to the control circuit for tuning. Therefore, using these methods for in-circuit (hot) tuning is not possible.

In [138], a built-in sensing mechanism based on the higher order differential mode of evanescent-mode cavity resonators was shown. Using this technique, an in-situ continuous tracking of the the center frequency of a tunable evanescent-mode cavity filter becomes possible. In this method, the capacitive loading post is split into two segments. Therefore, a second resonant mode, roughly at twice the resonant frequency of the resonator is introduced. The first and the higher-order modes are usually referred to as common and differential modes, respectively. Since the differential mode has a strong magnetic-field concentration inside the split in the post, a probe at this location can be used to measure its resonant frequency; ideally, without affecting the filter performance. In [138], it was shown that substrate-integrated cavities are very well suited for implementing this method. Although this method works very well especially for frequencies in the range of 1 to 4 GHz, implementation of the probe in higher frequencies requires precision fabrication steps like 3D laser patterning [139]. Additionally, because the resonant frequency of the differential mode is always higher than the main resonant frequency of the resonator, the frequency range of the differential mode in widely tunable filters might be quite large. Therefore, implementation of the control system involves circuit design at microwave frequencies which turns this technique into a very demanding approach.

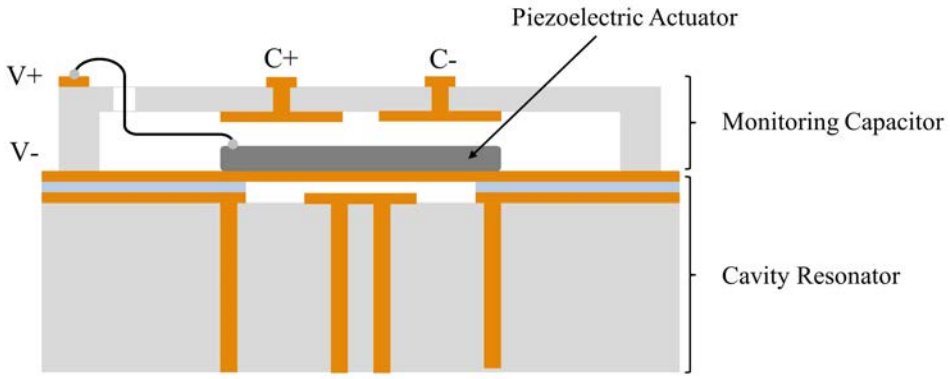

Figure 6.1: Proposed new sensing method using a monitoring capacitor on top of the actuator.

Therefore, in this work a different monitoring mechanism, with a much simpler circuit implementation, is utilized. The sensing circuit is realized by creating a top monitoring capacitor structure that goes over the piezoelectric actuator. The monitoring capacitor consists of a second cavity that is mounted above the actuator forming a second air-filled, metal-insulator-metal capacitor. In this structure, there exists a direct relationship between the monitoring capacitance and the post loading capacitance in the evanescent-mode cavity. Therefore, by tracking the monitoring capacitance, the center frequency of the filter can be monitored, which allows for direct, in-situ, closed-loop control of the filter.

Figure 6.1 shows the structure of the monitoring capacitor. The monitoring capacitor is formed using the same piezoelectric actuator that deflects the copper diaphragm in the tunable cavity resonator. In fact, the top electrode of the piezoelectric actuator will form the bottom plate of the parallel plate monitoring capacitor, while the structure itself hosts the top electrode of the monitoring capacitor. The monitoring capacitor is completely external to the filter structure and does not contribute to any additional losses.

The monitoring capacitor can be used in a variable oscillator as a res-

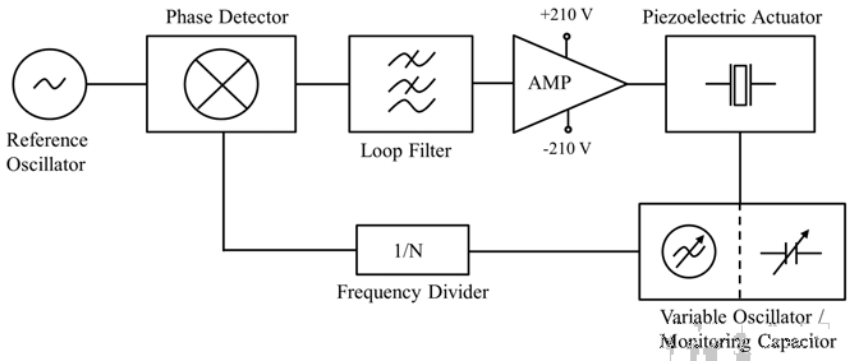

Figure 6.2: Filter tuning using a monitoring capacitor as part of the variable oscillator in the phase locked loop control system.

onating (tank) circuit while it is placed and controlled in a phase-locked loop system similar to what is shown in figure 6.2. The resonant frequency of the oscillator can be any practical value, and is not required to be close to the resonant frequency of the tunable cavity resonator. Frequency and phase locked loop systems have been previously used for tuning of the microwave resonator and filters [140], [141]. Since the piezoelectric actuators are biased with high DC voltages, the control system must be isolated from the biasing and actuation circuit. In order to provide the required isolation, the actual monitoring capacitor is fabricated as a series connection of two capacitors with a common bottom plate (which is the top electrode of the piezoelectric actuator). Although the sensing capacitance is reduced by a factor of two, the accuracy of the sensing mechanism is not impacted. In fact, the change in the capacitance is of interest, not its absolute value. Therefore, any series or parallel combination of the monitoring capacitor with some fixed capacitors, can be used to map the total value of the monitoring capacitor to the desired range of capacitance. Additionally, the series connection of two capacitors provides easy access to both electrodes of the monitoring capacitor. In the practical implementation of the monitoring capacitor, to provide complete isolation from

the actuator biasing circuit, a very thin (1 mil) liquid crystal polymer (LCP) layer (Rogers ULTRALAM 3850 laminate) is fabricated and attached using conductive epoxy on top of the piezoelectric actuator. The bottom layer of LCP provides the biasing voltage for the actuators while the top layer forms the common electrode of the monitoring capacitor.

6.3 Digital Feedback Control

The concept shown in figure 6.2, can also be implemented digitally using field programmable gate arrays (FPGA) or micro-controllers (μC). To this end, the analog output signal of the oscillator is required to be digitized using an analog-to-digital converter (ADC). The digital signal is then fed into an FPGA/μC where the tuning algorithm is performed. Through comparison of the input set value with the current value of oscillation frequency, a digital difference value known as the digital offset is obtained. The digital offset is then converted to an analog error voltage at one of the FPGA/μC output ports using an internal or external digital-to-analog converter (DAC). This analog error voltage is amplified using an operational amplifier to provide the required bias voltage for the piezoelectric actuator in a manner that reduces the digital offset or analog error voltage.

A family of devices, called capacitance-to-digital-converters (CDC), can be used to reduce the number of components in digital implementation of the feedback control system. As opposed to the conventional converters, by using a CDC, the value of the capacitor under test (the monitoring capacitor, for example) is directly converted to a digital data. Therefore, the variable oscillator can be eliminated. A comparison between the conventional and the modern capacitance to digital conversion is shown in figure 6.3.

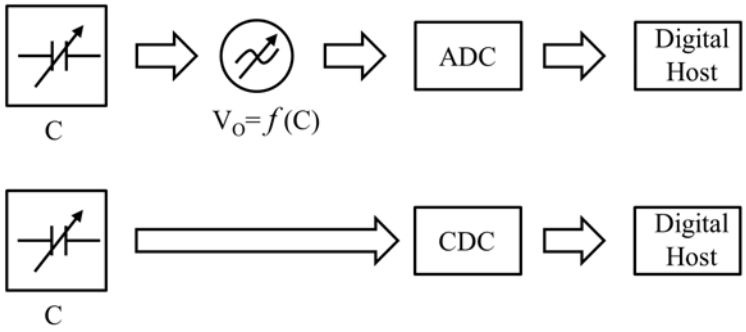

Figure 6.3: A comparison between conventional and modern capacitor to digital converters.

CDCs were first introduced by Analog Devices and are now commercially available from many other semiconductor manufacturers. The packaged chips AD7745, AD7746, and AD7747 are members of a family of CDCs from Analog Devices that operate based on delta-sigma modulation [142]. The architecture of these CDCs includes a patented analog front-end interface, that eliminates the negative effects of any external parasitic capacitances. These components provide a unique combination of high precision, small package, low power, low cost (less than $5), low temperature drift, and low noise. Therefore, they are suitable for medical and industrial instrumentation applications. In this work, AD7747 will be used. This chip has been designed for both single-ended or differential capacitive sensors with one plate connected to ground. Some of its features are high resolution (24-bit no missing codes, 18-bit effective resolution at a 16.6 Hz data rate), high linearity (±0.01%), and high accuracy (±4 fF factory calibrated). The AD7747 capacitance input range is from -8 to +8 pF (variable). However, it can accept up to +17 pF absolute capacitance (fixed), which is compensated by an on-chip digital-to-capacitance converter. More information about this component can be found from the manufacturer's data sheet [143].

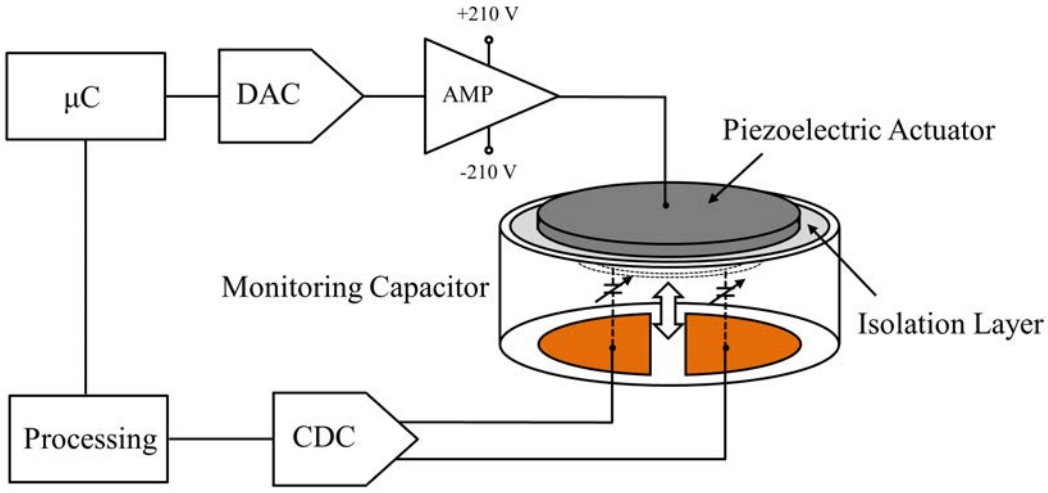

Figure 6.4: Block diagram of the digital feedback control system using a CDC.

Figure 6.4 shows the digital version of the block diagram in figure 6.2. The value of the monitoring capacitor is directly read by the CDC and then its digital value is fed into the FPGA/μC. This value is compared to a preset value corresponding to a specific frequency and provides a digital offset. The digital offset is converted to an analog error voltage, and after amplification by an operational amplifier, is used to bias the piezoelectric actuator. The final movement of the actuator in the loop is in the direction that reduces the digital offset or error voltage.

As previously mentioned, the monitoring capacitor is formed of a series connection of two capacitors with the top electrode of the piezoelectric actuator as the common bottom plate. This structure provides isolation between the feedback system and the piezoelectric actuator. Figure 6.5 shows the 3D structure of the monitoring capacitor designed for the second order bandpass filters demonstrated in Chapter 3. This structure is mounted on top of the filters to complete the sensing mechanism. This structure also hosts the required CDCs as well as other peripheral circuitry.

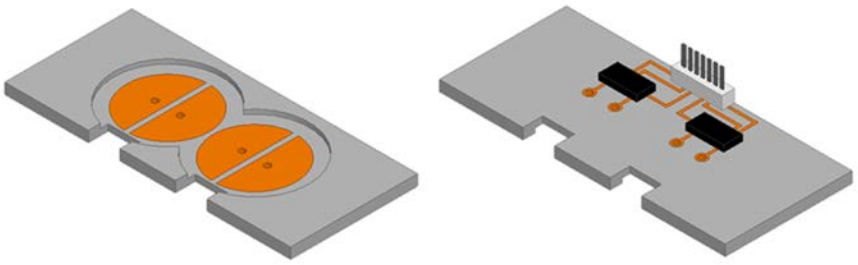

(a) (b)

Figure 6.5: 3D structure of the monitoring capacitor, (a) bottom view showing the capacitor plates, (b) top view showing the capacitive sensor circuitry.

6.4 Automatic Tuning System Implementation

The first step in implementation of the automatic tuning system is the fabrication of the monitoring capacitor for the bandpass filter, based on the structure shown in figure 6.5. The first monitoring capacitor prototype was fabricated using the EnvisionTEC 3D printer out of a commercial plastic material called E-Dentstone [144]. A photograph of the fabricated structure is shown in figure 6.6. In order to avoid plating and milling of the plastic platform, a patterned 1 mil LCP layer is fabricated and attached inside the platform to make one of the electrodes of the capacitor. The SMB connectors on top of the platform are utilized for connection to CDCs. In the first version of the tuning system, for ease of fabrication and troubleshooting, the CDCs were not integrated on the top of the monitoring capacitor board. Another two-layer, plated and patterned LCP laminate is also used to isolate the piezoelectric actuators from the monitoring capacitors and provide access to the surface of the actuators for biasing. A sample isolation layer, attached on top of a bandpass filter along with the complete assembly of the monitoring capacitor, are shown in figure 6.7.

Although the plastic material used in this fabrication run does not require

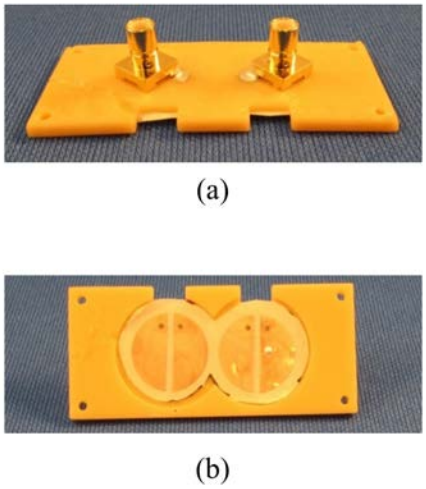

Figure 6.6: Monitoring capacitor fabricated using plastic, (a) top view, (b) bottom view showing top electrodes of the monitoring capacitor implemented using a LCP layer.

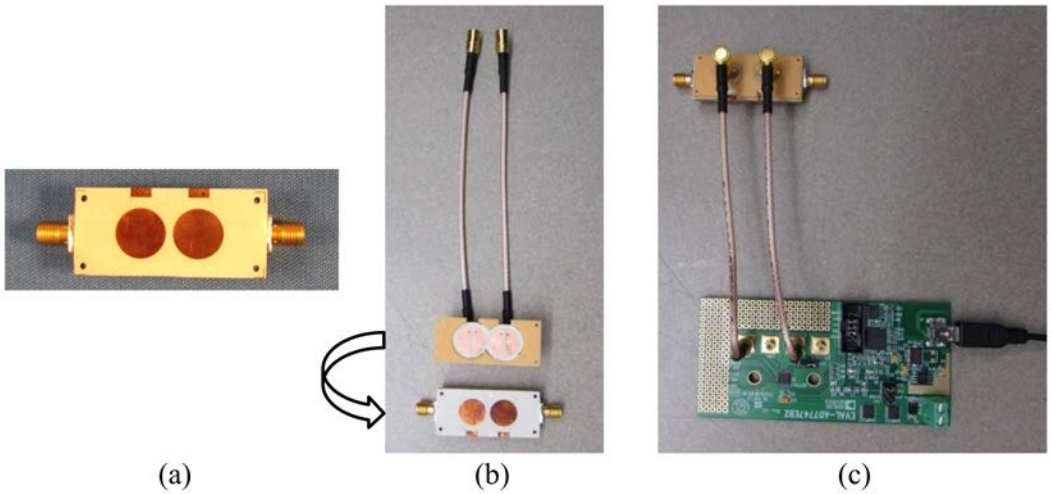

Figure 6.7: Monitoring capacitor assembly, (a) attachment of the isolation layer on top of bandpass filter, (b) mounting the monitoring capacitor on top of bandpass filter, and (c) the complete monitoring capacitor assembly connected to a CDC board.

any special curing process, due to the thin geometry of the monitoring capacitor, it started to gradually bend, making the structure unusable. Therefore, a second monitoring capacitor was fabricated using a Rogers RO 4350 circuit board. The detailed step-by-step fabrication process of the monitoring capac-

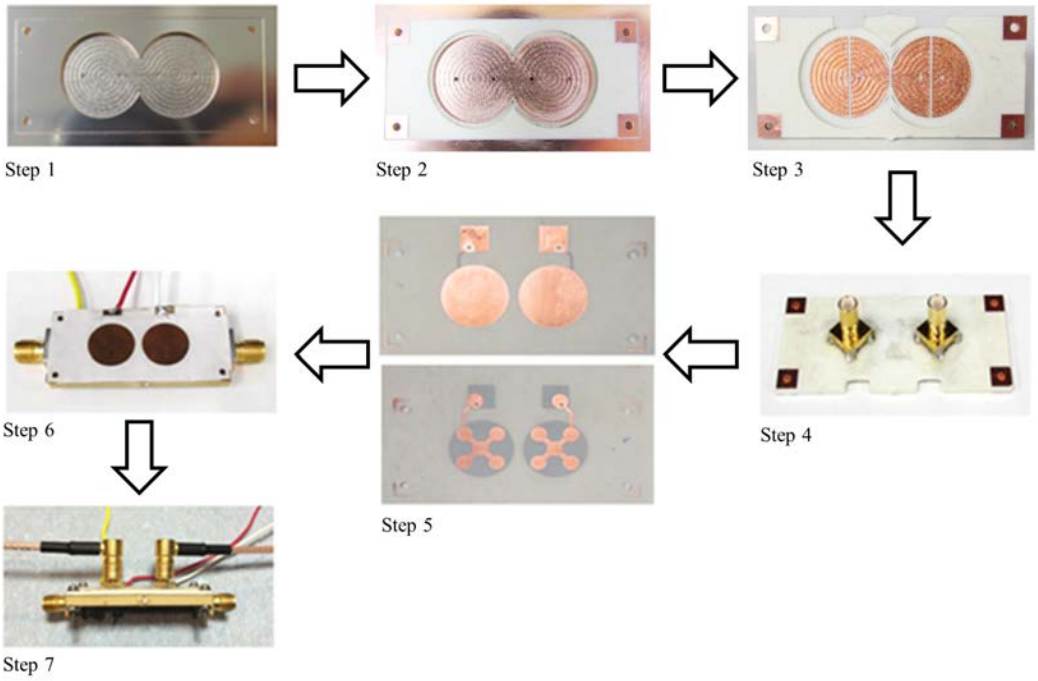

Figure 6.8: An overview of the fabrication process for the monitoring capacitor.

itor is shown in figure 6.8. In steps 1 through 3, the top electrodes of the monitoring capacitors are formed through milling, drilling, and plating of the RO 4350 board. Step 4 consists of mounting two SMB connectors on top of the board to provide the CDC interfaces. In step 5, an LCP layer is patterned and etched as the isolating layer between the top side of the piezoelectric actuators and the common electrode of each monitoring capacitor. The LCP layer is attached on top of the actuators using a conductive epoxy in step 6. Finally, in step 7 the monitoring structure is mounted on top of the filter.

In the next step, in order to simplify the implementation process of the digital feedback control system, a PC running an NI LabVIEW application is utilized. The PC temporarily replaces the μC that finally runs the feedback algorithm. The block diagram representation of the control system implementation is shown in figure 6.9. Since communication with the CDCs is performed

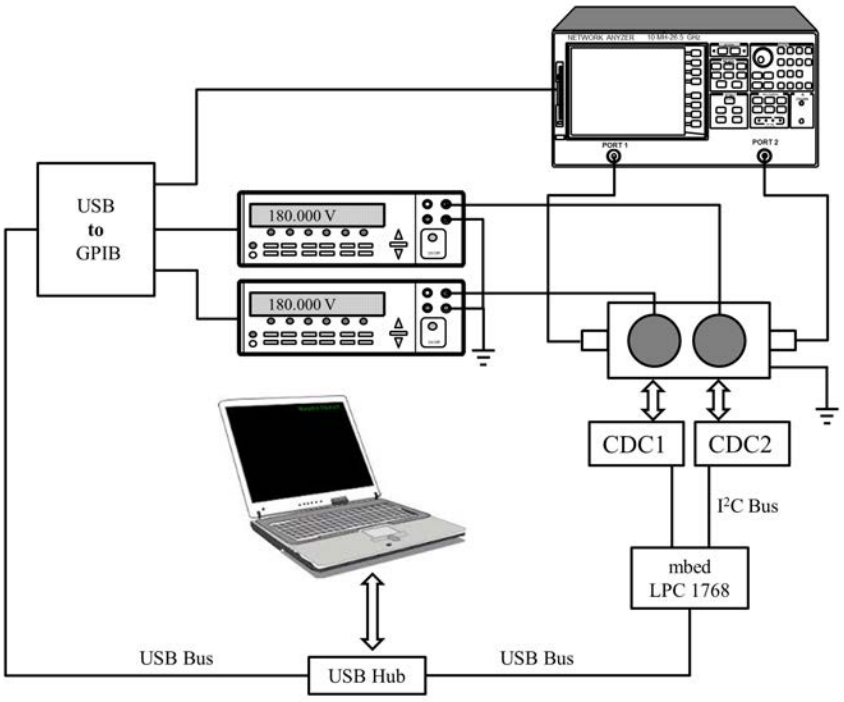

Figure 6.9: Block diagram of the initial control system.

through an I^2C serial bus, an mbed μC is used as a communication hub between the CDCs and the PC. In order to tune the filter, the PC, through the LabVIEW program, polls the mbed μC for capacitance measurements from the CDCs. Then, the capacitor values are compared to the required capacitances corresponding to the set frequency. LabVIEW then communicates with power supplies to apply the corresponding voltages to the piezoelectric actuators which are proportional to the digital offsets. This process continues until the desired frequency set-point is reached.

Due to the hysteresis that is inherent in the piezoelectric actuators, the output of the system without the monitoring capacitors is uncertain. In fact, the bending of the actuator is dependent on the excitation voltage and its previous position. Due to the physics and geometry of the filter and the monitoring structure, the center frequency of each resonator and the capacitance of

the monitoring capacitor are directly related to the movement of the actuators, regardless of the current or past excitation voltages. Therefore, the proposed monitoring structure exhibits a unique monotonic frequency-capacitance characteristic relationship. The algorithm used for the tuning includes an automatic characterization technique to initialize the process. The characterization procedure extracts this relationship (known as the characteristic function) for each filter pole. During this procedure, the NI LabVIEW application sweeps the biasing voltage for each filter pole individually via GPIB communication with the power supplies. Each pole moves from its low end frequency to its high end and vice versa. The filter return loss at each filter port, measured using the network analyzer, is captured for each applied bias voltage. At the same time the value of the monitoring capacitance is also measured and stored. The characterization routine eliminates the voltage dependence of the resonant frequency and provides the characteristic function for each pole. A typical characteristic function is shown in figure 6.10. The upward and downward sweep data matches well. Due to the sensitivity limitations of the CDCs, some noise is evident in the measured data, although the parasitic capacitance of cables and other peripheral circuits are de-embedded using a calibration procedure. This is while the resonant frequency variation versus upward and downward voltage sweep exhibits hysteresis behavior as shown in figure 6.11. The simplest voltage sweep method, as shown in figure 6.12, monotonically increases and decreases the bias voltage of each pole while keeping the second pole away as far as possible. This method, however, requires that the voltages of both poles change from one end to the other end, at the mid point. This change introduces mechanical stress coupling in the diaphragms of the resonators resulting in a large deflection change. Therefore, in order to mitigate

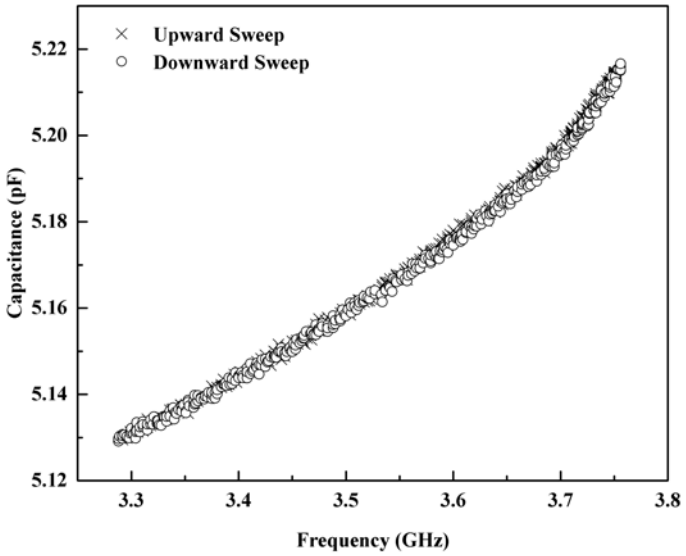

Figure 6.10: Typical capacitance-frequency characteristic function.

the effect of jumping from one voltage extreme to another, a new method for the voltage sweep was implemented. In the new method, shown in figure 6.13, phase shifted triangle waves are used to avoid pole-pole interaction. When this sweep method is utilized, the characterization data is better behaved compared to the data extracted from the previous method. The characteristic function depicted in figure 6.14 was obtained from this new voltage sweep method, while for generation of the characteristic function shown in figure 6.10 the first voltage sweep method was used.

Sub-range excitation of the actuators verifies that the characteristic function holds constant even when different starting and ending voltages are selected. In order to accurately measure the changes in the monitoring capacitors, the characterization procedure must be performed for each monitoring structure. During each iteration, a frequency set-point is chosen, and the characteristic function is evaluated giving a capacitance set-point for each

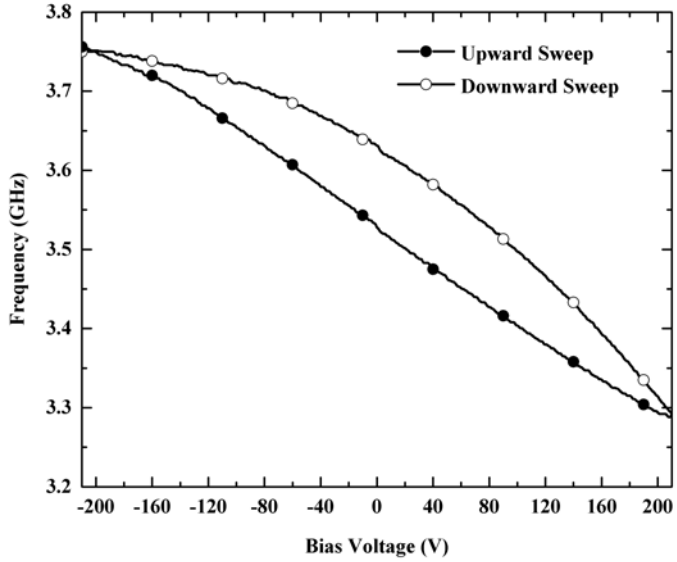

Figure 6.11: Typical resonant frequency as a function of ascending and descending bias voltage for a piezoelectric actuator.

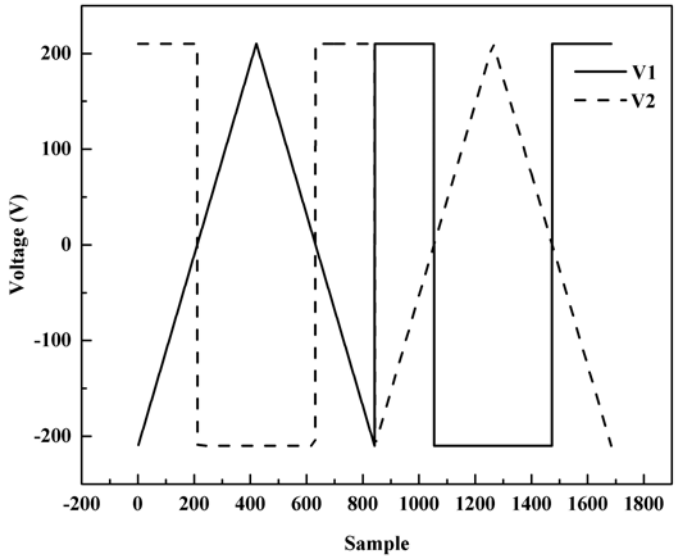

Figure 6.12: Simple voltage sweep method using the min/max interference avoidance method.

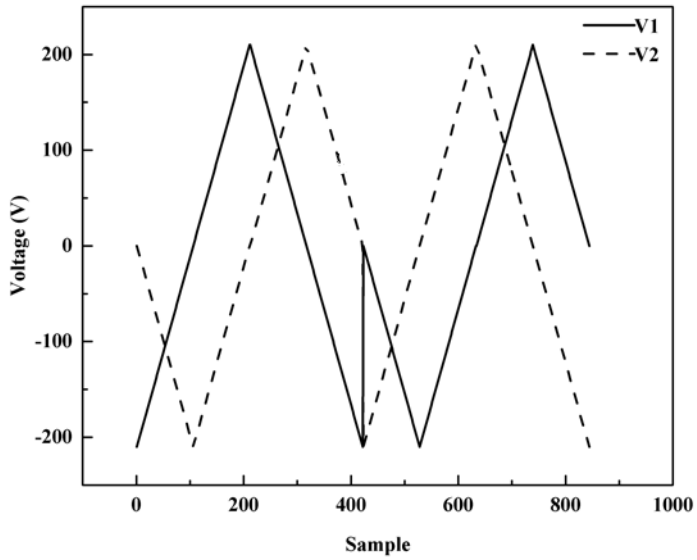

Figure 6.13: New voltage sweep method using the offset triangle wave approach.

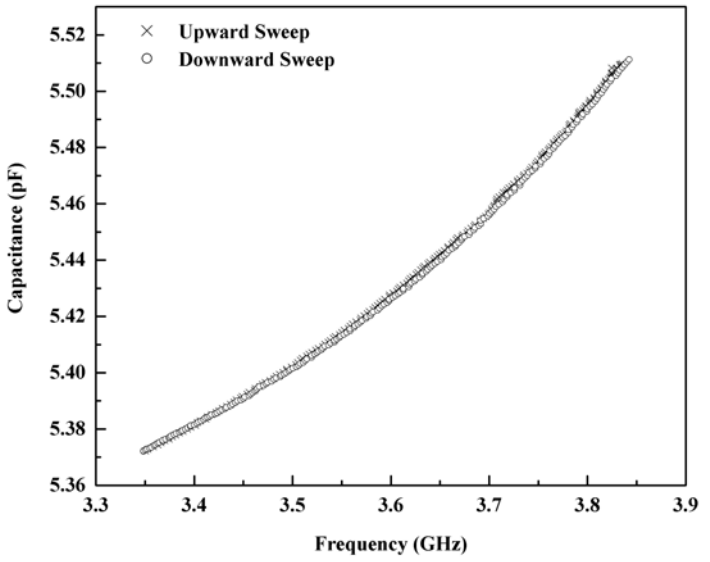

Figure 6.14: Capacitance-frequency characteristic function extracted using the offset triangle wave approach.

pole. Next, the control algorithm dynamically calculates an error based on the difference between the current capacitance of the pole, measured by the CDC, and the capacitance set-point. The error of each pole is then passed into the proportional derivative (PD) controller which generates a voltage output in response, reducing the current error. Finally, when the error reaches an acceptable threshold, the algorithm stops. Should the filter become detuned, the algorithm is re-enabled and returns the filter to the desired state.

6.4.1 Automatic Tuning Test Results

The 2%-fractional-bandwidth bandpass filter was tuned using the automatic tuning system. Figure 6.15 shows the transmission response of the filter, while tuned over the range from 3.3 to 3.7 GHz for both manual and automatic tuning using the closed-loop feedback control system. This figure shows that the control system is capable of tuning the filter as accurately as manual tuning. Additionally, this is accomplished with a greater speed. Table 6.1 summarizes the center frequency of the filter after being tuned manually and automatically for the same desired set point. These results verify the accuracy of the automatic tuning. The repeatability of the automatic frequency tuning is demonstrated by swapping one hundred times between two set-points as depicted in figure 6.16. The maximum deviation is 7 MHz, which is quite acceptable for practical applications. The relative percent error versus frequency for the insertion loss, in linear format, is shown in figure 6.17. The feedback control algorithm exhibits less than 2% error in the linear insertion loss scale. Finally, figure 6.18 compares the insertion loss and the bandwidth of the filter for both manual and automatic tuning. It can be seen that there is a very good agreement between the results in both cases. This also confirms the ef-

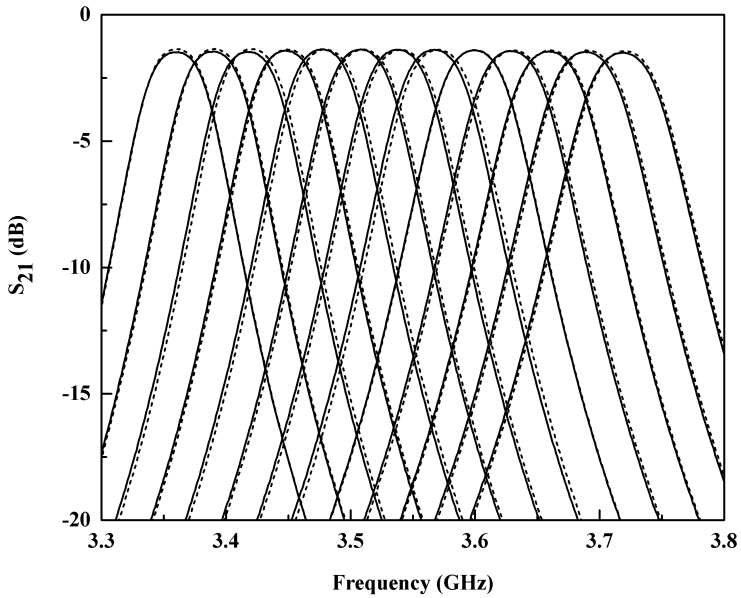

Figure 6.15: Tuning of the bandpass filter center frequency via manual tuning (dashed line) and automatic tuning (solid line).

fectiveness of the monitoring capacitors and the control algorithm. Video files showing both manual and automatic tuning of the 2%-fractional-bandwidth, bandpass filter are available upon request from Dr. Sigmarsson [145].

6.4.2 Standalone Automatic Filter Tuning System

In order to integrate all elements of the filter tuning system into a compact standalone control unit, the monitoring capacitors and the feedback circuits are fabricated on a single circuit board. This integration improves the accuracy of the control system due to elimination of nearly all parasitic capacitances. In the standalone system, the PC is eliminated from the feedback loop and instead an AVR μC (ATMEL Atmega328p) is used. The μC is used to implement the control algorithm and control all resonators in the filter (six resonators in the

Table 6.1: Comparison of the bandpass filter center frequency tuning

Frequency Set-Point (GHz)	**Manual Tuning (GHz)**	**Automatic Tuning (GHz)**
3.360	3.360	3.362
3.390	3.390	3.390
3.420	3.421	3.417
3.450	3.450	3.448
3.480	3.479	3.478
3.510	3.511	3.508
3.540	3.540	3.539
3.570	3.570	3.567
3.600	3.601	3.599
3.630	3.632	3.628
3.660	3.658	3.659
3.690	3.688	3.688
3.720	3.721	3.720

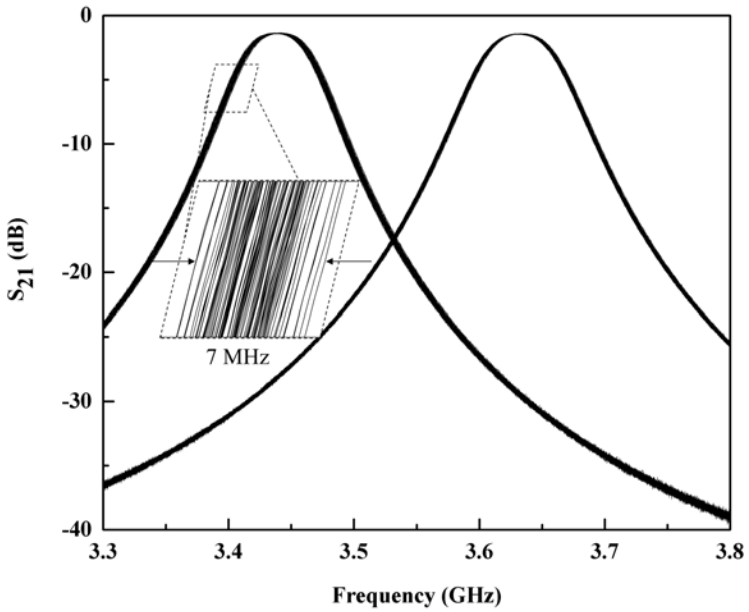

Figure 6.16: Tuning repeatability test with two set-points tuned 100 times each, with inset showing 7 MHz of deviation.

case of BP-BS filter cascade). A 16×2 dot matrix liquid crystal display (LCD) is directly connected to μC as a user interface. Also, a keypad communicating

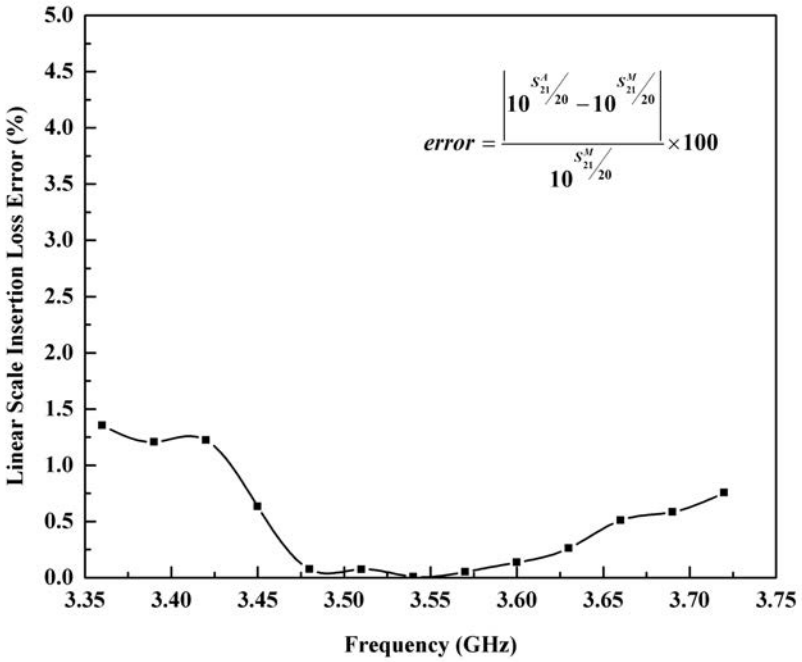

Figure 6.17: Linear scale error in insertion loss using automatic tuning relative to using manual tuning.

with the μC is used to allow the user to enter setpoint values. The circuits are designed modularly so that they can be used for automatic tuning of the bandpass, bandstop, and BP-BS filter cascades. In the final control system, only the filter and its monitoring capacitor is required to be replaced. Other boards like μC, amplifiers, and other peripherals are common. Instead of using six single DACs and I^2C buses for each of them, a single chip with six DACs is used to control all the analog channels. The AD5593 DAC from Analog Devices is a good candidate. It has a 12-bit DAC with eight channels as well as one I^2C interface. In this case, just one port of the μC is required for programming all the DACs. The complete block diagram of the control system implemented using the μC is shown in figure 6.19.

To control all six resonators, six CDCs and six DACs are required. Because the addresses of all CDCs on the I^2C bus are the same, an 8-channel multi-

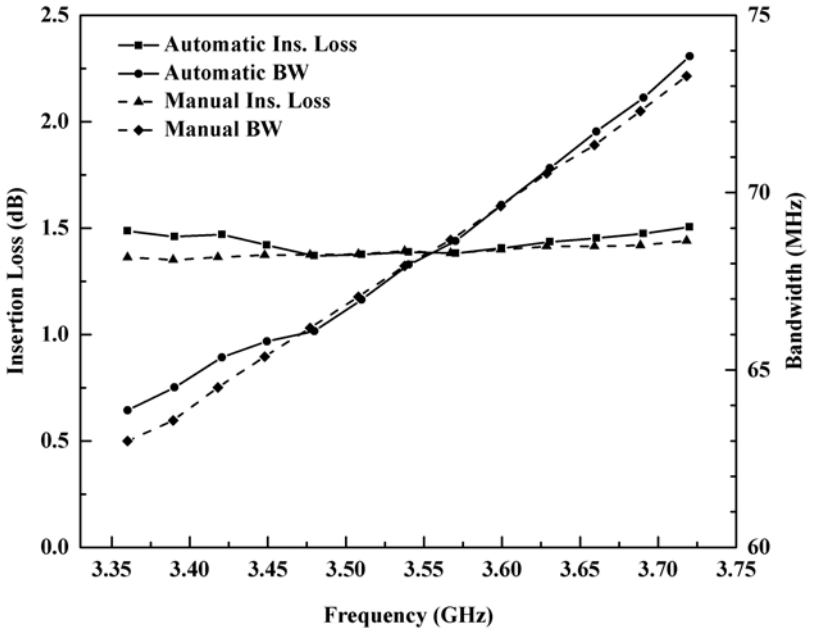

Figure 6.18: Measured insertion loss and bandwidth of the filter for automatic and manual tuning.

plexer is used to read the capacitance value from each CDC. Therefore, by programming the multiplexer through an I^2C bus, the desired channel will be selected. After reading the first CDC, the channel is indexed to read from the next CDC. This process is repeated until all CDCs are read. Since the DAC needs to be programmed through I^2C bus, it is also connected to the multiplexer as a slave device. The μC implements a PD controller, similar to the previous case, and the resonators are tuned sequentially. Once an acceptable error value for a resonator is reached, the next resonator is tuned.

As opposed to the fabricated monitoring capacitor for the bandpass filter, the monitoring capacitor for the bandstop filter and BP-BS filter cascade is fabricated in two pieces. One piece forms the top side of the monitoring capacitor and the second part is used as a spacer to control the required air

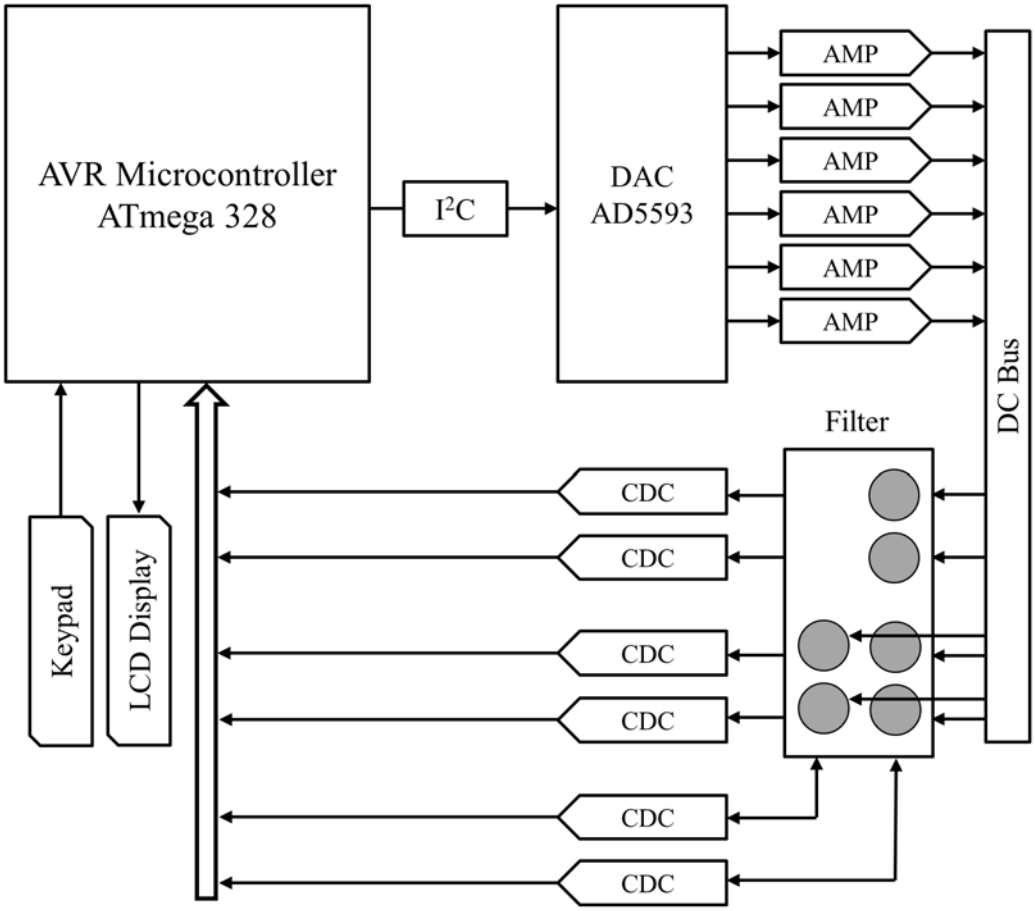

Figure 6.19: Block diagram of the control system implemented using a μC and its connections to the other peripheral circuits.

gap in the capacitor. This method greatly simplifies the fabrication process because the existing copper cladding layer on the PCB can be used as the capacitors' plates, and additional milling steps are avoided. These two pieces are installed on top of the filters using regular bolts and screws similar to the bandpass filter. The bottom sides of the monitoring capacitors are formed using an LCP layer as before. The fabricated monitoring capacitor for the bandstop filter and the BP-BS filter cascade are shown in figure 6.20 and figure 6.21, respectively.

A complete filter tuning system has been fabricated, packaged, and tested.

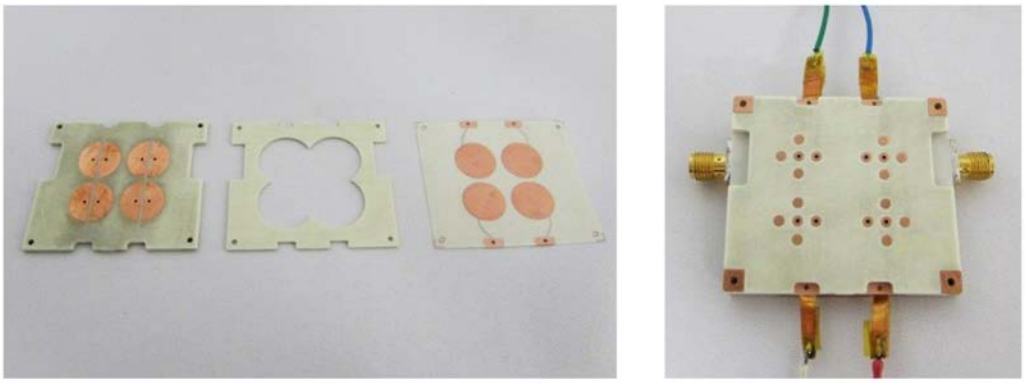

(a) (b)

Figure 6.20: Bandstop filter monitoring capacitor, (a) fabricated pieces for the monitoring capacitor, (b) assembled bandstop filter with the monitoring capacitor and biasing circuitry.

The system was developed as a universal package that can be used for bandpass filters, bandstop filters and filter cascades. Filter control, programming and calibration can be done without opening the package. The system is designed in a modular architecture structure that consists of six sections, which are: the power supply board, the high voltage (HV) amplifier board, the CDCs and filter, the μC and digital board, the keypad, and the LCD. A photograph showing the internal modules of the fabricated control system is in figure 6.22. This architecture provides the flexibility to change, debug, or redesign each section as needed. Every board is fabricated and tested separately. After building all the boards and mounting them in the box, a program for characterization is uploaded to the μC to extract the capacitance versus frequency curves. Then, the μC is loaded with the main program for tuning. The box has four ports as shown in figure 6.23:

1. 12 V DC input. The whole system requires one 12 V DC input. The built-in power supply board generates the required voltages for other

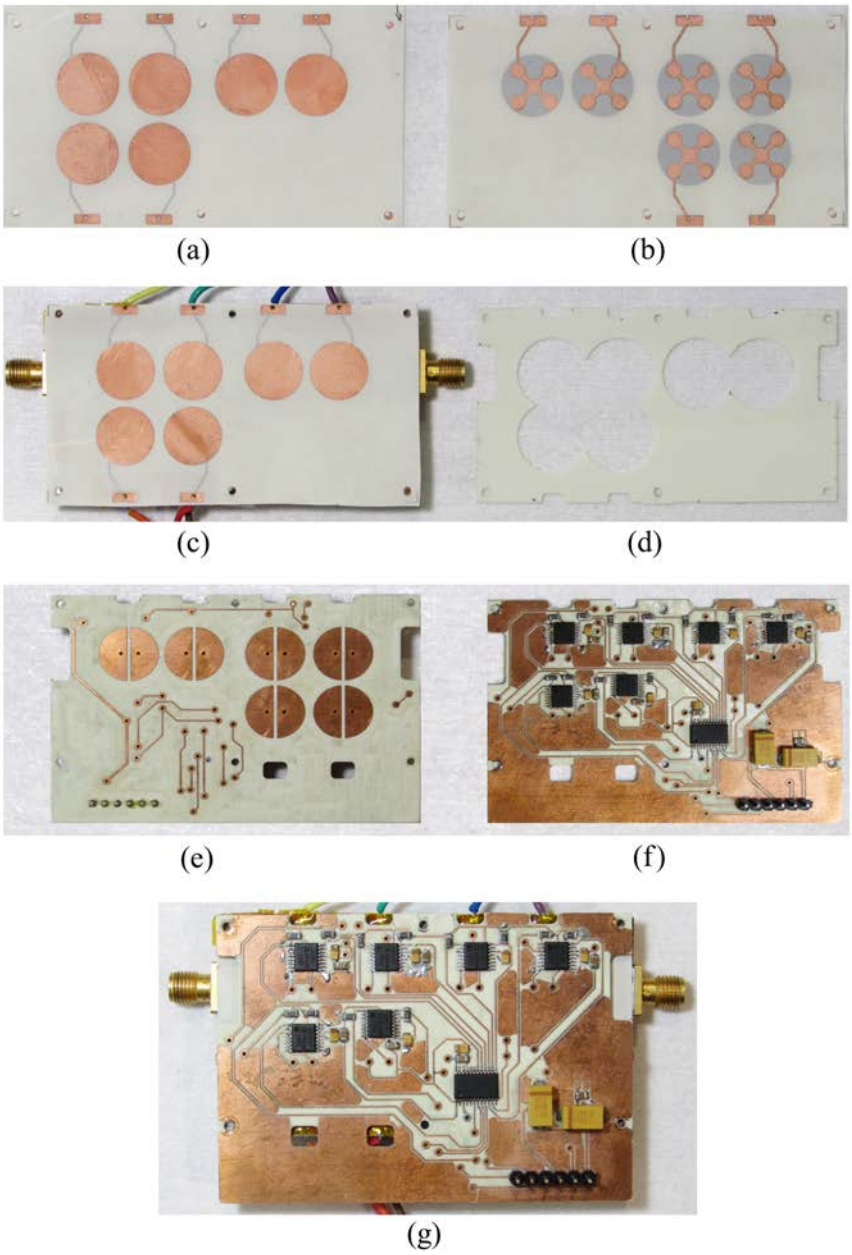

Figure 6.21: BP-PS filter cascade monitoring capacitor, (a) top view of the isolating LCP layer, (b) bottom view of the isolating LCP layer, (c) LCP layer attached on top of the filter cascade, (d) second piece of the monitoring capacitor used as a spacer to provide air gap in monitoring capacitor, (e) bottom view of the monitoring capacitor, (f) top view of the monitoring capacitor including the CDCs and the 8-channel multiplexer, and (g) complete monitoring capacitor assembled on top of filter cascade.

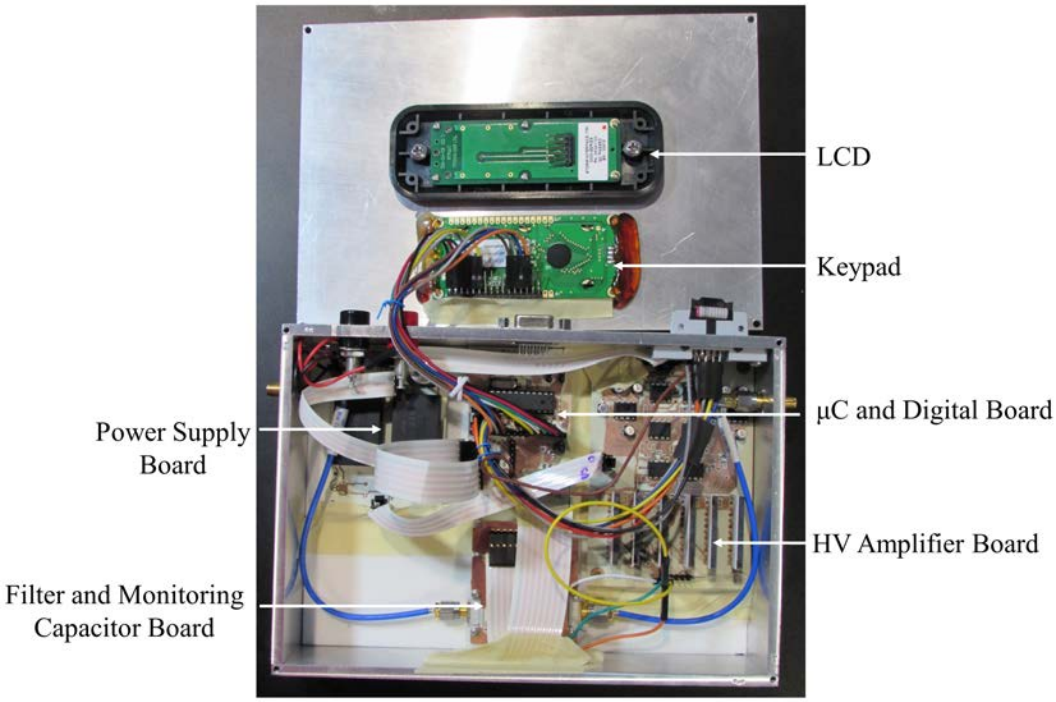

Figure 6.22: Internal view of the control system.

parts of the system. Total current concumption is approximately 400 mA.

2. Serial communication port. This port is placed on the box for serial communication with a PC through the RS-232 protocol. It is utilized for calibration and monitoring, as required.

3. Programming port. An IDC bulkhead connector is placed on the box for programming the μC and providing chip debug capability, which eliminates the need for opening the package to access the μC.

4. Input and output RF ports. There are two SMA bulkhead connector that are directly connected to the tunable filter ports using coaxial cables.

The automatic filter tuning unit was finalized with the filter integrated into the package. The filter is completely tuned using the control panel on the enclosure. The only input, other than the frequency set points, which

Figure 6.23: Ports of the packaged, tunable filter control system.

are provided by pressing the keypad buttons, is the 12 V DC biasing from a standard power supply. The packaged control system was successfully tested with multiple filters. Photographs of the control system tuning a bandpass, as well as a BP-BS filter cascade are shown in figure 6.24. Video files showing practical operation of the automatic filter tuning system are available upon request from Dr. Sigmarsson [145]. Details about the schematic and layout of the control system circuits, as well as the programs can also be obtained.

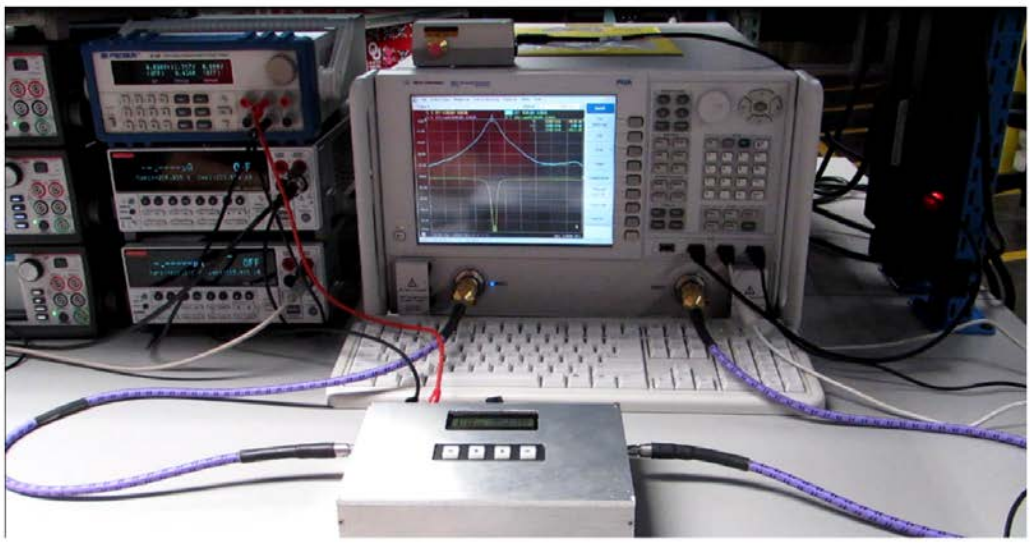

(a)

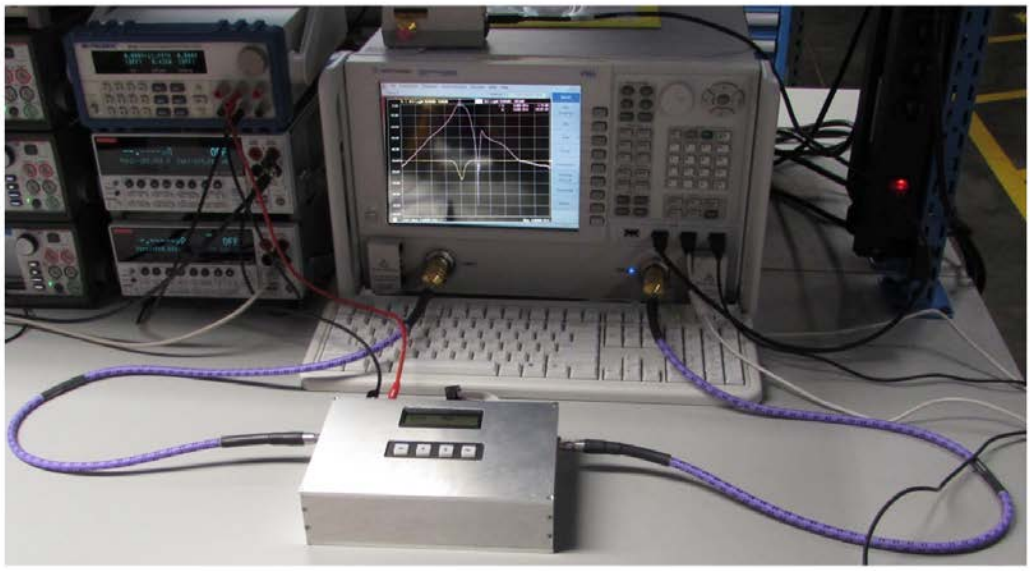

(b)

Figure 6.24: Final packaged control system tuning, (a) a bandpass filter, (b) a BP-BS filter cascade.

Chapter 7

Conclusions and Future Work

7.1 Summary of Work

The goal of this research was to develop state-of-the-art, frequency-agile, microwave filters for the current and next generation of radar systems capable of simultaneous transmit and receive. Many stringent system requirements are imposed upon reconfigurable filters in terms of high quality factor, wide tuning range, high power handling, etc. In this work, novel substrate-integrated evanescent-mode, cavity resonator filters have been presented and implemented to address such requirements.

First, substrate-integrated, evanescent-mode, cavity resonators as the building blocks for the design of higher-order filters were modeled and characterized. Active, tunable, substrate-integrated, evanescent-mode cavity resonators were also demonstrated. Design and implementation of active resonators opens up a new door for microwave filter designers to realize a wide range of low-loss reconfigurable filters for the next generation of spectrally-agile wireless systems. The substrate-integrated, evanescent-mode, cavity resonator was then utilized to design and develop a wide range of microwave tunable bandpass filters including low-loss (a fraction of a dB), wideband (up to 40% fractional

bandwidth), and high power tolerant (beyond 25 W) filters. As a step in the design of substrate-integrated, evanescent-mode, cavity tunable filter with high power handling capability, an accurate method for predicting the power handling capability of this type of filters was shown.

A novel approach for the design of microwave tunable bandstop filters based on phase cancellation was proposed. The coupling matrix synthesis method for this type of bandstop filter was presented. The expressions for re-synthesis of a new coupling matrix, when a predefined coupling value is forced into the matrix, were developed. Through this technique, the same coupling implementation methods used for bandpass filters can be used for designing and implementing bandstop filters. Therefore, despite the conventional bandstop filter design method, the bandstop filter can be implemented without source-to-load coupling. It was demonstrated that when this technique was used, substrate-integrated, evanescent-mode cavity bandstop filters can be implemented using a single substrate, which reduces the complexity of the fabrication process compared to currently reported implementations and makes it amenable for integration with other standard components.

In the next step, a compact single layer BP-BS cascade, with the capability of dynamically tuning its passband and stopband at any two independent frequencies within the desired frequency range, was presented. Due to the modular design approach, that was used to develop the filter cascade, the coupling matrix for the cascade was readily found by directly cascading the synthesized coupling matrices of the bandpass and bandstop filters. It was shown that a very short transmission line between the filters can be used as an NRN with minimum frequency dependency. Additionally, the special asynchronous tuning mode in the bandstop filter can be utilized to provide

the required matching between the filters. Tunable filter cascades were also demonstrated to improve system-level performance of a communications link by eliminating LNA compression as well as shaping the receiver noise floor.

Finally, an automatic control system, for tuning the tunable and reconfigurable filters developed during this research, was designed and implemented. The core idea was the creation of a second external cavity on top of the evanescent-mode cavity resonator in order to track the position of the movable diaphragm through a capacitance sensor. It was demonstrated that the relationship between the resonant frequency of the original cavity and variation of the capacitor in the monitoring structure is unique and can be used to eliminate the non-linear and non-repeatable behavior of piezoelectric actuators. A complete, packaged, and modular automatic control system was developed, fabricated, and successfully tested for tuning of both a simple tunable bandpass filter and a more complex BP-BS filter cascade.

7.1.1 Contributions

- Accurate modeling and characterization of substrate-integrated, evanescent-mode, cavity resonators.
- Development of active, tunable, substrate-integrated, evanescent-mode cavity resonators.
- Design and fabrication of high-Q tunable bandpass filters with insertion losses as low as a fraction of a dB.
- Design and implementation of wideband tunable bandpass filters with fractional bandwidth up to 40%.
- Design and fabrication of tunable, substrate-integrated, evanescent-mode

cavity bandpass filters with power handling capabilities of more than 25 W along with an accurate prediction method.

- Design, development, and implementation of single layer, substrate-integrated, evanescent-mode, cavity tunable bandstop filters.

- Design, development, and implementation of compact single layer, substrate-integrated, evanescent-mode cavity BP-BS filter cascades with the capability of dynamic relocation of transmission zeros and passband.

- Demonstration of the system-level benefits of using BP-BS filter cascades instead of conventional bandpass filters in systems with high dynamic range.

- Design, development, and implementation of a standalone modular automatic control system for automatic tuning of evanescent-mode cavity resonators and filters.

7.2 Future Work

The work presented in this dissertation can be expanded in the following areas.

7.2.1 Theory Expansion for Active Resonator Design

One of benefits of active resonators compared to their tradition passive peers is improved unloaded quality factor through compensation of loss in the resonator. However, this improvement is yet to be investigated quantitatively. The other inherent issue with this type of resonators, as mentioned before, is the stability of the active resonator. A more accurate and systematic approach for the design of stable active resonators is required. Also, investigation

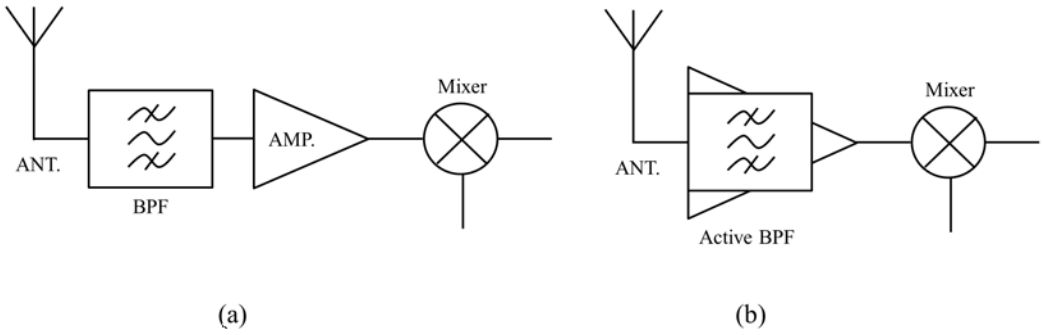

Figure 7.1: Two front-end configurations, (a) classic configuration, (b) configuration based on active filter.

of other active circuit topologies in addition to negative resistance circuits is necessary.

The other important topic that is required to be expanded is noise analysis of active resonator filters. Figure 7.1 shows two different front-end scenarios. The configuration in figure 7.1(a) is the classic front-end in current radio systems where the received signal is first filtered and then amplified. The noise figure of such system can be easily calculated from Friis' formula. However, in the configuration shown in figure 7.1(b), the received signal is simultaneously filtered and amplified using an active filter. If both systems have the same chain gain, and if both filters have the same order, it is believed that the second configuration adds less noise to the signal. An accurate noise analysis of this configuration along with a one-to-one comparison between system properties of both configurations is considered as an important step forward in the development of active microwave filters for future applications.

7.2.2 All-pass, Bandpass, and Bandstop Reconfigurable Filters

In the design of the bandstop filter using phase cancellation, it was seen that by combining two bandpass filters, a bandstop filter notch can be embedded in the passband of a wideband bandpass filter. Figure 7.2 shows the coupling routing diagram of the designed bandstop filter with some modifications. Three RF switches have been included in the filter structure that can be used for implementing additional reconfigurability in the filter.

If only switch S_1 is closed, a wideband bandpass filter between the ports can be used as all-pass filter inside the filter passband. Although the filter bandwidth is not unlimited, the wide tunability feature of the bandpass filter can be used to compensate for this limitation. When switch S_1 is open and switches S_2 and S_3 are closed, a narrowband (in this example, fourth-order) tunable bandpass filter is placed between the ports. Finally, when all three switches are closed, the previously demonstrated tunable bandstop filter will be available. Therefore, by including three RF switches in the design a reconfigurable filter with all-pass, bandpass, and bandstop responses can be achieved. The frequency responses of such a reconfigurable filter for all three states with all resonators tuned at 3.3 GHz is shown in figure 7.3.

7.2.3 Filter Cascade Design Using Slow Resonating Node

In Chapter 5, it was discussed that an NRN may have any arbitrary frequency-independent susceptance (even zero). In narrowband applications, any susceptance with low frequency variation can be used to approximately model the NRN. When two filters with equal admittance inverters at their connecting ports are cascaded, the NRN with zero susceptance provides the simplest so-

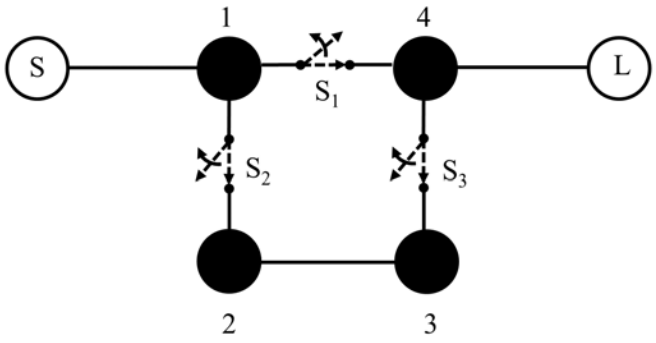

Figure 7.2: Coupling routing diagram for a reconfigurable filter with all-pass, bandpass, and bandstop responses.

lution. Therefore, the cascade can be formed without any physical element between the filters. Then, the two adjacent admittance inverters can be replaced with a transformer with the turn ratio of -1:1. This transformer actually does not do anything except change the phase of signal from $+90^\circ$ to -90° which is not important for this analysis. The transformer can, therefore, be eliminated without any impact on the filter response. This allows tandem placements of two resonators. Since the nodal capacitance will be doubled, but the inductance will be reduced by a factor of two, the resonant frequency will not change. This means that as long as the change in the impedance level of the node can be compensated, one of the resonators can be eliminated. In order to compensate the effect of eliminating one of the resonators, the values of the adjacent admittance inverters are multiplied by $\frac{1}{\sqrt{2}}$. This factor is introduced because the capacitance of the node has been reduced by half. It can be shown that the response of the new network is identical to the original cascade. This procedure works best when the two admittance inverters have the same value, which leads to a transformer with a turn ratio of -1:1. When inverters with different values are cascaded (similar to BP-BS filter cascade), the NRN can be implemented with a resonator that provides a non-zero sus-

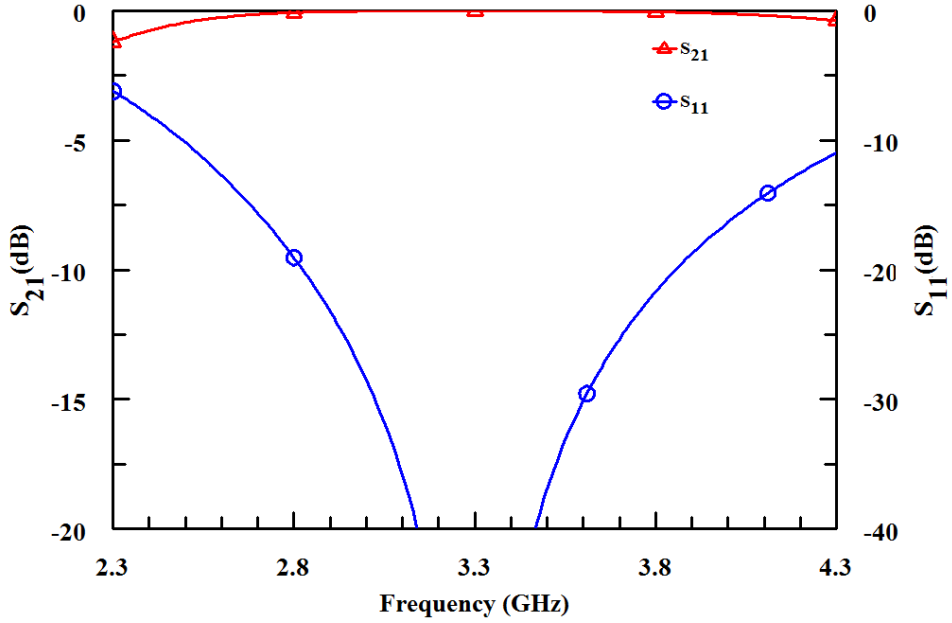

(a)

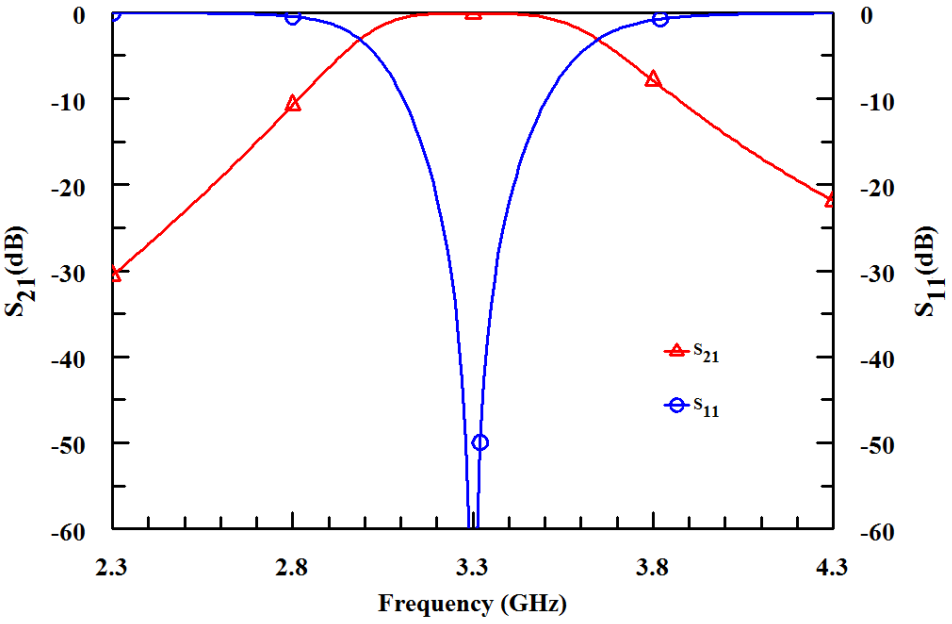

(b)

Figure 7.3: Responses of a typical reconfigurable filter, (a) allpass, (b) bandpass.

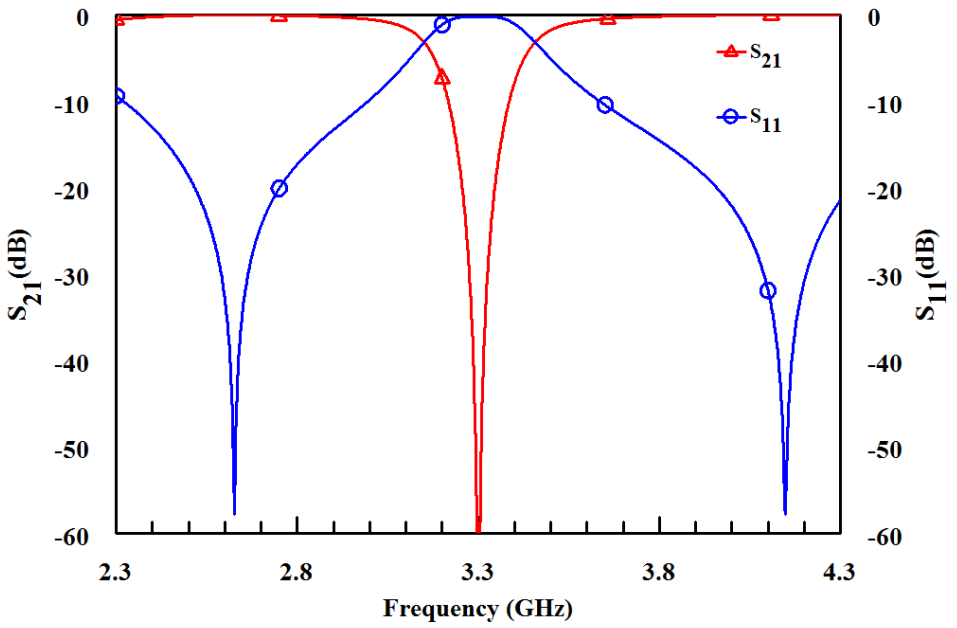

(c)

Figure 7.3: (continued) , and (c) bandstop.

ceptance. In this case, the NRN can be considered a parallel resonator similar to the main filter resonators. The only difference is that this resonator has much less frequency dependency. The new NRN can nominally resonate at either the bandpass filter center frequency, or the bandstop notch frequency, or even at some frequencies between these two. Therefore, this type of resonator is called a Slow Resonating Node (SRN). This resonator does not add a zero or a pole to the filter response as it is essentially transparent to the network nodal admittance. In fact, at the resonant frequency the added admittance to the node is zero and due to the very slow change in the frequency response of the resonator, SRN does not change the admittance of the node much. One way to have a resonator with a slow varying susceptance is to use a resonator with higher inductance and lower capacitance values (but still the same product) compared to the filter's resonator. Simulation shows that due to the slow varying behavior of the SRN, its quality factor does not have much effect on

the cascade response.

The introduction of the SRN concept is important, since it allows the value of couplings in the original individual filters to be maintained. Therefore, an indirect method can be used to modularly synthesize the coupling matrix of the filter cascade from the coupling matrices of the original filters. The coupling matrix of the cascade configuration of any two filters, can be constructed in lowpass domain according the following rules:

1. The coupling matrix of each filter is synthesized using any regular method.

2. The coupling matrices are then joined together using a SRN. Therefore, the element in the diagonal of the cascade coupling matrix must be the resonant frequency of the SRN.

3. All other couplings in the row and column crossing at SRN must be scaled by $\frac{1}{\sqrt{C_{SRN}}}$, where C_{SRN} is the capacitance of the slow resonating node.

To describe the reason for this scaling factor, the definition of the coupling matrix is considered. In (2.39), it was shown that the impedance matrix of the two-port lowpass network can be written as

$$[z'] = \mathbf{R} + j\mathbf{M} + s\mathbf{I} \ . \tag{7.1}$$

In order to have the identity matrix as the third term, all the diagonal elements in the impedance matrix in the form of $sC + jB$ are normalized by multiplying all rows and columns by $\frac{1}{\sqrt{C_{pi}}}$. This converts all diagonal elements to $s + jB$. Finally, all frequency variables on the main diagonal of the matrix are separated and represented as $s\mathbf{I}$, while $\frac{B_{pi}}{C_{pi}}$ forms the main diagonal of $\mathbf{M}$, representing the offset frequency from zero.

This can be described from another point of view in the bandpass domain. Since, in the filter cascade, the amount of energy passing through the inverters should not change, all admittance inverters must be kept at the same value before and after making the cascade. However, since the external couplings will no longer be external couplings after the connection of the filters, their value must be calculated using

$$J_{k,k+1} = \omega_0 \Delta \sqrt{C_{pi} C_{p(i+1)}}\ m_{k,k+1} \tag{7.2}$$

instead of

$$J_{0,1} = \sqrt{\omega_0 \Delta G_S C_1}\ m_{0,1} \tag{7.3}$$

or

$$J_{N,N+1} = \sqrt{\omega_0 \Delta G_L C_N}\ m_{N,N+1}\ . \tag{7.4}$$

A comparison of these three equations shows that the coupling value should be calculated as

$$m_{k,k+1} = \sqrt{\frac{G_s}{\omega_0 \Delta C_{SRN}}}\ m_{0,1}\ . \tag{7.5}$$

A closer look at the scaling factor for the coupling value (7.5), reveals that it is the same as the lowpass domain coupling scaling factor, $\frac{1}{\sqrt{C_{SRN}}}$ which has been transformed to bandpass domain by using the conventional lowpass-bandpass transformation ($\frac{C}{\omega_0 \Delta} \leftarrow C$) and impedance scaled using ($CG_S \leftarrow C$).

In short, the coupling matrix of a filter cascade designed using SRN can

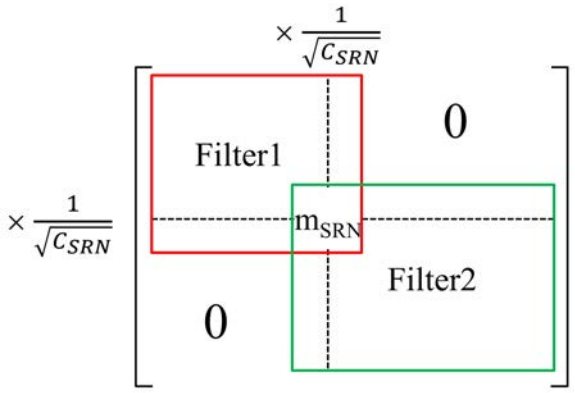

Figure 7.4: Construction of the coupling matrix for a filter cascade using SRN.

be graphically summarized as shown in figure 7.4. Implementation of a filter cascade using this method for wideband applications will be of great interest to the microwave community.

References

[1] W. J. Chappell, E. J. Naglich, C. Maxey, and A. C. Guyette, "Putting the radio in "software-defined radio": hardware developments for adaptable RF systems", *Proc. IEEE*, vol. 102, no. 3, pp. 307–320, Mar. 2014.

[2] E. J. Naglich, J. Lee, D. Peroulis, and W. J. Chappell, "Switchless tunable bandstop-to-all-pass reconfigurable filter", *IEEE Trans. Microw. Theory Techn.*, vol. 60, no. 5, pp. 1258–1265, May 2012.

[3] R. Gomez-Garcia, M.-A. Sanchez-Soriano, K.-W. Tam, and Q. Xue, "Switchless tunable bandstop-to-all-pass reconfigurable filter", *IEEE Microw. Mag.*, vol. 15, no. 5, pp. 43–45, Aug. 2014.

[4] J. Lee, E. J. Naglich, H. H. Sigmarsson, D. Peroulis, and W. J. Chappell, "New bandstop filter circuit topology and its application to design of a bandstop-to-bandpass switchable filter", *IEEE Trans. Microw. Theory Techn.*, vol. 61, no. 3, pp. 1114–1123, Mar. 2013.

[5] E. J. Naglich, J. Lee, D. Peroulis, and W. Chappell, "Tunable, substrate integrated, high-Q filter cascade for high isolation", in *IEEE MTT-S Int. Microw. Symp. Dig.*, IEEE, 2010, pp. 1468–1471.

[6] E. J. Naglich, J. Lee, D. Peroulis, and W. J. Chappell, "Bandpass–bandstop filter cascade performance over wide frequency tuning ranges", *IEEE Trans. Microw. Theory Techn.*, vol. 58, no. 12, pp. 3945–3953, 2010.

[7] H. H. Sigmarsson, E. Naglich, J. Lee, D. Peroulis, and W. Chappell, "Tunable bandpass and bandstop filter cascade for dynamic pole allocation", in *IEEE AP-S Int. Symp.*, 2012, pp. 1–2.

[8] T.-C. Lee, J. Lee, and D. Peroulis, "Dynamic bandpass filter shape and interference cancellation control utilizing bandpass–bandstop filter

cascade", *IEEE Trans. Microw. Theory Techn.*, vol. 63, no. 8, pp. 2526–2539, 2015.

[9] M. Makimoto and S. Yamashita, *Microwave resonators and filters for wireless communication: theory, design and application*. Springer Science & Business Media, 2001, vol. 4.

[10] A. I. Zverev, *Handbook of filter synthesis*. New York, NY, USA: Wiley, 1967.

[11] S. Darlington, "Synthesis of reactance 4-poles which produce prescribed insertion loss characteristics, including special applications to filter design", *IEEE transactions on circuits and systems*, vol. 18, no. 1, pp. 257–353, 1939.

[12] ——, "A history of network synthesis and filter theory for circuits composed of resistors, inductors, and capacitors", *IEEE transactions on circuits and systems*, vol. 31, no. 1, pp. 3–13, 1984.

[13] W. Cauer, *Synthesis of linear communication networks*. New York, NY, USA: McGraw-Hill, 1958.

[14] D. M. Pozar, *Microwave Engineering 4e*. New York, NY, USA: Wiley, 2012.

[15] R. Levy and S. B. Cohn, "A history of microwave filter research, design, and development", *IEEE Trans. Microw. Theory Techn.*, vol. 32, no. 9, pp. 1055–1067, 1984.

[16] E. M. T. Jones, "Coupled-strip-transmission-line filters and directional couplers", *IRE Trans. Microw. Theory Techn.*, vol. 4, no. 2, pp. 75–81, 1956.

[17] S. B. Cohn, "Dissipation loss in multiple-coupled-resonator filters", *Proc. IRE*, vol. 47, no. 8, pp. 1342–1348, 1959.

[18] ——, "Direct-coupled-resonator filters", *Proc. IRE*, vol. 45, no. 2, pp. 187–196, 1957.

[19] ——, "Parallel-coupled transmission-line-resonator filters", *IRE Trans. Microw. Theory Techn.*, vol. 6, no. 2, pp. 223–231, 1958.

[20] G. L. Matthaei, L. Young, and E. M. T. Jones, *Microwave filters, impedance matching networks, and coupling structures*. Norwood, MA, USA: Artech House, 1980.

[21] D. D. Grieg and H. F. Engelmann, "Microstrip-a new transmission technique for the klilomegacycle range", *Proc. IRE*, vol. 40, no. 12, pp. 1644–1650, 1952.

[22] R. Levy, R. V. Snyder, and G. Matthaei, "Design of microwave filters", *IEEE Trans. Microw. Theory Techn.*, vol. 50, no. 3, pp. 783–793, 2002.

[23] M. Dishal, "Alignment and adjustment of synchronously tuned multiple-resonant-circuit filters", *Proc. IRE*, vol. 39, no. 11, pp. 1448–1455, 1951.

[24] M Dishal, "A simple design procedure for small percentage bandwidth round-rod interdigital filters (correspondence)", *IEEE Trans. Microw. Theory Techn.*, pp. 696–698, 1965.

[25] J. S. Wong, "Microstrip tapped-line filter design", *IEEE Trans. Microw. Theory Techn.*, vol. 27, pp. 44–50, 1979.

[26] R. J. Cameron, "Advanced filter synthesis", *IEEE Microw. Mag.*, vol. 12, no. 6, pp. 42–61, 2011.

[27] R. M. Kurzrok, "General three-resonator filters in waveguide", *IEEE Trans. Microw. Theory Techn.*, vol. 14, no. 1, pp. 46–47, 1966.

[28] R. Kurzrok, "General four-resonator filters at microwave frequencies", *IEEE Trans. Microw. Theory Techn.*, vol. 14, no. 6, pp. 295–296, 1966.

[29] A. E. Atia and A. E. Williams, "New types of waveguide bandpass filters for satellite transponders", *COMSAT Tech. Review*, vol. 1, no. 1, pp. 20–43, 1971.

[30] ——, "Narrow-bandpass waveguide filters", *IEEE Trans. Microw. Theory Techn.*, vol. 20, no. 4, pp. 258–265, 1972.

[31] ——, "Non-minimum phase, optimum amplitude, bandpass waveguide filters", in *IEEE G-MTT Int. Microw. Symp.*, 1973, pp. 210–212.

[32] A. E. Atia, A. E. Williams, and R. W. Newcomb, "Narrow-band multiple-coupled cavity synthesis", *IEEE Trans. Circuit Syst.*, vol. 21, no. 5, pp. 649–655, 1974.

[33] R. Cameron, "General prototype network-synthesis methods for microwave filters", *European Space Agency (ESA) Journal*, vol. 6, no. 2, pp. 193–206, 1982.

[34] D. Deslandes and K. Wu, "Integrated microstrip and rectangular waveguide in planar form", *IEEE Microw. Wireless Compon. Lett.*, vol. 11, no. 2, pp. 68–70, 2001.

[35] X.-P. Chen and K. Wu, "Substrate integrated waveguide filter: basic design rules and fundamental structure features", *IEEE Microw. Mag.*, vol. 15, no. 5, pp. 108–116, 2014.

[36] D. Deslandes and K. Wu, "Accurate modeling, wave mechanisms, and design considerations of a substrate integrated waveguide", *IEEE Trans. Microw. Theory Techn.*, vol. 54, no. 6, pp. 2516–2526, Jun. 2006.

[37] Y. Cassivi, L Perregrini, P. Arcioni, M Bressan, K. Wu, and G Conciauro, "Dispersion characteristics of substrate integrated rectangular waveguide", *IEEE Microw. Wireless Compon. Lett.*, vol. 12, no. 9, pp. 333–335, 2002.

[38] F. Xu and K. Wu, "Guided-wave and leakage characteristics of substrate integrated waveguide", *IEEE Trans. Microw. Theory Techn.*, vol. 53, no. 1, pp. 66–73, 2005.

[39] W. Che, K. Deng, D. Wang, and Y. Chow, "Analytical equivalence between substrate-integrated waveguide and rectangular waveguide", *IET Microw. Antennas Propag.*, vol. 2, no. 1, pp. 35–41, 2008.

[40] K. Entesari, A. P. Saghati, V. Sekar, and M. Armendariz, "Tunable SIW structures: antennas, VCOs, and filters", *IEEE Microw. Mag.*, vol. 16, no. 5, pp. 34–54, 2015.

[41] X.-P. Chen and K. Wu, "Substrate integrated waveguide filters: design techniques and structure innovations", *IEEE Microw. Mag.*, vol. 15, no. 6, pp. 121–133, 2014.

[42] ——, "Substrate integrated waveguide filters: practical aspects and design considerations", *IEEE Microw. Mag.*, vol. 15, no. 7, pp. 75–83, 2014.

[43] D. K. Cheng, *Field and Wave Electromagnetics, 2nd Ed.* New York, NY, USA: Addison-Wesley, 1989.

[44] K. Fujisawa, "General treatment of klystron resonant cavities", *IRE Trans. Microw. Theory Techn.*, vol. 6, no. 4, pp. 344–358, 1958.

[45] R. F. Harrington, *Time-harmonic electromagnetic fields.* New York, NY, USA: McGraw-Hill, 1961.

[46] T. Moreno, *Microwave Transmission Design Data.* New York, NY, USA: McGraw-Hill, 1948.

[47] I. Lebedev and E. Guttsait, "Resonator of the subcritical waveguide type", *Radiotekh. Elecktron*, vol. 1, no. 10, p. 1303, 1956.

[48] E. T. Jaynes, "Ghost modes in imperfect waveguides", *Proc. IRE*, vol. 46, no. 2, pp. 416–418, 1958.

[49] G. F. Craven and C. Mok, "The design of evanescent mode waveguide bandpass filters for a prescribed insertion loss characteristic", *IEEE Trans. Microw. Theory Techn.*, vol. 19, no. 3, pp. 295–308, 1971.

[50] R. V. Snyder, "New application of evanescent mode waveguide to filter design", *IEEE Trans. Microw. Theory Techn.*, vol. 25, pp. 1013–1021, 1977.

[51] H. Joshi, H. H. Sigmarsson, S. Moon, D. Peroulis, and W. Chappell, "High-Q fully reconfigurable tunable bandpass filters", *IEEE Trans. Microw. Theory Techn.*, vol. 57, no. 12, pp. 3525–3533, 2009.

[52] D. Peroulis, E. Naglich, M. Sinani, and M. Hickle, "Tuned to resonance: transfer-function-adaptive filters in evanescent-mode cavity-resonator technology", *IEEE Microw. Mag.*, vol. 15, no. 5, pp. 55–69, 2014.

[53] X. Liu, L. P. Katehi, W. J. Chappell, and D. Peroulis, "High-Q tunable microwave cavity resonators and filters using SOI-based RF MEMS tuners", *J. Microelectromech. Syst.*, vol. 19, no. 4, pp. 774–784, 2010.

[54] L. Rainie, *Cell phone ownership hits 91 percent of adults*, The Pew Research Center, 2013, (Accessed: 2 Nov. 2015). [Online]. Available: `http://www.pewresearch.org/fact-tank/2013/06/06/cell-phone-ownership-hits-91-of-adults/`.

[55] A. Smith, *Smartphone ownership 2013*, The Pew Research Center, 2013, (Accessed: 2 Nov. 2015). [Online]. Available: `http://www.pewinternet.org/2013/06/05/smartphone-ownership-2013/`.

[56] C. Baylis, M. Fellows, L. Cohen, and R. J. Marks, "Solving the spectrum crisis: intelligent, reconfigurable microwave transmitter amplifiers for cognitive radar", *IEEE Microw. Mag.*, vol. 15, no. 5, pp. 94–107, 2014.

[57] W. H. Lehr, "The path to market success for dynamic spectrum access technology", *IEEE Commun. Mag.*, vol. 45, no. 8, pp. 96–103, May 2007.

[58] Q. Zhao and B. M. Sadler, "A survey of dynamic spectrum access", *IEEE Signal Process. Mag.*, vol. 24, no. 3, pp. 79–89, May 2007.

[59] S. Haykin, "Cognitive radar: a way of the future", *IEEE Signal Process. Mag.*, vol. 23, no. 1, pp. 30–40, Jan. 2006.

[60] J. R. Guerci, *Cognitive Radar: The Knowledge-Aided Fully Adaptive Approach*. Norwood, MA, USA: Artech House, 2010.

[61] J de Graaf, H Faust, J Alatishe, and S Talapatra, "Generation of spectrally confined transmitted radar waveforms: experimental results", in *2006 IEEE Conference on Radar*, IEEE, 2006, pp. 1–8.

[62] M. Van Valkenburg, *Modern Network Synthesis*. New York, NY, USA: Wiely, 1964.

[63] H. Y. Lam, *Analog and digital filters; design and realization*. Englewood Cliffs, NJ, USA: Prentice Hall, 1979.

[64] R. J. Cameron, C. M. Kudsia, and R. R. Mansour, *Microwave filters for communication systems*. Hoboken, NJ, USA: Wiley-Interscience, 2007.

[65] I. C. Hunter, *Theory and design of microwave filters*. London, United Kingdom: IET, 2001.

[66] J.-S. Hong, *Microstrip Filters for RF/Microwave Applications*. Hoboken, NJ, USA: Wiley, 2011.

[67] D. Kajfez and E. J. Hwan, "Q-factor measurement with network analyzer", *IEEE Trans. Microw. Theory Techn.*, vol. 32, no. 7, pp. 666–670, 1984.

[68] J. B. Ness, "A unified approach to the design, measurement, and tuning of coupled-resonator filters", *IEEE Trans. Microw. Theory Techn.*, vol. 46, no. 4, pp. 343–351, 1998.

[69] J. B. Thomas, "Cross coupling in coaxial cavity filters – a tutorial overview", *IEEE Trans. Microw. Theory Techn.*, vol. 51, no. 4, pp. 1368–1376, 2003.

[70] S. Amari and U. Rosenberg, "Direct synthesis of a new class of bandstop filters", *IEEE Trans. Microw. Theory Techn.*, vol. 52, no. 2, pp. 607–616, 2004.

[71] S. Amari, "Synthesis of cross-coupled resonator filters using an analytical gradient-based optimization technique", *IEEE Trans. Microw. Theory Techn.*, vol. 48, no. 9, pp. 1559–1564, 2000.

[72] W. A. Atia, K. A. Zaki, and A. E. Atia, "Synthesis of general topology multiple coupled resonator filters by optimization", in *IEEE MTT-S Int. Microw. Symp. Dig.*, IEEE, vol. 2, 1998, pp. 821–824.

[73] M. Bekheit, S. Amari, and W. Menzel, "Modeling and optimization of compact microwave bandpass filters", *IEEE Trans. Microw. Theory Techn.*, vol. 56, no. 2, pp. 420–430, 2008.

[74] H. Bell, "The coupling matrix in low-pass prototype filters", *IEEE Microw. Mag.*, vol. 2, no. 8, pp. 70–76, 2007.

[75] S.-J. Park, I. Reines, C. Patel, and G. M. Rebeiz, "High-Q RF-MEMS 4–6 GHz tunable evanescent-mode cavity filter", *IEEE Trans. Microw. Theory Techn.*, vol. 58, no. 2, pp. 381–389, 2010.

[76] X. Gong, A. Margomenos, B. Liu, W. J. Chappell, and L. P. Katehi, "High-Q evanescent-mode filters using silicon micromachining and polymer stereolithography (sl) processing", in *IEEE MTT-S Int. Microw. Symp. Dig.*, IEEE, vol. 2, 2004, pp. 433–436.

[77] R. G. Carter, J. Feng, and U. Becker, "Calculation of the properties of reentrant cylindrical cavity resonators", *IEEE Trans. Microw. Theory Techn.*, vol. 55, no. 12, pp. 2531–2538, 2007.

[78] S. M. Hou, J. H. Lang, A. H. Slocum, A. C. Weber, and J. R. White, "A high-Q widely tunable gigahertz electromagnetic cavity resonator", *J. Microelectromech. Syst.*, vol. 15, no. 6, pp. 1540–1545, 2006.

[79] X. Liu, L. P. Katehi, W. J. Chappell, and D. Peroulis, "A 3.4–6.2 GHz continuously tunable electrostatic MEMS resonator with quality factor of 460–530", in *IEEE MTT-S Int. Microw. Symp. Dig.*, IEEE, 2009, pp. 1149–1152.

[80] W. C. Chew and J. A. Kong, "Effects of fringing fields on the capacitance of circular microstrip disk", *IEEE Trans. Microw. Theory Techn.*, vol. 28, no. 2, pp. 98–104, 1980.

[81] H. Joshi, H. H. Sigmarsson, and W. J. Chappell, "Analytical modeling of highly loaded evanescent-mode cavity resonators for widely tunable high-Q filter applications", *Proc. Union Radio Sci. Int.(URSI)*, 2008.

[82] S. P. Morgan Jr, "Effect of surface roughness on eddy current losses at microwave frequencies", *J. Appl. Phys.*, vol. 20, no. 4, pp. 352–362, 1949.

[83] A. F. Horn III, J. W. Reynolds, P. A. LaFrance, and J. C. Rautio, "Effect of conductor profile on the insertion loss, phase constant, and dispersion in thin high frequency transmission lines", *DesignCon 2010 Proceedings, Santa Clara, CA*, 2010.

[84] H. Arslan, *Cognitive radio, software defined radio, and adaptive wireless systems*. Dordrecht, The Netherlands: Springer, 2007, vol. 10.

[85] A. R. Brown and G. M. Rebeiz, "A varactor-tuned RF filter", *IEEE Trans. Microw. Theory Techn.*, vol. 48, no. 7, pp. 1157–1160, Jul. 2000.

[86] J. Lee and K. Sarabandi, "An analytic design method for microstrip tunable filters", *IEEE Trans. Microw. Theory Techn.*, vol. 56, no. 7, pp. 1699–1706, 2008.

[87] M. Sánchez-Renedo, R. Gómez-García, J. Alonso, C. Briso-Rodríguez, *et al.*, "Tunable combline filter with continuous control of center fre-

quency and bandwidth", *IEEE Trans. Microw. Theory Techn.*, vol. 53, no. 1, pp. 191–199, 2005.

[88] S.-J. Park and G. M. Rebeiz, "Low-loss two-pole tunable filters with three different predefined bandwidth characteristics", *IEEE Trans. Microw. Theory Techn.*, vol. 56, no. 5, pp. 1137–1148, 2008.

[89] W. M. Fathelbab and M. B. Steer, "A reconfigurable bandpass filter for RF/microwave multifunctional systems", *IEEE Trans. Microw. Theory Techn.*, vol. 53, no. 3, pp. 1111–1116, 2005.

[90] W.-H. Tu, "Switchable microstrip bandpass filters with reconfigurable on-state frequency responses", *IEEE Microw. Wireless Compon. Lett.*, vol. 20, no. 5, pp. 259–261, 2010.

[91] S. Atash-bahar, S. Saeedi, and H. H. Sigmarsson, "Active resonator using comb-shaped defected ground structure with negative resistance", in *2015 IEEE 16th Annual Wireless and Microwave Technology Conference (WAMICON)*, IEEE, 2015, pp. 1–4.

[92] Y. Liu, A. Anand, and X. Liu, "Design of low phase-noise voltage-controlled oscillator using tunable evanescent-mode cavity", in *2014 IEEE Radio and Wireless Symposium (RWS)*, IEEE, 2014, pp. 82–84.

[93] S. Moon, H. H. Sigmarsson, H. Joshi, and W. J. Chappell, "Substrate integrated evanescent-mode cavity filter with a 3.5 to 1 tuning ratio", *IEEE Microw. Wireless Compon. Lett.*, vol. 20, no. 8, pp. 450–452, 2010.

[94] B. Kapilevich, "A varactor-tunable filter with constant bandwidth and loss compensation", *Microwave Journal*, vol. 50, no. 4, p. 106, 2007.

[95] N. Zahirovic, S. Fouladi, R. R. Mansour, and M. Yu, "Tunable suspended substrate stripline filters with constant bandwidth", in *IEEE MTT-S Int. Microw. Symp. Dig.*, IEEE, 2011, pp. 1–4.

[96] H. Joshi, H. H. Sigmarsson, S. Moon, D. Peroulis, and W. J. Chappell, "High-Q narrow-band tunable filters with controllable bandwidth", in *IEEE MTT-S Int. Microw. Symp. Dig.*, IEEE, 2009, pp. 629–632.

[97] E. J. Naglich, J. Lee, D. Peroulis, and W. J. Chappell, "High-Q tunable bandstop filters with adaptable bandwidth and pole allocation", in *IEEE MTT-S Int. Microw. Symp. Dig.*, IEEE, 2011, pp. 1–4.

[98] E. J. Naglich, J. Lee, and D. Peroulis, "Tunable bandstop filter with a 17-to-1 upper passband", in *IEEE MTT-S Int. Microw. Symp. Dig.*, IEEE, 2012, pp. 1–3.

[99] M. Yu, "Power-handling capability for RF filters", *IEEE Microw. Mag.*, vol. 8, no. 5, pp. 88–97, 2007.

[100] K. Entesari and G. M. Rebeiz, "RF MEMS, BST, and GaAs varactor system-level response in complex modulation systems", *Int. J. RF Microw. C. E.*, vol. 18, no. 1, pp. 86–98, 2008.

[101] P. Blondy and D. Peroulis, "Handling RF power: the latest advances in RF-MEMS tunable filters", *IEEE Microw. Mag.*, vol. 14, no. 1, pp. 24–38, 2013.

[102] X.-P. Chen and W. K, "Concept of substrate integrated circuits applied to filter design and reachable performances", *IEEE Proc. Eur. Microw. Conf. Workshop Recent Advances in Substrate Integrated Wavegnide Filters: Simulations, Technologies and Performances, Paris, France*, pp. 1–30, 2010.

[103] X.-P. CHEN and K Wu, "Systematic overview of substrate integrated waveguide (SIW) filters: design and performance tradeoffs", in *Asia-Pacific Microw. Conf. Workshop on Recent Progress in Filters and Couplers, Yokohama, Japan*, 2010, pp. 1–24.

[104] T. Djerafi, K. Wu, and D. Deslandes, "A temperature-compensation technique for substrate integrated waveguide cavities and filters", *IEEE Trans. Microw. Theory Techn.*, vol. 60, no. 8, pp. 2448–2455, 2012.

[105] R. R. Mansour, B. Jolley, S. Ye, F. S. Thomson, and V. Dokas, "On the power handling capability of high temperature superconductive filters", *IEEE Trans. Microw. Theory Techn.*, vol. 44, no. 7, pp. 1322–1338, 1996.

[106] G. Schennum and G Rosati, "Minimizing passive intermodulation product generation in high power satellites", in *IEEE Proc. Aerosp. Appl. Conf.*, IEEE, vol. 3, 1996, pp. 155–164.

[107] G. M. Rebeiz, *RF MEMS: theory, design, and technology*. Hoboken, NJ, USA: Wiley, 2004.

[108] X. Liu, L. P. Katehi, W. J. Chappell, and D. Peroulis, "Power handling capability of high-Q evanescent-mode RF MEMS resonators with flexible diaphragm", in *Proc. Asia–Pacific Microw. Conf.*, IEEE, 2009, pp. 194–197.

[109] ——, "Power handling of electrostatic MEMS evanescent-mode (EVA) tunable bandpass filters", *IEEE Trans. Microw. Theory Techn.*, vol. 60, no. 2, pp. 270–283, 2012.

[110] A. Semnani, K. Chen, and D. Peroulis, "Microwave gas breakdown in tunable evanescent-mode cavity resonators", *IEEE Microw. Wireless Compon. Lett.*, vol. 24, no. 5, pp. 351–353, 2014.

[111] K. Chen, H. H. Sigmarsson, and D. Peroulis, "Power handling of high-Q evanescent-mode tunable filter with integrated piezoelectric actuators", in *IEEE MTT-S Int. Microw. Symp. Dig.*, IEEE, 2012, pp. 1–3.

[112] K. Chen, A. Semnani, and D. Peroulis, "High-power microwave gas discharge in high-Q evanescent-mode cavity resonators and its instantaneous long-term effects", in *IEEE MTT-S Int. Microw. Symp. Dig.*, IEEE, 2013, pp. 1–4.

[113] C. Ernst, V. Postoyalko, and N. G. Khan, "Relationship between group delay and stored energy in microwave filters", *IEEE Trans. Microw. Theory Techn.*, vol. 49, no. 1, pp. 192–196, 2001.

[114] E. Jones, L Young, and G. Matthaei, "Microwave band-stop filters with narrow stop bands", *IRE Trans. Microw. Theory Techn.*, vol. 10, no. 6, pp. 416–427, 1962.

[115] J. D. Rhodes, "Waveguide bandstop elliptic function filters", *IEEE Trans. Microw. Theory Techn.*, vol. 20, no. 11, pp. 715–718, 1972.

[116] I. Hunter and J. D. Rhodes, "Electronically tunable microwave bandstop filters", *IEEE Trans. Microw. Theory Techn.*, vol. 30, pp. 1361–1367, 1982.

[117] S. Han, X.-L. Wang, and Y. Fan, "Analysis and design of multiple-band bandstop filters", *Progr. Electromagn. Res.*, vol. 70, pp. 297–306, 2007.

[118] B. H. Ahmad and I. C. Hunter, "Design and fabrication of a substrate integrated waveguide bandstop filter", in *IEEE 38th Eur. Microw. Conf.*, 2008, pp. 40–42.

[119] R. J. Cameron, "Advanced coupling matrix synthesis techniques for microwave filters", *IEEE Trans. Microw. Theory Techn.*, vol. 51, no. 1, pp. 1–10, 2003.

[120] S. Saeedi, J. Lee, and H. H. Sigmarsson, "Double conversion method for synthesis of inverse filters", in *IEEE MTT-S Int. Microw. Symp. Dig.*, IEEE, 2015, pp. 1–4.

[121] D. R. Jachowski and C. Rauscher, "Frequency-agile bandstop filter with tunable attenuation", in *IEEE MTT-S Int. Microw. Symp. Dig.*, 2009.

[122] A. Abunjaileh, I. C. Hunter, *et al.*, "Tunable bandpass and bandstop filters based on dual-band combline structures", *IEEE Trans. Microw. Theory Techn.*, vol. 58, no. 12, pp. 3710–3719, 2010.

[123] J. Lee, E. J. Naglich, and W. J. Chappel, "Frequency response control in frequency-tunable bandstop filters", *IEEE Microw. Wireless Compon. Lett.*, vol. 20, no. 12, pp. 669–671, 2010.

[124] E. J. Naglich, J. Lee, D. Peroulis, and W. J. Chappell, "Extended passband bandstop filter cascade with continuous 0.85–6.6 GHz coverage", *IEEE Trans. Microw. Theory Techn.*, vol. 60, no. 1, pp. 21–30, 2012.

[125] T. Snow, J. Lee, and W. J. Chappell, "Tunable high quality-factor absorptive bandstop filter design", in *IEEE MTT-S Int. Microw. Symp. Dig.*, IEEE, 2012, pp. 1–3.

[126] T.-H. Lee, C.-S. Ahn, Y.-S. Kim, and J. Lee, "Extension of bandstop filter topology with inter-resonator coupling structures to higher-order filters", *IEEE Microw. Wireless Compon. Lett.*, vol. 23, no. 8, pp. 403–405, 2013.

[127] E. J. Naglich, A. C. Guyette, and D. Peroulis, "High-Q intrinsically-switched quasi-absorptive tunable bandstop filter with electrically-short resonators", in *IEEE MTT-S Int. Microw. Symp. Dig.*, IEEE, 2014, pp. 1–4.

[128] K. Lee, T.-H. Lee, C.-S. Ahn, Y.-S. Kim, and J. Lee, "Reconfigurable dual-stopband filters with reduced number of couplings between a transmission line and resonators", *IEEE Microw. Wireless Compon. Lett.*, vol. 25, no. 2, pp. 106–108, 2015.

[129] S. Amari and U. Rosenberg, "A universal building block for advanced modular design of microwave filters", *IEEE Microw. Wireless Compon. Lett.*, vol. 13, no. 12, pp. 541–543, 2003.

[130] ——, "New building blocks for modular design of elliptic and self-equalized filters", *IEEE Trans. Microw. Theory Techn.*, vol. 52, no. 2, pp. 721–736, 2004.

[131] S. Amari, U. Rosenberg, and J. Bornemann, "Singlets, cascaded singlets, and the nonresonating node model for advanced modular design of elliptic filters", *IEEE Microw. Wireless Compon. Lett.*, vol. 14, no. 5, pp. 237–239, 2004.

[132] *Piezo Systems, Inc.* (Accessed: 2 Nov. 2015). [Online]. Available: `http://www.piezo.com/prodmaterialprop.html/`.

[133] H. H. Sigmarsson, "Widely tunable, high-Q, evanescent-mode cavity filters: fabrication, control, and reconfigurability", PhD dissertation, Purdue University, West Lafayette, IN, USA, 2010.

[134] J. Dunsmore, "Tuning band pass filters in the time domain", in *IEEE MTT-S Int. Microw. Symp. Dig.*, IEEE, vol. 3, 1999, pp. 1351–1354.

[135] V. Miraftab and R. R. Mansour, "Computer-aided tuning of microwave filters using fuzzy logic", *IEEE Trans. Microw. Theory Techn.*, vol. 50, no. 12, pp. 2781–2788, 2002.

[136] J. Gorin, B. Erickson, and D. Rath, *YIG filter tuning system*, US Patent Application US 2007/0 139 132 A1, Jun. 2007, (Accessed: 2 Nov. 2015). [Online]. Available: `http://www.patentlens.net/patentlens/patent/US20070139132A1/en/`.

[137] N. Zahirovic, R. R. Mansour, and M. Yu, "Scalar measurement-based algorithm for automated filter tuning of integrated chebyshev tunable filters", *IEEE Trans. Microw. Theory Techn.*, vol. 58, no. 12, pp. 3749–3759, 2010.

[138] H. H. Sigmarsson, A. Christianson, H. Joshi, S. Moon, D. Peroulis, and W. J. Chappell, "In-situ control of tunable evanescent-mode cavity filters using differential mode monitoring", in *IEEE MTT-S Int. Microw. Symp. Dig.*, IEEE, 2009, pp. 633–636.

[139] H. H. Sigmarsson, E. Binkerd, J. Maas, J. Lee, D. Peroulis, and W. J. Chappell, "Practical implementation of frequency monitoring for widely tunable bandpass filters", in *Int. Symp. Microelectron.*, International Microelectronics Assembly and Packaging Society, 2010, pp. 874–880.

[140] D Robben and S. Peik, "Microwave resonator and filter tuning by an ultrasonic piezo motor in a phased locked loop", in *IEEE MTT-S Int. Microw. Symp. Dig.*, IEEE, 2011, pp. 1–4.

[141] J. R. De Luis, Q. Gu, A. S. Morris, and F. De Flaviis, "A novel frequency control loop for tunable notch filters", *IEEE Trans. Microw. Theory Techn.*, vol. 59, no. 9, pp. 2265–2274, 2011.

[142] *Analog to digital converters*, (Accessed: 2 Nov. 2015). [Online]. Available: `http://www.analog.com/en/products/analog-to-digital-converters.html`.

[143] *AD7747, 24-bit capacitance-to-digital converter with temperature sensor*, (Accessed: 2 Nov. 2015). [Online]. Available: `http://www.analog.com/en/products/analog-to-digital-converters/ad-converters/ad7747.html`.

[144] *3D printing materials*, (Accessed: 2 Nov. 2015). [Online]. Available: `http://envisiontec.com/3d-printing-materials`.

[145] *Dr. Sigmarsson Research Group*, The University of Oklahoma, Advanced Radar Research Center, 3190 Monitor Ave. Norman, OK 73019, USA. Phone: (+1) 405-325-2971. Email: h.sigmarsson@ou.edu.

[146] I. S. Gradshteyn and I. M. Ryzhik, *Table of Integrals, Series, and Products*. Burlington, MA, USA: Academic Press, 2007.

[147] H. W. Bode, *Network Analysis and Feedback Amplifier Design*. New York, NY, USA:Van Nostrand, 1945.

[148] *Rapid PCB prototyping*, (Accessed: 2 Nov. 2015). [Online]. Available: http://www.lpkfusa.com/products/pcb_prototyping/machines/protomat_s103/.

[149] *Online source of copper*, (Accessed: 2 Nov. 2015). [Online]. Available: http://basiccopper.com/.

[150] *Pyralux LF copper clad laminate*, (Accessed: 2 Nov. 2015). [Online]. Available: http://www.dupont.com/products-and-services/electronic-electrical-materials/flexible-rigidflex-circuit-materials/brands/pyralux-flexible-circuit/products/pyralux-lf.html.

[151] *Silver conductive epoxy adhesive*, (Accessed: 2 Nov. 2015). [Online]. Available: http://www.mgchemicals.com/products/adhesives/electrically-conductive/silver-conductive-epoxy-8331/.

Appendix A

A New Property of Butterworth Lowpass Prototype

In Chapter 2, it was discussed that for a Butterworth lowpass prototype filters with 3.0 dB of attenuation at the corner frequency of $\omega_0 = 1$ rad/s, the polynomials and the constants are found as,

$$P(s) = 1 \tag{A.1a}$$

$$F(s) = s^N \tag{A.1b}$$

$$\varepsilon_R = 1 \tag{A.1c}$$

$$\varepsilon = 1 \tag{A.1d}$$

where N is the order of the filter. $E(s)$ can be found using (2.4) and the Hurwitz polynomial property for the lossless case.

Also, the transfer function for a Butterworth lowpass filter can be written

in terms of its poles as [65],

$$S_{21}(s) = \frac{1}{\prod_{k=1}^{N}(s - p_k)} = \frac{1}{s^N - (\sum_{k=1}^{N} p_k)s^{(N-1)} + \ldots - \prod_{k=1}^{N} p_k} \tag{A.2}$$

where the poles are defined by

$$p_k = -\sin(\theta_k) + j\cos(\theta_k) \tag{A.3a}$$

$$\theta_k = (2k-1)\frac{\pi}{2N} \qquad \text{for } k = 1, 2, 3, ..., N \tag{A.3b}$$

Then $S_{11}(s)$ can be found from $S_{21}(s)$ using (2.4) which is used to construct the input driving point impedance to extract the prototype coefficients (g_k) for the filter [65]. These values are tabulated in literature [20], [65] for different filter orders. However, as mentioned before, closed form expressions have been developed [20], which directly give the prototype filter normalized element values (with cutoff frequency of 1 rad/s and unitary terminations) as

$$\mathrm{g}_0 = \mathrm{g}_{N+1} = 1\ \Omega \tag{A.4a}$$

$$\mathrm{g}_k = 2\ \sin\left(\frac{(2k-1)\pi}{2N}\right) = 2\sin(\theta_k) \qquad \text{for } k = 1, 2, 3, ..., N \tag{A.4b}$$

where ladder lowpass prototypes with the elements definition have been shown in figure 2.5. Knowing p_k, the coefficient of the second term in the denominator of (A.2) can be simplified in two different ways. First, using (A.3a), it can be

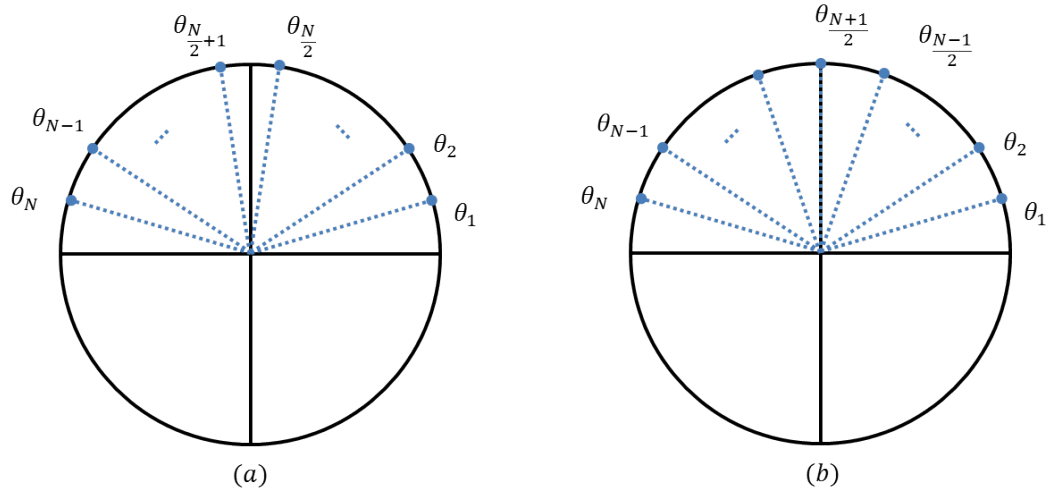

Figure A.1: Positions of the angles of poles, θ_k, defined in (A.3b) for the Butterworth lowpass prototype on the real unit trigonometric circle, (a) N even, (b) N odd.

written

$$-\sum_{k=1}^{N} p_k = \sum_{k=1}^{N} \sin(\theta_k) - j\sum_{k=1}^{N} \cos(\theta_k) \tag{A.5}$$

Distribution of θ_k for both odd and even orders can been seen in figure A.1 where they are equally spaced on the circumference. For all even orders, the angles are symmetrically distributed about the vertical axis and form supplementary pairs. Therefore, any combination of θ_k and $\theta_{(N-k+1)}$ has equal sine and opposite cosine contributions. Thus when evaluating the sum in (A.5), the imaginary part is canceled and the real part is doubled. This is correct for odd orders as well, with the exception of the middle angle which is always $\pi/2$ rad/s and does not contribute to the imaginary part. Therefore, (A.5) can written as

$$-\sum_{k=1}^{N} p_k = \begin{cases} \sum_{k=1}^{\frac{N}{2}} 2\sin(\theta_k) & \text{for } N \text{ even} \\ \sum_{k=1}^{\frac{N-1}{2}} 2\sin(\theta_k) + \sin(\theta_{\frac{N+1}{2}}) & \text{for } N \text{ odd} \end{cases} \tag{A.6}$$

Applying (A.4b) to (A.6) will give,

$$-\sum_{k=1}^{N} p_k = \begin{cases} \sum_{k=1}^{\frac{N}{2}} \mathrm{g}_k & \text{for } N \text{ even} \\ \sum_{k=1}^{\frac{N-1}{2}} \mathrm{g}_k + \frac{1}{2}\mathrm{g}_{(\frac{N+1}{2})} & \text{for } N \text{ odd} \end{cases} \tag{A.7}$$

Multiplying (A.7) by two and making use of the symmetry property of the prototype filter coefficients ($\mathrm{g}_k = \mathrm{g}_{N-k}$), we can rewrite it in a more closed form by combining the odd and even cases as

$$-2\sum_{k=1}^{N} p_k = \sum_{k=1}^{N} \mathrm{g}_k \qquad \text{for all } N(\text{even and odd}) \tag{A.8}$$

Now, (A.5) is evaluated using the following identities [146],

$$\sum_{k=1}^{N} \sin(2k-1)x = \sin^2(Nx)\csc(x) \tag{A.9a}$$

$$\sum_{k=1}^{N} \cos(2k-1)x = \frac{1}{2}\sin(2Nx)\csc(x) \tag{A.9b}$$

by setting $x = \frac{\pi}{2N}$, (A.9a) and (A.9b) can be written as

$$\sum_{k=1}^{N} \sin(2k-1)\frac{\pi}{2N} = \csc(\frac{\pi}{2N}) \tag{A.10a}$$

$$\sum_{k=1}^{N} \cos(2k-1)\frac{\pi}{2N} = 0 \tag{A.10b}$$

or by using (A.3b)

$$\sum_{k=1}^{N} \sin(\theta_k) = \csc(\frac{\pi}{2N}) \tag{A.11a}$$

$$\sum_{k=1}^{N} \cos(\theta_k) = 0 \tag{A.11b}$$

Therefore, using (A.11a) and (A.11b), (A.5) is written as

$$-\sum_{k=1}^{N} p_k = \csc(\frac{\pi}{2N}) = \frac{1}{\sin(\theta_1)} \tag{A.12}$$

and finally using (A.4b), (A.12) becomes

$$-2\sum_{k=1}^{N} p_k = \frac{4}{\mathrm{g}_1} \tag{A.13}$$

Comparison between (A.8) and (A.13), reveals that for the Butterworth normalized prototype filter,

$$\sum_{k=1}^{N} \mathrm{g}_k = \frac{4}{\mathrm{g}_1} \tag{A.14}$$

which is an interesting property that shows for a Butterworth prototype fil-

ter, the summation of all prototype coefficients can be found from the first coefficient.

Using the same procedure, it can be shown that (A.13) holds for Chebyshev prototype lowpass filter regardless of the ripple value. In fact, (A.2) still holds for a lowpass Chebyshev filter with ripple constant ε, where its poles are defined by

$$p_k = -\eta \sin(\theta_k) - j\sqrt{1+\eta^2}\cos(\theta_k) \tag{A.15}$$

where θ_k is defined the same as (A.3b) and

$$\eta = \sinh\left(\frac{1}{N}\sin^{-1}(\frac{1}{\varepsilon})\right) \tag{A.16}$$

Therefore, similar to (A.5), we can write

$$-\sum_{k=1}^{N} p_k = \eta\sum_{k=1}^{N}\sin(\theta_k) + j\sqrt{1+\eta^2}\sum_{k=1}^{N}\cos(\theta_k) \tag{A.17}$$

Using (A.11a) and (A.11b), (A.17) is simplified to

$$-\sum_{k=1}^{N} p_k = \eta\csc(\frac{\pi}{2N}) = \frac{\eta}{\sin(\theta_1)} \tag{A.18}$$

On the other hand, the first coefficient of the lowpass prototype has been defined [20] as

$$\mathrm{g}_1 = \frac{2}{\eta}\sin(\frac{\pi}{2N}) = \frac{2}{\eta}\sin(\theta_1) \tag{A.19}$$

Finally, comparing (A.18) and (A.19) gives

$$-\sum_{k=1}^{N} p_k = \frac{2}{\mathrm{g}_1} \tag{A.20}$$

which is the same as the (A.13).

Though, (A.14) does not hold for Chebyshev filters, (A.20) by itself is of great importance. It shows that the coefficient of the second term in the denominator of $S_{21}(s)$ for both Butterworth and Chebyshev filters is only a function of g_1. This property has application in direct frequency scaling of coupling matrix for designing filters with predefined coupling values.

A common use of the sum of the lowpass prototype coefficients, that is (A.14), is the calculation of a filter insertion loss in the presence of loss. Cohn [17] has shown that dissipative loss in a lowpass (bandpass) multi-coupled prototype filter at $\omega = 0$ rad/s ($\omega = \omega_0$) can be estimated by

$$L_0 = \frac{4.343}{\Delta} \sum_{k=1}^{N} \frac{\mathrm{g}_k}{Q_{uk}} \quad \mathrm{dB} \tag{A.21}$$

where Δ is the filter fractional bandwidth and Q_{uk} is the unloaded quality factor of the k-th resonator. In the case of uniform quality factor for all resonators, which is of considerable practical interest, (A.21) is written as

$$L_0 = \frac{4.343}{\Delta Q_u} \sum_{k=1}^{N} \mathrm{g}_k \quad \mathrm{dB} \tag{A.22}$$

Using the new property of Butterworth filters (A.14), (A.22) can be expressed as

$$L_0 = \frac{17.372}{\Delta Q_u \mathrm{g}_1} = \frac{8.686}{\Delta Q_u \sin(\frac{\pi}{2N})} \quad \mathrm{dB} \tag{A.23}$$

which eliminates the need for the summation of g_k, and the prototype coefficient table. In other words, knowing the unloaded quality factor of resonators and the filter fractional bandwidth, the insertion loss of a Butterworth filter (at $\omega = 0$ rad/s and $\omega = \omega_0$ in the case of lowpass and bandpass filters, respectively) can be calculated quickly using an ordinary calculator for different filter orders without referring to any tables or software. For higher order filters where the sine contribution can be approximated by its argument, (A.23) can be written as

$$L_0 \approx \frac{5.530N}{\Delta Q_u} \quad \text{dB} \tag{A.24}$$

Figure A.2 shows the percent error due to using of (A.24) instead of (A.23) as a function of filter order. It can be seen, for filters with orders higher than four the error is less than 2%. Additionally, based on the Cohn's and Bode's [147] approximate formulas, it was shown in [20] that the group delay of a Butterworth lowpass filter at $\omega = 0$ rad/s is expressed as

$$\tau_0 = \frac{1}{2}\sum_{k=1}^{N} g_k \tag{A.25}$$

which can be simplified using (A.14). A comparison of (A.14) and (A.25) reveals that

$$\tau_0 = \frac{2}{g_1} = \frac{1}{\sin(\frac{\pi}{2N})} \tag{A.26}$$

This equation shows that the group delay of a Butterworth lowpass filter at $\omega = 0$ rad/s is only a function of the first element value in the prototype filter.

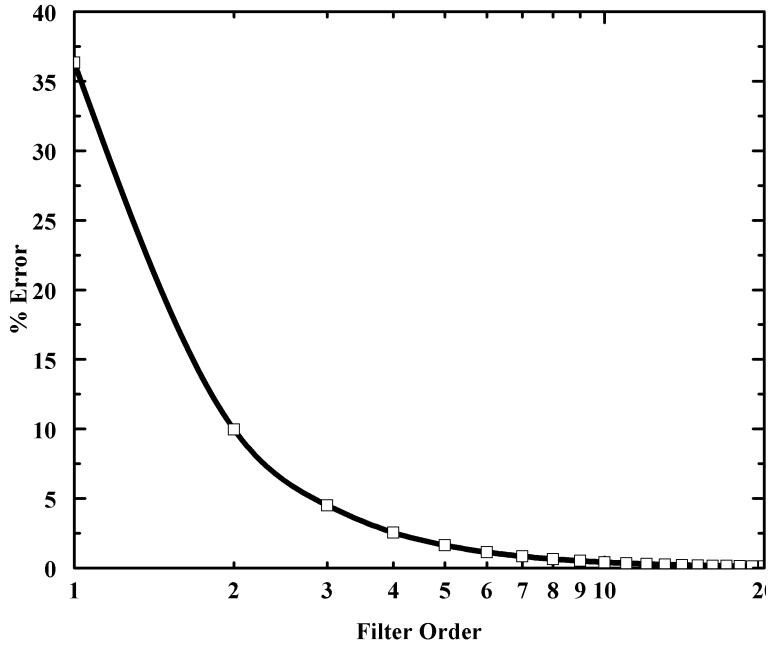

Figure A.2: Error introduced by using the approximation introduced in (A.24) instead of using the full expression in (A.23).

A comparison of the group delay evaluated using (A.26) and its exact value found from circuit analysis using the admittance method is shown in figure A.3 which confirms the accuracy of (A.26). Evaluation of this equation for different filter orders, gives the constant value tabulated in [20] for the calculation of excess loss due to dissipative resonators. Finally, inserting (A.26) into (A.23) gives

$$L_0 = \frac{8.686}{\Delta Q_u}\,\tau_0 \quad \text{dB} \tag{A.27}$$

which is Bode's formula for the excess loss of Butterworth filters with finite quality factor resonators [147]. Therefore, comparing the formulas for the excess loss of the Butterworth filters derived by Bode [147], Cohn [17], and Matthaei [20] to what is presented in this appendix shows that they are all the

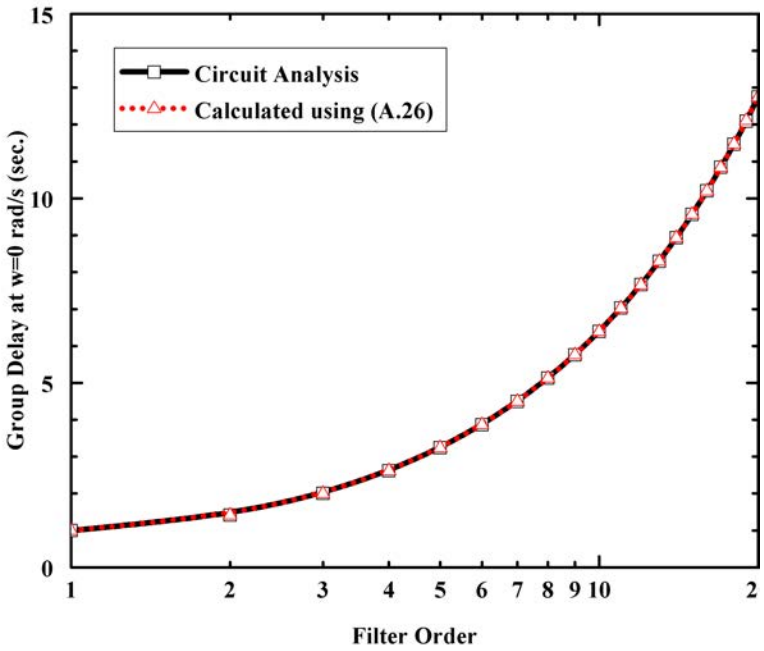

Figure A.3: Comparison between the group delay from the circuit analysis and (A.26) of a normalized, Butterworth, lowpass filter at $\omega = 0$ rad/s.

same in essence. However, the equations presented here are more convenient to evaluate than the others.

Appendix B

Fabrication Process

The step by step fabrication process used throughout this research is presented in this appendix. All drilling and patterning fabrication steps has been performed using an LPKF ProtoMat S103 milling machine [148].

Figure B.1 shows an overview of the fabrication flow and figure B.2 shows a cross-sectional view of the resonator at each step that affects the cross-section. The first step is to drill the via holes forming the side walls of the post. Electroless copper plating is used to form a 1.5 μm seed layer followed by thick copper electroplating. The copper on the top of the PCB is then selectively milled, leaving the top plate of the capacitive post and the outer part of the top metal layer, as shown in step 2 in figure B.1. When the size of air gap is chosen to be less than 20 μm, a thin Parylene layer is deposited on top of the post to protect it from short circuiting to the copper diaphragm. However, due to the high gap size used in this work, the dielectric barrier was deemed unnecessary. To create the top of the cavity, a 25 μm copper foil (from Basic Copper [149]) is laminated on top of the substrate using a 51 μm thick patterned LF0200 Dupont Pyralux assembly adhesive [150]. Step 3 in figure B.1 shows the patterning of the adhesive through the copper foil. The initial capacitive gap is defined by the assembly adhesive. Via holes are drilled

through the new stack and copper plated to form the cavity sidewalls as shown in step 4. In step 5, both the RF feed lines and the external coupling slots are created in the bottom copper layer using a circuit board plotter. SMA connectors are soldered onto the feeds and finally, a 12.7-mm-diameter, commercially available, 2-layer piezoelectric disc actuator from Piezo Systems Inc [132] is attached using conductive silver epoxy, in step 6. Two different epoxies were investigated; one that is MG Chemicals 8331 [151], a commercially available two-part silver epoxy, with a relatively low silver loading, and the second one is a custom made, highly flexible silver epoxy called HFF from Shiva Electronics in Indianapolis, Indiana. HFF provides more mechanical flexibility and is preferred. The resonator cross-section remains unchanged in step 5 and 6.

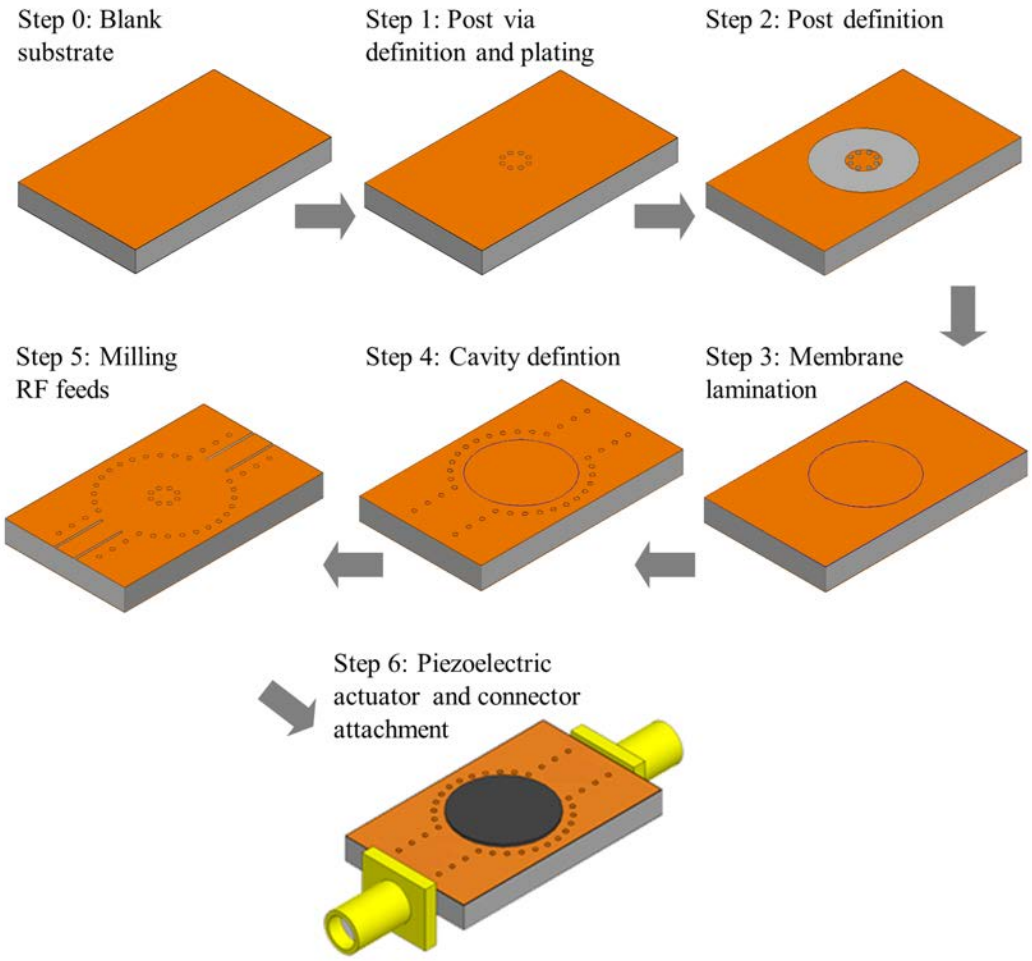

Figure B.1: Substrate-integrated, evanescent-mode, cavity resonator step by step fabrication procedure.

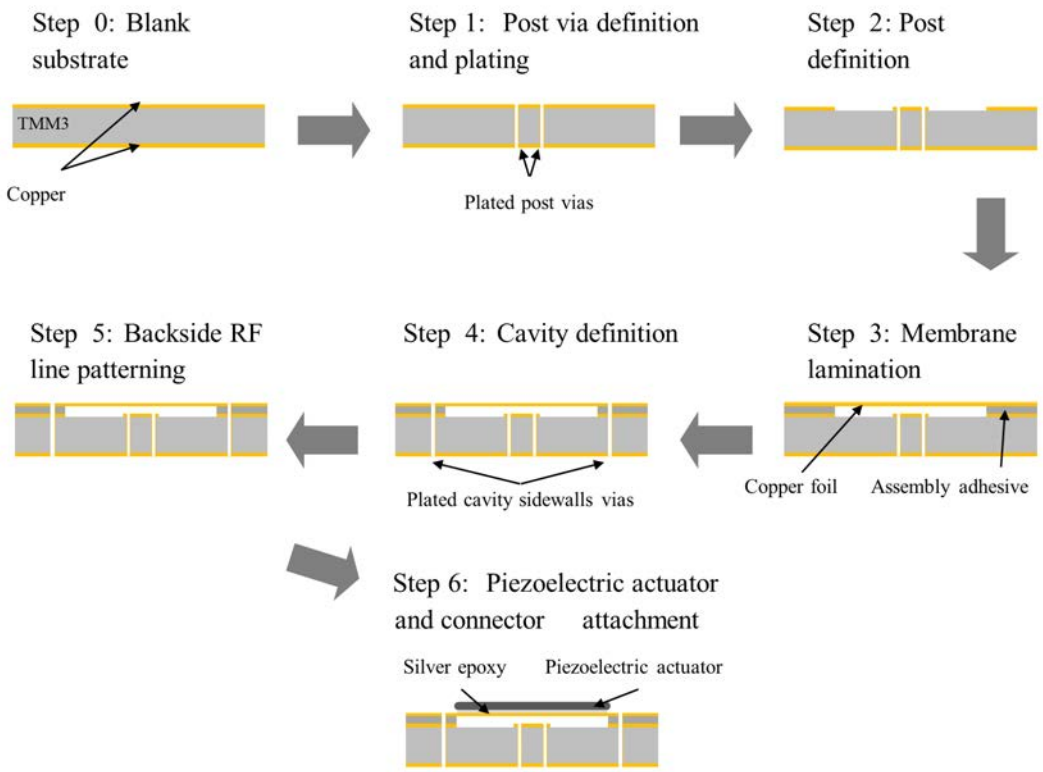

Figure B.2: Cross section of a single resonator used in the tunable, substrate-integrated, evanescent-mode filters, as it is stepped through the fabrication procedure.

Appendix C

List of Acronyms and Abbreviations

μC	Micro-Controller
ADC	Analog-to-Digital Converter
$BP-BS$	Bandpass-Bandstop
CAD	Computer-Aided Design
CDC	Capacitance-to-Digital Converters
CR	Cognitive Radio
CTE	Coefficient of Thermal Expansion
DAC	Digital-to-Analog Converter
DGS	Defective Ground Structure
DSA	Dynamic Spectrum Access
EM	Electromagnetic
EVM	Error Vector Magnitude
FIR	Frequency-Independent Reactive
FM	Frequency Modulation
$FPGA$	Field Programmable Gate Array
$GCPW$	Grounded Coplanar Waveguide
HTS	High-Temperature Superconductors
HV	High Voltage
IMD	Intermodulation Distortion

LCD	Liquid Crystal Display
LCP	Liquid Crystal Polymer
LNA	Low Noise Amplifire
$LTCC$	Low-Temperature Co-fired Ceramics
$MEMS$	Microelectromechanical System
$MMIC$	Monolithic Microwave-Integrated Circuit
NRN	Non Resonating Node
$NTIA$	National Telecommunications Information Administration
PA	Power Amplifire
PC	Personal Computer
PCB	Printed Circuit Board
QAM	Quadrature Amplitude Modulation
$QPSK$	Quadrature Phase Shift Keying
$RSEC$	Radar Spectrum Engineering Criteria
$RTSA$	Real-Time Spectrum Analyzer
SD	Software-Defined
SIW	Substrate-Integrated Waveguide
SRN	Slow Resonating Node
TE	Transverse Electric
TM	Transverse Magnetic
TMM	Thermoset Microwave Material
TZ	Transmission Zero

Appendix D

Summary of Contributions

Journal Papers:

[1] S. Saeedi, J. Lee, and H. H. Sigmarsson, "Novel Coupling Matrix Synthesis for Single-Layer Substrate-Integrated Evanescent-Mode Cavity Tunable Bandstop Filter Design", *IEEE Trans. Microw. Theory Techn.*, Vol. 63, No. 12, pp. 3929-3938, Dec. 2015.

[2] S. Saeedi, J. Lee, and H. H. Sigmarsson, "Tunable, High-Q, Substrate-Integrated, Evanescent-Mode Cavity Bandpass-Bandstop Filter Cascade", Accepted for publication in *IEEE Microw. and Wireless Compon. Lett.*, Nov. 2015.

[3] S. Saeedi, J. Lee, and H. H. Sigmarsson,"A New Property of Maximally-Flat Lowpass Filter Prototype Coefficients With Application in Dissipative Loss Calculations", *in preparation.*

[4] S. Saeedi, J. Lee, and H. H. Sigmarsson, " Prediction of Power Handling in Tunable, High-Q, Substrate-Integrated, Evanescent-Mode Cavity Bandpass Filters", *in preparation.*

[5] S. Saeedi, J. Lee, and H. H. Sigmarsson, "Tunable Bandpass-Bandstop Filter Cascade for Simultaneous Transmission and Reception (STAR) Systems", *in preparation.*

[6] S. Saeedi, J. Lee, and H. H. Sigmarsson, "Application of Slow-Resonating-Nodes (SRNs) in Filter Cascade Design", *in preparation.*

Conference Papers:

[1] S. Saeedi, J. Lee, and H. H. Sigmarsson, "Broadband Implementation of Tunable, Substrate-Integrated, Evanescent-Mode, Cavity Bandpass Filters", in *IEEE 44th Eur. Microwave Conf. (EUMC)*, 2014, pp. 849-852.

[2] S. Saeedi, W. S. Wilson, T. R. Ashley, J. Lee, and H. H. Sigmarsson, "Capacitive-Based, Closed-Loop Frequency Control of Substrate-Integrated Cavity Tunable Filters", in *47th Int. Symp. Microelectronics (iMAPS)*, 2014, pp. 826-831.

[3] S. Saeedi, J. Lee, and H. H. Sigmarsson, "Double Conversion Method for Synthesis of Inverse Filters", in *IEEE MTT-S Int. Microw. Symp Dig. (IMS)*, 2015, pp. 1-4.

[4] S. Atash-bahar, S. Saeedi, and H. H. Sigmarsson„ "Active Resonator Using Comb-Shaped Defected Ground Structure With Negative Resistance", in *IEEE Wireless and Microw. Conf. Proc. (WAMICON)*, 2015, pp. 1-4.

[5] S. Saeedi, S. Atash-bahar, and H. H. Sigmarsson, "Active, Tunable, Substrate-Integrated, Evanescent-Mode Cavity Resonator Using Negative Resistance", accepted in *IEEE Radio Wireless Symp. (RWS)*, 2016.